UNIVERSITAT POLITÈCNICA DE VALÈNCIA

Department of Mechanical and Materials Engineering

PhD Thesis

ADVANCED TECHNIQUES FOR THE TIME-DOMAIN MODELLING OF HIGH-FREQUENCY TRAIN/TRACK INTERACTION

Presented by: Juan Giner Navarro

Supervised by: Prof. Luis Baeza González
Dr. José Martínez Casas

Valencia, September 2017

PhD THESIS

ADVANCED TECHNIQUES FOR THE TIME-DOMAIN MODELLING OF HIGH-FREQUENCY TRAIN/TRACK INTERACTION

---

for the degree of

Doctor in Engineering and Industrial Production

presented by

Juan Giner Navarro

at the

Department of Mechanical and Materials Engineering

Universitat Politècnica de València

Supervised by

Prof. Luis Baeza González
Dr. José Martínez Casas

Valencia, September 2017

PHD THESIS

ADVANCED TECHNIQUES FOR THE TIME-DOMAIN MODELLING OF HIGH-FREQUENCY TRAIN/TRACK INTERACTION

Presented by: Juan Giner Navarro

Supervised by: Prof. Luis Baeza González
Dr. José Martínez Casas

QUALIFYING COMITEE

PRESIDENT: Prof. Ernesto García Vadillo

VOCAL: Dr. Francisco David Denia Guzmán

SECRETARY: Dr. Inés López de Arteaga

Valencia, September 2017

This Thesis has been supported by the Ministerio de Economía y Competitividad and the European Regional Development Fund (projects TRA2010-15669 and TRA2013-45596-C2-1-R), as well as by the Generalitat Valenciana (project Prometeo/2016/007).

Abstract

The aim of the present Thesis is to develop models for the study of very high-frequency phenomena associated with the coupled dynamics of a railway vehicle with the track. Through these models, this Thesis intends to address squeal noise as a particular case of rolling noise when the train negotiates a small radius curve.

Wheel/rail interaction is the predominant source of noise emission in railway operations. Rolling contact couples the wheel and the rail through a very small area, characterised by strongly non-linear and non-steady state dynamics that differentiates rolling noise from any other noise problem. Wheel/rail contact problem is studied based on Kalker's variational theory and the local falling behaviour of the coefficient of friction is introduced by means of a regularisation of Coulomb's law. Its implementation shows that the influence of the falling friction on the creep curves can be assumed negligible, thus rolling contact is finally modelled using a constant coefficient of friction.

Flexibility is introduced in railway substructures through the Finite Element (FE) method in order to cover the high-frequency range. This work adopts a rotatory wheelset model that takes computational advantage of its rotational symmetry. It also develops a cyclic flexible rail model that fixes the translational contact force in a spatial point of the mesh through a technique called Moving Element (ME) method. A modal approach is used to reduce significantly the number of degrees of freedom of the global problem and a diagonalisation technique permits to decouple the resulting modal equations of motion in order to reduce the computational requirements of the time integrator.

Simulations in curving conditions in the time domain are carried out for constant friction conditions in order to study if the proposed interaction model can reproduce squeal characteristics for different curve radii and coefficients of friction.

Keywords: train/track dynamic interaction, rotatory wheelset, cyclic track, wheel/rail rolling contact, falling friction, regularisation of Coulomb's law, Moving Element Method, decoupling techniques, curve squeal.

Resumen

El objetivo de la presente Tesis es desarrollar modelos para el estudio de fenómenos de muy alta frecuencia asociados a la dinámica acoplada de un vehículo ferroviario con la vía. A través de estos modelos, esta Tesis pretende abordar el fenómeno de los chirridos como un caso particular de ruido de rodadura en condiciones de curva cerrada.

La interacción rueda/carril es la fuente predominante de ruido en las operaciones ferroviarias. El contacto es el responsable del acoplamiento entre la rueda y el carril a través de un área muy pequeña caracterizada por una dinámica fuertemente no lineal y no estacionaria. El problema de contacto rueda/carril se estudia mediante la teoría variacional de Kalker y la caída local del coeficiente de fricción se introduce por medio de una regularización de la ley de Coulomb, que muestra que su influencia sobre las curvas de fluencia se puede despreciar. Como consecuencia, el coeficiente de fricción se considera constante.

La flexibilidad se introduce en las subestructuras ferroviarias a través del método de los Elementos Finitos (EF) para cubrir el rango de las altas frecuencias. La Tesis adopta un modelo de eje montado rotatorio que toma ventaja computacional de su axisimetría. También desarrolla un modelo de carril flexible y cíclico que fija la fuerza de contacto en un punto espacial de la malla mediante el método de los Elementos Móviles (EM). Se utiliza un enfoque modal para reducir significativamente el número de grados de libertad del problema global; las ecuaciones de movimiento resultantes en coordenadas modales se desacoplan mediante una técnica de diagonalización para aumentar las prestaciones computacionales del integrador temporal.

Las simulaciones en condiciones de curva en el dominio del tiempo se llevan a cabo en condiciones de fricción constante con el objetivo de estudiar si el modelo de interacción propuesto puede reproducir las características del chirrido en curva para diferentes radios de curva y coeficientes de fricción.

Palabras clave: interacción dinámica tren/vía, eje montado rotatorio, vía cíclica, contacto rueda/carril, caída de fricción, regularización de la ley de Coulomb, método de los Elementos Móviles, técnicas de desacoplamiento, chirrido en curva.

Resum

L’objectiu de la present Tesi és desenvolupar models per a l’estudi de fenòmens de molt alta freqüència associats amb la dinàmica acoblada d’un vehicle ferroviari amb la via. A través d'aquests models, aquesta Tesi pretén abordar el fenomen dels grinyols com un cas particular de soroll de rodament en condicions de corba tancada.

La interacció roda/carril és la font predominant de l’emissió de soroll en les operacions ferroviàries. El contacte acobla la roda i el carril a través d’una àrea molt reduïda que es caracteritza per una dinàmica fortament no lineal i no estacionària. El problema de contacte roda/carril s’estudia mitjançant la teoria variacional de Kalker i el descens local del coeficient de fricció s’introdueix per mitjà d’una regularització de la llei de Coulomb, que demostra que la seua influència en les corbes de fluència es pot suposar insignificant. Per tant, s’utilitza un coeficient de fricció constant per a modelar el contacte.

La flexibilitat s’introdueix en les subestructures de ferrocarril a través del mètode d’Elements Finits (EF) per tal de cobrir el rang d’alta freqüència. La present Tesi adopta un model d’eix muntat rotatori que s’aprofita de la seua la axisimetria. També desenvolupa un model de carril flexible i cíclic que fixa la força de contacte en un punt espacial de la malla a través del mètode dels Elements Mòbils (EM). S’empra un enfocament modal per reduir significativament el nombre de graus de llibertat del problema global, al temps que s’implementa una tècnica de diagonalització que permet desacoblar les equacions modals de moviment per tal d’augmentar les prestacions computacionals de l’integrador temporal.

Les simulacions en les condicions de corba en el domini del temps es duen a terme per a condicions de fricció constant per tal d’estudiar si el model d’interacció proposat pot reproduir les característiques del soroll grinyolant per a diferents radis i coeficients de fricció.

Paraules clau: interacció dinàmica tren/via, eix muntat rotatori, via cíclica, contacte de rodament roda/carril, fricció descendent, regularització de la llei de Coulomb, mètode dels Elements Mòbils, tècniques de desacoblament, soroll grinyolant.

Acknowledgements

Thanks for your support: family, friends, supervisors and fellows.

The author gratefully acknowledges the financial support of:

- Ministerio de Economía y Competitividad through the FPI grant (TRA2010-15669).
- Ministerio de Economía y Competitividad and the European Regional Development Fund (project TRA2013-45596-C2-1-R).
- Generalitat Valenciana (project Prometeo/2016/007, Conselleria d'Educació, Investigació, Cultura i Esport).
- European Commission, through the project "RUN2Rail - Innovative RUNning gear soluTiOns for new dependable, sustainable, intelligent and comfortable RAIL vehicles" (Horizon 2020 Shift2Rail JU call 2017).

Contents

1 INTRODUCTION

1.1 MOTIVATION AND BACKGROUND

The present Doctoral Thesis is part of the research of railway dynamics carried out in the Mechanical Engineering Research Centre (CIIM) of the Universitat Politècnica de València (UPV). Within this line of research, dynamic models for the wheelset, the track and the interaction between both of them have been developed. This interaction affects different types of abnormal wear, e.g. rail corrugation or wheel flats, as well as noise problems.

Noise appears as one of the more important environmental drawbacks of the railway transportation. Although its sound levels are lower than noise from aircraft and road traffic and less annoying in perception at the same sound level [1,2], railway facilities use to be located in the vicinity of urban zones being a source of considerable annoyance for residents. Hence, traffic operators, infrastructure administrators, train manufacturers and society in general all have an interest in the reduction of wheel/rail noise.

Three categories of wheel/rail noise can be distinguished: rolling noise, impact noise, and squeal noise [3]. Rolling noise is caused by the roughness of the wheel and rail running surfaces; the wheelset, the rail and the sleepers radiate noise from the excitation introduced by the roughness in the vertical relative motion [3], while the carbody and the bogies do not contribute significantly [4]. Impact noise is generated by wheel flats, switches and crossings and rail joints, which introduce discrete irregularities [3]. Both are broad-band phenomena involving a large range of frequencies in the audible range. Squeal noise is generally a tonal sound which occurs when the vehicle runs over sharp curves involving high lateral forces; the literature associates this phenomenon with two different mechanisms, one that only can be associated with a falling friction coefficient and other that can be simulated with a constant friction coefficient.

A better physical understanding of the noise generation process, fundamental to assess possible noise reduction measures, requires sophisticated wheel and rail models to address a high-frequency range such as the wheel/rail noise. Nevertheless, both wheel and rail models demand high computational cost, sometimes unapproachable for standard PCs, then numerical strategies to reduce the number of degrees of freedom of the complete railway system are required.

The thesis arises through an investigation into three fundamental elements in the train/track dynamic interaction: a realistic wheel/rail contact model, the introduction of an improved flexible track model and the role of the wheelset dynamics. The main motivation of this thesis is therefore to determine the influence of these three elements in the squeal noise.

1.2 OBJECTIVES

The aim of this thesis is the development of an efficient model for the combined vertical and tangential wheel/rail interaction in the high-frequency range that allows predicting squeal noise. The proposed objectives in the present thesis are:

- Implementation of a three-dimensional contact model that allows considering, in the tangential contact problem, the transient effects; and in the normal contact problem, the non-Hertzian effects, such as the non-elliptical contact patch, the asymmetric traction distribution and the displacement of the contact patch centre respect to the vertical projection of the wheel centre.

- Introduction of the falling friction coefficient in the contact formulation and study of its influence on the creep forces.

- Development of a flexible cyclic track model based on the Moving Element Method (MEM) in order to optimise its computational efficiency. Study of the influence of the boundary conditions of a finite track. Implementation of three different configurations for the rail support: discrete supports (sleepers), Winkler bedding of independent springs and elastic pad layer.

- Development of a complete wheelset/track interaction model and implementation of an efficient modal approach. Introduction of one decoupling technique on the modal equations.

- Analysis of the influence of the instationary wheel/rail contact in the estimation of curve squeal.

1.3 OUTLINE

The general structure of the thesis is as follows:

Chapter 2 details one of the types of excitation detailed in the previous chapter, which will consist of a fundamental part of the scope of the present thesis: the friction-induced vibrations that originate curve squeal.

Chapter 3 provides a literature review of railway vehicle/track dynamic interaction, giving an overview of the most commonly used models to describe the wheelset, the track and the rolling contact between the wheel and the rail.

In Chapter 4, the rolling wheel/rail contact is analysed, with the hypotheses considered in its modelling and the associated formulation. The instationary contact model employed in the thesis is presented and validated by means of comparisons to existing established models. Finally, falling friction coefficient is evaluated for steady-state contact conditions and compared to measurement data.

Chapter 5 describes the formulation used to simulate the dynamic interaction between the railway vehicle and the track. Firstly, the model of the vehicle is detailed, consisting of a wheelset model that includes flexibility and the gyroscopic effects associated with the rotation. Secondly, a flexible cyclic track model is developed through the Moving Element Method (MEM) and the rail support is included with three different configurations: discrete supports (sleepers), a continuous viscoelastic Winkler bedding of independent springs and a finite element (FE) elastic layer (different material than the rail). Advanced techniques for the integration solution of the equation of motion are proposed, including a modal approach to reduce the dimension of the system, a diagonalisation method to decouple the equations and Magnus expansion as a new approach to address first-order linear equation systems.

Chapter 6 presents simulation results of the interaction model. Three different studies are carried out as application of the implemented model. The first one evaluates the frequency-range extension of the complete model by adopting an efficient FE track model based on MEM compared to the Timoshenko beam commonly used in the literature; randomly corrugated rails and wheel flats are the sources of excitation considered. In the second one, curve squeal is investigated using a combination of models for linear complex stability analysis in the frequency domain and non-linear wheel/rail interaction in the time domain. The third one concerns the investigation of stick/slip oscillations due to frictional instability; simulations are carried out with a constant friction law.

The most important conclusions and the main contributions of the thesis are listed in Chapter 7. Future work is also proposed in this chapter.

In the final part of the document, it is included appendices with complementary information about the calculation of the elastic influence coefficients for rectangular elements, which relate the tractions to the displacements (Appendix A) and the Hertzian theory to solve the normal contact problem (Appendix B). Appendix C lists the published papers during the development of the thesis. It is concluded with a list of the literature references consulted and cited therein.

2 **CURVE SQUEAL**

2.1 INTRODUCTION

Curve squeal is a high-frequency and strongly tonal noise which frequently appears when railway vehicles negotiate sharp curves or even in straight tracks for vehicles with independent rotating wheels. The term curve squeal may be used to include several different phenomena with a wide range of dominant frequencies and potentially with different excitation mechanisms. Some authors have made a distinction between 'curve squeal' and the more intermittent, higher frequency and less tonal (more broad-band character) noise that is sometimes called 'flanging noise', associated with contact at the wheel flange.

Squeal is more likely to occur in unfavourable conditions, such as in small radius curves. According to Rudd [5] and Remington [6], the curve radius/bogie wheelbase ratio can be used as indicator whether squeal will occur or not. Generally, if the ratio is lower than 100, curve squeal is expected to occur, although squeal can also be encountered even for ratios higher than 100. Thompson [7] extends this criterion for squeal occurrence in curves of different radius: mostly no squeal for curve radii higher than 500 m; sporadic occurrence between 200 and 500 m; common occurrence for lower than 200 m. Nevertheless, field measurements and experimental tests reveal that the likelihood of occurrence widely differs even on apparently similar conditions [8], indicating an unpredictable character of squeal. Some authors have suggested that not only the tight curves but the deterioration of some aspects of the maintenance of the railway facilities increases the likelihood of occurrence [8]: insufficient lubrication leading to wear as well as noise; poor rail profiles leading to high stresses; or poorly steering rolling stock leading to increased wear and fuel consumption.

This type of noise is usually generated in the most sensitive human ear frequency band between 2 and 8 kHz [7,9] and sometimes even up to 10 kHz [10], which dominates the radiated sound. Thompson [7], Koch *et al.* [11], Hsu *et al.* [12] and Pieringer [13] showed that the tonal frequency during squeal events correspond to eigenfrequencies of axial wheel modes with zero nodal circles and higher harmonics of these excited modes. Remington [14] observed a higher vibration response of the wheel compared to that of the rail, and its sound radiation efficiency is also higher than the corresponding to the rail [7,15]. These results indicate that the tonal nature of squeal is significantly related to the railway wheel dynamics. The combination of the tonal nature and sound pressure levels of up to 130 dB at 0.9 m from the wheel [5] makes squeal one of the loudest and most disturbing types of railway noise. Urban areas are significantly exposed to the annoying tonal noise from curve squeal due to the high number of tight curves in cities. This explains the importance to study the fundamentals of this phenomenon in order to comprehend them and, after that, be able to reduce its potential hazard for public health.

Curve squeal is associated with friction-induced vibrations. Rudd [5] suggested three different mechanisms for energising wheel squeal: longitudinal creepage due to differential slip, flange rubbing between the wheel flange and the gauge face on the rail, and lateral creepage of the wheel tyre on the top of the rail. All three phenomena are closely linked to the curving behaviour of the vehicle. Longitudinal creepage (1) occurs since the outer wheel on a wheelset has a longer running distance through the curve than the inner wheel and the conicity of the wheels can only partly compensate for this difference in running distance in tight curves. Furthermore, in small radius curves, the outer wheel of the leading wheelset in a bogie (and possible the inner trailing wheel) will run into flange contact. Especially the leading wheelset in a bogie rolls with a high angle of attack against the rail in tight curves, which gives rise to a large lateral creepage.

Rudd finally discarded the first two mechanisms from observations that the elimination of longitudinal creepage (by independently driven wheels) and the absence of flange rubbing creepage (the situation at the inner leading wheel) do not prevent squeal [5]. The lateral creepage at the wheel/rail contact is nowadays widely accepted as the most likely reason to induce squeal noise. According to Rudd, unstable vibrations can arise from a falling behaviour of the wheel/rail friction coefficient, which shows dependence with the local slip velocity in the contact area [7,6]. These vibrations are associated with modes of the wheel and they will grow in amplitude until the non-linearities in the creep forces result in a limit cycle. The falling friction law was interpreted by Rudd as negative damping, in which the negative slope of the friction curve is responsible for feeding energy into the system in each period of vibration. These results in self-induced and self-sustained vibrations of the wheel and rail persist as long as there is an external source of energy (as lateral creepage during curve negotiation). His model was preceded by more detailed models of curve squeal based on the concept of ‘falling friction’.

Glocker *et al.* [9] and Pieringer [13] recently presented a curve squeal model that shows stick/slip oscillations. The mechanism has been called wheel modal coupling in the literature [16,13], whose main characteristic is to be able to reproduce squeal with a constant friction coefficient. Therefore, the present thesis has chosen to refer to this mechanism as constant friction mechanism. Glocker and Pieringer identified one axial mode with zero nodal circles and two radial modes of the wheel, which occur at similar frequencies, as essential for the squeal mechanism. Thompson supports this research line [7] proposing that curve squeal originates due to friction-induced vibrations at frequencies corresponding to axial modes of the railway wheel; he points out that the wheel mobility exceeds that of the rail making the wheel to become the dominating noise source at squeal frequencies. By using a non-rotating wheel loaded by a wheel/rail contact force travelling at constant speed around the wheel perimeter, Thompson was able to account for the splitting of resonance peaks even though neglecting inertia effects due to rotation [7].

Pieringer *et al.* [17] investigated the influence of inertia effects due to wheel rotation on squeal predictions. Three models were compared: stationary wheel, stationary wheel with rotating force and full model of wheel rotation including gyroscopic effects and centrifugal stiffening. At 50 km/h no difference was found between the rotating force and the rotating wheel models. Although the rotation of the wheel delays the build-up of the stick/slip oscillation, the stationary wheel model was found to be sufficient to capture the tendency to squeal.

Ding *et al.* [18] included the rail dynamics in a curve squeal model from Huang [19] in both frequency and time domains. Huang's time-domain model was updated to include the rail dynamics in terms of an equivalent state space representation in various directions. Their results showed an important role of the rail especially under constant friction conditions, modifying the unstable frequency from 2 kHz without the rail to 1.1 kHz when it is included.

In order to detail the origin of the phenomenon, the behaviour of a wheelset negotiating a curve is explained in Section 2.2. Both falling and constant friction mechanisms are detailed through simple oscillator models in Section 2.3. Other excitation mechanisms that will be used in this work are described in Section 2.4. The chapter ends with some conclusive remarks in Section 2.5.

2.2 CURVING BEHAVIOUR

Curve squeal can be attributed to ‘imperfect’ curving behaviour of railway vehicles. From a classic approach, the conicity of the wheel and the subsequent difference between the velocities of the inner and the outer wheels naturally steer the wheelset around a curve. Assuming a simplified wheelset model with conic geometry of the wheel profile that circulates on knife-edge rails (see Fig. 2.1), and adopting a non-slip rolling condition, wheelset would adopt a radial position moving laterally outwards the curve according to the following expression:

$$y^k = \frac{e_0 r_0}{\gamma_0 \rho} \tag{2.1}$$

where e_0 is the half distance between contact points (0.75 m for standard track width), r_0 the wheel radius, ρ the curve radius and γ_0 the conicity of the wheel profile. This position, which will be referred as *kinematic position of the wheelset in a curve*, is approximately the quasi-static position that a wheelset in a curve would adopt on which no forces are applied in the track plane. Forces transmitted by the suspensions lead to displacements of the wheelset with respect to the kinematic position. These displacements induce the wheel/rail contact forces that equilibrate the wheelset in a curve. Assuming steady-state conditions, the forces that act in the contact are:

a) **Normal contact forces**. In general, they produce a very small component in the track plane, except in case of flange contact. Depending on the profiles geometry, the range of lateral displacements from which the contact is located in the flange varies between 5 and 10 mm. Except in the perfectly conic wheel profiles on knife-edge rails, a normal force appears in the lateral direction; it progressively increases with the lateral displacement and whose effect is known as gravitational stiffness.

b) **Creep longitudinal contact forces**. They are the creep forces that appear in the rolling direction. Due to the moment equilibrium in the wheelset axis, they must be equal in module and opposite in direction in the inner and outer wheels. As observed in Fig. 2.1, when the lateral displacement is larger than the kinematic one, a velocity at the contact point appears with an approximated value of

$$v_x = \frac{V\gamma_0}{r_0} \Delta y, \tag{2.2}$$

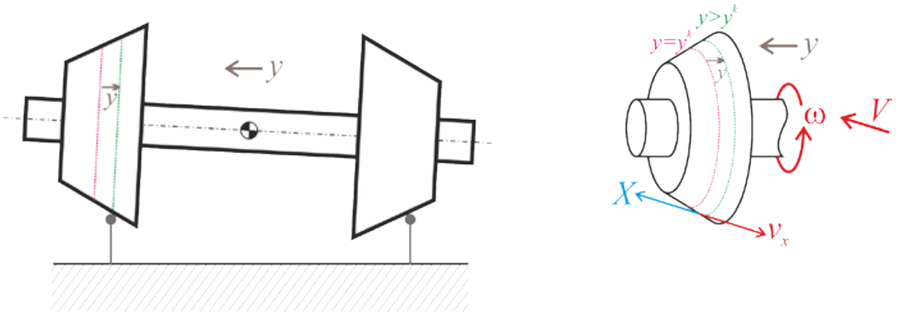

Fig. 2.1. Simplified geometric model for the wheelset (left: elevation view).

being Δy the radius increment with respect to the kinematic displacement. As a consequence of this velocity, creep forces opposite to the velocity appear on the wheelset. If the direction of Δy is outward the curve, the net effect of the longitudinal creep forces is a torque in the vertical axis that leads to oversteer the wheelset (see Fig. 2.2).

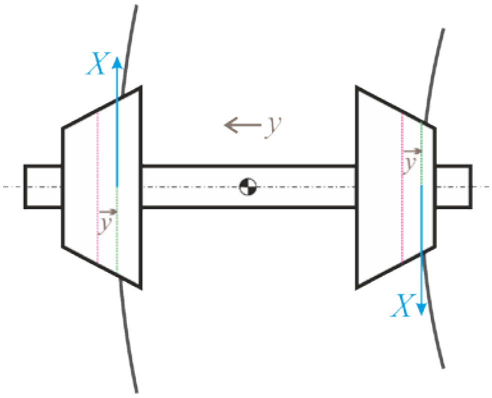

Fig. 2.2. Longitudinal steering forces that come from a lateral displacement outwards the curve with respect to the kinematic position.

c) **Lateral creep forces**. As shown in Fig. 2.3, the existence of an angle of rotation with respect to the vertical axis (yaw angle ψ) leads to lateral forces in the wheel/rail contact. The velocity of the wheelset V is sum of a component in the rolling direction and the lateral creep velocity $V\sin\psi \approx V\psi$. When the yaw angle is oversteering, the forces are directed towards the centre of the curve.

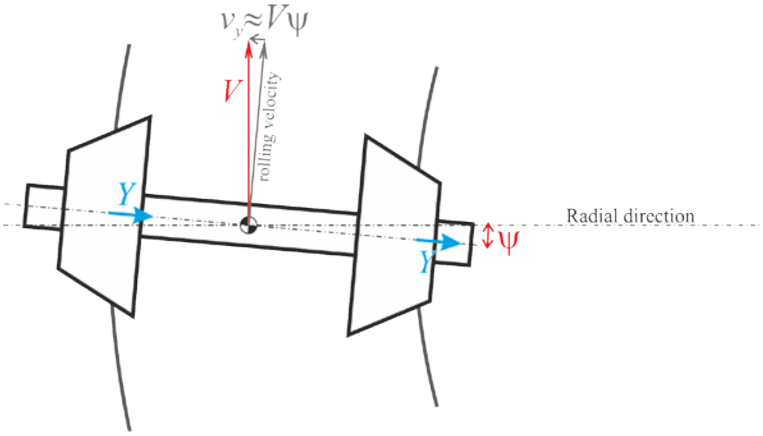

Fig. 2.3. Lateral steering forces that come from an oversteering yaw angle.

2.2.1 Insertion of a free wheelset in a curve

A wheelset in conditions of zero cant deficiency on which no forces act in the track plane due to the primary suspension will adopt a position in which forces due to contact will not appear (which corresponds to the kinematic position of the wheelset in a curve). If lateral actions act on the free wheelset outwards the curve (i.e. "*centrifugal forces*"), they will push the wheelset beyond its kinematic displacement leading to longitudinal forces. In turn, these longitudinal forces will produce a torque that will lead to an oversteering yaw angle (thousandths of a degree). The yaw angle will produce creep velocities that lead to lateral forces that compensate the external action. Fig. 2.4 shows a sketch of the forces on the wheelset, in which it can be observed that there is not moment equilibrium in the direction normal to the track plane. This equilibrium comes from the forces transmitted by the suspension and other steering effects that appear in more realistic models. It must be highlighted that the critical velocity (hunting instability) of a free wheelset is almost zero.

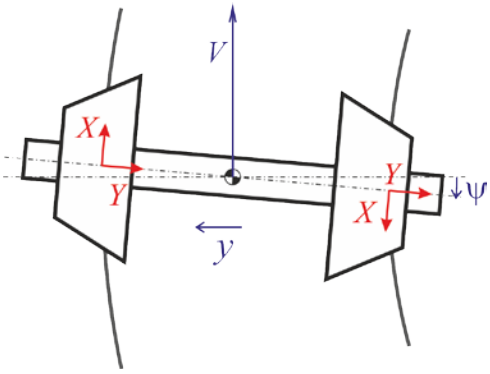

Fig. 2.4. Forces acting on a free wheelset in a curve.

The relative displacements with respect to the kinematic position able to equilibrate the wheelset are very small (there is still no reliable method to measure them in field tests with precision). This position may not be reached if the flange width is not enough, so according to Eq. (2.1) it is more likely to occur when:

- curve radius is very small,
- conicity of the wheel profile is very small,
- wheel diameter is very large,
- track width is big.

In any of these situations, when the wheelset laterally moves less than the corresponding kinematic value, creep forces that understeer the wheelset arise. As a consequence, lateral creep forces push the wheelset outwards the curve, so that wheel/rail contact is produced in the flange of the wheel producing a creep force that equilibrates the wheelset (see Fig. 2.5). In the technical literature, the angle ψ of the wheel with respect to the direction tangential to the curve (especially in cases in which understeers the wheelset) is known as angle of attack.

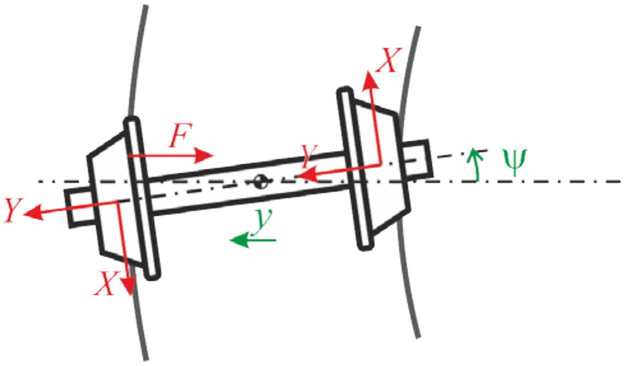

Fig. 2.5. Situation of flange contact due to the displacement of the wheelset outwards the curve in an inadequate steering case. F is the flange normal contact force that compensates the lateral creep forces Y.

2.2.2 Insertion of a bogie in a curve

A first analysis of a bogie in a curve is carried out assuming an infinitely rigid primary suspension (see Fig. 2.6). In this case, the angle of attack of the leading wheelset is approximately $w/(2\rho)$, where w is the wheelbase. This angle is relatively large (understeering), thus the leading wheelset will move until touching wheel flange. Note that in this case the angle of attack is very large, being in some cases around 0.5º.

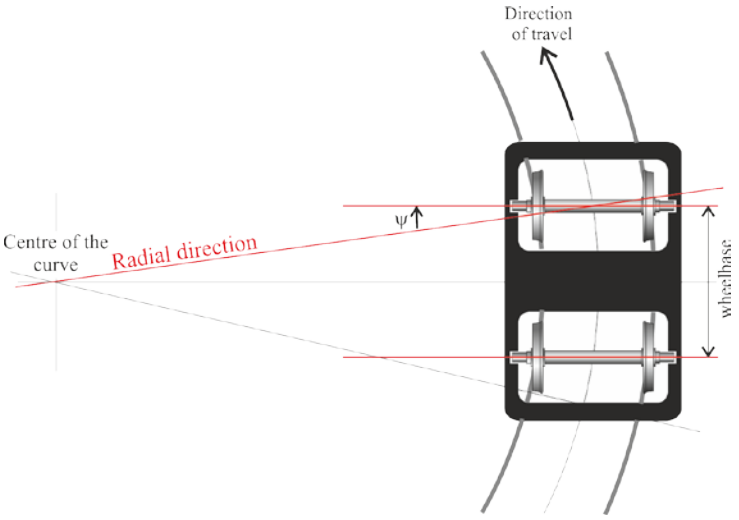

Fig. 2.6. Bogie negotiating a curve.

In general, railway vehicles have a very rigid but finite primary suspension; so that wheelsets have the possibility to reduce the angle of attack or even get a good insertion in the curve through a negative (oversteering) angle of attack (see Fig. 2.7). Regarding the second wheelset, favourable conditions for the insertion are more likely to occur since a negative angle of attack is reached.

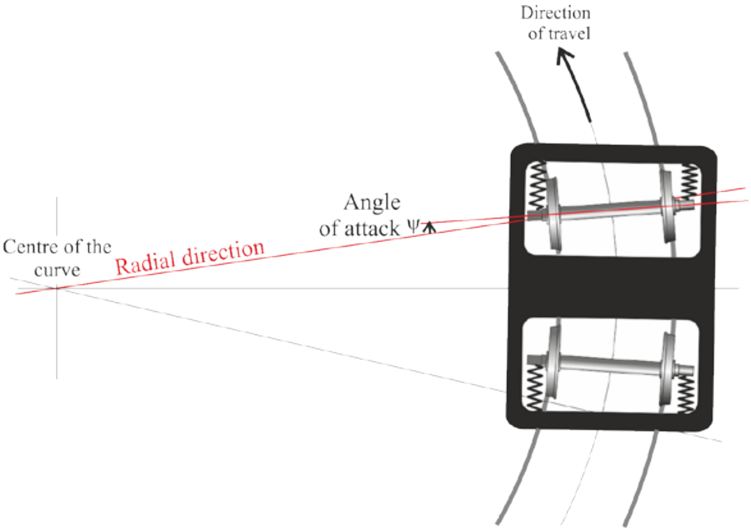

Fig. 2.7. Bogie negotiating a curve with the angle of attack and primary suspensions depicted.

2.3 FRICTIONAL EXCITATION MECHANISMS

Curve squeal remains a difficult problem, with the phenomenon appearing random rather than deterministic. According to different authors, both falling and constant friction mechanisms may coexist in reality [20, 21,13], but their relative importance is still under controversy. The measurements of friction that are available from test rigs are quasi-static [9]. What happens at small amplitudes and high frequencies may be quite different from this quasi-static behaviour that can be measured and indeed may not contain a negative slope at all. To illustrate both mechanisms, and the basic physics behind it, simple oscillator systems with friction are considered consisting of a single mode of vibration or a pair of modes.

2.3.1 Negative friction slope model

In order to illustrate the stick/slip mechanism, a simple model of a mass on a belt moving at velocity V_0 can be used (see Fig. 2.8). The mass *m* is attached to a rigid foundation by a spring of stiffness *k* and damper *c* and held against the belt by a constant normal load *N*. This model can be used to represent a wheel vibrating in a single natural mode. The sliding velocity between the mass and the belt represents the steady-state lateral creep velocity (not the rolling velocity).

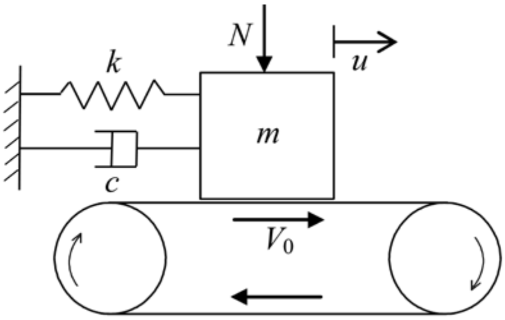

Fig. 2.8. Friction-induced vibration of a mass spring oscillator.

Two friction coefficients are considered to characterise the friction behaviour according to Coulomb’s law: the static coefficient μ_s (when there is no relative motion) and the kinematic one μ_k (when there is slip), with $\mu_s > \mu_k$. The stick phase occurs when the mass moves at the same velocity as the belt and the friction force $T(v)$, which depends on the relative velocity $v = V_0 - \dot{u}$, satisfies $|T(v)| < \mu_s N$. The spring is extended since the mass moves, until the spring force exceeds the friction limit and the slip phase initiates. Hence, two equations of motion are needed to characterise both stick and slip phases:

$$\begin{cases} m\ddot{u} + c\dot{u} + ku = T(v) = \mu_k(v)N\,\mathrm{sign}(v) & \text{for } \dot{u} \neq V_0 \\ \dot{u} = V_0 & \text{for } |ku| \leq T(0) \end{cases} \tag{2.3}$$

where u represents the vibration displacement and $\mathrm{sign}(v)$ denotes the sign of the relative velocity v. Since it is assumed $v = V_0 - \dot{u} > 0$, the sign function may be removed from the above. The first equation applies whenever the relative velocity is non-zero $\dot{u} \neq V_0$ (slip condition) whereas the second equation applies if the elastic force

ku is lower than the static friction force $T(0)$ (stick condition). However, in the case of a wiper-windscreen contact, the instability is observed about a non-zero sliding velocity and the vibration velocity $\dot{u}$ never reaches the sliding velocity V_0 so that $|\dot{u}| < V_0$. According to the first equation, the mass describes an harmonic motion at the natural frequency $\omega_0 = \sqrt{k/m}$. Nevertheless, this frequency is affected by a non-dimensional parameter which quantifies the relative importance of the stick and slip phases [7]:

$$\beta = (\mu_s - \mu_k)\frac{N}{V_0 m \omega_0}. \tag{2.4}$$

This parameter is usually between 0.1 and 1 for curve squeal situations [7] and it makes the period of oscillation longer than the natural period associated with the mass-spring system. For small values of β the slip phase predominates and the oscillation frequency is close to ω_0; for large values of β the stick phase predominates and the oscillation frequency is lower than ω_0 [7]. Moreover, as the motion is not purely sinusoidal, its spectrum will contain higher harmonics in addition to the fundamental frequency, a feature often seen in squeal measurements.

Coulomb's law establishes a step transition between the static μ_s and the kinematic μ_k friction coefficients since $\mu_s > \mu_k$. Nevertheless, the friction coefficient is often found to fall with increasing sliding velocity (see Section 4.5). The slope of the relation between force and velocity can be equivalent to a damper since it establishes a proportional relationship between both force and relative velocity; thus a force which falls in magnitude with increasing relative velocity corresponds to a negative damper. If there is a negative damping greater than the positive damping inherent in the oscillator, unstable self-excited vibration occurs [5] and its amplitude would grow exponentially. In reality, the non-linear effects in the creep force limit the amplitude, as there is a region with positive slope close to the origin of the force-creepage relation.

Le Rouzic *et al.* [22] analysed the stability problem for this kind of friction-induced self-excited oscillators through a Hopf bifurcation leading to a cycle solution, i.e. a periodic vibration. Through the first Lyapunov method, the authors concluded that the range of instability for the slope of friction coefficient is:

$$\frac{d\mu}{d\tilde{v}} \in \left]-2(1+\zeta), -2\zeta\right[, \tag{2.5}$$

where damping ratio is $\zeta = c/(2m\omega)_0$ and dimensionless relative velocity is defined as $\tilde{v} = kv/(\omega N)$. This result discards any instability for a constant friction coefficient ($\mu_s = \mu_k$ and, hence, $d\mu/d\tilde{v} = 0$) due to this mechanism.

From its non-linear formulation, the introduction of the falling friction in instationary contact models leads to a numerical problems in the time integration of the complete dynamics of a railway interaction model. Even techniques for the softening of Coulomb's law such as the regularisation [23] (see Section 4.5) continue to humper the numerical convergence of the instationary contact process. For a time-domain model based on Green's functions, Zenzerovic [24] introduced the falling friction not as local parameter, but as relationship between the lateral creep force and the creepage, obtaining stick/slip cycles in the tangential contact dynamics.

2.3.2 Constant friction mechanism

There is an increase of interest in the direction of mode-coupling phenomena in addressing curve squeal, which have been explained in a simplified form by Hoffmann *et al.* [25,26] and Sinou and Jezequel [27], through frequency-domain models. This type of instability can occur even considering a constant coefficient of friction, arising from non-conservative displacement-dependent forces.

Fig. 2.9 shows the typical system adopted to illustrate this mechanism, in which the friction coefficient μ is constant. Here the mass has two degrees of freedom and two springs. As the mass vibrates, variations in the normal load occur, leading to variations in the friction force. The modes of the wheel may have both vertical and lateral components and the contact angle α of the wheel with the rail may vary. At least two modes are necessary to initiate this mechanism.

By considering small oscillations around the equilibrium of steady-state sliding, the system in Fig. 2.9 can be mathematically described as

$$\begin{pmatrix} m & 0 \\ 0 & m \end{pmatrix} \begin{Bmatrix} \ddot{x} \\ \ddot{y} \end{Bmatrix} + \begin{pmatrix} k_{11} & k_{12} - \mu K_H \\ k_{21} & k_{22} \end{pmatrix} \begin{Bmatrix} x \\ y \end{Bmatrix} = \begin{Bmatrix} 0 \\ 0 \end{Bmatrix}, \tag{2.6}$$

where the terms $k_{ij}(\alpha_1, \alpha_2)$ in the stiffness matrix depend on the orientation and stiffness of the springs which in turn depend on angles α_1 and α_2 [27]. K_H represents the linearised Hertzian contact stiffness [30]; x and y are the vibration displacements in tangential and normal directions, respectively, and F and N are the corresponding friction and normal forces. The effect of damping in this system has been studied in [26] and [27] and will be briefly discussed below. The most important feature of Eq. (2.6) is that the stiffness matrix is non-symmetric. It can be shown [25] that if the upper diagonal term of the stiffness matrix $k_{12} - \mu K_H \leq 0$, due to the value of friction coefficient μ, the system can become unstable.

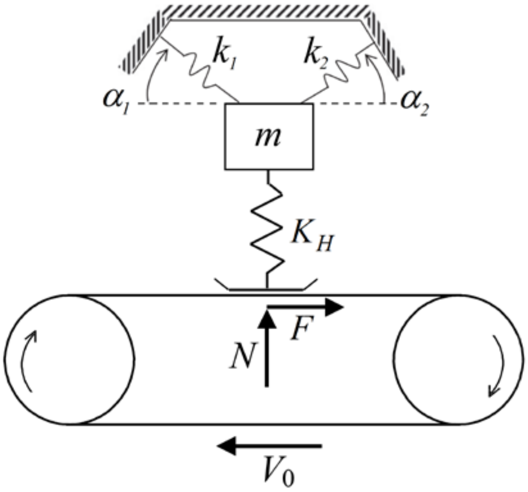

Fig. 2.9. Two-degree-of-freedom system on moving belt.

Hoffmann *et al.* [25] investigated the effect of the inclination of the contact plane (or contact angle) between wheel and rail by analysing the real part of the eigenvalues of the system for different values of contact angle and friction coefficient. For the 2-modes model of the wheel proposed in [25], instability was found for contact angles between 30º and 80º for a friction coefficient of at least 0.4, showing that, for these two modes, mode coupling can appear at relatively high contact angles. Such values of contact angle are typically found on the outer wheel of the front axle when the contact point moves toward the flange. Another interesting feature of the response due to mode coupling is that the effect of damping in the case of mode coupling is not straightforward [26,27]; in fact, an increase in damping can favour instability in some situations or can improve stability in others.

In order to model this mechanism by means of time-domain models, studies in the literature typically apply a non-rotating wheel modelled using the FE method [29,13].

Viewed from the wheel/rail contact, the rotation causes some of the wheel resonance peaks to split corresponding to waves travelling in opposite directions. By using a non-rotating wheel loaded by a wheel/rail contact force travelling at constant speed around the wheel perimeter, Thompson was able to account for the splitting of resonance peaks even though neglecting inertia effects due to rotation [7]. Although most cases reported involve 0-nodal-circle axial modes excited at the leading inner wheel, some unusual occurrences have been highlighted where different phenomena are involved. Even for the axial modes at the leading inner wheel, the dominant mode may vary over a wide frequency range, with values of n from 2 to 9. The reasons for this are not clear.

2.4 OTHER TYPES OF EXCITATION

Two other excitation mechanisms are described below: excitation by roughness and by discrete irregularities. Both will be applied in Section 6.2 for some simulations in order to validate the Moving Element (ME) model for the rail (see Section 5.4).

2.4.1 Excitation by roughness

Roughness of wheel and rail running surfaces is now generally accepted as the predominant cause of the occurrence of rolling noise [3]. 0.1 – 30 μm is the range for typical roughness amplitudes, although even higher ones can occur for severely corrugated rail. Thompson [3] estimated that the range of wavelength of 300 μm – 10 mm is the most important for the occurrence of rolling noise.

Most of the available wheel/rail interaction models assume that the roughness distribution acts in one point even though wheel and rail make contact in a small area denoted contact patch. This assumption impedes that the roughness influences the contact-patch size and shape; thereby, the models with one-point contact assumption have to include the effects of roughness in their pre-processing, which are:

- The contact-filter effect: wavelengths in the order of, or shorter than, the length of the contact patch in the rolling direction excite a lesser extent the system than longer wavelengths.

- The variations in the roughness profile height across the width also affect the wheel/rail excitation. The more correlated the roughness is across the contact patch, the greater this excitation is.

Remington [30] proposed an analytic model for introducing the contact filter as a correction in frequency-domain models for circular contact patches. Remington and Webb [31] presented their '3D distributed point reacting spring' (3D-DPRS) model introducing a Winkler bedding in the contact patch, including hence both effects mentioned above without adding a correction. This model permitted Thompson [32] to conclude that the analytic correction gives excessive attenuation at short wavelengths and reasonable results for wavelengths smaller than the contact-patch length when compared to the 3D-DPRS model.

The contact-filter effect has barely attempted to extend to the time domain in the literature. The calculation of an equivalent roughness as a pre-processing step for each wheel position on the rail (using for instance the 3D-DPRS model) seems to be one way to introduce this effect. Another possibility is to directly use a more realistic contact model (e.g., CONTACT [142]), which considers the finite size of the contact patch at each time step.

2.4.2 Excitation by discrete irregularities

The occurrence of impact noise is mostly due to two discrete irregularities on the wheel and rail surfaces: wheel flats and rail joints. A wheel flat occurs when the wheel locks and slides along the rail because of a malfunction in the brakes or lack of wheel/rail adhesion; this sliding leads to flatten the wheel on one side [33]. Rail joints are present throughout the tracks in order to compensate thermal displacements or insulate electrically both rails.

Wheel flats are generally introduced through simple analytic irregularity functions. The most commonly used are the proposed by Newton and Clark [34] and Wu and Thompson [35], who included quadratic functions to describe the dipped rail at a joint.

These discrete irregularities cannot be 'seen' for one-contact point models; thereby a correction must also be included by calculating equivalent irregularity shapes. Wu and Thompson follow this procedure for wheel flats [36] and rail joints [35]. Baeza *et al.* [37] used the same equivalent irregularity shape for wheel flats, also pre-calculating stiffness functions for each angular position of the wheel flat with a 3D contact model in order to include the changes in stiffness.

2.5 CONCLUSIONS

From the review of the curve squeal phenomenon, the following conclusions are derived:

- Curve squeal remains a controversial problem since it appears random rather than deterministic. This phenomenon consists of a high-frequency tonal noise that arises especially in the leading wheelset of a bogie negotiating a tight curve.

- Insertion of a wheelset in a curve is a process in which creep forces arise to steer the wheelset. Steering mechanism depends on wheel profile and diameter, curve radius, track width and stiffness of the primary suspension. In unfavourable conditions of the previous parameters, the wheelset moves outwards the curve, displacing the contact to the wheel flange that produces a normal contact force that re-equilibrates the wheelset.

- Most cases reported involve 0-nodal-circle axial modes excited at the leading inner wheel but some unusual occurrences have been highlighted where different phenomena are involved.

- Falling friction, which acts as negative damping, has been recognised the most accepted mechanism for the generation of squeal.

- Recent works indicate that the instabilities associated with squeal can arise even for contact models with constant friction coefficient.

- The difficulty of measuring the local contact parameters (creepages) for unsteady conditions at high frequencies, instead of quasi-static situations measured by test rigs, leads to the need of developing models that permit to distinguish the influence of both mechanisms.

3 REVIEW OF THE VEHICLE/ TRACK DYNAMIC INTERACTION MODEL

3.1 INTRODUCTION

In the literature, the coupled railway vehicle/track dynamics is associated with a set of important phenomena that are related to rolling noise, rail corrugation, polygonalisation and ovalisation of the wheels and, in general, the vibrational response originated from discrete defects, short wavelength irregularities of the rail or the wheels and other excitation sources generated in the contact area. The growing sensitivity to these problems has resulted in an increased demand of reliable vehicle/track interaction models in order to investigate their causes and develop solutions and effective treatments.

Nowadays, almost all rail vehicles are fitted with bogies (in order to solve problems related to hunting instability and insertion in curve) and have two levels of suspensions. The classical railway dynamics, regulated by the EN 14363 [38] (and the former UIC518), studies the dynamic behaviour of the railway vehicle in a curve guidance, stability and passenger comfort, critical in a frequency range below 20 Hz. For this purpose, the suspensions must guarantee that the modes of the bogie and the carbody are in this range, isolating the passenger from the high-frequency vibrations [39]. Below 20 Hz, the track vibration is negligible and thus the track is considered rigid or only its flexibility is taken into account. Nevertheless, at higher frequencies the track vibration becomes more important, while the vehicle sprung masses are less significant [39] since the suspension decouples the bogie frame and the carbody dynamics from the wheelset/track interaction.

The secondary suspension, located between the bogie and the carbody, confers to the carbody (assumed rigid) vibration modes whose frequencies are between 0.75 Hz for the vertical oscillatory carbody mode and 1.5 Hz for the carbody roll motion [39]. This suspension provides a cut-off frequency for the transmitted vibrations from the bogie around 2 Hz (and hence, the carbody structure must have natural frequencies sufficiently above this limit). The bogie frame (that oscillates on the primary suspension) has natural frequencies in the range of 8−10 Hz, about three octaves higher than the carbody modes, around three octaves below the lowest frequencies of the unsprung masses (about 50 Hz, in this the unsprung masses oscillate on the bed of the ballast, P2 frequency, see Fig. 3.1(a)). The cut-off frequency associated with the primary suspension would be about 15 Hz.

The wheelset and the track are located below the primary suspension. The wheelset is a very low-damped structure, whose response is governed by its resonances (starting slightly below 100 Hz). The rail is much more damped; it is an infinite system and, hence, there are no modes, but waves that propagate longitudinally. It has a cut-on frequency from which waves propagate; below this frequency, a deflection is produced and governed by the static behaviour. This frequency is located between 100 and 200 Hz. Between the cut-on frequency and about 1.5 kHz, there are two waves that propagate in the vertical and horizontal plane for each frequency; when the frequency increases, the shape and number of transmitted waves become more complex. A certain dynamic amplification is detected for the cut-on frequency, although this motion is much damped. The waves along the rail are best transmitted when their wavelength is twice the distance between spans (see Fig. 3.1(b)): the so-called pinned-pinned frequencies. These waves appear in the range of 1 kHz in the vertical vibration and 500−700 Hz in the horizontal plane, generating an important dynamic amplification around this frequency.

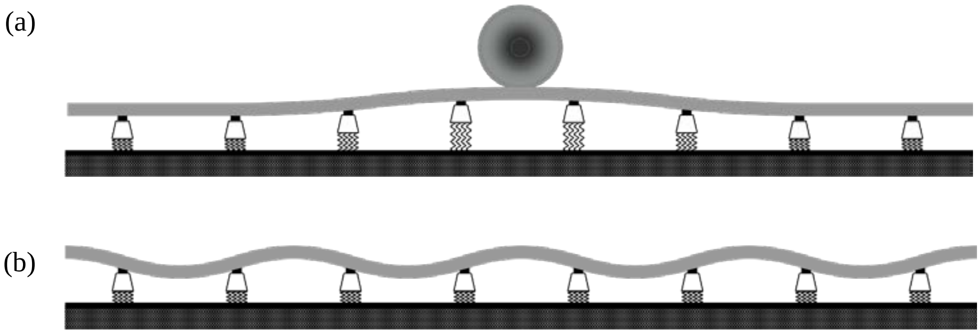

Fig. 3.1. Rail deformed configuration for the P2 (a) and pinned-pinned (b) frequencies.

The vehicle/track interaction occurs mainly in a frequency range (from a few tens of hertz to cover the spectrum of audible frequencies) for which the unsprung masses of the vehicle intervene. This case contrasts with those aspects related to safety against derailment and rolling quality, which are analysed in a range below 20 Hz. In the intermediate and high-frequency range (from 20 Hz to 5 kHz), suspensions permit to decouple the dynamic behaviour of the unsprung masses, hence reducing the vehicle model to a wheelset model [40], which considers the proportional part of the carbody and bogie weights as a force applied to the wheelset. In this frequency range, bogie models consisting of a frame and two wheelsets are widely used since Popp *et al.* [40] indicate that the deformation of the bogie frame is not relevant. Thus the frame is commonly modelled as a rigid solid while the wheelset can be considered rigid or flexible.

A literature review corresponding to the railway wheelset/track dynamic interaction modelling is carried out in this chapter. This analysis supports the study of curve squeal problem. The review describes different models for the three subsystems that are part of this problem: vehicle, track and wheel/rail contact. Taking into account the above mentioned aspects, the vehicle is reduced to the wheelset in the interaction problem. With regard to other problems that analyse the vehicle/track coupled dynamics, in curve squeal it is fundamental to consider the flexibility of the wheelset. Section 3.2 shows the main published developments.

Roughly speaking, the literature shows that the vehicle/track dynamic interaction is solved in the frequency and the time domain. The first one requires a linearisation of the vehicle, track and wheel/rail contact models, simplifying the global model and limiting the complexity of the problems to be addressed. On the other hand, the time-domain models allow considering the non-linear behaviour of particular elements of the track, such as rail pads and the ballast, and the wheel/rail contact. In Ref. [41], an exhaustive review of the dynamic track models is done, a summary being presented in Section 3.3 and examples of methods of resolution in Section 3.5.

The wheel/rail contact is one of the most important elements for curve squeal. Advancing certain keys that will be detailed later, squeal arises due to friction-induced vibrations, and the tribological contact conditions are the main factor that conditions the occurrence of this phenomenon. Section 3.4 sumarises some of the most suitable contact models for the study of squeal.

3.2 WHEELSET MODELS

There exist three types of flexible wheelset models: multibody, continuous and finite element models. The first ones incorporate the flexibility by means of rigid masses interconnected through viscoelastic elements, hence reducing the number of degrees of freedom of the system and, consequently, the computational cost. But they cannot represent adequately the elasticity of the wheelset for intermediate and high frequencies. Continuous models implement the deformation of the wheelset axle (flexion, torsion and elongation) and the wheels (flexion and umbrella modes) and incorporate the gyroscopic and inertial effects due to the rotation. Szolc [42] evidenced that the gyroscopic effects were responsible for the separation of the resonance peak associated with the wheelset natural frequencies in two peaks, and the strong coupling between the lateral and vertical flexion. Most of the flexible wheelset models in the literature include the flexibility exclusively in the wheelset axle, while the wheels are represented as rigid solids (e.g. in Refs. [43,44]). It is insufficient for frequencies of interest above 200 Hz, thus the flexibility of the wheels must be implemented in order to get into detail on the contact. The vertical and lateral wheel deformations affect the creepages in the wheel/rail contact and, then, the tangential forces.

As mentioned above, the present thesis requires capturing the high-frequency dynamics of the railway system to address dynamic phenomena characteristic of this range. In order to extend the range of validity, finite element (FE) method has been adopted for modelling the railway wheelset through beam elements [45–51] and three-dimensional solid elements [52–54]. The main inconveniences of the latter technique are found when the solid interacts with a non-rotating structure. The force that the non-rotating system exerts on the rotating one is applied at fixed spatial points, and consequently there is a relative motion between the load and the rotating solid (moving load problem). This fact requires the computation of the external force contribution to the generalised force term in each integration step during the simulation. The work presented by Fayos *et al.* [55], extended and applied by Baeza *et al.* [56] and Torstensson *et al.* [57], proposes a method that solves the above mentioned problems. The method is applied to undamped solids with geometry of revolution; it is based on Eulerian modal coordinates and provides satisfactory results. Lagrangian coordinates are the most frequently adopted reference in classic Mechanics; by means of this coordinate system, the position vectors and other kinematic properties are associated with material points of the solid. Eulerian coordinates are commonly used in Fluid Mechanics, and they relate spatial points through a fixed coordinate frame. These coordinates determine spatial points through which the material flows as time passes. The technique exploits the properties of the solids of revolution whose mode shapes in a fixed coordinate frame do not depend on the rotation of the solid. Consequently the mode shapes of the solid are used as basis functions in order to define a generic displacement of the flexible solid.

3.3 TRACK MODELS

The track models can be classified according to their constructive ways in ballasted track or slab track [58]. In the ballasted tracks, the rails are supported by sleepers, and these in turn are supported by a ballast layer on the platform. In the concrete slab tracks, the rails can be embedded in a concrete slab (directly or through an intermediate elastic element) or supported by discrete supports embedded in the concrete. This permits, in turn, to distinguish between continuous supported track models and discrete supported track models. Another common classification concerns if the track length is infinite or finite. The first one is a priori closer to the reality but it must be simple in order to solve analytically or numerically the dynamic interaction. Finite track models are a possible alternative, but a sufficient length is required to avoid wave reflection in the edges of the track (edge effect). The track models can also be classified according to their method of solving the dynamic interaction: in the frequency domain and in the time domain. The first one is commonly associated with infinite track models and the second one to the finite ones.

Knothe and Grassie [39] reviewed the modelling of the different types of supports through the ballast and the platform, distinguishing four different models. The simplest one considers the rail supported discretely by the sleepers and the ballast is under them; it is modelled through a spring-damper pair with coefficients extracted from experimental measurements. The second one represents the ballast and the platform together through elastic or viscoelastic half-space and it is used for the study of the propagation of the vibrations through the soil from the wheel/rail interaction. The third one represents the ballast as punctual masses under the sleepers; viscoelastic elements connect themselves and with the sleepers and the platform. The fourth model considers discrete supports and a continuous ballast layer on a 3D half-space representing the platform.

Historically, the rail has often been modelled as an Euler-Bernoulli beam, neglecting shear deformation and rotational inertia. Such simple beam models can only represent the track vertical dynamics up to about 500 Hz [39]. Using a Timoshenko beam model for the rail, which includes rotational inertia and shear deformation, the frequency range of validity of the track model can be extended, the upper limit being a subject of discussion. Knothe and Grassie [39] estimate that the rail can be modelled as a single Timoshenko beam up to 2.5 kHz if only vertical vibrations are of interest. Wu and Thompson [59] state that such models are adequate up to about 2 kHz since the occurring cross-sectional deformations of the rail (not modelled by Timoshenko beam models) are not important in terms of the vertical wheel/rail interaction in this frequency range (see also Refs. [60,61]). A Timoshenko beam model of the rail is for instance implemented in the wheel/rail interaction model DIFF developed by Nielsen and Igeland [62]. In order to include the cross-sectional deformations that become significant above about 1.5 kHz [63], different types of rail models are required. One example is the multi-layer model by Scholl [64], who represented rail head, web and foot by three infinitely long, homogeneous layers with different densities and Young's moduli. Vibrational shapes with cross-sectional deformation can at least in principle be modelled by this approach. A second example is the model by Thompson [63] who used a detailed FE mesh for a short length of the rail, which he extended to infinity using periodic structure theory. Gry [65] presented a third alternative model based on a description of waves travelling through the rail.

Andersson [66] showed significant cross-sectional deformation of the rail already at frequencies around 200 Hz. This implies that the track model needs to capture the 3D dynamic behaviour of the rail at higher frequencies in order to capture phenomena closely linked to the high-frequency domain as this thesis pretends to study. This requires modelling the rail by 3D solid elements through FE models, which seems crucial for the precise representation of the contact dynamics in the contact patch, which strongly depends on displacements on the rail head. This will represent one of the fundamental contributions of the present thesis. An alternative is to use waveguide finite elements, which take advantage of the 2D geometry of the rail having a constant cross-section, but nonetheless consider the 3D nature of the vibration by assuming a wave-type solution along the rail [67,13].

The most important subjection element of the rail is the railpad, giving viscoelastic properties to the rail-sleeper union. Popp *et al.* [40] pointed out that the behaviour of the base plate affects significantly the train/track interaction from 200 to 700 Hz. The base plate is commonly modelled as viscoelastic elements through one spring-damper pair for 2D models or some spring-damper pairs for 3D models. Some models adopt three parameters to represent the increasing stiffness with the frequency [68]. Similar to the base plate, the elastic behaviour of the ballast is non-linear due to the contact between the stones and the sleepers. Nordborg [69] found that the inclusion of discrete supports is important for lower frequencies around the sleeper-passing frequency and for higher frequencies around the pinned-pinned resonance frequency of the rail. The sleeper-pinned frequency, $\omega_{sl} = v / L_{sl}$, is the frequency at which the wheelset passes the sleepers, v being the train speed and L_{sl} the sleeper spacing. At the pinned-pinned frequency, ω_{pp}, which typically lies around 1 kHz, the bending wavelength of the rail corresponds to the length of two sleeper spans, $\lambda_{pp} = 2L_{sl}$, with nodes located at the sleeper positions. The simplest and widely used sleeper model consists of a punctual mass interconnected with the other elements through viscoelastic elements. When flexibility is required, continuous Bernoulli or Timoshenko beam models use to be adopted. Knothe and Grassie [39] indicate that modelling the sleepers as rigid solids is adequate up to 1 kHz.

3.4 CONTACT MODELS

The contact theories are formulations that relate kinematic magnitudes associated with the wheel and rail to forces transmitted in the wheel/rail contact. The different wheel/rail contact theories in rolling conditions developed so far can be included in the classification proposed by Kalker [70] according to the following criteria: modelling of the elastic problem, consideration of the inertial effects, representation of the transient process in the contact and the dimension of the contact problem.

Considering the first criterion, Kalker distinguishes between *Simplified Theories*, in which the relationships between the displacements associated with the deformations and the stresses in the contact are obtained from approximated analytic expressions, and *Exact Theories*, in which the mentioned relationships are obtained from the Linear Elasticity Theory and semi-analytic or numerical procedures are calculated from the Boussinesq-Cerruti integral equations [71,72].

On the other hand, *Dynamic Theories* encompass the contact models which consider the inertial effects associated with the mass differentials near the contact. *Quasi-static*

Theories neglect these effects against the contact forces. According to Kalker, these inertial effects are only important for velocities above 500 km/h, thus the current models do not require *Dynamic Theories*. The third criterion distinguishes between *Instationary Theories* and *Stationary Theories* if the contact models permit to represent the transient process as consequence of the variation of the contact forces or consider insignificant its influence on the vehicle dynamics. The last criterion divides the contact theories between *Bidimensional Theories* if the displacements, deformations and stresses are contained on the plane defined by the longitudinal and vertical axes, and *Tridimensional Theories* which permit to represent the contact problem in a realistic way.

Two other classifications can be added. Regarding the formulation of the elastic problem, there exist *Non-Conformal Contact* models (Hertzian models and the ones based on infinite half-space) and *Conformal Contact* models (mainly through finite elements). If the tangential force saturation is considered according to Coulomb's law, the contact models are part of the *Non-Linear Theories*. If a linear relationship between forces and creepages is considered (through an infinite friction coefficient assumption), *Linear Theories* are referred.

3.4.1 Normal contact problem

The normal contact model applied in most of the available interaction models is the Hertzian contact model due to the simplicity of obtaining the normal force from the elastic penetration; see e.g. the models in Refs. [73,74]. This standard model goes back to Heinrich Hertz who published his theory "*On the contact of elastic solids*" in 1882 [75]. A comprehensive description of the Hertzian contact theory is found in Refs. [28] and [76]. The Hertzian theory of normal contact between two bodies relies on the following assumptions [28]:

- Linear elasticity: the bodies are perfectly linear elastic solids.
- Half-space assumption: the surfaces of the bodies are non-conforming surfaces, i.e. they first make contact at a point (or along a line). Even under load, the dimensions of the contact patch are small in comparison to the dimensions of the bodies and the radii of curvature of the surfaces. This implies that the bodies can be considered as a semi-infinite elastic solid with a plane surface (an elastic half-space) for the purpose of stress and deformation calculations.

- The surfaces are perfectly smooth and can be described by quadratic functions in the vicinity of the contact patch.

Under these assumptions, the contact patch is an ellipse and the normal pressure distribution is ellipsoidal. The case of contact over a long strip, as it occurs for two cylindrical bodies with their axes lying parallel, is a limit case of elliptical contact. This case has to be treated separately and it is not further considered here. Appendix B presents the relevant formulas for contact dimensions, loads and deformations in elliptical contact, mainly following the presentation by Lundberg and Sjövall [76].

Real wheel and rail surfaces never meet the Hertzian assumptions exactly and, in consequence, the Hertzian solution can only be an approximate one. In many situations, the Hertzian contact theory might still be sufficient, but it is important to be aware of its limitations and discuss its adequacy for the wheel/rail contact on the basis of a literature review. The scope is hereby on non-Hertzian geometry; the influence of friction and plasticity is not investigated. This section also presents available non-Hertzian contact models.

The most important limitation of the Hertzian theory concerns the definition of the contact surfaces by means of constant radii of curvature of the (undeformed) bodies in the contact patch. The transversal radii of curvature of wheel and rail profiles are however defined by different radii of curvature, polynomial functions, etc. The standard rail profile UIC60 (used in the present thesis) consists of a sequence of circular arcs with the radii of 30, 80 and 13 mm [77]. As consequence, the lateral contact position of the wheel on the rail varies during operation and the normal traction distribution differs from the Hertzian distribution [77−79]. Wheel flats are other clear example in which radii of curvature of the wheel surface change quickly.

The half-space assumption is valid when the bodies are non-conformal implying that the dimensions of the contact patch are small in comparison to the characteristic dimensions of the contacting bodies, e.g. the diameter and the radii of curvature. This assumption is reasonable for wheel/rail tread contact (Fig. 3.2(a)), but it is violated for flange contact and contact near the gauge corner of the rail (Fig. 3.2(b)) [80], case in which the flange thickness and the radius of curvature at the gauge corner are of the same order of magnitude as the contact length and the contact is conformal. Nevertheless, Yan and Fischer [77] found surprisingly good agreement in the pressure distribution between Hertzian theory and a FE model for one case of rail gauge corner contact between the rail UIC60 and the wheel UICORE.

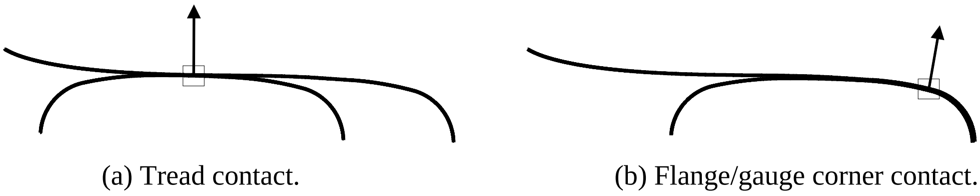
(a) Tread contact. (b) Flange/gauge corner contact.

Fig. 3.2. Wheel/rail contact cases.

The limitation to one single contact patch of the standard Hertzian contact theory precludes the multi-point contact which uses to appear in guiding wheels in curves with one contact patch on the wheel tread and one on the wheel flange. Additionally, Hertzian contact model assumes smooth wheel and rail surfaces, but roughness changes the geometry of the contacting surfaces and thereby the stiffness of the contact and the size and shape of the contact patch. Locally, the actual pressure is several times higher than the maximum Hertzian one [80].

These deviations of the real contact conditions from the Hertzian assumptions have driven the development of non-Hertzian contact models. In order to solve the 3D contact problem for arbitrary non-Hertzian geometries, the continuum equations of elasticity have to be solved (see e.g. Appendix A in Ref. [81]). This is, in the most general case, only possible numerically, e.g. by using FE methods. If the contacting bodies are subject to certain regularity conditions, the constitutive relations can be brought into a surface mechanical form that will be described in Section 4.2. These constitutive equations will be utilised in Section 4.3 to detail the formulation of the CONTACT algorithm [81].

Many of the contact models published in the 1970s and 1980s for non-Hertzian geometry use a special type of Boundary Element (BE) approach based on the Boussinesq-Cerruti expressions for the elastic half-space. Only some examples are cited here. The best known is the Kalker's CONTACT algorithm [81], based on the *Exact Theory*, which employees a variational method to calculate the normal and tangential traction distributions in a potential contact patch discretised by rectangular elements, in which constant contact magnitudes are assumed. Its high computational cost is linked to its mathematical rigor. Paul and Hashemi [82] solved the conformal contact problem between the rail and the wheel flange using a boundary element method and employing an approximated analytic expression to get the influence function. Le-The [83] considered the contact bodies as revolution solids with quasi-parallel axes, thus the contact patch and the normal traction distribution were virtually symmetrical about the x_2-axis and perpendicular to the rolling direction x_1. Thereby, the contact patch is discretised in strips in the x_1-direction, and each strip has a semi-elliptical traction distribution which remains constant in each x_2 strip. Le-The found that particular wheel/rail profiles combinations clearly resulted in non-elliptical contact patches.

Nowadays, there exist two lines of development for non-Hertzian normal contact models: FE formulations and low computational cost formulations. The first line allows incorporating complex contact geometries and non-linear effects but the computational cost for 3D models is still very high even for current very powerful computers. The second line intends to develop approximated contact formulations with rapid solution in order to implement them to dynamic train/track interaction for high frequencies. In turn, this second line is divided into two by Piotrowski and Chollet [84]: multi-Hertzian models and virtual elastic penetration models. Pascal and Sauvage [85] developed a method with a set of ellipses which replace multi-point contact and non-elliptical contact patch. Regarding the virtual elastic penetration models, Ayasse and Chollet [86], and Piotrowski and Kik [87], the contact patch is estimated from the virtual elastic penetration of two undeformed surfaces. Additionally, the Square Root Simplified Theory (SRST) proposed by Alonso and Giménez [88] does not need to consider the undeformed wheel/rail distance as quadratic function as Hertzian theory does, allowing real profiles.

3.4.2 Tangential contact models

Regarding the models for the tangential contact, Cattaneo [89] and later Mindlin [90] proposed independently an analytic solution to the non-rolling 2D tangential contact problem between two cylinders when there exists partial slip on the contact patch. Based on Mindlin’s methodology, Carter [91] developed in 1926 the first rolling contact theory for railway dynamics, considering the friction effect and the elasticity of the solids in contact. Carter formulated a non-linear theory which allows obtaining in an exact way the tangential contact forces between a cylinder of radius R and infinite length, and an infinite plane (both are close to infinite half-spaces) from the creepages, considering a 2D stationary problem. A year after, Fromm [92] solved the 2D rolling contact problem for two cylinder with the same elastic properties without considering them as infinite half-spaces.

Theories developed by Kalker prevail in the topic of the tangential problem in non-Hertzian contacts. The most detailed, fully transient and non-linear theory is Kalker's Variational Contact Theory [81], which he called the *Exact Theory*. This theory is implemented in Kalker's CONTACT program. Details about the formulation and implementation of Kalker's variational theory will be found in Section 4.3, where the method will be extended to a falling friction coefficient through the Coulomb's regularisation; friction coefficient will be dependent of the slip velocity using two characteristic parameters: the static and the kinematic coefficient.

Kalker's variational method is based on the principle of maximum complementary energy. The model consists of two algorithms: NORM for the normal contact and TANG for the tangential problem. Both algorithms apply an iterative solution procedure, which Kalker calls active-set algorithm [81]. The potential contact patch is discretised into regular elements in which pressure and tractions are constant. The NORM algorithm solves the normal contact problem and determines the contact shape and size, along with the normal pressure distribution. The contact deformations are obtained from the elastic half-space assumption. It is because Kalker implemented the exact Boussinesq-Cerruti equations for the elastic half-space influence coefficients, that he called this theory 'exact'.

The TANG algorithm solves the kinematic equation (see Section 4.3.2) for the transient rolling contact for each discretisation element in contact. The division of the contact patch in stick and slip regions is determined, along with the distribution of tangential tractions. The model can handle both vanishing and large creepages, making it very versatile for many practical problems.

To sum up, Kalker's variational theory, in its general formulation, is applicable to [93,94]:

- transient processes;
- Hertzian and non-Hertzian contacts;
- considerations with any combination of the three creepages;
- contact of bodies made out of different materials;
- cases with varying normal force, creepages and/or contact geometry.

Kalker's model is limited by the elastic half-space assumption. Conformal contact cannot, therefore, be solved using this model. In addition, the price is high for this detailed and capable rolling contact model in terms of high computation time [95].

An effort to minimise the computational cost while retaining accuracy was made by Kalker in 1967 and resulted in the *Exact Theory* [81,96], a semi-analytic technique for the calculation of the tangential contact force from the Hertzian theory and assuming an infinite friction coefficient (equivalent to consider full-stick in the contact patch). Later, Kalker developed the FASTSIM algorithm [95] based on the *Simplified Theory* [97] in order to solve the stationary tangential contact problem with a low computational cost. In this model, the displacements in a point depend exclusively on the tractions applied in that point through the flexibility coefficients L (adjusted by comparing with the results of the *Exact Theory*), as a Winkler bedding.

FASTSIM joins an acceptable precision, with deviations around 10% from CONTACT if the spin is small, and a very low computational cost, being 1000 times faster than CONTACT [81], which has led it to be the most widely used model for the dynamic wheelset/track interaction. According to Kalker [81], this approach is considered to have the best precision-to-computational cost ratio [98], but it is, however, a steady-state model.

Vermeulen and Johnson [99] extended the Carter's theory to a 3D problem with two spheres in rolling contact, considering the longitudinal and transversal creepages but neglecting the spin, and adopting the Hertzian theory. They also carried out an inexact assumption of the shape and position of the stick zone inside the contact patch, which penalises the precision of the method. To include the effects of spin, Shen *et al.* [100] extended the model of Vermeulen and Johnson. Shen *et al.* note that with increasing spin creepage the differences between their method, Kalker's FASTSIM and Kalker's variational theory increase.

Polach [101] developed a tangential contact model for the case of large creepages. Under these circumstances the contact is dominantly in slip and the resulting tangential force is close to the traction limit. Polach applied Kalker's *Linear Theory* to determine contact shear stiffness and to approximate the effects of spin. The effects of running on the traction limit were included by different reduction factors. These factors are determined by comparison of measurements and simulation results [101]. However, the model is limited to elliptical contact patches and stationary contact conditions. Additionally, Knothe and Groβ-Thebing [102] developed a non-steady state linear model which calculates complex creepage coefficients dependent of the frequency for small harmonic oscillations of the creepage from a reference state.

The precision and computational cost of a contact model are key factors for the dynamic simulation. Vollebregt *et al.* [103] compared results of some contact models with CONTACT, concluding that USETAB [104], based on the interpolation of tabulated contact parameters (extracted from CONTACT), and FASTSIM give a better precision for the tangential forces than the *Linear Theory* [105], the Vermeulen and Vermeulen's model [99], Shen and Li's model [106] and Polach's model [107], when high spin creepages appear in the contact.

Significant work in extending Kalker's *Simplified Theory* to transient processes has been made by Shen and Li [106], Alonso and Giménez [108] and Guiral *et al.* [109]. Shen and Li considered the case of moderate creepage and small spin in the transient case. They included transient effect by including the term $\partial u_\kappa / \partial t$ (where u_κ is the displacement in the κ-direction) in the kinematic equation of the simplified model. Good correlation with the variational theory results was found, except for the case with significant spin.

To better describe transient effects, Alonso and Giménez [98] introduced an additional term next to Kalker's flexibility coefficient. While Shen and Li [106] used Kalker's flexibility coefficient for both stationary and transient terms, Alonso and Giménez introduced the dynamic flexibility coefficient. This additional coefficient is related only to the transient term. The contact patch was assumed to be elliptical and only one creepage was considered to vary in time. They pointed out that the model can be easily extended to include non-Hertzian contacts [98,108]. Guiral *et al.* [109] extended the model by Alonso and Giménez [98] to address a more general case. An arbitrary combination of creepages was included, along with the variation of the normal contact force. Good agreement with Kalker's variational theory results was found in the case of large harmonic variation of creepages. Some researchers have developed the original algorithm to extend its validation range: Alonso and Giménez considered non-elliptical contact patches [108]. Additionally, Vollebregt [110] has recently presented a new version of the software, FASTSIM2, which allows representing the contact magnitudes with a higher precision requiring a lower number of elements to calculate the tangential forces.

Significant research is nowadays concentrated on improving the *Simplified Theory* to include falling friction laws, rather common in curve squeal modelling. Uncertainties whether a transient contact model is needed are part of the explanation (see Section

3.4.3). Originally, Kalker developed the model with a constant friction coefficient in mind, but a slip-velocity dependent friction law can be implemented as well. This was done by Croft [16] and Pieringer [94], who implemented the friction model from Kraft [111]. They, however, had issues with multiple solutions of the tangential contact problem and unphysical instabilities. Périard [74], Huang *et al.* [112] and Squicciarini *et al.* [113,114] implemented a falling friction law in FASTSIM for squeal modelling purposes. Xie *et al.* [115] applied it for simulations of the vehicle curving behaviour to determine input creepages for the squeal model. Vollebregt and Schuttelaars [116] and Giménez *et al.* [117] also performed work on including the slip-velocity dependent friction law into FASTSIM. Vollebregt [118] implemented a falling friction law, but introduced what he calls ‘friction memory’ to reduce the irregularity of results. This topic is still a subject of on-going research.

3.4.3 Transient contact conditions during squeal

Most existing models assume quasi-stationary contact, independent of the temporal history of the contact conditions, since it has been traditionally considered that the transient effects in the wheel/rail contact does not have significant influence in the dynamic interaction [81]. Nevertheless, if the contact parameters present high-frequency temporal variations when a particle runs across the contact patch, the transient effect must be considered in the modelling. Curve squeal, for instance, leads to fast changes in contact conditions, which are expressed via the contact variables defined on the contact particle level. In this case of fast changing conditions, a particle will ‘see’ a significant change during the time it travels through the contact patch. Such conditions are called transient contact conditions, and contact models able to describe such processes, transient contact models.

Let assume a contact length in the rolling direction a_1 to characterise contact conditions and a characteristic wavelength L used to describe the rate of change of a contact variable. For a low-frequency motion of the contact variable, $L >> a_1$ and the contact variable along the contact patch would be approximately the same, hence the variation along a_1 could be neglected without introducing a significant error in the results. However, for a high-frequency motion characterised by $L \approx a_1$, the variable change would significant and this should not be neglected. Knothe and Groβ-Thebing [102,119] used the ratio L/a_1 of the characteristic motion wavelength L and the contact length in the rolling direction a_1 to characterise contact conditions. A ratio $L/a_1 < 10$ characterises transient conditions [119]. Although they consider rail corrugation, the same approach can be used to determine conditions during squeal. A case of $\omega = 2\,\mathrm{kHz}$ squeal with $V = 50\,\mathrm{km/h}$ rolling velocity and $a_1 = 12\,\mathrm{mm}$ contact length gives the characteristic motion wavelength of $L = V/\omega = 0.007\,\mathrm{m}$ and the L/a_1 ratio is 0.58. The contact conditions during squeal are, thus, transient.

Whether a transient contact model is required for squeal modelling is still not clear. Refs. [102,119] established a criteria to estimate when a transient model is required (not to introduce important errors in calculations). However, in response Kalker [81] compared steady-state and transient analyses results of a rail corrugation case. The steady-state approach resulted in a slight overestimation of the frictional work compared to the full transient model results. Kalker concluded that the effect of transient contact conditions is not pronounced, questioning conclusions of Ref. [102]. He concludes that transient contact processes can be described as a succession of steady-states.

Baeza *et al.* [23] investigated the influence of transient processes on contact variables. A harmonically varying force was imposed on the contact and the resulting creepages were observed. In cases with rapid force variations, steady-state models did not give satisfactory results. Differences between steady-state and transient model results were found to depend on the L/a_1 ratio. Specific values that would define the validity limit of steady-state models were not given.

3.5 TRAIN/TRACK DYNAMIC INTERACTION MODELS

3.5.1 Frequency-domain models

The dynamic interaction models in the frequency domain are based on the previous receptance calculation/measurements of the vehicle and the track, after being excited by a force applied at a point. In this type of models, it is assumed a steady-state dynamic interaction and a linear behaviour of the vehicle/track system, being the response proportional to the excitation.

Knothe and Grassie [39] make a distinction between receptance from a static punctual force and a moving punctual force. Additionally, they distinguish between discrete supports and continuous supports. Among the models based on receptances from a static punctual force, Grassie *et al.* [120] represented the rail as a Timoshenko beam supported by a continuous layer of rigid or elastic sleepers. This model permitted to calculate two resonances of the track: the P2 resonance just above 100 Hz (rail and sleepers oscillate on the ballast) and the $P1^{1/2}$ resonance between 300 and 500 Hz (rail oscillates in phase opposition to the sleepers). Being a continuously supported track model, it cannot predict the behaviour of the track around resonances related to the discrete supports of the rail, such as the pinned-pinned resonance.

This limitation was solved by Ripke and Knothe [121] by introducing discrete supports and calculating the direct vertical and lateral receptances for the excitation force applied in the sleeper and the half span as shown in Fig. 3.3. The receptances calculated by these authors are used in this section to present the main resonances and anti-resonances in the vertical receptance (Fig. 3.3(a)), which can be important regarding the wheel/rail interaction force magnitude and the irregular wear that can induce. The first resonance, known as P2 resonance, appears between 50 and 200 Hz, depending on the track properties. At this frequency, the rails and sleepers vibrate in phase on the ballast, which provide stiffness and a high damping, so that the corresponding peaks appears wide and flat. The second resonance, $P1^{1/2}$, appears at a frequency between 300 and 500 Hz, depending on the stiffness baseplates. At this resonance, the rails and sleepers vibrate in antiphase and its corresponding peak also appears flat due to the fact that most of the damping at this frequency is provided by the ballast. The third resonance, known as pinned-pinned, occurs in the range between 700 and 1200 Hz. At this resonance, the rails vibrate with a wavelength that is twice the span, with nodes located on the sleepers, when the excitation force is applied on a point located on the half-span. This is a low-damped resonance, so that the corresponding peak is tight since only the rail provides damping in this case.

Two antiresonances are also detected in Fig. 3.3(a). At the first one, between the two first resonances, the sleeper vibrates between the rail and the ballast, acting as a dynamic absorber of vibrations, while the rail barely moves. The second antiresonance appears at a frequency above the pinned-pinned resonance, when the excitation force is applied on a sleeper, indicating that the stiffness of the rail at this position and the corresponding frequency is very high.

In the lateral receptance (see Fig. 3.3(b)), similar to the vertical one, it can be observed that the resonance frequencies are lower than the previous case, while the receptance magnitudes are higher since the track is more flexible in the lateral direction. The first pinned-pinned resonance appears at 560 Hz and the second one, in which the head and the foot of the rail vibrate in antiphase around 2 kHz.

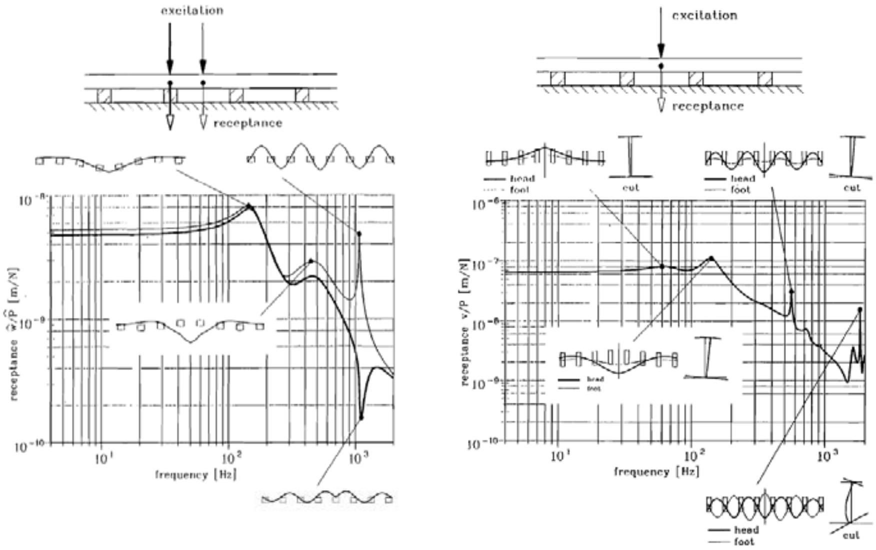

(a) (b)

Fig. 3.3. Direct receptances of a UIC60 rail on rigid sleepers, 0.6 m of span. The excitation is applied at the sleeper or at the half-span. (a) Vertical receptance; (b) lateral receptance. From Refs. [122,123].

When considering moving harmonic excitation force, Ilias and Knothe [124] and Ilias and Müller [125] observed that the moving force influenced significantly the response of the track around the pinned-pinned frequency, dividing it in two resonance peaks, whose separation increased with the velocity of the force, as observed in Fig. 3.4. The latter authors gave approximated expressions for both peaks of the pinned-pinned resonance from the frequency of this resonance for zero-velocity, the velocity of the moving force and the span. The authors also investigated the most realistic case, consisting of considering the excitation from a moving mass (a moving wheelset) driving along a rail with a sinusoidal corrugation. Fig. 3.5 shows the relationship between displacement and vertical force (transmission ratio) of the track originated by a moving mass, as a function of the speed of the moving mass and the frequency. The authors observed that the peaks of the first resonances were displaced towards lower frequencies when speed increases. The pinned-pinned resonance is also divided into two peaks, whose separation increases with the speed; but the difference of the amplitudes of both peaks is due to the modulation of the normal force, which is maximum in the frequency range close to the pinned-pinned resonance. Therefore, at the frequency corresponding to the pinned-pined resonance which appears with the static force model and with the moving irregularity model, an antiresonance will appear with the moving mass model.

Additionally, Ilias and Müller carried out a comparison of several excitation models. They observed that the A2 (moving force) in Fig. 3.6 and A3 models (moving mass) could represent the division of the maximum normal contact force associated with the division of the pinned-pinned resonance, while the A1 model (static force) could not represent that effect.

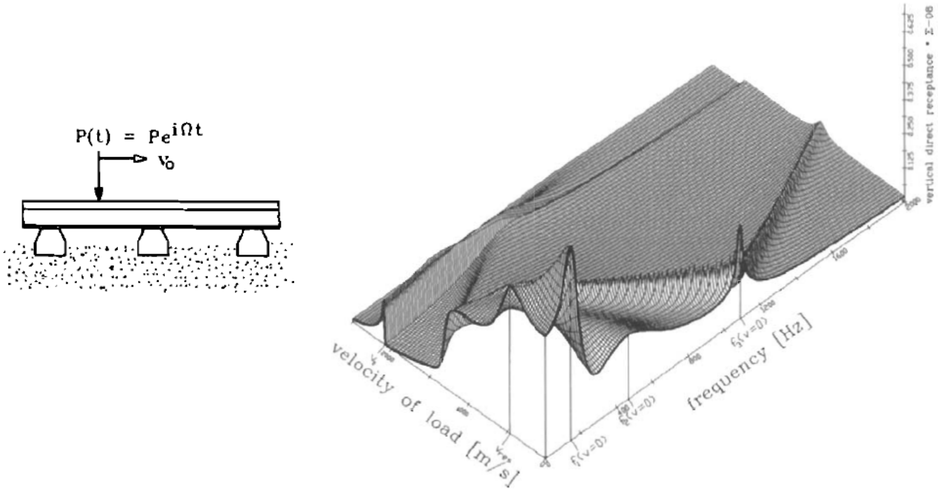

Fig. 3.4. Direct vertical receptances of a UIC60 rail on rigid sleepers, 0.6 m of span, as a function of the speed of the moving excitation force. From Ref. [125].

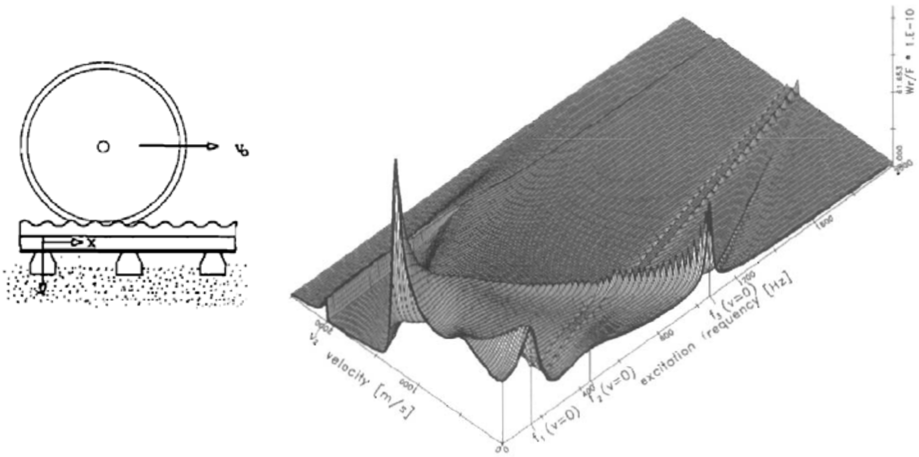

Fig. 3.5. Transmission ratio (displacement/force) of a UIC60 rail on rigid sleepers, 0.6 m of span, as a function of the speed of the moving mass. From Ref. [125].

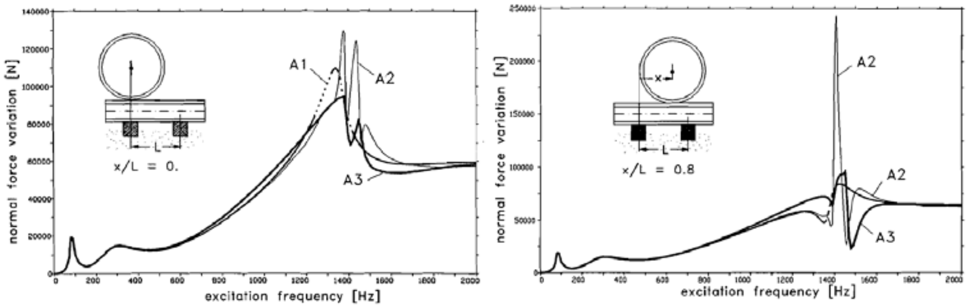

(a) (b)

Fig. 3.6. Variation of the wheel/rail normal contact force as a function of the excitation frequency, using different excitation models (A1 static force model; A2 moving force model; A3 moving mass model). (a) Wheel located on the sleeper; (b) wheel located on the half-span. From Ref. [125].

The most well-known frequency-domain model for the calculation of rolling noise is a model going back to Remington [14,30,126,127], which has been generalised and further improved by Thompson [63,128–130]. His formulation is implemented in the software package TWINS [131] which is widely used in industry today.

The range of validity of the linearity assumption necessary in frequency-domain models has been investigated by Wu and Thompson [59] using a time-domain model for roughness excitation. They found that non-linearities in the contact model cannot be neglected in the cases of severe roughness and/or a low static contact preload, which can cause loss of contact between wheel and rail. These results have been confirmed by Nordborg [69], who used both a frequency-domain model and a time-domain model based on Green’s functions to study non-linear effects in the vertical interaction. If the response to discrete irregularities such as wheel flats and rail joints is to be calculated, time-domain models are the only option. They are able to capture the discrete nature of the phenomena and model the loss of contact that is likely to occur [35,36]. As curve squeal is an intrinsically non-linear and transient phenomenon, time-domain models are also here the only option if the magnitude of squeal is to be predicted.

3.5.2 Time-domain models

Time-domain models present a higher computational cost as main disadvantage against the frequency-domain models. Nevertheless, the computational power of the current computers has made these models the preferred ones by most researchers, permitting them to introduce non-linearities from the ballast, baseplates, the wheel/rail contact and the interaction transient phenomena. These models are divided in two sets [39]: FE and semi-analytic models. The FE models consider a finite track with at least 15 spans to reduce the influence of the boundary conditions at the edges. The 3D models are limited in general to the vertical dynamics (and the longitudinal in some cases) due to the high number of degrees of freedom. Ilias [132] used a combination of both techniques in the time domain: the FE method was employed to simulate the vertical and longitudinal motion of the track, while the lateral dynamics was introduced through the transformation of the receptances to the time domain. The only non-linearity considered was the wheel/rail contact.

Nielsen and Igeland [102] studied the vertical dynamic behaviour of a bogie on a rail discretely supported by sleepers on elastic bedding. They analysed the bogie-track dynamic interaction with different irregularities such as: sinusoidal corrugation on the rolling surface of the rail, a wheel flat and a sleeper badly supported on the ballast. The interaction problem was solved in the time domain by applying a modal superposition technique to describe the track.

Anderson and Abrahamsson [133] extended the DIFF model [62] to consider the vertical, longitudinal and lateral dynamics in order to analyse the wear; the new version was called DIFF3. The vehicle model was reduced to a bogie model, with a rigid frame and the wheelset consisted of two rigid wheels and a rigid or elastic axle. The axle was model through FEM and a modal reduction was carried out to decrease the number of degrees of freedom. They employed a contact model which permitted to detect the contact zone and calculate the normal and tangential contact forces. Comparing the results using a rigid and flexible axle, they observed that the longitudinal force of the rigid axle was much higher. For the vertical force, the differences were not significant.

Nielsen and Oscarsson [134] proposed a numerical method to consider the non-linearities of the track associated with the ballast, baseplates and the platform, in a train/track dynamic interaction model developed previously [62]. This model included a lumped vehicle model, a linear FE track model and adopted a non-linear wheel/rail contact model. In the new model, a complex modal superposition technique is adopted in order to decouple the equations of motion of the linear track model developed previously by one of the authors [135]. The non-linearities of the track are considered applying equivalent transient forces to the corresponding nodes of the track FE model. An alternative, more computationally efficient approach has been demonstrated by Wu and Thompson [36]. They modelled the dynamics of the track using a single differential equation obtained from a transfer function. Their technique is, however, not suitable to include track models with discrete supports.

Infinite track models based on wave propagation seem to be a very promising approach to represent the track by moving Green's functions that describe the dynamic behaviour of the track in a moving contact point. This approach is computationally efficient and allows including discrete supports. This technique, going back to Manfred Heckl's proposal for a railway simulation program [136], has been used by Nordborg [69] and recently by Mazilu [26]. As a matter of course, the wheel can also be represented by Green's functions. This approach has been chosen by Maria Heckl and Abrahams [137] who formulated a squeal model for the wheel represented as an annular disc. Pieringer [133] has recently developed a model which represents the wheels and rails through a set of impulsional response functions to study the squeal noise, modelling the wheel/rail contact as instationary and non-Hertzian from the Kalker's variational theory.

Correa *et al.* [138] have applied a modified method of the polynomial rational fraction to transform their track model from the frequency domain to the time domain. The dynamic vertical interaction in the time domain is used to study the dynamic effects arising from the passage of the wheel on rail defective welds.

3.6 CONCLUSIONS

Curve squeal is recognised as a complex problem, which seems random rather than deterministic, associated with different phenomena that require different modelling approaches and different treatments. The falling and constant friction coefficient mechanisms appear as two accepted mechanisms of squeal, but their relative importance remains as the main controversy on this topic.

The modelling for instationary contact seems fundamental for the adequate approach to this high-frequency phenomenon and it has represented much of the effort of researchers. Kalker's variational theory as an *Exact Theory* achieves the necessary level of detail required to capture the high-frequency stick/slip cycles in the contact area and the consequences on the tribology of the creep forces. The non-linearities introduced by Coulomb's law make the contact dynamics a complex and time-consuming numerical problem. Therefore, frequency-domain models can be discarded since they require linearised models and cannot predict amplitudes of the contact parameters, which can be used as good indicators of squeal. In addition, the introduction of a falling friction coefficient that falls from a static to a kinematic value with the slip velocity requires numerical techniques that soften the contact equations. The difficulty of measuring the local contact parameters (creepages) for unsteady conditions at high frequencies, instead of quasi-static situations measured by test rigs, also leads to the need of developing such models.

For the high-frequency range, scope of the present Thesis, the modelling of the vehicle can be reduced to the modelling of the wheelset. This range requires models that introduce flexibility through FE techniques. Curve squeal seems to be associated closely with one or more 0-nodal-circle wheel axial modes excited at the leading inner wheel, but some unusual occurrences have been highlighted where different phenomena are involved. The inertial and gyroscopic effects associated with the rotation of the wheelset should be included in a detailed high-frequency dynamic formulation since some authors indicate their influence in the build-up of the stick/slip oscillations. Moreover, the inclusion of the rail dynamics is pointed out as relevant factor especially under constant friction conditions. Flexible and finite beam models usually employed in the literature do not model the real geometry of the rail profile, neglecting the influence of the contact point location on the contact dynamics. In addition, these models do not account FOR the cross-sectional deformation of the rail, hence limiting the frequency range up to 1.5 kHz, below the range of study required for curve squeal. New efficient modelling techniques need to be developed in order to overcome the previous limitations while preserving the rail length, thus minimising wave reflections at the rail edges.

4 WHEEL/RAIL ROLLING CONTACT MODEL

4.1 INTRODUCTION

Wheel/rail interaction models intended for noise prediction should cover the frequency range from approximately 100 Hz to 5 kHz. At frequencies below 100 Hz the human perception of sound is substantially reduced; the rolling noise spectrum decreases rapidly above 5 kHz [139]. As squeal is linked to the wheel being excited in one of its resonances [7], squeal may also occur at higher frequencies (see e.g. Ref. [140]). The main squeal tones are nevertheless covered by a frequency range up to 5 kHz [7]. Such wheel/rail interaction models are denoted high-frequency models to distinguish them from models of the classical vehicle/track dynamics considering, for instance, running stability, curving behaviour and passenger comfort, which typically include frequencies up to 20 Hz [39].

As mentioned in the previous chapter, Kalker stated in Ref. [70] that the transient effects in the wheel/rail contact are not especially relevant in the railway dynamic simulation, hence it is enough to consider the variations of the contact magnitudes as a succession of stationary states. Therefore, most contact models used in simulations of train/track dynamic interaction are stationary. Nevertheless, some railway problems are closely related to fast temporal variations in the contact magnitudes, e.g. short wave corrugation, rolling noise and squeal noise, and the transient process in the wheel/rail contact can become more important, especially when $L/a_1 < 10$ as Knothe and Groβ-Thebing [102,119] stated. In curve squeal in particular, the dynamics in the contact are crucial to describe the stick/slip process in the contact patch, cyclic process in which part of the contact area moves into adhesion and slipping conditions, successively. According to the literature [5], this process could be essential to explain the mechanism for the occurrence of squeal.

The assumption of an elliptical wheel/rail contact patch located on the same vertical than the centre of the wheel does not correspond to the reality since the Hertzian assumptions do not fit the reality. The presence of roughness or corrugation can significantly affect the shape of the contact patch and the normal traction distribution. Notwithstanding, simulations with the wheelset negotiating sharp curves will be carried out in Section 6.3, in which contact near the wheel flange can occur; thereby, the Hertzian half-space assumption is not met since the dimensions of the contact patch can be around the same order of the geometry radii that define the wheel and rail curvatures, and multi-contact point can occur in this type of geometry.

With this purpose, the wheel/rail contact problem is modelled through *Exact Theories*. The resolution of the contact problem is made through the following steps (see sketch of Fig. 4.1):

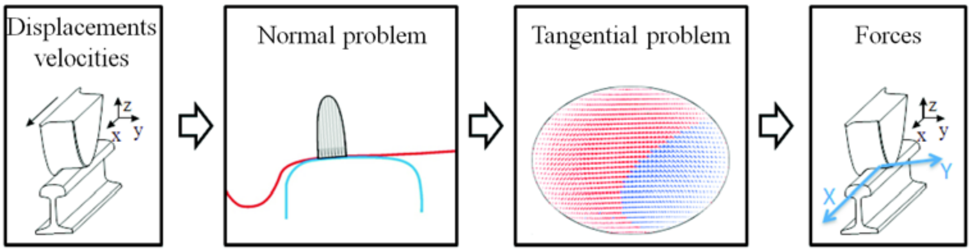

Fig. 4.1. Wheel/rail contact problem.

1. From the generalised coordinates associated with the wheelset, calculation of the positions and velocities of the contact point relative to the rail.
2. Normal contact problem. Determination of the wheel/rail contact area and the normal traction distribution.
3. Tangential contact problem. Calculation of the tangential traction distribution.
4. Integration of the tractions over the contact area in order to calculate the resultant forces.

This chapter begins with the description of the wheel/rail rolling contact in Section 4.2, studying the behaviour of elastic bodies in rolling contact, and developing the elastic (influence coefficients) and the kinematic formulations for half-spaces representing the solids in contact. Section 4.3 details the numerical algorithm employed in the present thesis for solving the normal and the tangential problems, based on Kalker’s variational theory; the tangential contact model in steady-state conditions is also derived. The numerical errors of the method are evaluated in Section 4.4. A falling friction coefficient characterised by kinematic and static values is introduced in the steady-state algorithm, finding a numerical discontinuity around the stick and the slip regions due to the separated set of equations employed in the original method. Section 4.5 implements the regularisation of Coulomb's law as an efficient numerical strategy to avoid this discontinuity. The influence of the falling friction on the rolling contact parameters and a comparison to experimental data from test-bench is presented in Section 4.6. This chapter ends with the main conclusions in Section 4.7.

4.2 WHEEL/RAIL ROLLING CONTACT MODEL

Contact theories provide laws which allow relating the tangential forces to the creepages. The complexity of the real problem comes from its 3D nature, so that there will be force and creepages in the rolling direction and also in the lateral direction. Solving the wheel/rail contact problem requires determining the size and shape of the contact patch, normal and tangential distributions, displacement and local slip velocity distributions and forces and moment transmitted through the contact. Previously, it is needed to know the wheel and rail profile geometry around the contact, the penetration (or approach) between them, the relative velocities between wheel and rail, the material properties and tribological state of the surface in contact. Sometimes, some inputs and previous results can be interchanged. For instance, instead of prescribing penetration, the normal force can be considered as input to obtain the penetration as output; or tangential forces as input instead of creepages. When forces are considered as inputs from which movement is calculated, the problem is known as direct dynamic problem; otherwise, inverse dynamic problem. In railway contact models, penetration and creepages are used as inputs to obtain the forces and moment in the contact (inverse problem).

If both bodies in contact behave elastically equal (the same displacements for the same actions), then the elastic quasi-identity conditions are met. More concretely, the elastic quasi-identity is met if both bodies behave elastically as infinite half-spaces and if their mechanical properties (Young's modulus and Poisson's ratio) match. Thus the properties of the elastic quasi-identity are:

- In the normal contact problem, the normal displacements due to the tangential tractions are not considered in the formulation.

- In the tangential contact problem, the contribution of the normal tractions on the tangential displacements is not considered in the formulation.

- The tangential conditions do not influence the normal contact problem. It is then possible to solve the normal problem and, once known the contact area, calculate the tangential problem.

The dimensions of the contact area in the wheel/rail contact are between 1 and 4 cm, thus the curvature radii are much higher than the dimensions of the contact patch. This is a case of non-conformal contact. The main consequences of the non-conformal contact are the following:

- Since both contact surfaces are close to be parallel, it is possible to establish a normal direction and a plane tangential to the contact.

- If a wheel point is going to contact other rail point once a normal load is transmitted, both points will be on a line whose direction is the normal one to the contact.

- The assumption of solids behaving elastically as infinite half-spaces can be considered. Hence, quasi-identity conditions are met and the normal contact problem does not depend on the tangential one (since both solids in contact are made of the same material).

Conformity conditions (contact area and curvature radii are similar) can be met whether the wheelset is laterally displaced and the contact is located e.g. between the flange and the tread of the wheel profile; this is the case for the vehicle negotiating a sharp curve, condition in which curve squeal can occur. Nevertheless, the present thesis adopts the non-conformal contact model in order to simplify the contact formulation, as assumed in recent works for curve squeal [13,17,44,94].

As initial step to solve the contact problem, it is needed to establish a formulation that relates displacements, tractions and slip velocities by means of elasticity equations and kinematic constraints that must be satisfied in the contact.

4.2.1 Elastic model

A reference system is defined in order to model the elastic problem. An inertial reference system $\mathbf{X}_1\mathbf{X}_2\mathbf{X}_3$ moving with the vehicle with a velocity (corresponding to the rolling or longitudinal velocity) V is adopted (see Fig. 4.2). The origin of the system is the theoretical contact point (point where wheel and rail profiles would be in contact if both were rigid). The $\mathbf{X}_1$-axis refers to the rolling direction and the $\mathbf{X}_2$-axis is associated to the lateral direction in such a way that $\mathbf{X}_1\mathbf{X}_2$ is the tangential contact plane. The $\mathbf{X}_3$-axis is normal to the contact in a positive direction towards the wheel. The precise definition of these axes will be carried out in Section 5.6.

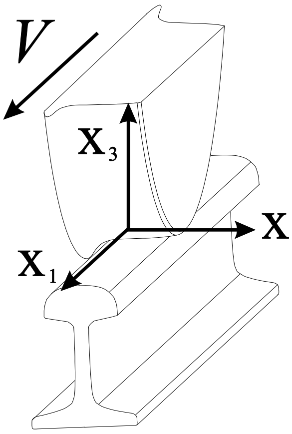

Fig. 4.2. Reference system used in the contact.

Let define $p_j(x_1,x_2)$ as the traction in a point (x_1,x_2) according to the $\mathbf{X}_j$-direction. $u_j(x_1,x_2)$ is the field of the displacements the $\mathbf{X}_j$-direction associated with the deformations in the contact. The normal problem, which permits to calculate the contact area, involves tractions p_3 and displacements u_3 normal to the contact. The tangential problem is associated with the tractions p_1 and p_2 and the displacements u_1 and u_2. From now, the magnitudes contained in the tangential plane will be referred using the notation p_τ, u_τ and x_τ will be utilised (hence, $\tau = 1,2$). Taking into account it is not needed to locate a point outside the contact plane $x_3 = 0$, it is defined $\mathbf{x} = (x_1, x_2)$ (and hence, $p_j \equiv p_j(\mathbf{x})$ and $u_j \equiv u_j(\mathbf{x})$). The relationship between the tractions and deformations fields is based on the application of the Elasticity Theory. In general, the elastic models that relate both tractions and deformations in the contact area are used to find the influence coefficients $A_{ij}(\mathbf{x},\mathbf{y})$, defined as the displacement in the point $\mathbf{x}$ in the *i*-direction when a unitary traction is applied in the *j*-direction of the point $\mathbf{y}$. The elastic half-space is one of the few geometries in 3D elasticity for which the influence functions are explicitly known; in the general case they can only be evaluated numerically. Thus the half-space assumption considerably simplifies the solution of the three-dimensional contact problem.

Assuming linear elastic behaviour of the bodies in contact, the superposition principle is applied, thus the constitutive equation that describes the displacements field in the contact area is calculated through the extended integral on the frontier of the contact area ∂C:

$$u_i(\mathbf{x}) = \sum_{j=1}^{3} \int_{\partial C} A_{ij}(\mathbf{x},\mathbf{y}) p_j(\mathbf{y}) \, \mathrm{d}s(\mathbf{y}), \quad i = 1,2,3, \tag{4.1}$$

where the integral is extended to the contact surface through the integration variable vector $\mathbf{y} = \{y_1, y_2\}^{\mathrm{T}}$. There exists a cross influence between the tangential and the normal problem. Assuming properties of elastic quasi-identity, it is not useful to study the contribution of normal stresses over normal displacements and vice versa as detailed in Section 3.4.1, so that the formulation for normal problem will be:

$$u_3(\mathbf{x}) = \int_{\partial C} A_{33}(\mathbf{x},\mathbf{y}) p_3(\mathbf{y}) \, \mathrm{d}s(\mathbf{y}), \tag{4.2}$$

and for the tangential problem:

$$u_\tau(\mathbf{x}) = \sum_{\kappa=1}^{2} \int_{\partial C} A_{\tau\kappa}(\mathbf{x},\mathbf{y}) p_\kappa(\mathbf{y}) \, \mathrm{d}s(\mathbf{y}), \quad \tau = 1,2, \tag{4.3}$$

where $\int_{\partial C} \mathrm{d}s$ indicates the extended integral in the contact area.

When the non-conformity condition is met in the wheel/rail contact, the displacements close to the contact are similar than the ones in an infinite half-space. Eq. (4.1) particularised to an infinite half-space is known as Boussinesq-Cerruti integral (the influence functions for the elastic half-space have been derived by Boussinesq [71] and

Cerruti [72] and may also be found in Ref. [81]), with analytical solutions for some types of load distributions. One of these is a constant pressure on a rectangle surface.

Let define an infinite half-space which occupies $x_3 < 0$. There exists a rectangle on it of dimensions $2b_1 \times 2b_2$ loaded by a constant traction p_3. The rectangle is centred at the origin $\mathbf{x} = (0,0)^{\mathrm{T}}$, corresponding the dimensions $2b_1$ and $2b_2$ to the $\mathbf{X}_1$- and $\mathbf{X}_2$-directions, respectively. The displacements in the $\mathbf{X}_3$-direction on the surface of the half-space are calculated through the following expression:

$$\begin{aligned} u_3(x_1,x_2) = \frac{p_3(1-\nu^2)}{\pi E}\Bigg[& (x_1+b_1)\ln\left(\frac{(x_2+b_2)\sqrt{(x_1+b_1)+(x_2+b_2)}}{(x_2-b_2)\sqrt{(x_1+b_1)+(x_2-b_2)}}\right) \\ & +(x_2+b_2)\ln\left(\frac{(x_1+b_1)\sqrt{(x_1+b_1)+(x_2+b_2)}}{(x_1-b_1)\sqrt{(x_1-b_1)+(x_2+b_2)}}\right) \\ & +(x_1-b_1)\ln\left(\frac{(x_2-b_2)\sqrt{(x_1-b_1)+(x_2-b_2)}}{(x_2+b_2)\sqrt{(x_1-b_1)+(x_2+b_2)}}\right) \\ & +(x_2-b_2)\ln\left(\frac{(x_1-b_1)\sqrt{(x_1-b_1)+(x_2-b_2)}}{(x_1+b_1)\sqrt{(x_1+b_1)+(x_2-b_2)}}\right)\Bigg], \end{aligned} \tag{4.4}$$

where E and ν are Young's modulus and Poisson's ratio, respectively.

Now, two tangential tractions in the $\mathbf{X}_1$- and $\mathbf{X}_2$-directions on the rectangle are applied. The displacement in the $\mathbf{X}_1$-direction on the surface of the half-space is calculated through:

$$u_1(x_1,x_2) = \frac{(1+\nu)}{2\pi E}\left[\left(J_1(x_1,x_2)+(1-\nu)J_2(x_1,x_2)\right)p_1 + \nu J_4(x_1,x_2)p_2\right], \tag{4.5}$$

and in the $\mathbf{X}_2$-direction is

$$u_2(x_1,x_2) = \frac{(1+\nu)\nu}{2\pi E}\left(J_3(x_1,x_2)p_1 + J_4(x_1,x_2)p_2\right), \tag{4.6}$$

where:

$$\begin{aligned} J_1(x_1,x_2) = {} & (x_2+b_2)\ln\left(\frac{(x_1+b_1)\sqrt{(x_1+b_1)^2+(x_2+b_2)^2}}{(x_1-b_1)\sqrt{(x_1-b_1)^2+(x_2+b_2)^2}}\right) \\ & +(x_2-b_2)\ln\left(\frac{(x_1-b_1)\sqrt{(x_1-b_1)^2+(x_2-b_2)^2}}{(x_1+b_1)\sqrt{(x_1+b_1)^2+(x_2-b_2)^2}}\right), \end{aligned} \tag{4.7}$$

$$\begin{aligned} J_2(x_1,x_2) = {} & (x_2+b_2)\ln\left(\frac{(x_1+b_1)\sqrt{(x_1+b_1)^2+(x_2+b_2)^2}}{(x_1-b_1)\sqrt{(x_1+b_1)^2+(x_2-b_2)^2}}\right) \\ & +(x_2-b_2)\ln\left(\frac{(x_1-b_1)\sqrt{(x_1-b_1)^2+(x_2-b_2)^2}}{(x_1+b_1)\sqrt{(x_1-b_1)^2+(x_2+b_2)^2}}\right), \end{aligned} \tag{4.8}$$

$$\begin{aligned} J_4(x_1,x_2) = {} & \sqrt{(x_1-b_1)^2+(x_2+b_2)^2}-\sqrt{(x_1+b_1)^2+(x_2+b_2)^2} \\ & -\sqrt{(x_1-b_1)^2(x_2-b_2)^2}+\sqrt{(x_1+b_1)^2+(x_2-b_2)^2}. \end{aligned} \tag{4.9}$$

For more details about the functions J_1, J_4 and J_4 (used for the definition of the influence coefficients), see Appendix A.

4.2.2 Kinematic model

The methodology employed to model the kinematics of the contact is a general approach in Continuum Mechanics of the type proposed by Mase and Mase [141]. In order to model the kinematic of the contact, let take the "configuration" concept, commonly employed in Continuum Mechanics, which permits to model displacements and velocities of flexible solid points (see Fig. 4.3). The reference configuration corresponds to an arbitrary and fixed (non-dependent of time) position of the undeformed solid. Frequently, it is chosen the one that the undeformed solid occupies in the instant $t=0$, but it can be even defined a position that the solid cannot physically occupy. The deformed configuration corresponds to a space occupied by a flexible solid in the instant t. It is defined the intermediate configuration between the reference one and the undeformed one, known as non-deformed. This one depends (the same than the deformed one) on time and it presents the property that the transformation from the deformed configuration to the undeformed one consists of a small displacement.

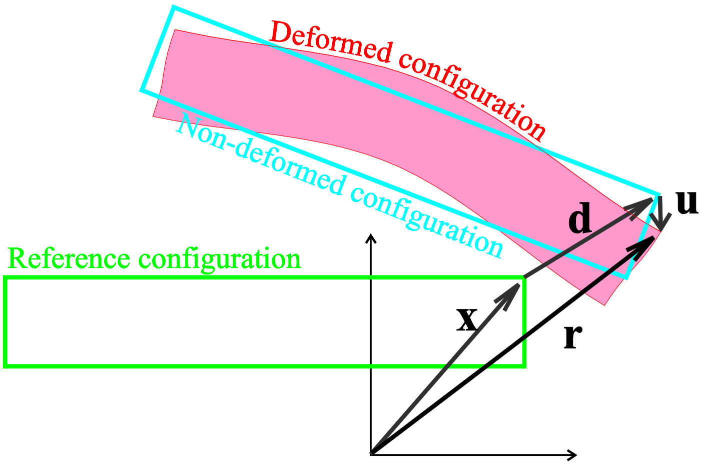

Fig. 4.3. Reference configuration, non-deformed and deformed one.

According to the scheme presented in Fig. 4.3, the position of a material particle which in the reference configuration occupies the position $\mathbf{x}$, is calculated as

$$\mathbf{r} = \mathbf{x} + \mathbf{d} + \mathbf{u}, \tag{4.10}$$

where $\mathbf{d}$ is the vector that describes the displacement of the rigid solid from the reference position, and $\mathbf{u}$ is the displacement vector associated with the deformations. Vectors $\mathbf{r}$, $\mathbf{d}$ and $\mathbf{u}$ are functions of $\mathbf{x}$ and t. The reason that justifies this approach is that there exist formulations to model the kinematic of rigid bodies (Euler angles, equation of the velocities field, etc.) and others to model small displacements associated with deformations (linear elasticity, vibrations, etc.). Eq. (4.10) is derived with respect to time by means of the material derivative denoted by $\mathrm{D}/\mathrm{D}t$:

$$\frac{\mathrm{D}\mathbf{r}}{\mathrm{D}t} = \frac{\mathrm{D}\mathbf{d}}{\mathrm{D}t} + \frac{\mathrm{D}\mathbf{u}}{\mathrm{D}t}. \tag{4.11}$$

The use of the material derivative of the displacements associated with the deformations, defined as $\mathrm{D}/\mathrm{D}t = \partial/\partial t + V\,\partial/\partial x_1$, comes from the moving nature of the contact load, which requires accounting the convective term since the reference system is moving with a velocity V.

4.2.2.1 Kinematics of the normal contact

Based on the proposed methodology, the configurations shown in Fig. 4.4 have been defined for the rail and the wheel:

- The reference configurations for the rail and the wheel correspond to the positions of both undeformed solids when they have an only one contact position (assuming that both solids are rigid), known as theoretical contact point. The reference system associated with the rail $\mathbf{X}_1\mathbf{X}_2\mathbf{X}_3$ is centred on this theoretical contact point, according to the criteria defined in Section 4.2.1. A function $h(x_1,x_2)= z^r(x_1,x_2)-z^w(x_1,x_2)$ measures the distance between both wheel and rail surfaces, according to $\mathbf{X}_3$-direction. This function, known as distance between undeformed surfaces, depends on the geometry of both surfaces and the relative position between them.

- The undeformed wheel configuration corresponds to the movement of the rigid solid itself of the wheel. The rail does not move, hence it matches the reference and undeformed configurations. The component of the wheel displacement normal to the contact plane, known as elastic penetration between the undeformed surfaces or approach δ, is of interest.

- The deformed configuration will be the final position in the wheel/rail contact. In this configuration, the displacements associated with the deformation in the $\mathbf{X}_3$-direction of the wheel u_3^w and the rail u_3^r will be calculated.

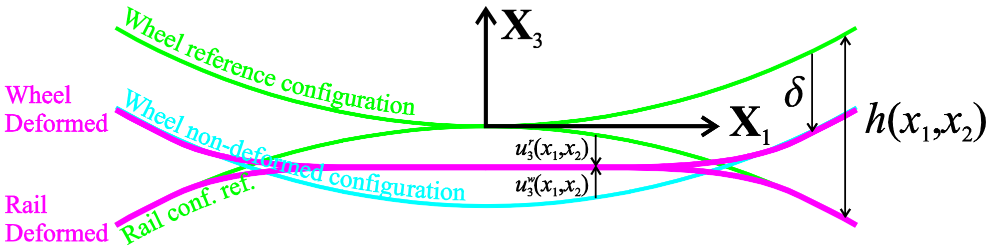

Fig. 4.4. Reference configuration, non-deformed and deformed one for the rail and the wheel.

According to the Newton's Third Law, the wheel traction distribution p_3^w is equal, but with opposite sign, to the rail traction distribution p_3^r. As a consequence of this, and taking into account that both solids have an identical response to the same type of actions (since they behave elastically as half-spaces), the displacements associated with the deformations of the wheel u_3^w and the rail u_3^r are equal and with opposite sign. From now, u_3 and p_3 are referred to the rail ($u_3 = u_3^r = -u_3^w$, and $p_3 = p_3^r = -p_3^w$). According to this, the following expression is satisfied:

$$\delta = h(x_1, x_2) - 2u_3(x_1, x_2). \tag{4.12}$$

4.2.2.2 Kinematics of the tangential contact

Creepages are defined in the tangential contact problem as the reduced magnitudes that represent the tangential velocity of the contact point for slip conditions. In order to calculate them, assuming rigid wheelset and rigid track, the undeformed velocity of the nominal contact point is computed through the equation of the velocity field:

$$\mathbf{v} = \mathbf{v}_G + \boldsymbol{\omega} \times \mathbf{r}, \tag{4.13}$$

being $\mathbf{v}_G$ the velocity of the centre of mass of the wheelset referred to the $\mathbf{X}_1\mathbf{X}_2\mathbf{X}_3$ system, $\boldsymbol{\omega}$ the angular velocity of the wheelset and $\mathbf{r}$ the position vector which links the centre of mass with the theoretical contact point. Therefore, the component v_3 must be zero (if a contact model based on kinematic constraints is adopted) or very small (if a contact model with a penalty formulation is taken). The components v_1 and v_2 are defined as creepages respect to the longitudinal and lateral directions; using adimensionalised magnitudes (with no units), tangential creepages are:

$$\xi_\tau = \frac{v_\tau}{V}, \quad \tau = 1{,}2. \tag{4.14}$$

Fundamentally due to the wheel conicity, a spin velocity also appears between wheel and rail. The spin is, hence, the component normal to the contact of the absolute angular velocity vector of the wheelset $\boldsymbol{\omega}$. The spin creepage is estimated similarly to the tangential creepages, but with units in [rad/m] in this case:

$$\xi_{sp} = \frac{\boldsymbol{\omega} \cdot \mathbf{i}_3}{V}. \tag{4.15}$$

Once defined the creepages, the kinematic of the tangential contact is derived from Eq. (4.11). Let assume the points of the rail P_r and wheel P_w in contact. The difference in both point velocities will correspond to the relative slip velocity between both surfaces (or local slip velocity) $\mathbf{s}$:

$$\mathbf{s}=\frac{\mathrm{D}\mathbf{r}^w}{\mathrm{D}t}-\frac{\mathrm{D}\mathbf{r}^r}{\mathrm{D}t}, \tag{4.16}$$

being $\mathbf{r}^r$ and $\mathbf{r}^w$ the position vectors of the contact points P_r and P_w. According to Eq. (4.11), the velocity of both bodies can be described through the movement of the rigid solid and the displacements associated with the deformations as:

$$\mathbf{s}=\left(\mathbf{w}+\frac{\mathrm{D}\mathbf{u}^w}{\mathrm{D}t}\right)-\frac{\mathrm{D}\mathbf{u}^r}{\mathrm{D}t}, \tag{4.17}$$

being $\mathbf{w}$ the velocity associated with the undeformed configuration, which is computed through the equation of the velocities field:

$$\mathbf{w}=\begin{Bmatrix} v_1-\omega_{sp}x_2 \\ v_2+\omega_{sp}x_1 \end{Bmatrix}=V\begin{Bmatrix} \xi_1-\xi_{sp}x_2 \\ \xi_2+\xi_{sp}x_1 \end{Bmatrix}, \tag{4.18}$$

where ω_{sp} is the spin term. Vectors $\mathbf{u}$, $\mathbf{s}$ and $\mathbf{w}$ are in the $\mathbf{X}_1\mathbf{X}_2$ contact plane (they contain longitudinal and lateral components), and they are functions of the point $\mathbf{x}=\{x_1,x_2\}^{\mathrm{T}}$ within the contact area. Taking into account that the displacements associated with the wheel deformations are equal and with opposite sign than the rail ones, $\mathbf{u}=\mathbf{u}^w=-\mathbf{u}^r$, and developing the material derivative, the tangential components of the local slip velocity can be calculated as

$$\mathbf{s}=\mathbf{w}+2\frac{\mathrm{D}\mathbf{u}}{\mathrm{D}t}=\mathbf{w}+2\frac{\partial\mathbf{u}}{\partial t}+2V\frac{\partial\mathbf{u}}{\partial x_1}. \tag{4.19}$$

The formulation for the tangential contact problem for steady-state conditions will be required in Section 4.6 in order to address a tribological study of the influence of the falling friction on creep curves. The original instationary method is modified in order to obtain the steady-state solution of the rolling contact problem. By introducing the constitutive Eq. (4.3) in Eq. (4.19), the instationary kinematic equation for the tangential contact results

$$
\begin{aligned}
s_\tau &= w_\tau + 2\int_{\partial C} A_{\tau\kappa}(\mathbf{x},\mathbf{y})\frac{\partial p_\kappa(\mathbf{y})}{\partial t}\,\mathrm{d}S(\mathbf{y}) \\
&+ 2V\sum_{\kappa=1}^{2}\int_{\partial C}\left(\frac{\partial A_{\tau\kappa}(\mathbf{x},\mathbf{y})}{\partial x_1}p_\kappa(\mathbf{y}) + A_{\tau\kappa}(\mathbf{x},\mathbf{y})\frac{\partial p_\kappa(\mathbf{y})}{\partial x_1}\right)\mathrm{d}s(\mathbf{y}),\quad \tau = 1,2.
\end{aligned}
\tag{4.20}
$$

The partial derivative with respect to t in Eq. (4.20) is zero if the steady-state conditions are imposed:

$$
s_\tau = w_\tau + 2V\sum_{\kappa=1}^{2}\int_{\partial C}\left(\frac{\partial A_{\tau\kappa}(\mathbf{x},\mathbf{y})}{\partial x_1}p_\kappa(\mathbf{y}) + A_{\tau\kappa}(\mathbf{x},\mathbf{y})\frac{\partial p_\kappa(\mathbf{y})}{\partial x_1}\right)\mathrm{d}s(\mathbf{y}),\quad \tau = 1,2, \tag{4.21}
$$

Since $\mathbf{y}$ is the integration variable in Eq. (4.21), it is independent of x_1. Therefore, the derivative $\partial p_\kappa(\mathbf{y})/\partial x_1$ is zero. Thus Eq. (4.21) results

$$
s_\tau = w_\tau + 2V\sum_{\kappa=1}^{2}\int_{\partial C}\frac{\partial A_{\tau\kappa}(\mathbf{x},\mathbf{y})}{\partial x_1}p_\kappa(\mathbf{y})\,\mathrm{d}s(\mathbf{y}),\quad \tau = 1,2. \tag{4.22}
$$

4.3 NUMERICAL ALGORITHM

In the present thesis, the contact problem is addressed through a methodology that solves the normal problem and later the tangential one following CONTACT algorithm [81,142]. CONTACT is based on a spatial discretisation of the contact patch as a variation of the so-called Boundary Elements (BE) method, in which each magnitude is considered constant and equal to the value in the centre of the element. Once established a reference system $\mathbf{X}_1\mathbf{X}_2\mathbf{X}_3$ and the contact plane $x_3 = 0$, it is defined the potential contact area as a rectangular region on the contact plane that contains, at least, all the points of the contact area. The potential contact area is discretised in a regular mesh with rectangular elements of dimension $2b_1 \times 2b_2$.

The fundamental assumption adopted consists of considering that the traction distribution is constant for each element of the mesh. Therefore, it is defined a traction p_j^I as the one which appears in the I-th element of the mesh in the j-direction. u_j^I are the displacements, $h^I = z^{I,r} - z^{I,w}$ are the undeformed distance and w^I the velocity associated with the undeformed configuration, respectively, all of these calculated in the centre of the *I*-th element of the mesh. x_1^I and x_2^I are the coordinates of the *I*-th element. Assuming elastic quasi-identity conditions are met, it is possible to uncouple the normal problem from the tangential one.

4.3.1 Algorithm for solving the normal contact problem

This methodology is based on NORM [81] algorithm from CONTACT, which solves the normal contact problem. Let consider that the *J*-th rectangle of the potential contact area is loaded with a normal pressure p_3^J. According to the Linear Elastic Theory, the normal displacement of the *I*-th element of the mesh will be

$$u_3^I = D_{33}^{IJ} p_3^J, \tag{4.23}$$

where D_{33}^{IJ} is the elastic influence coefficient and it is easily calculated through Eq. (4.4) replacing x_1 by $x_1^I - x_1^J$ and x_2 by $x_2^I - x_2^J$ and making $p_3^J = 1$ (see Appendix A). Applying the superposition principle, the constitutive equation permits to calculate the displacements due to the loads in the contact:

$$u_3^I = \sum_{J=1}^{N} D_{33}^{IJ} p_3^J, \tag{4.24}$$

where the summation is extended to all the N elements of the contact area. Replacing Eq. (4.24) in Eq. (4.12), the following expression is obtained:

$$\delta^I = h^I - 2\sum_{J=1}^{N} D_{33}^{IJ} p_3^J. \tag{4.25}$$

Eq. (4.25) provides a linear equations system, where the normal tractions are the unknowns. The problem is to know which elements of the potential contact area are part of that area. For the dynamic interaction model, as the points of the elastic half-space are coupled, the vertical displacements of the rail, $w^{I,r}(t_i)$, and the wheel nodes, $w^{I,w}(t_i)$, on the potential contact patch at the current time step are introduced in the NORM algorithm to evaluate the normal problem time step by time step. The rail, $r^{I,r}$, and wheel roughness, $r^{I,w}$ can be also included as inputs to consider irregularities on the surfaces in contact. A new variable to compute the distance between the deformed bodies is defined:

$$d^I = \delta^I + w^{I,r}(t_i) - w^{I,w}(t_i) + r^{I,r} - r^{I,w}. \tag{4.26}$$

The contact conditions are formulated as

$$d^I \geq 0, \tag{4.27}$$

$$p_3^I \geq 0, \tag{4.28}$$

$$d^I p_3^I = 0. \tag{4.29}$$

If contact occurs in a surface element, the distance is zero and the contact pressure is positive. If contact does not occur, the distance is positive and the pressure is zero. A negative value of the distance would mean the two bodies penetrate into each other, which is physically impossible. A negative contact pressure would correspond to adhesion. Both penetration and adhesion are excluded by Eqs. (4.27) to (4.29).

Eqs. (4.25) to (4.29) form a non-linear equation system that completely describes the normal contact problem at each time step. An explicit equation for u_3^I is only available for the element that are in contact, where $d^I = 0$; from Eqs. (4.25) and (4.26):

$$u_3^I = -h^I - w^{I,r}(t_i) + w^{I,w}(t_i) - r^{I,r} + r^{I,w}, \tag{4.30}$$

and it is a priori unknown which elements are in contact.

An efficient iterative method to solve the normal contact problem is the algorithm proposed by Kalker [81]. He used a variational method and formulated the normal contact problem as a minimisation problem of an appropriate energy functional. To solve this problem, Kalker developed his active set algorithm NORM. The reason why this algorithm is called active set algorithm is as follows. The solution, in the form of the contact pressure distribution, is subjected to the inequality constraint $p_3^I \geq 0$. The elements in the potential contact patch are divided into two sets.

In the following, the indices I and J denote an element in the set of elements forming the potential contact patch P, i.e. $I \in P$ and $J \in P$, if not stated differently. The potential contact patch consists of the contact patch C and the exterior area E. The set of elements where the inequality constraint is active, i.e. $p_3^I = 0$, is called the active set A. The remaining elements form the set N. In the normal contact problem, the active set thus comprises the elements which are not in contact, i.e. $A = E$ and $N = C$. Initially, an assumption is made about which elements belong to the active set. The active set is then updated step-by-step in the algorithm until the final solution is found. In detail, the active set algorithm used works as follows:

1. Initially, all elements are placed in the active set $A = E$ (which means $p_3^I = 0$ in all elements).

2. The distance is calculated for all elements from Eq. (4.26), which reduces to

$$d^I = w^{I,r}(t_i) - w^{I,w}(t_i) + h^I + r^{I,r} - r^{I,w}, \tag{4.31}$$

since $u_3^I = 0$ (due to $p_3^I = 0$ in all elements).

3. All points with a negative distance, $d^I < 0$, are removed from the set E and added to the set of contact elements C.

4. For the elements in the contact set C, the distance is zero and the surface displacement u_3^I is calculated from Eq. (4.30).

5. The contact pressure of all elements in contact is evaluated by setting up Eq. (4.24) for all N_c elements in C:

$$u_3^I = \sum_{J=1}^{N_c} D_{33}^{IJ} p_3^J, \quad I \in C, \tag{4.32}$$

and solving the resulting linear equation system for the unknown p_3^J.

6. All elements with negative pressure, $p_3^I < 0$, are removed from C and added to E.

7. Steps 4-6 are repeated until no negative pressure is present anymore.

8. It has to be verified whether the solution found fulfils Eq. (4.27). Therefore the displacement u_3^I is calculated for all elements in E with Eq. (4.24) and the distance is evaluated according to Eq. (4.26).

9. If there are any points with negative distance, $d^I < 0$, these points are removed from the exterior area E and added to the contact patch C.

10. Steps 4-9 are repeated until no negative distance is present anymore.

At the end of this iterative procedure, the size and shape of the contact zone and the contact pressure distribution are known. The contact deformation compensates only for part of the rigid slip and wheel/rail dynamic response contribution. The rest is compensated through slip, which is the difference between the rigid slip and a combination of the contact deformation and the wheel/rail dynamic contribution.

4.3.2 Algorithm for solving the tangential contact problem

This methodology is based on TANG [81] algorithm from CONTACT, which solves the tangential contact problem. Let consider that the *J*-th rectangle of the potential contact area is loaded with a normal pressure p_3^J. Following a procedure analogous to the normal problem and according to the Linear Elastic Theory, the tangential displacements of the *I*-th element of the mesh will be (for $\tau = 1,2$):

$$u_\tau^I = \sum_{\kappa=1}^{2} \sum_{J=1}^{N} D_{\tau\kappa}^{IJ} p_\kappa^J, \tag{4.33}$$

where $D_{\tau\kappa}^{IJ}$ is the elastic influence coefficient (see Appendix A). Hence, the integral throughout the contact area that define the kinematic relationship of Eq. (4.20) can be replaced by the summation of the contributions of each element of the contact mesh:

$$s_\tau^I = w_\tau^I + 2\frac{\partial u_\tau^I}{\partial t} + 2V \sum_{\kappa=1}^{2} \sum_{J=1}^{N} \frac{\partial D_{\tau\kappa}^{IJ}}{\partial x_1} p_\kappa^J. \tag{4.34}$$

The temporal discretisation establishes an approximation to the partial time derivative $\partial u_\tau^I / \partial t$ by means of finite differences:

$$\frac{\partial u_\tau^I}{\partial t} \approx \frac{u_\tau^I - u_{\tau 0}^I}{\Delta t}, \tag{4.35}$$

where Δt is the time step and $u_{\tau 0}^I$ represents the displacements in the *I*-th element of the mesh associated with the traction distribution calculated at a previous instant $t - \Delta t$, applied in a mesh delayed with respect to the current one a distance $V\Delta t$ in the $\mathbf{X}_1$-direction.

It is important to highlight that the method depends on time because it is an integration algorithm of an ordinary differential equations system. By definition, $\partial x_1 = V\partial t$; hence, for the temporal discretisation:

$$\Delta x_1 = V\Delta t. \tag{4.36}$$

Replacing Eq. (4.36) in the tangential kinematic equation (4.34), it results:

$$s_\tau^I = w_\tau^I + 2\sum_{\kappa=1}^{2}\sum_{J=1}^{N} D_{\tau\kappa}^{IJ} p_\kappa^J + 2V\left(\sum_{\kappa=1}^{2}\sum_{J=1}^{N}\frac{\partial D_{1\kappa}^{IJ}}{\partial x_1} p_\kappa^J - \frac{u_{\tau 0}^I}{\Delta x_1}\right), \quad I \in C. \tag{4.37}$$

For each element in contact ($p_3^I < 0$), there are two corresponding equations for $\tau = 1,2$. *I*-th element is slipping if the local slip velocity is not zero ($\left\|\mathbf{s}^I\right\| > 0$), which occurs when the tangential tractions reach the friction bound:

$$p_3^I \mu = \sqrt{\left(p_1^I\right)^2 + \left(p_2^I\right)^2}, \quad I \in S, \tag{4.38}$$

being μ the friction coefficient between the wheel and rail surfaces. If in the *I*-th element the slip conditions are met, then s_1^I and s_2^I are unknowns and the tangential tractions of this element are calculated in function of the local slip velocity following the Coulomb's law:

$$p_\tau^I = -p_3^I \mu \frac{s_\tau^I}{\sqrt{\left(s_1^I\right)^2 + \left(s_2^I\right)^2}}, \quad I \in S. \tag{4.39}$$

Conversely, in the elements in which there exist adhesion conditions, the local slip velocity is zero ($\left\|\mathbf{s}^I\right\| > 0$), and the unknowns will be the tangential tractions p_1^I and p_2^I . The problem is now knowing which elements in the contact area are slipping or in adhesion.

An efficient algorithm to solve the non-linear set of equations (4.37)–(4.39) is based on Kalker's active set algorithm TANG [81], also summarised in Ref. [143]. This algorithm, which has been used here, is very similar to the algorithm NORM described previously and works as follows. The set of contact elements is divided into two sets, the active set A and the set of remaining elements N . The active set comprises the elements where the constraint $\left(p_1^I\right)^2 + \left(p_2^I\right)^2 \le \left(\mu p_3^I\right)^2$ is active. This is the case for the elements in the slip zone, where $\left(p_1^I\right)^2 + \left(p_2^I\right)^2 = \left(\mu p_3^I\right)^2$, i.e. $A = S$. Consequently, the set

N consists of the elements in the stick zone; i.e. $N = H$. The steps in the algorithm, as used here, are:

1. Initially all elements are placed in the stick zone H (i.e. the initial estimation of the active set is $A = \varnothing$).

2. For the current division of the contact zone into stick zone and slip zones, the non-linear system of equations consisting of Eq. (4.38) and

   $$s_\tau^I = 0, \quad I \in H, \tag{4.40}$$

   $$p_1^I s_2^I - p_2^I s_1^I = 0, \quad I \in S, \tag{4.41}$$

   is solved for the unknown tractions, making use of the definition of s_τ^I in Eq. (4.37). Eq. (4.41), which is taken from reference [143], replaces Eq. (4.39) and allows in contrast to Eq. (4.38) also that the slip occurs in the direction of the tangential traction (not only in the opposite direction).

3. All elements in H with tangential tractions exceeding the traction bound, i.e. $\left(p_1^I\right)^2 + \left(p_2^I\right)^2 > \left(\mu p_3^I\right)^2$, are removed from H and added to S.

4. Steps 2 and 3 are repeated until there are no stick elements anymore that exceed the traction bound.

5. Now, it has to be verified whether the slip in all slip elements is opposite to the tangential tractions. All elements violating this condition are removed from S and added to H.

6. Steps 2-4 are repeated until the slip is opposite to the tangential tractions in all slip elements.

The non-linear equation system in step 2 is solved via Newton-Raphson iteration [144] using an initial estimation of the solution. An error function is set to the left member of Eq. (4.37) as objective function. The resulting equation is

$$f_\tau^I = w_\tau^I + 2\sum_{\kappa=1}^{2}\sum_{J=1}^{N} D_{\tau\kappa}^{IJ} p_\kappa^J + 2V\left(\sum_{\kappa=1}^{2}\sum_{J=1}^{N} \frac{\partial D_{1\kappa}^{IJ}}{\partial x_1} p_\kappa^J - \frac{u_{\tau 0}^I}{\Delta x_1}\right) - s_\tau^I, \quad I \in S. \tag{4.42}$$

Hence, successive iterations will seek that the error function approaches zero, $\left\|\mathbf{f}^I\right\| = \sqrt{\left(f_1^I\right)^2 + \left(f_2^I\right)^2} = 0$, within a set tolerance, so that Eq. (4.37) is satisfied. At the end of the iterative procedure, the division of the contact zone in stick and slip zones and the tangential stresses are known.

Once solved the tangential problem, the resulting forces are obtained by integrating (adding the contribution of each element) the tractions p_τ^J throughout the contact area. Since the rectangular dimensions of element J are $2b_1^J \times 2b_2^J$, the total forces are

$$F_j = 4\sum_{J=1}^{N} b_1^J b_2^J p_j^J, \quad j = 1,2,3. \tag{4.43}$$

The algorithm presented in this subsection has a number of computational disadvantages listed below:

- The elements in the slip zone S present twice unknowns that the elements in the stick zone H. For high creepages, the total number of unknowns doubles, quadrupling the dimension of the Jacobian matrix needed for the Newton-Raphson iteration.
- It is required to check iteration by iteration the state of each element, in order to verify if it is in the slip zone S or stick zone H, as well as estimations to predict if the element will change its state to control possible numerical divergences in next time steps.
- The Jacobian matrix is bad conditioned. Both sets of equations fragment the Jacobian matrix, featuring important jumps in the order of magnitude of its elements depending on their location in the matrix. The active control of the Jacobian conditioning further increases the computational cost.
- Strong non-linearity of the set of equations (4.37)–(4.41) to be solved. Step from H to S or vice versa impedes smooth numerical convergence of the solution.

4.3.2.1 Algorithm for steady-state conditions

The discretisation of the contact area into a regular mesh is also applied in the steady-state tangential formulation [145] previously derived from the instationary one in Section 4.2.2.2. From Eq. (4.22), the kinematic equation is written as (for $\tau = 1,2$):

$$s_\tau^I = w_\tau^I + 2V \sum_{J=1}^{N} \sum_{\kappa=1}^{2} \int_{\partial C^J} \frac{\partial A_{\tau\kappa}^J(\mathbf{x},\mathbf{y})}{\partial x_1} p_\kappa^J(\mathbf{y}) \, \mathrm{d}s(\mathbf{y}). \tag{4.44}$$

By assuming half-space elastic behaviour of the solids, a closed-form solution of the integrals in Eq. (4.44) can be obtained. The corresponding integrals can be arranged in a matrix, giving

$$s_\tau^I = w_\tau^I + 2V \sum_{J=1}^{N} \sum_{\kappa=1}^{2} C_{1\kappa}^{IJ} p_\kappa^J . \tag{4.45}$$

4.3.2.2 Implementation of the tangential algorithm in a study case

Eq. (4.44), together with the previous Eqs. (4.38) and (4.39), are applied to calculate the tangential traction and slip velocity distributions for a 2D study case; the contact data and kinematic parameters of the case are detailed in Tables 4.1 and 4.2. These three equations are simplified to a 2D tangential problem by reducing the contact patch to a contact line in the rolling direction $\mathbf{X}_1$ ($\tau = 1$), discretised uniformly into $N_1 = 200$ elements. Friction coefficient has a constant value of $\mu = 0.35$, the normal contact force F_3 is introduced as a constant input and both wheel and rail are made of a type of rubber much softer than steel. The rolling velocity is very slow (25.0×10^{-3} m/s), thus the time needed for stabilising the tangential distribution is on the order of seconds.

Fig. 4.5(a) represents two numerical solutions for the traction distribution: a snapshot of the instationary solution (from Eq. (4.37)) for the instant *t*=15 s once the solution is stabilised after the contact transient; and the steady-state solution. Both curves perfectly overlap in the figure, as expected. The stick zone is located in the rear part with respect to the wheel speed (right side) of the contact line. During the transient, the traction increases but still maintains a margin with respect to the bound curve $\mu p_3(x_1)$, proportional to the ellipsoidal contact pressure distribution.

When an element in the stick zone reaches $\mu p_3(x_1)$, it does not pull over since it cannot generate more friction that opposes the slip, so slides remaining on the bound curve; Fig. 4.5(b) shows how the slip velocity of the corresponding element is $s_1 > 0$. The elements in the slip zone are located on the outer discontinuous curve at the leading part of the contact line (left side), which correspond to the elements with non-zero slip velocity.

In Fig. 4.5(a), both curves for the tangential traction fit accurately the dashed curve corresponding to Carter solution [91]. This solution is analytically calculated through a stationary and exact non-linear theory for the tangential contact forces between a cylinder and an infinite plane subjected to longitudinal creepage and constant friction coefficient. This can be interpreted as the tangential formulation adopted in this thesis reproduces accurately the contact process for simple cases.

Shear modulus, G [N/m^2]	1.0×10^6
Poisson's ratio, ν [-]	0.28
Roller 1 radius, r_{11} [mm]	337.5
Roller 2 radius, r_{21} [mm]	337.5
Roller 1 radius, r_{12} [mm]	0
Roller 2 radius, r_{22} [mm]	1.0×10^9 (flat)
Normal contact force, F_{30} [N]	470.5
Longitudinal creepage, ξ_1 [-]	-8.0×10^{-3}

Table 4.1. Material and geometric contact data.

Rolling velocity, V [m/s]	25.0×10^{-3}
Time step, Δt [s]	0.01
Friction coefficient, μ	0.35
Number of elements in spatial discretisation, N_1	200

Table 4.2. Parameters of the model.

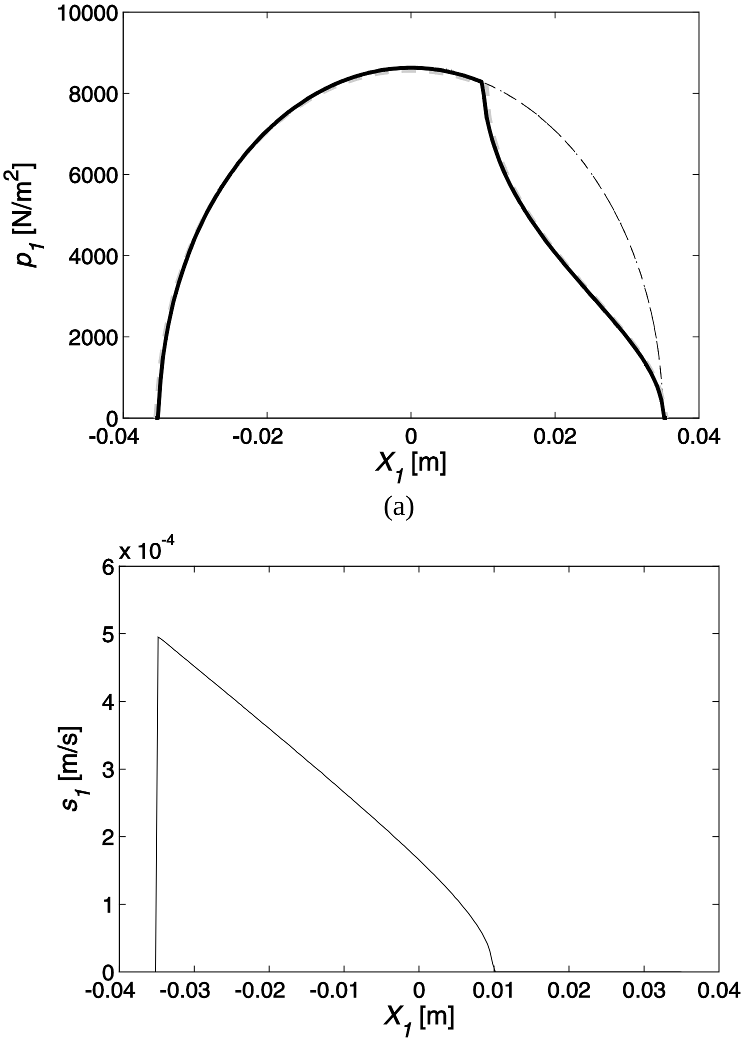

(a)

(b)

Fig. 4.5. (a) Tangential traction distribution. — — —: Carter analytic solution; ——: instationary contact model; ▪▪▪▪▪▪: steady-state numerical model; — · — · —: maximum tangential force that can be transmitted $\mu p_3(x_1)$. (b) Slip velocity distribution.

4.4 NUMERICAL ISSUES

Kalker’s tangential variational theory [81] is potentially a good approach since it is based on realistic assumptions of the rolling contact problem and does not introduce unrealistic hypotheses as *Simplified Theories* do. Nevertheless, the literature shows cases of numerical errors associated with continuity problems in the tangential traction distribution for high creepages when the entire contact patch slides (full-slip) [116,146–148]. These continuity problems become more important when adopting Kalker’s *Simplified Theory* [97] to solve the tangential problem. Vollebregt [118] presents traction distribution plots with peaks following a saw-teeth shape in the stick zone when using FASTSIM algorithm [95]. He points out that these instabilities appear in transient rolling scenarios using CONTACT and also in steady-state situations adopting FASTSIM. Despite getting a numerical strategy to avoid these peaks in a later work, he ignores the origin of these, even if they are physically possible or associated with FASTSIM algorithm itself.

This section pretends to investigate the numerical errors associated with the algorithm implemented so far. For this purpose, in Section 4.4.1 the instationary method is firstly evaluated for different spatial/temporal discretisations. The influence of a falling friction coefficient is studied in Section 4.4.2 for the instationary theory and the steady-state formulation derived from the first one.

4.4.1 Numerical errors due to spatial/time discretisations

A parameter investigation to study how the spatial/temporal discretisations influence the traction distribution in the instationary tangential contact model proposed is carried out. Again, the contact model has been simplified to a 2D case, considering a contact line instead of an area. The contact parameters imposed are the corresponding to the Table 4.2, with a longitudinal creepage $\xi_1 = $ -0.008. The curves shown in the figures below correspond to snapshots of the tangential traction distribution along the contact patch for an instant (around t=15 s) in which the solution is stabilised after the transient process. The solution for the steady-state formulation is also plotted and perfectly overlaps again the previous ones.

Eq. (4.36) related both spatial Δx_1 and temporal Δt steps through the rolling velocity V. The kinematic equation (4.37) for the instationary tangential contact is formulated in terms of Δx_1, which depends on the number of elements N_1 adopted in the mesh. Only a uniform discretisation is considered in this study.

In Figs. 4.5, $N_1 = 200$ elements were used to discretise the contact line. For both cases depicted in Figs. 4.6(a) and (b), two less refined meshes are implemented, with $N_1 = 30$ and $N_1 = 20$ elements, respectively. Fig. 4.6(a) shows that the grid resolution seems not to be critical for the continuity and stability of the solution since even for $N_1 = 30$ (85% less refined than Fig. 4.5) the traction solution follows adequately Carter analytic solution in the stick region (right side). Nonetheless, it affects the precision of the solution and the most noticeable deviation is produced around the stick/slip transition point.

For $N_1 = 20$ elements (90% less refined in Fig. 4.6(b)), an oscillating solution is developed with remarkable peaks, reproducing a saw-teeth shape in the stick region. Hence, for the 2D case studied, the problems in the continuity and precision of the solution arise when increasing the length of the line elements ten times, indicating that the spatial-dependent formulation of Eq. (4.37), in terms of Δx_1, presents a strong numerical robustness.

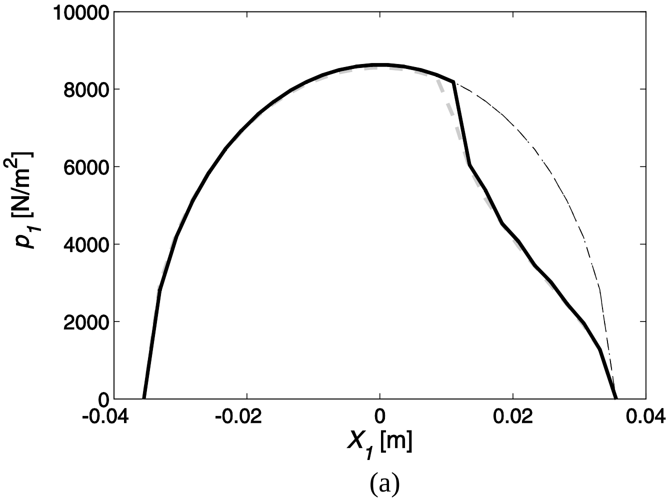

(a)

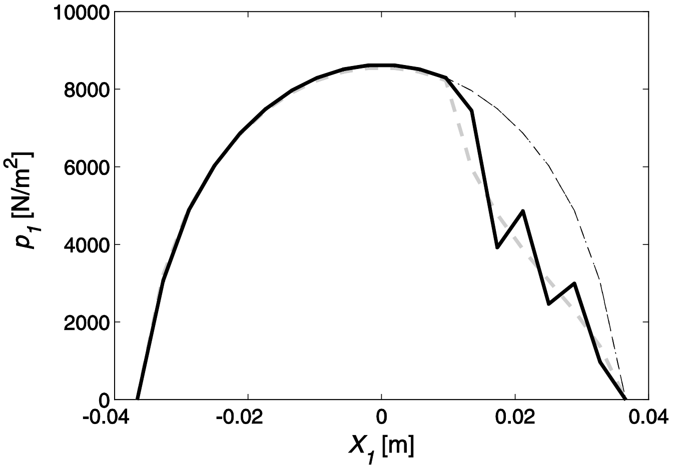

(b)

Fig. 4.6. Tangential traction distribution and slip velocity for $\xi_1 =$ -0.008: (a) $N_1 = 30$; (b) $N_1 = 20$ elements. – – – : Carter analytic solution; ―――: instationary contact model; ▪▪▪▪▪▪: steady-state numerical model; – · – · –: maximum tangential force that can be transmitted $\mu p_3(x_1)$.

If Eq. (4.37) was defined in terms of the temporal step Δt after the temporal discretisation proposed in Eq. (4.35), this had led to continuity problems in the numerical algorithm, as seen below. For this instationary formulation, three cases with different time steps have been evaluated and plotted in Figs. 4.7: (a) $\Delta t = 0.05\,\mathrm{s}$, (b) $\Delta t = 0.1\,\mathrm{s}$ and (c) $\Delta t = 0.2\,\mathrm{s}$. The three plots show snapshots of the instationary solution once stabilised.

Fig. 4.7(a) shows an identical solution than Fig. 4.5(a), which fits accurately Carter solution. After doubling the time step, Fig. 4.7(b) shows a saw-teeth shape for the tangential traction in the stick region (right side) instead of a smooth solution as a consequence of the poor resolution in time adopted. This traction distribution is similar than the results reported by Vollebregt [118] when using FASTSIM algorithm. When doubling again the time step Δt in Fig. 4.7(c), the number of peaks after the stick/slip transition point is reduced but the amplitude of the peaks is notably larger. Hence, it is deduced that the saw-teeth distribution mentioned in the literature can emerge, as one possible factor, from a poor time discretisation with a time-dependent formulation of the kinematic equation for the tangential contact problem.

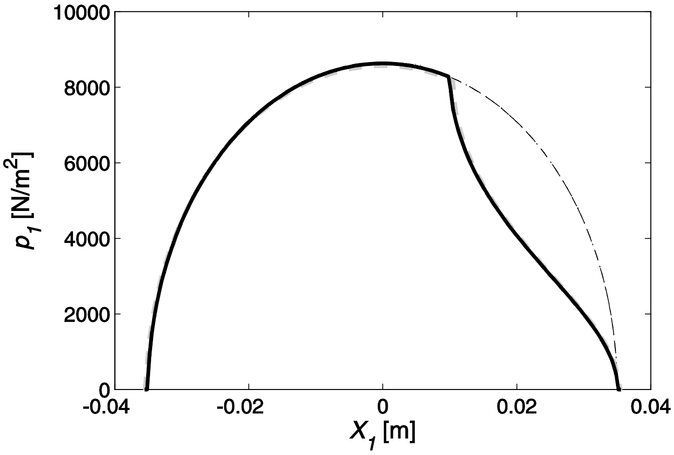
10000
8000
6000
4000
2000
0
p_1 [N/m^2]
-0.04
-0.02
0
0.02
0.04
X_1 [m]

(a)

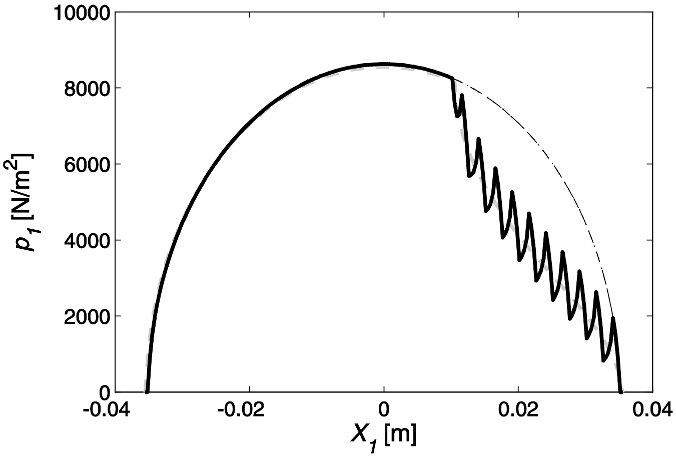
10000
8000
6000
4000
2000
0
p_1 [N/m^2]
-0.04
-0.02
0
0.02
0.04
X_1 [m]

(b)

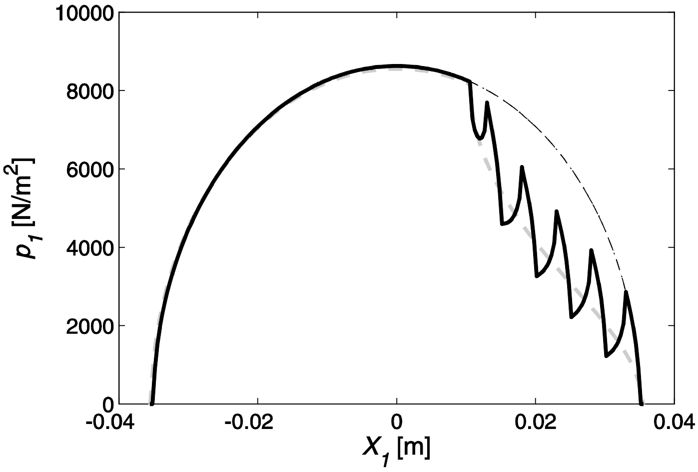

(c)

Fig. 4.7. Tangential traction distribution for $\xi_1 = \text{-}0.008$ and $N_1 = 200$: (a): $\Delta t = 0.05\,\text{s}$; (b) $\Delta t = 0.1\,\text{s}$; (c) $\Delta t = 0.2\,\text{s}$. – – – : Carter analytic solution; ——— : instationary contact model; –·–·– : maximum tangential force that can be transmitted $\mu p_3(x_1)$.

4.4.2 Numerical errors due to a falling friction coefficient

The effect of the implementation of a velocity-dependent friction coefficient on the robustness of the instationary tangential algorithm is investigated. The inclusion of a new non-linear term makes the physics strongly non-linear, and multiple solutions could satisfy the rolling contact problem equations.

An exponential falling model for the local slip velocity-dependent friction coefficient is chosen in the present work since it is widely used in the literature as a simplification of the Stribeck's friction law [22], without considering the hydrodynamic ascending regime for high slip velocities. Based on the experimental results from Ref. [149], in which the total tangential force is stabilised for high creepages, a constant kinematic friction coefficient was taken into account, giving the following formula

$$\mu(\mathbf{s}) = \mu_k + (\mu_s - \mu_k)\,\mathrm{e}^{-c_\mu |\mathbf{s}|}, \tag{4.46}$$

where μ_s and μ_k are the static and the kinematic friction coefficients, respectively. c_μ is an exponential parameter, which is defined from the local slip velocity for a value 1% above the kinematic friction coefficient, denoted as $\breve{s}$. From this definition:

$$\mu(\breve{\mathbf{s}}) = \mu_k + 0.01(\mu_s - \mu_k), \tag{4.47}$$

and c_μ can be written as

$$c_\mu = -\frac{\log(0.01)}{|\breve{\mathbf{s}}|}. \tag{4.48}$$

4.4.2.1 Falling friction on the instationary tangential contact model

A falling friction coefficient is included in the instationary contact model. For the case evaluated in Fig. 4.8, the local friction curve is characterised by a kinematic coefficient of $\mu_k = 0.35$, a static coefficient of $\mu_s = 0.40$ and a local slip saturation value $\breve{s} = 0.2$ m/s. The 2D case detailed in Tables 4.2 and 4.3 is studied.

This falling behaviour makes the algorithm unstable. Both coefficients force the solution to jump from the static bound to the kinematic one. Nevertheless, this new non-linearity, which should soften the falling transition, multiplies the number of possible solutions. So that the traction for the element that reaches the static bound seems to jump to different solutions until the algorithm stops computing even for small creepages, see zoomed view.

Multiple options to drive the solution to the expected one, as well as different definitions −linear, arctangential, etc.− for the falling behaviour apart from the exponential function used in Eq. (4.46), have been tested with unsatisfactory results.

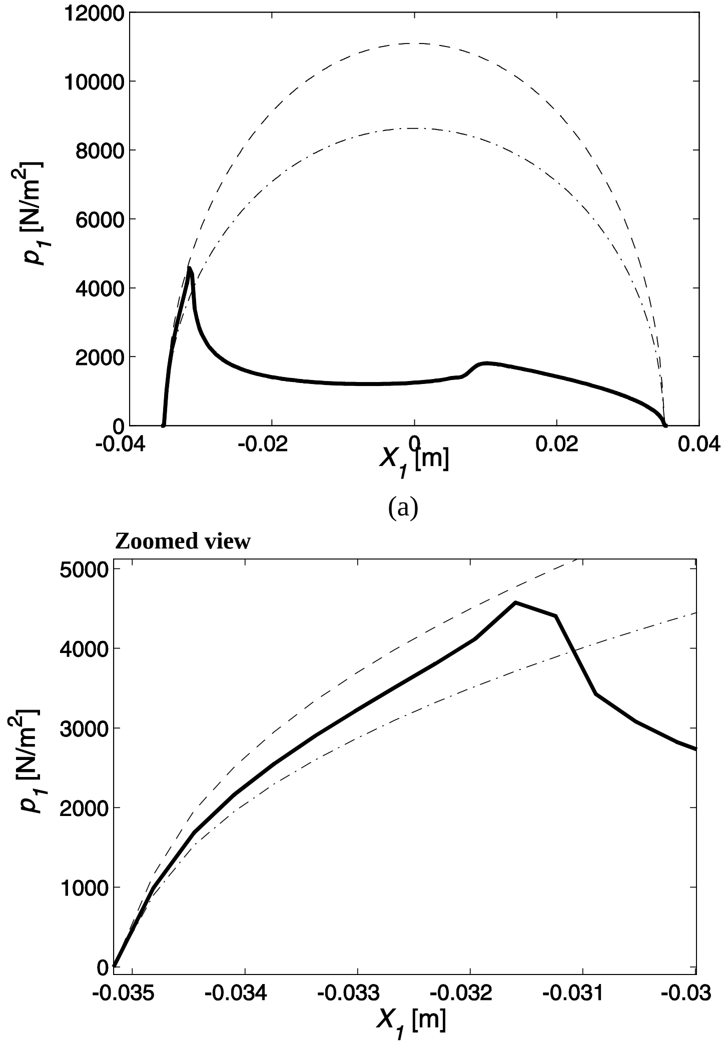

(a)

(b)

Fig. 4.8. Tangential traction distribution for $\xi_1 = -0.004$ and two friction coefficients: $\mu_k = 0.35$ and $\mu_s = 0.40$. (a) Full view; (b) zoomed view where the numerical solution jumps to different solutions until the algorithm stops. ——: instationary numerical model; —·—·—: $\mu_k p_3(x_1)$; – – – – –: $\mu_s p_3(x_1)$.

4.4.2.2 Falling friction on the steady-state tangential contact model

The main advantage of the steady-state tangential contact model derived above is that permits to estimate the steady-state solution of the tractions thorough the contact area [145]. The convergence problems of the temporal solution once included falling friction are hence avoided, finding a numerical solution. This has been the main reason for the development of the aforementioned formulation and a crucial step for a further study of the effect of this falling behaviour on the rolling parameters, carried out in Section 4.6.

Nevertheless, the current numerical algorithm results insufficient to find a suitable solution, as seen in Fig. 4.9. The figure plots the contact traction distribution for two different friction values: the kinematic coefficient, $\mu_k = 0.35$, and the static coefficient, $\mu_s = 0.45$, larger than the previous one. From both values, the friction coefficient is implemented through the model proposed in Eq. (4.46). Carter solution is also depicted, considering a single friction coefficient μ_k. Fig. 4.9 also shows the bound limits established by the kinematic and the static friction coefficients.

The steady-state numerical solution presents a peak and a subsequent dip around the stick/slip transition point as a discontinuity between both regions. This anomaly is not interpreted as physical, but a numerical error. This can be explained from the abrupt change of introducing a new variable (slip velocity) governing the friction coefficient in Eq. (4.47). The transition between the stick and the slip regions introduces two new equations in the system, Eqs. (4.37) and (4.39), when the transition element goes from adhesion H to slipping S. This leads to solving a different system in the slip region, doubling the unknowns and the number of equations respect to the stick zone. As a consequence, the numerical solution suffers a discontinuity between both regions.

The numerical disadvantages have been listed previously in Section 4.3.2, which compromise not only the continuity and physical reliability of the solution, but also the efficiency (time consumption) of the code. The regularisation of Coulomb's law, addressed in the next section, is proposed and implemented to overcome this problem associated with the numerical algorithm derived from Kalker's variational theory.

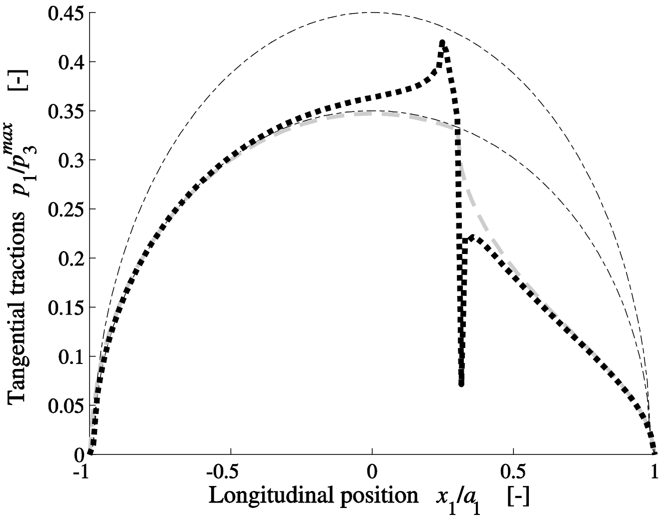

Fig. 4.9. Tangential traction distribution for falling exponential friction coefficient. — · — · —: static and kinematic bounds; — — —: Carter analytic solution; ▪▪▪▪▪▪: steady-state numerical solution.

4.5 REGULARISATION OF COULOMB’S LAW ON A STEADY-STATE TANGENTIAL CONTACT PROBLEM

4.5.1 Introduction of the regularisation of Coulomb’s law

The original Kalker’s method needs to establish in Eqs.(4.37)−(4.42) the elements of the mesh that are in adhesion and those that are slipping, making the algorithm less efficient and introducing certain problems of continuity between stick and slip regions in the contact area. In order to avoid the problems associated with the separation of the elements in two different sets, an alternative procedure is proposed, based on the regularisation of Coulomb’s law, where the local traction distribution is formulated from the local slip velocities through a smooth fitting function. This technique permits not to make distinction between both stick H and slip S sets of equations, while it relates the two unknown variables through a softer approach of Coulomb’s law, from which the distribution of tangential tractions vanishes as independent variables.

Figs. 4.10 show three models for the friction coefficient. The right plot is a zoomed view of the left one. The figure represents the p_1/p_3 ratio vs. the local slip velocity through different approaches. In continuous trace, the curve represents a typical falling friction coefficient following Eq. (4.46). The other curves adopt regularisation, and they present differentiable functions with a high gradient close to zero slip velocity. In dashed trace the regularisation adopts a constant friction coefficient; in dotted line it takes the former falling friction coefficient model.

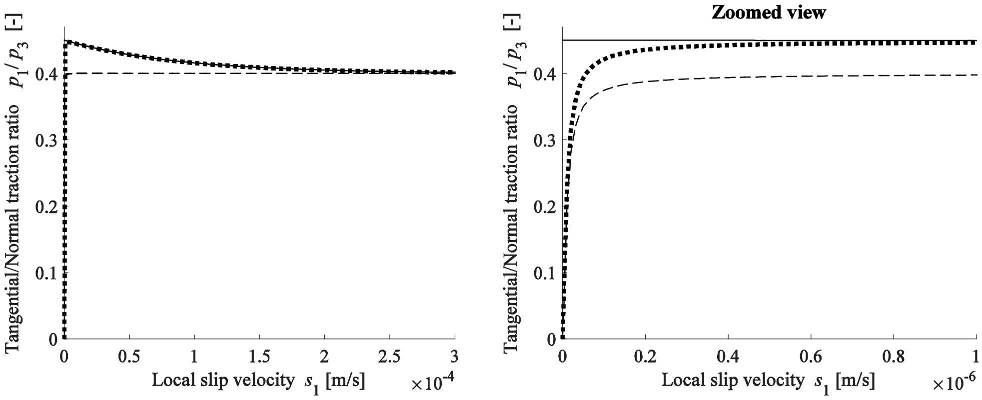

Fig. 4.10. Different friction coefficient models. ——: falling friction coefficient through Eq. (4.45), being $\mu_k = 0.45$, $\mu_k = 0.40$ and $c_\mu = 1.15 \times 10^4$ s/m. -------: regularisation of Coulomb’s law with constant friction coefficient $\mu = 0.40$. ▪▪▪▪▪▪: regularisation of Coulomb’s law.

Let assume now constant friction coefficient μ. The following approach applies such adjustment:

$$p_\tau^I \approx -\frac{2}{\pi} \arctan\left(\frac{\left|\mathbf{s}^I\right|}{\varepsilon}\right) \frac{\mu p_3^I s_\tau^I}{\left|\mathbf{s}^I\right|}. \tag{4.49}$$

This equation converges to the Coulomb’s law when ε approaches 0. The parameter ε must be chosen small enough such that the error of the regularisation is minimised, but the convergence to the solution is compromised if ε is too small. The present work adopts $\varepsilon = 10^{-8}$ m/s, which allows obtaining results in good agreement with the original Coulomb's law and avoids convergence problems.

Introducing Eq. (4.49) in (4.37), the solution of the contact problem is obtained through the system

$$
\begin{aligned}
s_\tau^I &= w_\tau^I - \frac{4\mu}{\pi}\sum_{\kappa=1}^{2}\sum_{J=1}^{N}\left(\arctan\left(\frac{\left|\mathbf{s}^J\right|}{\varepsilon}\right)\frac{p_3^J}{\left|\mathbf{s}^J\right|}D_{\tau\kappa}^{IJ}s_\kappa^J\right) \\
&\quad - 2V\left[\frac{2\mu}{\pi}\sum_{\kappa=1}^{2}\sum_{J=1}^{N}\left(\arctan\left(\frac{\left|\mathbf{s}^J\right|}{\varepsilon}\right)\frac{p_3^J}{\left|\mathbf{s}^J\right|}\frac{\partial D_{\tau\kappa}^{IJ}}{\partial x_1}s_\kappa^J\right) + \frac{u_{\tau 0}^I}{\Delta x_1}\right],
\end{aligned}
\tag{4.50}
$$

and operating to establish an error function compatible with the Newton-Raphson scheme:

$$
\begin{aligned}
0 = f_\tau^I &= w_\tau^I - \frac{4\mu}{\pi}\sum_{\kappa=1}^{2}\sum_{J=1}^{N}\left(\arctan\left(\frac{\left|\mathbf{s}^J\right|}{\varepsilon}\right)\frac{p_3^J}{\left|\mathbf{s}^J\right|}D_{\tau\kappa}^{IJ}s_\kappa^J\right) \\
&\quad - 2V\left[\frac{2\mu}{\pi}\sum_{\kappa=1}^{2}\sum_{J=1}^{N}\left(\arctan\left(\frac{\left|\mathbf{s}^J\right|}{\varepsilon}\right)\frac{p_3^J}{\left|\mathbf{s}^J\right|}\frac{\partial D_{\tau\kappa}^{IJ}}{\partial x_1}s_\kappa^J\right) + \frac{u_{\tau 0}^I}{\Delta x_1}\right] - s_\tau^I .
\end{aligned}
\tag{4.51}
$$

As can be seen, there are two equations for two unknowns, given the relationship $p_\kappa^J \equiv p_\kappa^J\left(s_1^J, s_2^J\right)$, $\kappa = 1,2$, established by Eq. (4.49). At the same time, this regularisation cannot distinguish between elements in the stick zone H and the slip zone S, without ceasing to be well established constraint associated with Coulomb's law. The regularisation introduces hence important computational advantages with respect to the previous algorithm based on Kalker's variational theory:

- There is no need to implement strategies to check if elements change their state (from H to S or vice versa).

- The number of unknowns is fixed: two per element of the contact patch.

- There is no need to implement strategies to check if elements change their state (from H to S or vice versa).

- The Jacobian is well conditioned due to it is calculated from only Eq. (4.51).

- The constraint introduced by Coulomb’s law is softened, preventing from numerical divergence. All the contact parameters are smooth distributions even in the border between the stick/slip areas.
- This regularisation also facilitates to implement a friction coefficient μ that depends on the local slip velocity.

Although the regularisation makes the stick/slip separation vanish and $\left|\mathbf{s}^J\right|$ of the *J*-th element is then always above zero, the text will continue to differentiate both zones if traction distribution is on the bound curve characterised by μp_3 (slip zone) or it is not (stick zone). This distinction pretends to facilitate the comprehension of the plot descriptions.

When replacing μ by $\mu(s)$ in Eqs. (4.46) to (4.48) to introduce the falling friction coefficient, the regularisation does not prevent from the non-convergent behaviour shown in the previous Section 4.4.2. The amount of non-linear terms that makes the traction distribution jump into multiple possible solutions around the stick/slip transition point during the simulation until the algorithm becomes totally uncontrolled and stops. Multiple techniques to drive the solution have been tested without success, being one topic for future research. This numerical problem leads to limit the simulations of the complete train/track system carried out in Chapter 6 to a constant friction coefficient.

Finally, the study has been restricted to the steady-state tangential problem in Section 4.5.2. The simplification allows avoiding the previous numerical instabilities and obtaining a reliable steady-state tangential traction distribution. This will allow the study of the influence of the falling friction on the rolling contact parameters in the creep curves (Section 4.6).

4.5.2 Regularisation on a steady-state tangential contact problem

Introducing the regularisation given by Eq. (4.49) in the kinematic equation (4.45) for steady-state conditions, and operating to establish an error function compatible with the Newton-Raphson scheme, it results:

$$f_\tau^I = w_\tau^I - \frac{4V\mu\left(\left|\mathbf{s}^I\right|\right)}{\pi}\sum_{J=1}^{N}\sum_{\kappa=1}^{2}\left(\arctan\left(\frac{\left|\mathbf{s}^J\right|}{\varepsilon}\right)\frac{p_3^J}{\left|\mathbf{s}^J\right|}C_{1\kappa}^{IJ}s_\kappa^J\right) - s_\tau^I . \qquad (4.52)$$

Results from calculations performed using the proposed model are presented. For the 2D case previously addressed (Tables 4.2 and 4.3), Fig. 4.11 shows the corresponding numerical solution for the tangential contact algorithm with regularisation. This model produces indistinguishable results compared with Carter solution, avoiding the discontinuity in the form of peak/dip in the transition element seen in Fig. 4.9. Additionally, the time consumption to get the solution is reduced a 45% respect to the simulation plotted in Fig. 4.9. Therefore, the regularisation reveals as an interesting mathematical tool to smooth the equations system behaviour and make the algorithm more robust, faster and efficient without loss of precision and reliability to the theoretical solution.

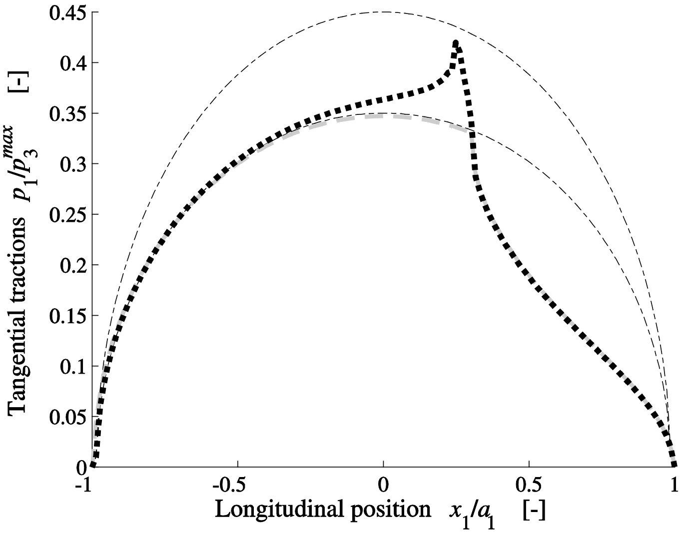

Fig. 4.11. Tangential traction distribution for falling exponential friction coefficient. — · — · —: static and kinematic bounds; ▬ ▬ ▬: Carter analytic solution; ▪▪▪▪▪▪: steady-state numerical solution with regularisation.

4.6 STUDY OF FALLING FRICTION EFFECT ON ROLLING CONTACT PARAMETERS

4.6.1 Introduction

The rolling contact model proposed in this chapter is used for a tribological study to evaluate how the falling friction effect affects the contact parameters that characterise the creep curves. For this purpose, the original instationary method has been modified in Section 4.3.2.1 in order to obtain the steady-state solution of the rolling contact problem, and the regularisation of Coulomb's law implemented in Section 4.5.2 allows introducing the falling friction behaviour on the steady-state formulation.

Fig. 4.12 shows the creep force vs. creepage when both a constant finite and an infinite friction coefficients are considered. The same plot presents the expected creep force when a falling friction coefficient is adopted, which is differentiated by a local minimum that would explain stick/slip phenomena.

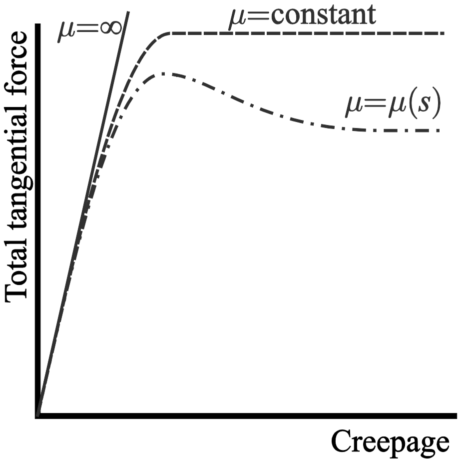

Fig. 4.12. Behaviour of the creep force on the friction coefficient: $\mu = \infty$ (adhesion model), $\mu =$ constant finite value, and $\mu = \mu(s)$ as a function of the slip velocity s.

Some researchers have developed rolling contact theories that represent the dependence of the friction coefficient on the slip velocity, generally by two coefficients of friction (static/kinematic). These models are either *Simplified Theories* [150,151] that somehow simplify the relationships between the contact traction distributions and the displacements in the contact patch, or they are based on the Kalker's tangential variational theory [81] (*Exact Theory*). These *Simplified Theories* are adjusted to converge to the results from the *Exact Theories*, giving a good agreement when comparing the velocity of the wheel/rail contact point (creepages) and forces [81]. However, this agreement does not occur for the local slip velocities [152] and consequently, high errors resulting in the slip velocities seem to make the *Simplified Theories* inadequate to model the contact process through a non-constant friction coefficient that depends on the slip velocity.

Kalker's variational theory adopted in this thesis is potentially a good approach since it is based on realistic assumptions of the rolling contact problem and does not introduce unrealistic hypotheses as *Simplified Theories* do. The implementation of the velocity dependent friction coefficient makes the physics strongly nonlinear, and multiple solutions could satisfy the rolling contact problem equations. The aforementioned regularisation implemented in the steady-state algorithm prevents the saw-teeth shape shown in the computed contact traction distribution when using FASTSIM algorithm [116], which is either considered as a reliable solution by some authors, or a numerical error. This implementation leads to a formulation that contains local parameters that define the friction coefficient as a function of the slip velocity (Eqs. (4.46) to (4.48)). These parameters are also related with the global parameters that characterise the creep curves.

The present approach adopts experimental results published in [149]. The literature shows creep curves measured in real field experiments (see examples provided in Refs. [118] and [153]) in order to study the locomotive traction capability. In such cases, the longitudinal creepage typically reaches values of 50% and higher whereas the creepage is lower than 3% in most of the railway dynamic problems within the scope of the present paper.

The *Linear Contact Theory* [97] neglects the local slip velocity (it is a so-called adhesion theory), and according with this theory the total force F_1 is $f_{11}\xi_1$, being f_{11} the creep (Kalker's) coefficient. The maximum longitudinal force per wheel in typical European networks rarely exceeds 50 kN and a typical creep coefficient f_{11} is around 1.5×10^7 N. If only the displacements associated with the elastic deformations would explain the creepage value, in this unfavourable scenario the creepage will be (through *Linear Theory* equation) only 0.3%. Consequently, creepages larger than 5% must be dominated by the slip velocity at the wheel/rail contact point, the full contact patch is slip area, and the role of the displacements associated with the elastic deformations is negligible.

Below creepages of 5%, the creep-force relationship presents a high gradient and the possible accuracy of the creepage measurement in a real railway vehicle cannot permit to obtain good precision if the creepage is low. The needed accuracy is reached in the laboratory bench of the Ref. [149] (with a 0.05% of error in creepage), for slightly larger creepages than the ones of the saturation conditions, which is the case of interest in the main problems in railway dynamics. The proposed approach tries to reproduce these experimental results where the displacements associated with the elastic deformations must be considered in the physical model.

4.6.2 First analysis through a 2D approach

The study is first focused on analysing the effect of adopting two different friction coefficients on the creep-force curves in a 2D contact approach from the steady-state formulation presented Section 4.5.2. Fig. 4.13 presents different creep curves for a fixed kinematic coefficient $\mu_k = 0.30$ and increasing values of the static coefficient. Tangential tractions are normalised by the normal load, thus the saturation value of all the curves matches μ_k. As shown in this figure, when both kinematic and static value are the same (constant friction coefficient), the creep curve reproduces the expected behaviour reported in the literature, which serves as a base for *Simplified Theories*. When increasing the static value, a maximum appears around the creepage value of 0.01.

Following with this parameter study, the static value is set now to 0.45 and the kinematic one increases from 0.30 to 0.45. As expected, Fig. 4.14 shows that the maximum is more pronounced for higher differences between static/kinematic coefficients. Two observations must be highlighted: firstly, higher values of μ_k displace the maximum to higher creepages; secondly, for a fixed μ_s, the higher the fall in the friction law is considered (lower μ_k), the sooner and more pronounced the reduction of the creep-curve initial slope will be.

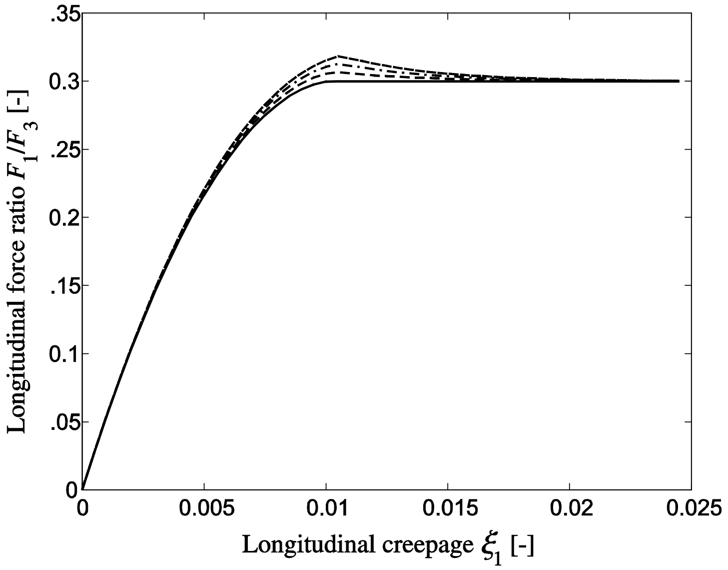

Fig. 4.13. Creep force curve setting the kinematic friction coefficient $\mu_k = 0.30$ and increasing the static one μ_s (———: $\mu_s = 0.30$; — —: $\mu_s = 0.35$; – · – · –: $\mu_s = 0.40$; – – – – –: $\mu_s = 0.45$).

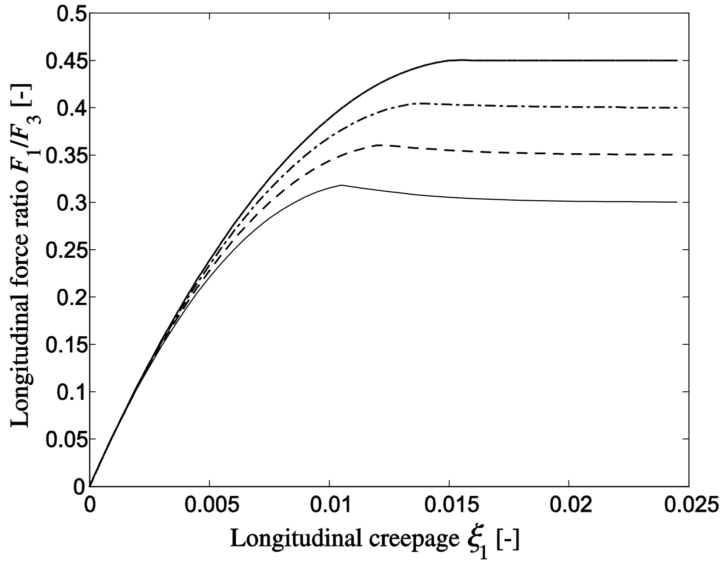

Fig. 4.14. Creep force curve setting the static friction coefficient $\mu_s = 0.45$ and increasing the kinematic one μ_k (———: $\mu_k = 0.30$; — —: $\mu_k = 0.35$; – · – · –: $\mu_k = 0.40$; – – – – –: $\mu_k = 0.45$).

The dependence of creep curves on vehicle velocity V is depicted in the Fig. 4.15, where the total force is lower for intermediate creepages when increasing velocity. Thus, the magnitude of the maximum decreases for higher velocities reaching earlier the saturation value.

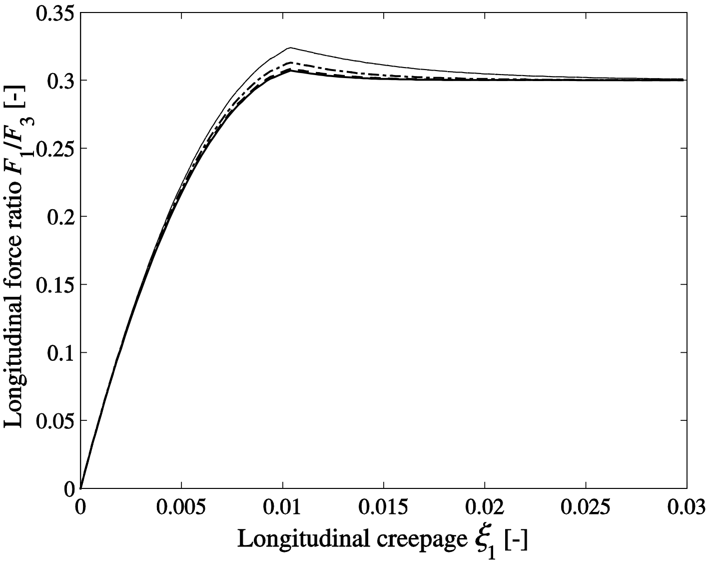

Fig. 4.15. Creep force curve setting the static friction coefficient $\mu_s = 0.40$ and the kinematic one $\mu_k = 0.30$ and increasing the vehicle velocity (———: $V = 15$ m/s; — —: $V = 25$ m/s; – · – · –: $V = 35$ m/s; - - - - -: $V = 40$ m/s).

Figs. 4.16 to 4.18 summarise the behaviour of previous curves depicting the normalised difference between the maximum longitudinal force $\widehat{F}$ with respect to the saturation point $\breve{F}$, defined as $\left(\widehat{F} - \breve{F}\right)/F_3$. Fig. 4.16 verifies that the creep-force maximum is more pronounced (close to a linear behaviour) compared to the saturation value when increasing μ_s. It is interesting to point out that, for a difference about 0.15 between both coefficients ($\mu_k = 0.35$ and $\mu_s = 0.50$), the normalised force difference is about 0.008 (or 6% for the relative percentage difference), while Ref. [154] showed estimations with higher differences, about 22% for similar velocity conditions. On the other hand, when μ_k increases, the force peak decreases while μ_k is approaching the fixed μ_s coefficient, as expected (see Fig. 4.17); its reduction seems to be close to an exponential behaviour. Finally, Fig. 4.18 shows that the magnitude of the maximum is reduced similarly to that of the previous figure while increasing the vehicle velocity V, without varying its creepage position.

It is also interesting to investigate how the initial slope of the normalised creep force vs. creepage is influenced by the previous three parameters analysed. In Fig. 4.19, the ordinate axis represents the increasing values of μ_s, μ_k (□ indicates that $\mu_k = \mu_s$) and $V\times10^{-2}$ for each corresponding curve. The abscissa axis shows the initial slope of the creep curve or the initial ratio between the normalised creep force and the creepage. Curve (a) and (b) indicate that this initial slope increases with both friction coefficients μ_s and μ_k, with a more remarked influence in the case of the static one. Conversely, when increasing the vehicle speed, the initial slope is reduced as seen in curve (c).

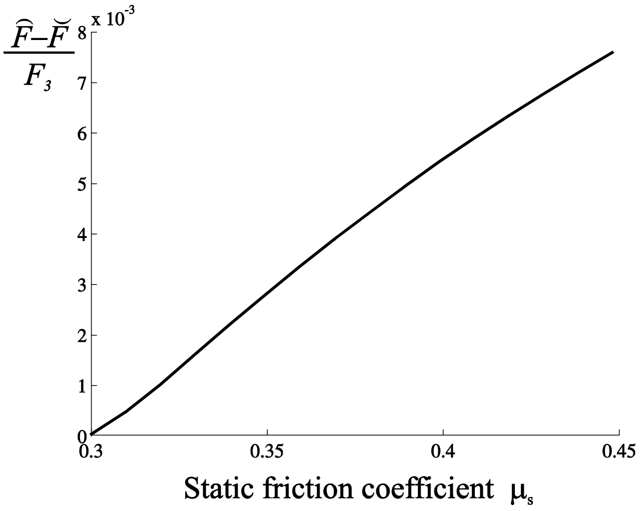

Fig. 4.16. Difference between the maximum and saturation values of the creep force setting the kinematic friction coefficient $\mu_k = 0.35$ and increasing the static one μ_s.

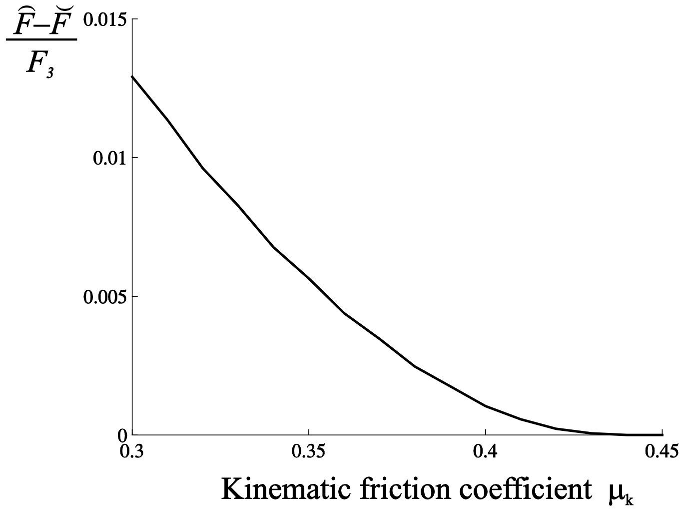

Fig. 4.17. Difference between the maximum and saturation values of the creep force setting the static friction coefficient $\mu_s = 0.45$ and increasing the kinematic one μ_k.

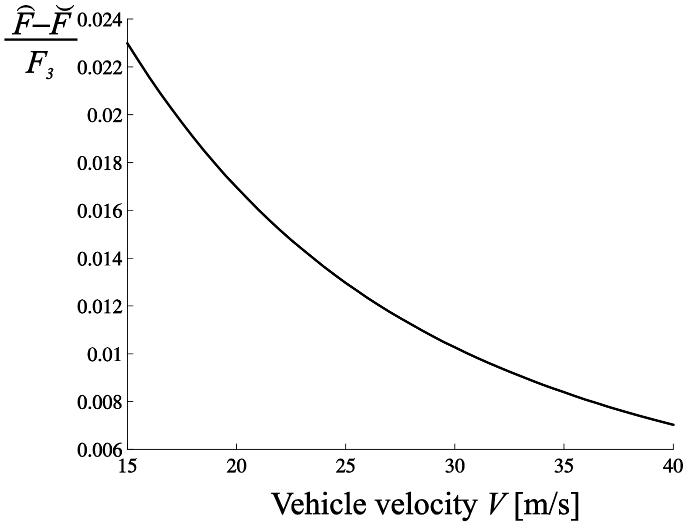

Fig. 4.18. Difference between the maximum and saturation values of the creep force setting the static friction coefficient $\mu_s = 0.40$ and the kinematic one $\mu_k = 0.30$ and increasing the vehicle velocity.

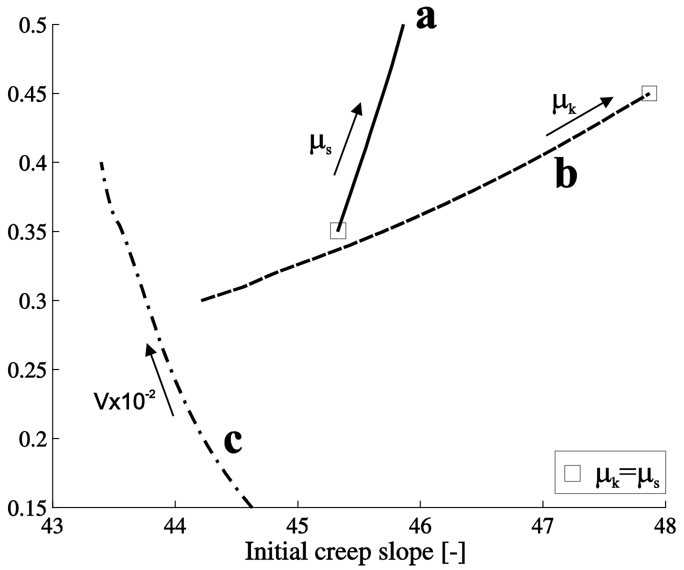

Fig. 4.19. Evolution of the initial slope of the creep force curve when increasing independently three parameters. ———: μ_s (a); –––––: μ_k (b); –·–·–: V (c).

4.6.3 Parameters of the rolling contact model

A methodology is proposed for relating the contact global properties associated with creepage velocities and total longitudinal forces, with local properties such as local slip velocity and dependent friction characteristics. These relationships avoid adopting incompatible contact parameter sets and allow estimating the local parameters that characterise the friction coefficient from the global parameters that describe the creep curve.

Fig. 4.20 schematises the main relationships that involve the tangential rolling contact problem. On the left, Fig. 4.20(a) shows a model of the local slip-velocity dependence of the friction coefficient. This model is associated with the local parameters of the wheel/rail contact corresponding to Eq. (4.46); the static, μ_s, and the kinematic, μ_k, friction coefficients and the critical local slip velocity, $\breve{s}$. Fig. 4.20(b) sketches the tangential contact relationship of the global parameters, following the results proposed in Ref. [154] for the rolling contact in the presence of a falling friction coefficient. The creep-total force curve presents a maximum of the contact force at the force-creepage pair $(\hat{F},\hat{\xi})$. The total tangential force saturates at $\breve{F}$ for large creepage values, and the creepage from which this happens is $\breve{\xi}$.

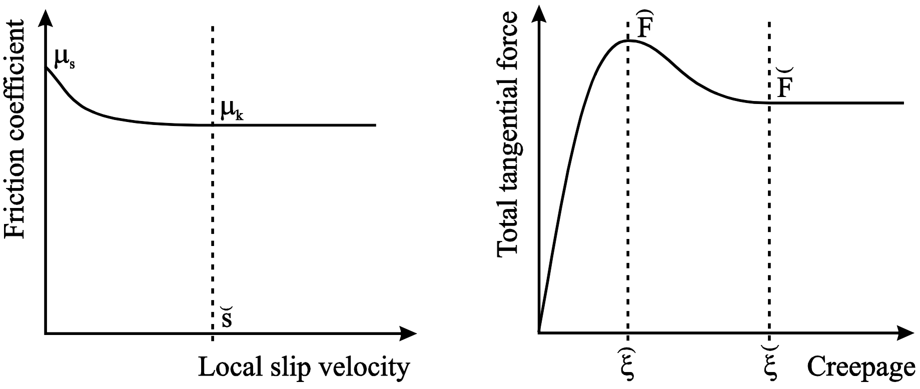

(a) (b)

Fig. 4.20. Sketch of global and local parameters of the wheel/rail contact.

A mathematical relationship between the local parameters $(\mu_s,\mu_k,\breve{s})$ and creep parameters $(\hat{F},\breve{F},\hat{\xi},\breve{\xi})$ can be revealed from the relationship between local slip velocity and contact tractions in Eq. (4.49) for steady-state condition. This would permit to set the local parameters of the present tangential contact model from any experimental creep-total force curve in order to reproduce the behaviour of the contact forces in global terms from a physical model evaluated locally in every contour element of the mesh covering the contact patch.

The saturation force $\breve{F}$ is obtained when the actual friction coefficient is μ_k for all the elements of the mesh, that is

$$\breve{F} = \mu_k \sum_{J=1}^{N} b_1^J b_2^J p_3^J . \tag{4.53}$$

Let consider the case where the total force is $\breve{F}$ and the creepage is $\breve{\xi}$. This case is reached when there is just one element where the local slip velocity is $\breve{s}$ (the other elements have $\left\|\mathbf{s}^I\right\| \geq \breve{s}$). This element must be at the leading edge of the contact patch. Without loss of generality, let consider now a 2D contact case, where the element at the leading position is numbered as L. Eq. (4.49) can be written for the present case as follows:

$$s_1^L = \breve{s} = V\breve{\xi} + 2V\sum_{J=1}^{N}\frac{\partial D_{11}^{LJ}}{\partial x_1}\mu_k\, p_3^J. \tag{4.54}$$

It must be pointed out that the friction coefficient model associated with Eq. (4.46) does not attain the precise kinematic value μ_k. The kinematic friction coefficient μ_k is assumed to be $\mu(\breve{s})$, obtaining the following constrain equation

$$s_1^L = \breve{s} = V\breve{\xi} + 2V\sum_{J=1}^{N}\frac{\partial D_{11}^{LJ}}{\partial x_1}\mu(\breve{s})p_3^J. \tag{4.55}$$

The peak force $\breve{F}$ and the creepage $\overset{\frown}{\xi}$ are related through the following equation

$$\left.\frac{\partial F}{\partial \xi}\right|_{\overset{\frown}{F},\overset{\frown}{\xi}} = 0. \tag{4.56}$$

The derivative of Eq. (4.56) can be obtained by means of finite differences. Eqs. (4.46), (4.55) and (4.56) constrain the values of the local parameters and the global parameters $\left(\overset{\frown}{F},\breve{F},\overset{\frown}{\xi},\breve{\xi}\right)$. Consequently, no more than four parameters can be set. Hence these equations permit to make a reliable approach for the local parameters that characterise the tangential contact model from the global parameters extracted from any experimental creep curve. μ_s, μ_k are needed for the definition the falling friction coefficient in Eq. (4.46), and $\breve{s}$ permits to evaluate the exponential c_μ from Eq. (4.48).

4.6.4 Comparison to experimental data

The present approach adopts experimental results published in Ref. [149] (see the test-bench picture in Fig. 4.21). The literature shows creep curves measured in real field experiments (see examples provided in Refs. [118] and [153]) in order to study the locomotive traction capability. In such cases, the longitudinal creepage typically reaches values of 50% and higher whereas the creepage is lower than 3% in most of the railway dynamic problems within the scope of the present thesis.

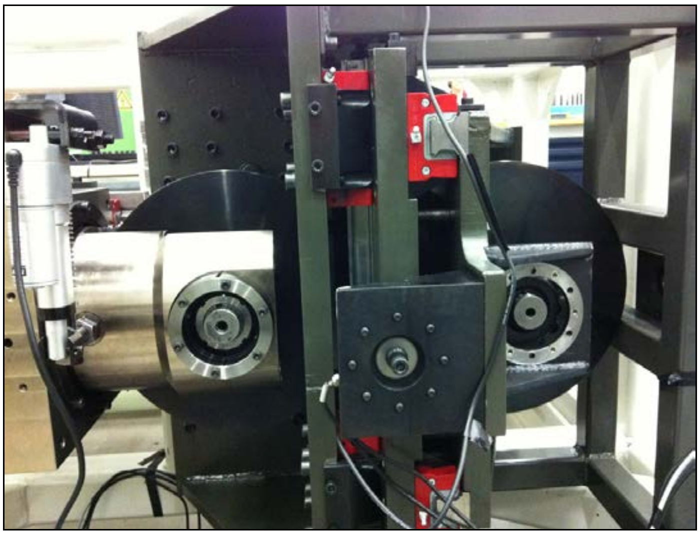

Fig. 4.21. Rolling contact test-bench in CEIT.

The tangential contact model is now extended to the 3D formulation presented in Section 4.3 and compared to the measurements made in CEIT (Centre for Technical Research and Studies –in English– in San Sebastian, Spain) by using its rolling contact scaled test-bench developed in Ref. [149]. Both wheel and rail are substituted by two steel rollers. The rotational velocity of one of the rollers is 500 rpm and the brake torque of the other is incremented with intervals of 20 Nm. This permits to increase the longitudinal creepage while the lateral one is set for each experiment. The material and the geometrical properties for this case are detailed in Table 4.3.

Shear modulus, G [N/m^2]	8.0×10^8
Poisson's ratio, ν [-]	0.28
Roller 1 (wheel) radius, r_{11} [mm]	170
Roller 1 (wheel) radius, r_{12} [mm]	300
Roller 2 (rail) radius, r_{22} [mm]	1.0×10^6 (flat)
Equivalent vehicle speed, V [km/h]	125
Spin creepage, ξ_{sp} [-]	0

Table 4.3. Scaled magnitudes values of the test-bench for each case.

Four different measured creep curves are presented for creepages up to 2.5%, varying the normal load (compressing both rollers) and the lateral creepage for each case. Table 4.4 compiles the corresponding values for each case. Results from FASTSIM and the proposed model have been plotted in Figs. 4.22(a) to (d) (corresponding to the cases from a to d) together with the experimental measurements.

	Case a	**Case b**	**Case c**	**Case d**
Normal contact force, F_3 [kN]	2.0	2.1	2.3	2.3
Lateral creepage, ξ_2 [º]	0	0	0.025	0.120
Friction coefficient, μ [-]	0.60	0.48	0.60	0.60

Table 4.4. Test-bench set values for each case.

FASTSIM solution is found from the friction coefficient μ set in the test-bench for each case. In order to evaluate the present tangential contact model, the local parameters $\left(\mu_s, \mu_k, \breve{s}\right)$ are needed to define the local falling friction curve $\mu(\mathbf{s})$ and hence run the tangential set of equations (4.53)–(4.56). The procedure detailed in the previous Section 4.6.3 is followed by detecting the characteristic points $\left(\hat{F}, \hat{\xi}\right)$ and $\left(\breve{F}, \breve{\xi}\right)$ of each experimental creep-force curve. Table 4.5 gathers the results obtained, which fit the measurements presented in Ref. [149].

	Case a	**Case b**	**Case c**	**Case d**
Static friction coefficient, μ_s [-]	0.61	0.49	0.61	0.60
Kinematic friction coefficient, μ_k [-]	0.59	0.45	0.58	0.57
Local slip saturation value, $\breve{s}$ [m/s]	0.51	0.41	0.46	0.47

Table 4.5. Parameters of the falling friction coefficient curve.

Experimental sets in Figs. 4.22(a) and (b) seem to certify the non-negligible effect of the slip-dependent friction coefficient as indicated by the falling behaviour of the total tangential force after the maximal transmitted force. Hence, it suggests that the rolling contact problem cannot be modelled in a realistic way through *Simplified Theories*, but it requires physical and exact theory that permits to include a variable friction coefficient. Furthermore, as mentioned previously, Fig. 4.22(a) and (b) show that experimental curves from CEIT present a less pronounced falling behaviour than creep curves for real locomotives. Together with the previous cases, in Figs. 4.22(c) and (d) it can be perceived how the total force measured for low creepages tends to be below the theoretical initial slope (defined by the Young's modulus) that FASTSIM fits. It seems to indicate that falling friction reduces the effect of the static coefficient even for low creepages (when it is assumed that no percentage of the area of contact is slipping). The numerical creep curve obtained evaluating the proposed steady-state model reproduces rather well this behaviour. As seen in Figs. 4.22(a) to (d), the creep curve matches the initial slope of the FASTSIM solution for low creepages, but decreases gradually adapting to the behaviour of the experimental data, even for negative creepages. The falling friction law by adopting a second coefficient μ_k lower than μ_s seems to reduce the initial slope of the curve compared to a single μ curve.

Without coinciding perfectly to the experimental set, the location and magnitude of the maximum matches notably well for Figs. 4.22(a) and (b), indicating that the previous procedure seems to be valid for relating both global and local curves. Finally, the curve is forced to match the saturation value for higher creepages through the kinematic coefficient estimated, showing hence that the difference between both maximum and saturation value is not strongly pronounced.

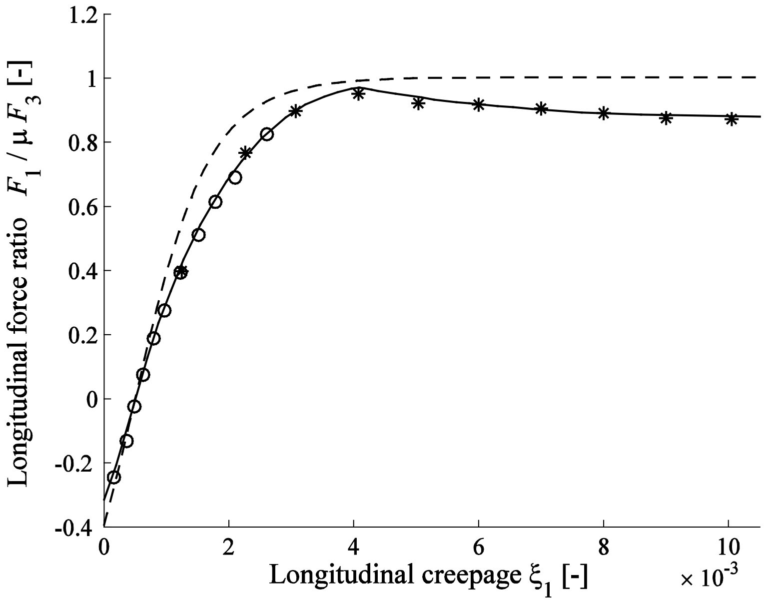

(a)

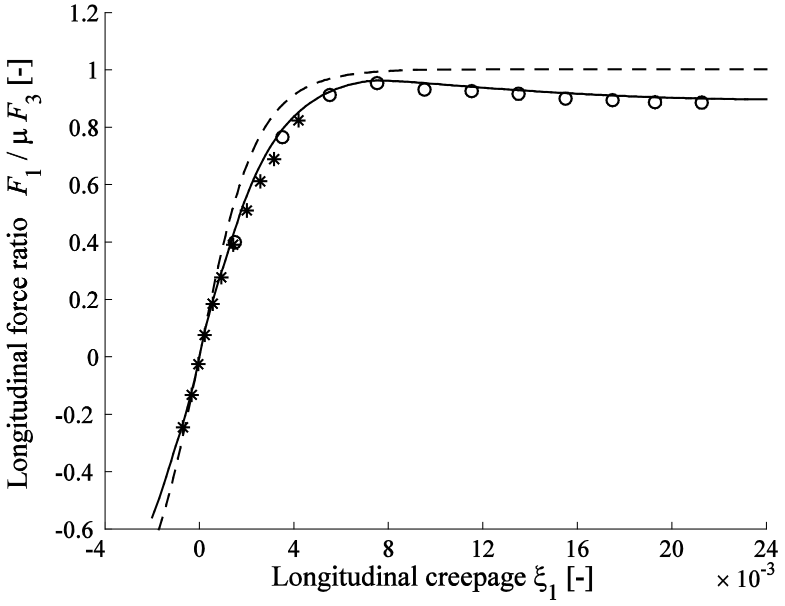
Longitudinal force ratio $F_1 / \mu F_3$ [-]
1.2
1
0.8
0.6
0.4
0.2
0
-0.2
-0.4
-0.6
-4
0
4
8
12
16
20
24
Longitudinal creepage ξ_1 [-]
$\times 10^{-3}$

(b)

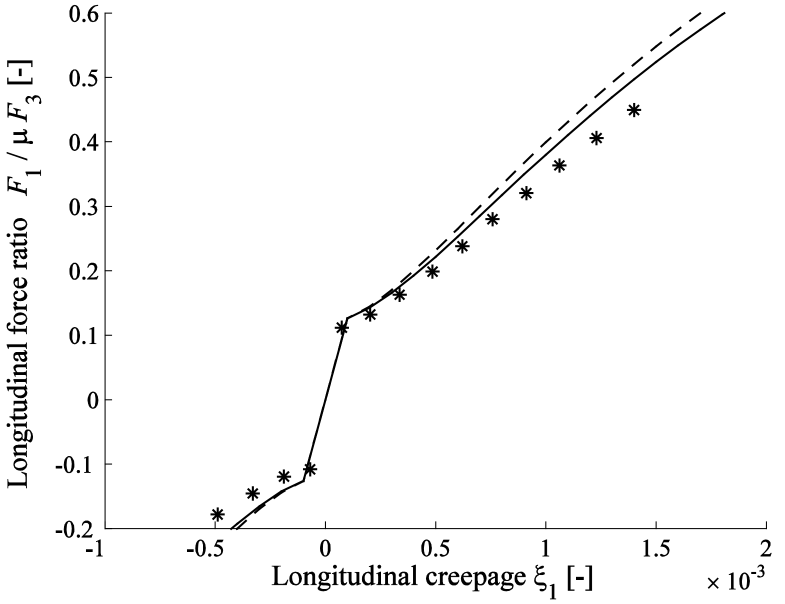
Longitudinal force ratio $F_1 / \mu F_3$ [-]
0.6
0.5
0.4
0.3
0.2
0.1
0
-0.1
-0.2
-1
-0.5
0
0.5
1
1.5
2
Longitudinal creepage ξ_1 [-]
$\times 10^{-3}$

(c)

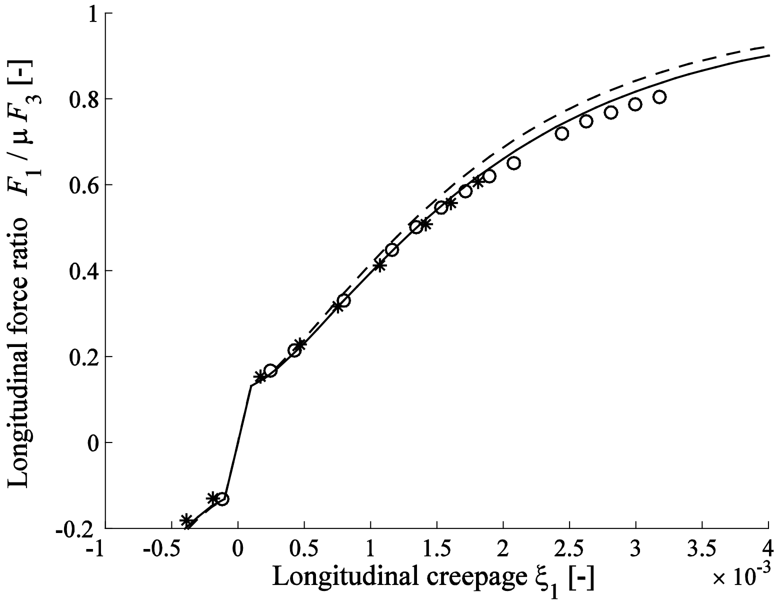

(d)

Fig. 4.22. Theoretical-experimental comparison of creep force curve (——: numerical solution from the proposed model; – – – – –: FASTSIM solution; ✱: experimental set 1 from CEIT ; ○: experimental set 2 from CEIT).

4.7 CONCLUSIONS

As regards to the development of an instationary 3D contact model, which is one of the central cores of the thesis, the following conclusions are derived:

- The theoretical fundamentals of the wheel/rail contact problem and the corresponding formulation have been presented.

- For the normal contact problem, Kalker's NORM algorithm has been presented as a non-Hertzian model. In this method, the contact patch is discretised in rectangular elements in which the contact magnitudes are constant. The formulation of the tangential contact problem is based on Kalker's TANG algorithm. The normal problem is independent of the tangential one since quasi-identity conditions are assumed.

- TANG algorithm shows numerical problems associated with the distinction between the stick and the slip regions inside the contact area, represented by two different sets of equations.

- In order to avoid the previous discontinuity, a new approach has been adopted modifying the original method by means of the regularisation of Coulomb's law, which eliminates the presence of such peaks. An additional advantage of the implementation of the regularisation is a significant reduction of the computational costs when compared to the original method thanks to the saving in the number of equation unknowns.

- Another contribution of this chapter is the implementation of a method for introducing a falling friction coefficient in rolling contact mechanics. This method is suitable for creepages that slightly exceed the saturation conditions (lower than 3% if the solids in contact are made of steel), which correspond to the creepage range in most of the railway dynamic studies. The technique adopts steady-state conditions and the friction coefficient is a function of the local slip velocity through a simplified Stribeck curve (an exponential function characterised by the static and kinematic coefficients).

- The implementation of the velocity-dependent friction coefficient adds new variables that frequently have been chosen *ad hoc* in the literature. The present work develops the constrain equations that establish mathematical relationships between the different parameters associated with the falling friction rolling contact problem. These constrain equations facilitates to build models that produce realistic results from experimental data. This respect, the proposed model reasonably fits the experimental creepage vs. creep-force curves obtained from high-precision test-bench measurements.

- The appearance of the creepage vs. creep-force curves obtained from the proposed methodology does not differ markedly from the one of a single friction coefficient. This conclusion is in accordance with previous test-bench measurements that present a slight decrease of the tangential force once the maximum is reached.

- A global model that fits all the creepage range level is to the authors' best knowledge, undone. By considering the negligible role of the displacements due to the elastic deformation in high creepage conditions, the present model can be adequate in traction locomotive problems if a suitable Stribeck curve is adopted. In such case, the above presented constrain equations associated with the parameter set have to be reconsidered.

5 VEHICLE/TRACK DYNAMIC INTERACTION MODEL IN THE TIME DOMAIN

5.1 INTRODUCTION

The complexity of the train/track interaction comes from the vibration coupling between the railway vehicle and the track, in which wheel/rail contact forces couple both sub-systems and their surface imperfections, such as rail roughness and wheel out-of-roundness, excite the global system. Unwanted phenomena such as damage of the rolling surfaces in the form of high levels of noise and vibration [7], wheelset axle fatigue [155], corrugation [156] and stress damage may appear in some cases due to large levels of vibration and dynamic fluctuations of the contact forces.

Vehicle models in high-frequency wheel/rail interaction models are generally simple. As the primary and secondary suspensions of the vehicle isolate the bogie and car body from the wheelset at frequencies of more than a few hertzs, the vehicle dynamic behaviour in the interaction model is sufficiently described by the dynamics of the wheelset. Knothe and Grassie [39] state that the vehicle's unsprung mass (including wheelset, bearings and axle-mounted components) is even satisfactorily represented as a rigid body for vertical interaction. If, however, lateral wheel/rail interaction is to be considered, more advanced wheel models are required, which include the wheel's flexibility [39]. FE models have strongly entered in railway research incorporating recently flexibility in the wheelset in order to widen the frequency range of analysis [7,157]. The main objective has been to extend the frequency range above 1 kHz to address rolling noise [3,158] and, only very recently, further works have considered the inertial effects due to wheelset rotation running on a tangent [159] and curved track [160].

This chapter is organised as follows. Section 5.2 describes the substructuring technique adopted for the train/track interaction model. A flexible and rotatory wheelset model in a generic track developed in this research group is detailed in Section 5.3; this model adopts Eulerian and modal approaches. Section 5.4 itemises the Moving Element

Method (MEM) used for the modelling of a 3D flexible finite rail; this method is based on a moving reference system associated with the vehicle. Section 5.5 formulates advanced techniques for the temporal solving of the train/track interaction. Section 5.6 introduces the wheel/rail contact forces into the railway system. This chapter closes with the conclusive remarks in Section 5.7.

5.2 GENERATION OF THE TRAIN/TRACK INTERACTION MODEL THROUGH SUBSTRUCTURING TECHNIQUES

The implementation of a realistic train/track interaction model has an important repercussion in the computational cost of the simulation. Therefore, this thesis combines a cyclic track model with a substructuring technique [161,162] in order to simulate the dynamic interaction between the vehicle and the track in the time domain.

The global system is divided in substructures of less complexity of analysis and the connection coordinates between the substructures are chosen, as well as the interior ones. Once defined the reduced equations of motion of each substructure, these are assembled through constraint equations to describe the compatibility of forces and displacements between the substructures. Impedance binding or modal union techniques can be adopted whether the reduction has carried out in physical or modal coordinates, respectively. In the impedance binding techniques mass, damping and stiffness matrices are assembled; while in the union modal techniques vibration modes, related to uncoupled differential equations systems, are assembled.

The substructuring method adopted in the present thesis considers three types of substructures (see Fig. 5.1): vehicle, rails and rail supports. Each substructure is described independently of the others by means of a set of ordinary differential equations. The different substructures are related to each other through external forces: the vehicle and the rails are connected through the contact forces, and the rails and the rail supports through the forces transmitted to the bedplate [162]. These forces are calculated from the displacements and velocities of the vehicle/track system. The numerical solving of the vehicle/track interaction in the time domain permits to consider the presence of non-linearities in the system, such as the unsteady contact process.

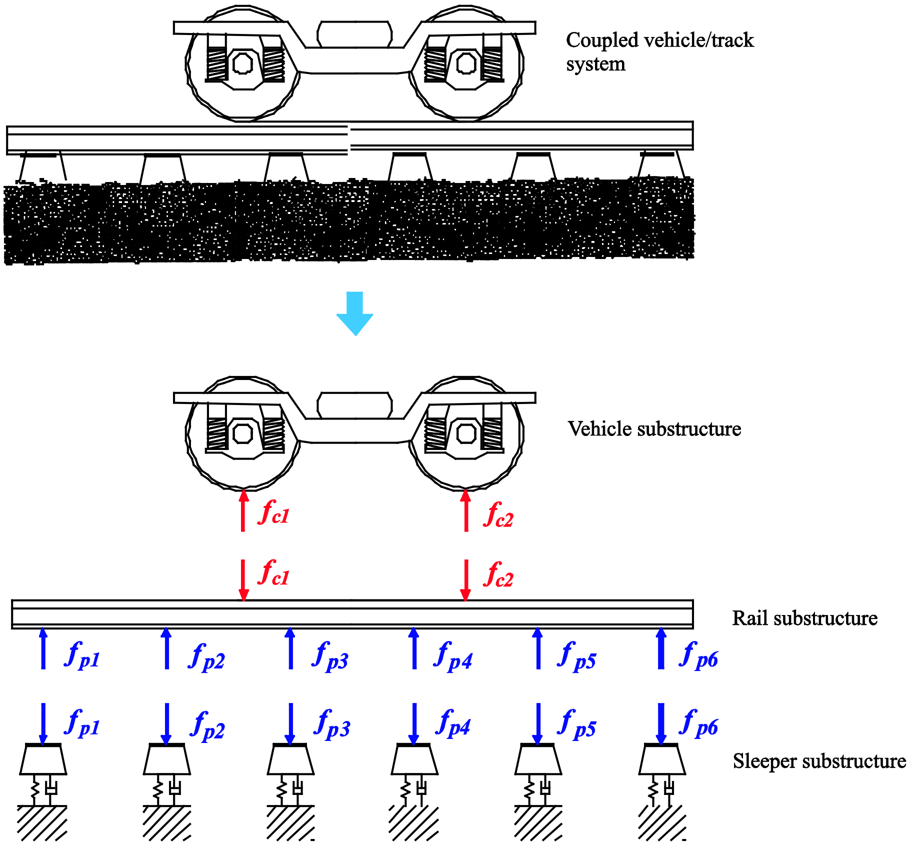

Fig. 5.1. Substructures of the train/track system and connection forces between substructures.

5.3 FLEXIBLE AND ROTATING WHEELSET MODEL

The present thesis adopts a model developed by Martínez-Casas *et al.* [160] for a flexible wheelset negotiating a curved track, based on a previous work for a tangent track [159]. This section details the equation of motion that takes into account the gyroscopic and inertial effects associated with the rotation of the wheelset and derived through an Eulerian-modal approach introduced by Fayos *et al.* [55]. This approach also reduces the dimension of the dynamic system and thus the computational cost.

Fig. 5.2 shows the reference frames and position vectors used to describe the motion of the wheelset in a curve. In order to model the flexible wheelset travelling on curved track, two reference frames are considered. The first one is an inertial frame $\mathbf{X}_0\mathbf{Y}_0\mathbf{Z}_0$ which is fixed at an arbitrary point. The second is a trajectory coordinate frame $\mathbf{X}_T\mathbf{Y}_T\mathbf{Z}_T$ that follows the theoretical motion of the wheelset centred on the track. The system $\mathbf{X}_T\mathbf{Y}_T\mathbf{Z}_T$ is centred in the undeformed configuration of the wheelset, with the $\mathbf{X}_T$-axis parallel to the forward speed, the $\mathbf{Y}_T$-axis parallel to wheelset axis and the $\mathbf{Z}_T$-axis pointing upwards. A vector referred to the fixed and trajectory frame is denoted by $\mathbf{a}_0$ and $\mathbf{a}$, respectively.

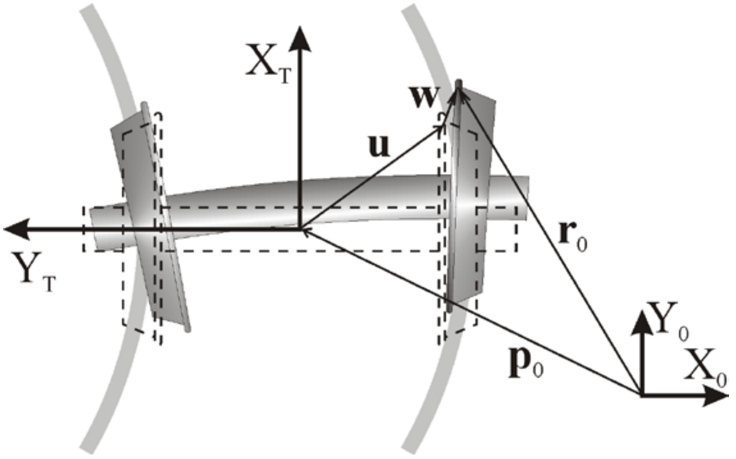

Fig. 5.2. Reference frames and position vectors. The undeformed configuration of the wheelset is shown in dashed trace; a generic position of the flexible wheelset is sketched in solid contours.

The coordinates that are implemented in the wheelset model do not follow the material points of the solid, which is the most common procedure in Mechanics, nonetheless they are associated with spatial points (Eulerian approach). The position vector $\mathbf{r}_0$ of a material particle, which is in the spatial position $\mathbf{u}$ at instant t for the undeformed configuration, can be defined by means of the following formula:

$$\mathbf{r}_0 = \mathbf{p}_0 + \mathbf{T}\left(\mathbf{u} + \mathbf{w}\left(\mathbf{u}, t\right)\right), \tag{5.1}$$

where $\mathbf{p}_0$ is the position vector of the track frame; $\mathbf{w}$ corresponds to the displacement vector due to the elastic deformation and small rigid body displacement of the solid; $\mathbf{T}$ is the rotation matrix that relates the trajectory frame of the track to the fixed frame.

Considering that the coordinate frame is chosen so that the wheelset rotation velocity Ω is in the second axis $\mathbf{Y}_{\mathrm{T}}$, the angular velocity tensor $\tilde{\mathbf{\Omega}}$ is defined as follows:

$$\tilde{\mathbf{\Omega}} = \begin{bmatrix} 0 & 0 & \Omega \\ 0 & 0 & 0 \\ -\Omega & 0 & 0 \end{bmatrix} = \Omega\,\mathbf{J}; \quad \mathbf{J} = \begin{bmatrix} 0 & 0 & 1 \\ 0 & 0 & 0 \\ -1 & 0 & 0 \end{bmatrix}. \tag{5.2}$$

The velocity due to the rigid body spinning is:

$$\mathbf{v} = \begin{pmatrix} v_1 & v_2 & v_3 \end{pmatrix}^{\mathrm{T}} = \tilde{\mathbf{\Omega}}\mathbf{u} = \Omega\,\mathbf{J}\,\mathbf{u} = \Omega\tilde{\mathbf{u}}, \tag{5.3}$$

where $\tilde{\mathbf{u}} = (u_3, 0, -u_1)^{\mathrm{T}}$. The velocity of the particle is computed through the material derivative of $\mathbf{r}_0$, and in the trajectory frame that is

$$\begin{aligned} \frac{\mathrm{D}\mathbf{r}}{\mathrm{D}t} &= \mathbf{T}^{\mathrm{T}}\,\dot{\mathbf{p}}_0 + \mathbf{T}^{\mathrm{T}}\,\dot{\mathbf{T}}\,(\mathbf{u}+\mathbf{w}) + \dot{\mathbf{w}} + \sum_i v_i \frac{\partial \mathbf{u}}{\partial u_i} + \sum_i v_i \frac{\partial \mathbf{w}}{\partial u_i} \\ &= \dot{\mathbf{p}} + \tilde{\boldsymbol{\omega}}\,(\mathbf{u}+\mathbf{w}) + \dot{\mathbf{w}} + \Omega\,\mathbf{J}\,\mathbf{u} + \Omega \sum_i \tilde{u}_i \frac{\partial \mathbf{w}}{\partial u_i}, \end{aligned} \tag{5.4}$$

where $\dot{\mathbf{p}}$ is the speed of centre of the track frame (expressed in the trajectory frame) and $\tilde{\boldsymbol{\omega}} = \mathbf{T}^{\mathrm{T}}\dot{\mathbf{T}}$ the angular velocity matrix of the track frame. The two first velocity terms are associated with translational and rotational movement of the track frame, respectively; $\dot{\mathbf{w}}$ represents the velocity of the spatial point due to the flexibility; the term $\Omega\mathbf{J}\mathbf{u}$ is the velocity due to the rigid body spinning; and the last term is the convective velocity associated with the Eulerian coordinate system.

In order to obtain the expression of the kinematic energy for the wheelset, the square of the particle velocity is obtained, which reads:

$$\begin{aligned}\frac{\mathrm{D}\mathbf{r}^{\mathrm{T}}}{\mathrm{D}t}\frac{\mathrm{D}\mathbf{r}}{\mathrm{D}t} &= \dot{\mathbf{p}}^{\mathrm{T}}\,\dot{\mathbf{p}} + 2\dot{\mathbf{p}}^{\mathrm{T}}\,\tilde{\boldsymbol{\omega}}\left(\mathbf{u}+\mathbf{w}\right) + 2\Omega\dot{\mathbf{p}}^{\mathrm{T}}\,\mathbf{J}\,\mathbf{u} + 2\dot{\mathbf{p}}^{\mathrm{T}}\,\dot{\mathbf{w}} + 2\Omega\dot{\mathbf{p}}^{\mathrm{T}}\left(\sum_i \tilde{u}_i \frac{\partial \mathbf{w}}{\partial u_i}\right)\\ &+ \left(\mathbf{u}^{\mathrm{T}}+\mathbf{w}^{\mathrm{T}}\right)\tilde{\boldsymbol{\omega}}^{\mathrm{T}}\,\tilde{\boldsymbol{\omega}}\left(\mathbf{u}+\mathbf{w}\right) + 2\left(\mathbf{u}^{\mathrm{T}}+\mathbf{w}^{\mathrm{T}}\right)\tilde{\boldsymbol{\omega}}^{\mathrm{T}}\,\dot{\mathbf{w}} + 2\Omega\left(\mathbf{u}^{\mathrm{T}}+\mathbf{w}^{\mathrm{T}}\right)\tilde{\boldsymbol{\omega}}^{\mathrm{T}}\,\mathbf{J}\,\mathbf{u}\\ &+ 2\Omega\left(\sum_i \tilde{u}_i \frac{\partial \mathbf{w}^{\mathrm{T}}}{\partial u_i}\right)\tilde{\boldsymbol{\omega}}\left(\mathbf{u}+\mathbf{w}\right) + \dot{\mathbf{w}}^{\mathrm{T}}\,\dot{\mathbf{w}} + 2\Omega\dot{\mathbf{w}}^{\mathrm{T}}\,\mathbf{J}\,\mathbf{u} + 2\Omega\dot{\mathbf{w}}^{\mathrm{T}}\left(\sum_i \tilde{u}_i \frac{\partial \mathbf{w}}{\partial u_i}\right)\\ &+ \Omega^2\,\mathbf{u}^{\mathrm{T}}\,\mathbf{J}^{\mathrm{T}}\,\mathbf{J}\,\mathbf{u} + 2\Omega^2\left(\sum_i \tilde{u}_i \frac{\partial \mathbf{w}^{\mathrm{T}}}{\partial u_i}\right)\mathbf{J}\,\mathbf{u} + \Omega^2\left(\sum_i \tilde{u}_i \frac{\partial \mathbf{w}^{\mathrm{T}}}{\partial u_i}\right)\left(\sum_i \tilde{u}_i \frac{\partial \mathbf{w}}{\partial u_i}\right).\end{aligned} \tag{5.5}$$

Due to its geometry of revolution, the displacement vector $\mathbf{w}$ can be calculated through superposition of mode shapes in the non-rotating trajectory frame $\mathbf{X}_{\mathrm{T}}\mathbf{Y}_{\mathrm{T}}\mathbf{Z}_{\mathrm{T}}$:

$$\mathbf{w}\left(\mathbf{u},t\right) = \boldsymbol{\Phi}^{w}\left(\mathbf{u}\right)\,\mathbf{q}^{w}\left(t\right), \tag{5.6}$$

where $\boldsymbol{\Phi}^{w}(\mathbf{u})$ is the mode shape functions matrix of the free-boundary wheelset and $\mathbf{q}^{w}(t)$ is the Eulerian-modal coordinate vector. The small rigid body displacements of the solid are considered in this approach through the rigid body modes of the wheelset. It must be pointed out that the mode shape functions do not depend on time since the rotation of the solid does not change the mode shapes functions in spatial coordinates, because of the axial symmetry of the wheelset. Once the formula Eq. (5.6) is applied in Eq. (5.5), the kinematic energy results in the following expression:

$$
\begin{aligned}
E_K &= \frac{1}{2}\int_V \frac{\mathrm{D}\mathbf{r}^{\mathrm{T}}}{\mathrm{D}t}\frac{\mathrm{D}\mathbf{r}}{\mathrm{D}t}\rho\,\mathrm{d}v = \frac{1}{2}\dot{\mathbf{p}}^{\mathrm{T}}\dot{\mathbf{p}}\,m_w + \dot{\mathbf{p}}^{\mathrm{T}}\tilde{\boldsymbol{\omega}}\int_V \rho\,\mathbf{u}\,\mathrm{d}v + \dot{\mathbf{p}}^{\mathrm{T}}\tilde{\boldsymbol{\omega}}\int_V \rho\,\boldsymbol{\Phi}^w\,\mathrm{d}v\,\mathbf{q}^w \\
&+ \mathit{\Omega}\dot{\mathbf{p}}^{\mathrm{T}}\mathbf{J}\int_V \rho\,\mathbf{u}\,\mathrm{d}v + \dot{\mathbf{p}}^{\mathrm{T}}\int_V \rho\,\boldsymbol{\Phi}^w\,\mathrm{d}v\,\dot{\mathbf{q}}^w + \mathit{\Omega}\dot{\mathbf{p}}^{\mathrm{T}}\int_V \rho\left(\sum_i \tilde{u}_i\frac{\partial\boldsymbol{\Phi}^w}{\partial u_i}\right)\mathrm{d}v\,\mathbf{q}^w \\
&+ \frac{1}{2}\int_V \rho\,\mathbf{u}^{\mathrm{T}}\tilde{\boldsymbol{\omega}}^{\mathrm{T}}\tilde{\boldsymbol{\omega}}\mathbf{u}\,\mathrm{d}v + \int_V \rho\,\mathbf{u}^{\mathrm{T}}\tilde{\boldsymbol{\omega}}^{\mathrm{T}}\tilde{\boldsymbol{\omega}}\boldsymbol{\Phi}^w\,\mathrm{d}v\,\mathbf{q}^w + \frac{1}{2}\mathbf{q}^{w,\mathrm{T}}\int_V \rho\,\boldsymbol{\Phi}^{w^{\mathrm{T}}}\tilde{\boldsymbol{\omega}}^{\mathrm{T}}\tilde{\boldsymbol{\omega}}\boldsymbol{\Phi}\,\mathrm{d}v\,\mathbf{q}^w \\
&+ \int_V \rho\,\mathbf{u}^{\mathrm{T}}\tilde{\boldsymbol{\omega}}^{\mathrm{T}}\boldsymbol{\Phi}^w\,\mathrm{d}v\,\dot{\mathbf{q}}^w + \mathbf{q}^{w^{\mathrm{T}}}\int_V \rho\,\boldsymbol{\Phi}^{w^{\mathrm{T}}}\tilde{\boldsymbol{\omega}}^{\mathrm{T}}\boldsymbol{\Phi}^w\,\mathrm{d}v\,\dot{\mathbf{q}}^w + \mathit{\Omega}\int_V \rho\,\mathbf{u}^{\mathrm{T}}\tilde{\boldsymbol{\omega}}^{\mathrm{T}}\mathbf{J}\mathbf{u}\,\mathrm{d}v \\
&+ \mathit{\Omega}\mathbf{q}^{w^{\mathrm{T}}}\int_V \rho\,\boldsymbol{\Phi}^{w^{\mathrm{T}}}\tilde{\boldsymbol{\omega}}^{\mathrm{T}}\mathbf{J}\mathbf{u}\,\mathrm{d}v + \mathit{\Omega}\mathbf{q}^{w^{\mathrm{T}}}\int_V \rho\left(\sum_i \tilde{u}_i\frac{\partial\boldsymbol{\Phi}^{w^{\mathrm{T}}}}{\partial u_i}\right)\tilde{\boldsymbol{\omega}}\mathbf{u}\,\mathrm{d}v \\
&+ \mathit{\Omega}\mathbf{q}^{w^{\mathrm{T}}}\int_V \rho\left(\sum_i \tilde{u}_i\frac{\partial\boldsymbol{\Phi}^{w^{\mathrm{T}}}}{\partial u_i}\right)\tilde{\boldsymbol{\omega}}\boldsymbol{\Phi}\,\mathrm{d}v\,\mathbf{q}^w + \frac{1}{2}\dot{\mathbf{q}}^{w^{\mathrm{T}}}\dot{\mathbf{q}}^w + \mathit{\Omega}\,\dot{\mathbf{q}}^{w^{\mathrm{T}}}\int_V \rho\,\boldsymbol{\Phi}^{w^{\mathrm{T}}}\mathbf{J}\mathbf{u}\,\mathrm{d}v \\
&+ \mathit{\Omega}\dot{\mathbf{q}}^{w^{\mathrm{T}}}\int_V \rho\,\boldsymbol{\Phi}^{w^{\mathrm{T}}}\left(\sum_i \tilde{u}_i\frac{\partial\boldsymbol{\Phi}^w}{\partial u_i}\right)\mathrm{d}v\,\mathbf{q}^w + \frac{1}{2}\mathit{\Omega}^2\int_V \rho\,\mathbf{u}^{\mathrm{T}}\mathbf{E}\mathbf{u}\,\mathrm{d}v \\
&+ \mathit{\Omega}^2\,\mathbf{q}^{w^{\mathrm{T}}}\int_V \rho\left(\sum_i \tilde{u}_i\frac{\partial\boldsymbol{\Phi}^{w^{\mathrm{T}}}}{\partial u_i}\right)\mathbf{J}\mathbf{u}\,\mathrm{d}v + \frac{1}{2}\mathit{\Omega}^2\,\mathbf{q}^{w^{\mathrm{T}}}\int_V \rho\left(\sum_i \tilde{u}_i\frac{\partial\boldsymbol{\Phi}^{w^{\mathrm{T}}}}{\partial u_i}\right)\left(\sum_i \tilde{u}_i\frac{\partial\boldsymbol{\Phi}^w}{\partial u_i}\right)\mathrm{d}v\,\mathbf{q}^w.
\end{aligned}
\tag{5.7}
$$

Once the kinematic energy is known, the two terms of Lagrange equation are computed as follows:

$$
\begin{aligned}
\left(\frac{\partial E_K}{\partial\mathbf{q}^w}\right)^{\mathrm{T}} &= \int_V \rho\,\boldsymbol{\Phi}^{\mathrm{T}}\mathrm{d}v\,\tilde{\boldsymbol{\omega}}^{\mathrm{T}}\dot{\mathbf{p}} + \mathit{\Omega}\int_V \rho\left(\sum_i \tilde{u}_i\frac{\partial\boldsymbol{\Phi}^{w^{\mathrm{T}}}}{\partial u_i}\right)\mathrm{d}v\,\dot{\mathbf{p}} + \int_V \rho\,\boldsymbol{\Phi}^{w^{\mathrm{T}}}\tilde{\boldsymbol{\omega}}^{\mathrm{T}}\tilde{\boldsymbol{\omega}}\mathbf{u}\,\mathrm{d}v \\
&+ \int_V \rho\,\boldsymbol{\Phi}^{w^{\mathrm{T}}}\tilde{\boldsymbol{\omega}}^{\mathrm{T}}\tilde{\boldsymbol{\omega}}\boldsymbol{\Phi}\,\mathrm{d}v\,\mathbf{q}^w + \int_V \rho\,\boldsymbol{\Phi}^{w^{\mathrm{T}}}\tilde{\boldsymbol{\omega}}^{\mathrm{T}}\boldsymbol{\Phi}^w\,\mathrm{d}v\,\dot{\mathbf{q}}^w + \mathit{\Omega}\int_V \rho\,\boldsymbol{\Phi}^{w^{\mathrm{T}}}\tilde{\boldsymbol{\omega}}^{\mathrm{T}}\mathbf{J}\mathbf{u}\,\mathrm{d}v \\
&+ \mathit{\Omega}\int_V \rho\left(\sum_i \tilde{u}_i\frac{\partial\boldsymbol{\Phi}^{w^{\mathrm{T}}}}{\partial u_i}\right)\tilde{\boldsymbol{\omega}}\mathbf{u}\,\mathrm{d}v + \mathit{\Omega}\int_V \rho\left(\sum_i \tilde{u}_i\frac{\partial\boldsymbol{\Phi}^{w^{\mathrm{T}}}}{\partial u_i}\right)\tilde{\boldsymbol{\omega}}\boldsymbol{\Phi}^w\,\mathrm{d}v\,\mathbf{q}^w \\
&+ \mathit{\Omega}\int_V \rho\,\boldsymbol{\Phi}^{w^{\mathrm{T}}}\tilde{\boldsymbol{\omega}}^{\mathrm{T}}\left(\sum_i \tilde{u}_i\frac{\partial\boldsymbol{\Phi}^w}{\partial u_i}\right)\mathrm{d}v\,\mathbf{q}^w + \mathit{\Omega}\int_V \rho\left(\sum_i \tilde{u}_i\frac{\partial\boldsymbol{\Phi}^{w^{\mathrm{T}}}}{\partial u_i}\right)\boldsymbol{\Phi}^w\,\mathrm{d}v\,\dot{\mathbf{q}}^w \\
&+ \mathit{\Omega}^2\int_V \rho\left(\sum_i \tilde{u}_i\frac{\partial\boldsymbol{\Phi}^{w^{\mathrm{T}}}}{\partial u_i}\right)\mathbf{J}\mathbf{u}\,\mathrm{d}v + \mathit{\Omega}^2\int_V \rho\left(\sum_i \tilde{u}_i\frac{\partial\boldsymbol{\Phi}^{w^{\mathrm{T}}}}{\partial u_i}\right)\left(\sum_i \tilde{u}_i\frac{\partial\boldsymbol{\Phi}^w}{\partial u_i}\right)\mathrm{d}v\,\mathbf{q}^w,
\end{aligned}
\tag{5.8}
$$

$$
\begin{aligned}
&\frac{\mathrm{D}}{\mathrm{D}t}\left(\frac{\partial E_K}{\partial \dot{\mathbf{q}}^w}\right)^{\mathrm{T}} = \int_V \rho \boldsymbol{\Phi}^{w^{\mathrm{T}}} \mathrm{d}v\, \ddot{\mathbf{p}} + \int_V \rho \boldsymbol{\Phi}^{w^{\mathrm{T}}} \dot{\tilde{\boldsymbol{\omega}}} \mathbf{u}\, \mathrm{d}v + \int_V \rho \boldsymbol{\Phi}^{w^{\mathrm{T}}} \dot{\tilde{\boldsymbol{\omega}}} \boldsymbol{\Phi}\, \mathrm{d}v\, \mathbf{q}^w \\
&+ \int_V \rho \boldsymbol{\Phi}^{w^{\mathrm{T}}} \tilde{\boldsymbol{\omega}} \boldsymbol{\Phi}^w\, \mathrm{d}v\, \dot{\mathbf{q}}^w + \ddot{\mathbf{q}}^w + \Omega \int_V \rho \boldsymbol{\Phi}^{w^{\mathrm{T}}} \left(\sum_i \tilde{u}_i \frac{\partial \boldsymbol{\Phi}^w}{\partial u_i}\right) \mathrm{d}v\, \dot{\mathbf{q}}^w + \Omega \int_V \rho \left(\sum_i \tilde{u}_i \frac{\partial \boldsymbol{\Phi}^{w^{\mathrm{T}}}}{\partial u_i}\right) \mathrm{d}v\, \dot{\mathbf{p}} \\
&+ \Omega \int_V \rho \left(\sum_i \tilde{u}_i \frac{\partial \boldsymbol{\Phi}^{w^{\mathrm{T}}}}{\partial u_i}\right) \tilde{\boldsymbol{\omega}} \mathbf{u}\, \mathrm{d}v + \Omega \int_V \rho \boldsymbol{\Phi}^{w^{\mathrm{T}}} \tilde{\boldsymbol{\omega}}\, \mathbf{J}\, \mathbf{u}\, \mathrm{d}v + \Omega \int_V \rho \left(\sum_i \tilde{u}_i \frac{\partial \boldsymbol{\Phi}^{w^{\mathrm{T}}}}{\partial u_i}\right) \tilde{\boldsymbol{\omega}} \boldsymbol{\Phi}^w\, \mathrm{d}v\, \mathbf{q}^w \\
&+ \Omega \int_V \rho \boldsymbol{\Phi}^{w^{\mathrm{T}}} \tilde{\boldsymbol{\omega}} \left(\sum_i \tilde{u}_i \frac{\partial \boldsymbol{\Phi}^w}{\partial u_i}\right) \mathrm{d}v\, \mathbf{q}^w + \Omega^2 \int_V \rho \left(\sum_i \tilde{u}_i \frac{\partial \boldsymbol{\Phi}^{w^{\mathrm{T}}}}{\partial u_i}\right) \mathbf{J}\, \mathbf{u}\, \mathrm{d}v - \Omega^2 \int_V \rho \boldsymbol{\Phi}^{w^{\mathrm{T}}} \mathbf{E} \mathbf{u}\, \mathrm{d}v \\
&+ \Omega^2 \int_V \rho \left(\sum_i \tilde{u}_i \frac{\partial \boldsymbol{\Phi}^{w^{\mathrm{T}}}}{\partial u_i}\right)\left(\sum_i \tilde{u}_i \frac{\partial \boldsymbol{\Phi}^w}{\partial u_i}\right) \mathrm{d}v\, \mathbf{q}^w - \Omega^2 \int_V \rho \boldsymbol{\Phi}^{w^{\mathrm{T}}} \left(\sum_{i=1,3} u_i \frac{\partial \boldsymbol{\Phi}^w}{\partial u_i}\right) \mathrm{d}v\, \mathbf{q}^w \\
&+ \Omega^2 \int_V \rho \boldsymbol{\Phi}^{w^{\mathrm{T}}} \left(\sum_i \sum_j \tilde{u}_i \tilde{u}_j \frac{\partial^2 \boldsymbol{\Phi}^w}{\partial u_i \partial u_j}\right) \mathrm{d}v\, \mathbf{q}^w ,
\end{aligned}
\tag{5.9}
$$

with $\mathbf{E} = -\mathbf{J}\,\mathbf{J} = \begin{bmatrix} 1 & 0 & 0 \\ 0 & 0 & 0 \\ 0 & 0 & 1 \end{bmatrix}$.

The equation of motion of the flexible and rotating wheelset is derived by means of Lagrange equation. Considering Eqs. (5.8) and (5.9) and taking into account that matrix $\tilde{\boldsymbol{\omega}}$ is anti-symmetric, the following equation is obtained:

$$
\begin{aligned}
&\ddot{\mathbf{q}}^w + \left[2\Omega \int_V \rho \boldsymbol{\Phi}^{w^{\mathrm{T}}} \left(\sum_i \tilde{u}_i \frac{\partial \boldsymbol{\Phi}^w}{\partial u_i}\right) \mathrm{d}v + 2 \int_V \rho \boldsymbol{\Phi}^{w^{\mathrm{T}}} \tilde{\boldsymbol{\omega}} \boldsymbol{\Phi}^w\, \mathrm{d}v \right] \dot{\mathbf{q}}^w \\
&+ \left[\Omega^2 \int_V \rho \boldsymbol{\Phi}^{w^{\mathrm{T}}} \left(\sum_i \sum_j \tilde{u}_i \tilde{u}_j \frac{\partial^2 \boldsymbol{\Phi}^w}{\partial u_i \partial u_j}\right) \mathrm{d}v - \Omega^2 \int_V \rho \boldsymbol{\Phi}^{w^{\mathrm{T}}} \left(\sum_{i=1,3} u_i \frac{\partial \boldsymbol{\Phi}^w}{\partial u_i}\right) \mathrm{d}v + \right. \\
&\left. 2\Omega \int_V \rho \boldsymbol{\Phi}^{w^{\mathrm{T}}} \tilde{\boldsymbol{\omega}} \left(\sum_i \tilde{u}_i \frac{\partial \boldsymbol{\Phi}^w}{\partial u_i}\right) \mathrm{d}v + \int_V \rho \boldsymbol{\Phi}^{w^{\mathrm{T}}} \dot{\tilde{\boldsymbol{\omega}}} \boldsymbol{\Phi}^w\, \mathrm{d}v - \int_V \rho \boldsymbol{\Phi}^{w^{\mathrm{T}}} \tilde{\boldsymbol{\omega}}^{\mathrm{T}} \tilde{\boldsymbol{\omega}} \boldsymbol{\Phi}^w\, \mathrm{d}v \right] \mathbf{q}^w \\
&= \Omega^2 \int_V \rho \boldsymbol{\Phi}^{w^{\mathrm{T}}} \mathbf{E} \mathbf{u}\, \mathrm{d}v - 2\Omega \int_V \rho \boldsymbol{\Phi}^{w^{\mathrm{T}}} \tilde{\boldsymbol{\omega}}\, \mathbf{J}\, \mathbf{u}\, \mathrm{d}v - \int_V \rho \boldsymbol{\Phi}^{w^{\mathrm{T}}} \dot{\tilde{\boldsymbol{\omega}}} \mathbf{u}\, \mathrm{d}v \\
&+ \int_V \rho \boldsymbol{\Phi}^{w^{\mathrm{T}}} \tilde{\boldsymbol{\omega}}^{\mathrm{T}} \tilde{\boldsymbol{\omega}} \mathbf{u}\, \mathrm{d}v - \int_V \rho \boldsymbol{\Phi}^{w^{\mathrm{T}}} \mathrm{d}v\, \mathbf{T}^{\mathbf{T}} \ddot{\mathbf{p}}_0 + \mathbf{Q}.
\end{aligned}
\tag{5.10}
$$

The modal properties are computed from a FE model; therefore it is adequate to use the FE methodology for computing the equation of motion numerically. The mode shape functions are obtained into the *e*-th element of the FE mesh as follows:

$$\boldsymbol{\Phi}^{w}(\mathbf{u}) = \mathbf{N}^{e}(\mathbf{u})\boldsymbol{\Phi}_{FE}^{w,e}, \tag{5.11}$$

where $\mathbf{N}^{e}(\mathbf{u})$ is the basis (or shape) function matrix of the *e*-th element, and $\boldsymbol{\Phi}_{\mathrm{FE}}^{w,e}$ the mode shapes computed in the nodes of the *e*-th element through the FE model.

This approach allows obtaining the matrices of the equation of motion by means of the matrices of the elements. These matrices have to be assembled in global matrices by following the standard FE assembling technique [159]. The first matrix in Eq. (5.10) is obtained by means of the approach in Eq. (5.11) as follows:

$$\begin{aligned}\tilde{\mathbf{V}} &= \int_{V} \rho \boldsymbol{\Phi}^{w\mathrm{T}} \left(\sum_{i} \tilde{u}_i \frac{\partial \boldsymbol{\Phi}^{w}}{\partial u_i} \right) \mathrm{d}v = \sum_{e=1}^{n_e} \int_{V^e} \rho \left(\boldsymbol{\Phi}_{\mathrm{FE}}^{w,e}\right)^{\mathrm{T}} \mathbf{N}^{e\mathrm{T}} \left(\sum_{i} \tilde{u}_i \frac{\partial \mathbf{N}^{e}}{\partial u_i} \right) \boldsymbol{\Phi}_{\mathrm{FE}}^{w,e}\, \mathrm{d}v \\ &= \left(\boldsymbol{\Phi}_{\mathrm{FE}}^{w}\right)^{\mathrm{T}} \left(\sum_{e=1}^{n_e} \int_{V^e} \rho \mathbf{N}^{e\mathrm{T}} \left(\sum_{i} \tilde{u}_i \frac{\partial \mathbf{N}^{e}}{\partial u_i} \right) \mathrm{d}v \right) \boldsymbol{\Phi}_{\mathrm{FE}}^{w},\end{aligned} \tag{5.12}$$

where n_e is the number of elements in the FE mesh, V is the volume domain associated with the undeformed solid and V^e is the volume of the *e*-th element. Defining the *e*-th element matrix $\mathbf{V}^{e}$ as

$$\mathbf{V}^{e} = \int_{V^e} \rho \mathbf{N}^{e\mathrm{T}} \left(\sum_{i} \tilde{u}_i \frac{\partial \mathbf{N}^{e}}{\partial u_i} \right) \mathrm{d}v, \tag{5.13}$$

the following compact expression of $\tilde{\mathbf{V}}$ is obtained:

$$\tilde{\mathbf{V}} = \left(\boldsymbol{\Phi}_{\mathrm{FE}}^{w}\right)^{\mathrm{T}} \left(\sum_{e=1}^{n_e} \mathbf{V}^{e} \right) \boldsymbol{\Phi}_{\mathrm{FE}}^{w}. \tag{5.14}$$

Following the same procedure as in Eq. (5.12), the remaining matrices of the equation of motion are obtained:

$$\mathbf{P}^{e} = \int_{V^e} \rho \mathbf{N}^{e\mathrm{T}} \tilde{\boldsymbol{\omega}} \mathbf{N}^{e}\, \mathrm{d}v, \quad \tilde{\mathbf{P}} = \left(\boldsymbol{\Phi}_{\mathrm{FE}}^{w}\right)^{\mathrm{T}} \left(\sum_{e=1}^{n_e} \mathbf{P}^{e} \right) \boldsymbol{\Phi}_{\mathrm{FE}}^{w}, \tag{5.15}$$

$$\mathbf{A}^e = \int_{V^e} \rho \mathbf{N}^{e\mathrm{T}} \left(\sum_i \sum_j \tilde{u}_i \, \tilde{u}_j \frac{\partial^2 \mathbf{N}^e}{\partial u_i \, \partial u_j} \right) \mathrm{d}v, \quad \tilde{\mathbf{A}} = \left(\mathbf{\Phi}_{\mathrm{FE}}^w \right)^{\mathrm{T}} \left(\sum_{e=1}^{n_e} \mathbf{A}^e \right) \mathbf{\Phi}_{\mathrm{FE}}^w, \tag{5.16}$$

$$\mathbf{C}^e = \int_{V^e} \rho \mathbf{N}^{e\mathrm{T}} \left(\sum_{i=1,3} u_i \frac{\partial \mathbf{N}^e}{\partial u_i} \right) \mathrm{d}v, \quad \tilde{\mathbf{C}} = \left(\mathbf{\Phi}_{\mathrm{FE}}^w \right)^{\mathrm{T}} \left(\sum_{e=1}^{n_e} \mathbf{C}^e \right) \mathbf{\Phi}_{\mathrm{FE}}^w, \tag{5.17}$$

$$\mathbf{S}^e = \int_{V^e} \rho \mathbf{N}^{e\mathrm{T}} \, \tilde{\boldsymbol{\omega}} \left(\sum_i \tilde{u}_i \frac{\partial \mathbf{N}^e}{\partial u_i} \right) \mathrm{d}v, \quad \tilde{\mathbf{S}} = \left(\mathbf{\Phi}_{\mathrm{FE}}^w \right)^{\mathrm{T}} \left(\sum_{e=1}^{n_e} \mathbf{S}^e \right) \mathbf{\Phi}_{\mathrm{FE}}^w, \tag{5.18}$$

$$\mathbf{R}^e = \int_{V^e} \rho \mathbf{N}^{e\mathrm{T}} \, \dot{\tilde{\boldsymbol{\omega}}} \, \mathbf{N}^e \, \mathrm{d}v, \quad \tilde{\mathbf{R}} = \left(\mathbf{\Phi}_{\mathrm{FE}}^w \right)^{\mathrm{T}} \left(\sum_{e=1}^{n_e} \mathbf{R}^e \right) \mathbf{\Phi}_{\mathrm{FE}}^w, \tag{5.19}$$

$$\mathbf{B}^e = \int_{V^e} \rho \mathbf{N}^{e\mathrm{T}} \, \tilde{\boldsymbol{\omega}}^{\mathrm{T}} \, \tilde{\boldsymbol{\omega}} \, \mathbf{N}^e \, \mathrm{d}v, \quad \tilde{\mathbf{B}} = \left(\mathbf{\Phi}_{\mathrm{FE}}^w \right)^{\mathrm{T}} \left(\sum_{e=1}^{n_e} \mathbf{B}^e \right) \mathbf{\Phi}_{\mathrm{FE}}^w, \tag{5.20}$$

$$\mathbf{c}^e = \int_{V^e} \rho \mathbf{N}^{e\mathrm{T}} \, \mathbf{E} \, \mathbf{u} \, \mathrm{d}v, \quad \tilde{\mathbf{c}} = \left(\mathbf{\Phi}_{\mathrm{FE}}^w \right)^{\mathrm{T}} \left(\sum_{e=1}^{n_e} \mathbf{c}^e \right), \tag{5.21}$$

$$\mathbf{U}^e = \int_{V^e} \rho \mathbf{N}^{e\mathrm{T}} \, \tilde{\boldsymbol{\omega}} \, \mathbf{J} \, \mathbf{u} \, \mathrm{d}v, \quad \tilde{\mathbf{U}} = \left(\mathbf{\Phi}_{\mathrm{FE}}^w \right)^{\mathrm{T}} \left(\sum_{e=1}^{n_e} \mathbf{U}^e \right), \tag{5.22}$$

$$\mathbf{H}^e = \int_{V^e} \rho \mathbf{N}^{e\mathrm{T}} \, \dot{\tilde{\boldsymbol{\omega}}} \, \mathbf{u} \, \mathrm{d}v, \quad \tilde{\mathbf{H}} = \left(\mathbf{\Phi}_{\mathrm{FE}}^w \right)^{\mathrm{T}} \left(\sum_{e=1}^{n_e} \mathbf{H}^e \right), \tag{5.23}$$

$$\mathbf{N}^e = \int_{V^e} \rho \mathbf{N}^{e\mathrm{T}} \, \tilde{\boldsymbol{\omega}}^{\mathrm{T}} \, \tilde{\boldsymbol{\omega}} \, \mathbf{u} \, \mathrm{d}v, \quad \tilde{\mathbf{N}} = \left(\mathbf{\Phi}_{\mathrm{FE}}^w \right)^{\mathrm{T}} \left(\sum_{e=1}^{n_e} \mathbf{N}^e \right), \tag{5.24}$$

$$\mathbf{G}^e = \int_{V^e} \rho \mathbf{N}^{e\mathrm{T}} \, \mathrm{d}v, \quad \tilde{\mathbf{G}} = \left(\mathbf{\Phi}_{\mathrm{FE}}^w \right)^{\mathrm{T}} \left(\sum_{e=1}^{n_e} \mathbf{G}^e \right) \mathbf{T}^{\mathbf{T}} \, \ddot{\mathbf{p}}_0, \tag{5.25}$$

resulting the following equation of motion for the flexible wheelset running along a curved track:

$$\begin{aligned} &\ddot{\mathbf{q}}^w + \left(2\,\Omega\,\tilde{\mathbf{V}} + 2\,\tilde{\mathbf{P}} \right) \dot{\mathbf{q}}^w + \left(\Omega^2 \left(\tilde{\mathbf{A}} - \tilde{\mathbf{C}} \right) + 2\,\Omega\,\tilde{\mathbf{S}} + \tilde{\mathbf{R}} - \tilde{\mathbf{B}} + \tilde{\mathbf{D}} \right) \mathbf{q}^w \\ &= \Omega^2\,\tilde{\mathbf{c}} - 2\,\Omega\,\tilde{\mathbf{U}} - \tilde{\mathbf{H}} + \tilde{\mathbf{N}} - \tilde{\mathbf{G}} + \mathbf{Q}_c + \mathbf{Q}_s. \end{aligned} \tag{5.26}$$

Matrices $\tilde{\mathbf{V}}$ and $\tilde{\mathbf{P}}$ are associated with the inertial force due to Coriolis acceleration originated by the rotations of the wheelset and track frames, respectively; matrix $\tilde{\mathbf{A}}$ is related to the force due to the convective acceleration; $\tilde{\mathbf{C}}$ is the centrifugal stiffening matrix; matrix $\tilde{\mathbf{S}}$ introduces the inertial force due to the convective velocity and the angular velocity of the track frame; matrix $\tilde{\mathbf{R}}$ takes into account the force due to the tangential acceleration of the track frame that is associated with the deformed configuration; matrix $\tilde{\mathbf{B}}$ considers the centrifugal effect due to the deformation of the solid that is associated with the track frame rotation; $\tilde{\mathbf{D}}$ is the wheelset modal stiffness matrix, a diagonal matrix formed by the squares of the undamped natural frequencies of the free-boundary wheelset; vector $\tilde{\mathbf{c}}$ is the modal force due to the centrifugal effect associated with the wheel rotation in the undeformed configuration; vector $\tilde{\mathbf{U}}$ contains the constant forces associated with Coriolis effect; vector $\tilde{\mathbf{H}}$ accounts for the forces due to the tangential acceleration of the track frame that is associated with the undeformed configuration; $\tilde{\mathbf{N}}$ is the generalised force vector of the centrifugal forces related to track frame rotation; vector $\tilde{\mathbf{G}}$ accounts for the centrifugal effects associated with the translation motion of the track frame; vectors $\mathbf{Q}_c$ and $\mathbf{Q}_s$ contain the generalised forces acting on the flexible wheelset resulting respectively from wheel/rail contact forces and from the forces applied by the primary suspension. The details of the numerical methodology are detailed in Ref. [160].

5.4 CYCLIC AND FLEXIBLE TRACK MODEL BASED ON THE MOVING ELEMENT METHOD

Historically, a frequency-domain approach has been used to address the moving load problem by means of the Fourier Transform Method (FTM) and a moving coordinate system. Mathews [163,164] considered an arbitrary load moving along an infinite beam resting on an elastic foundation and solved the problem by using FTM. Jézéquel [165] utilised the same methodology for an Euler-Bernoulli infinite beam (considering the rotational and transverse stiffness) with a Winkler foundation subjected to a concentrated force moving with constant speed. Other extended focus is based on a time-domain approach based on Timoshenko flexible beam model [166] which considers a simply supported infinite beam subjected to moving loads.

These mentioned works consider rail beams as continuum and solve the equation of motion through an analytic approach. This makes them inappropriate when replacing a moving load by a complete moving vehicle system of massive number of degrees of freedom; for instance, the Timoshenko beam is only valid up to 1.5 kHz for lateral rail vibration and up to 2 kHz for vertical vibration [7]. Therefore, researchers have widely been using the well-known Finite Element Method, which physically discretises the track into a finite number of elements. Numerical time-stepping integrators are needed to solve the resulting equations of motion after assembling the element matrices. FEM permits to extend the range of validity above the previous limit of 1.5 kHz and allows hence the complete wheelset/track model to comprise high frequency dynamic phenomena.

Two fundamental problems of considering a fixed global coordinate system in the FE model are:

(a) There is the need of truncating the infinitely long track into a finite one with two corresponding artificial boundary ends, but the vehicle is moving forwards to the ‘downstream’ side; thereby, the rail length required for reasonable simulation time-spans (without the vehicle exceeding the ‘downstream’ end), while preserving the refinement of the mesh, leads to an unapproachable number of degrees of freedom in the FEM.

(b) The vehicle moves along the elements with time, thus the load vector has to be updated at each time step of the integrator scheme.

Problem (a) is solved by adopting cyclic boundary conditions at the model edges (same displacements and derivatives) as presented in Ref. [162]. The cyclic track approach models a circumferential constant radius track negotiated by a set of identical vehicles, uniformly distributed in such a way that each vehicle is set at a constant distance L apart from the adjacent ones and travel at the same velocity V. The model can be interpreted as an infinite track negotiated by an infinite number of identical vehicles separated uniformly by a distance L and travels at the same velocity V. The constant distance L will be set large enough to avoid the dynamic interaction between the vehicles and cyclic boundary conditions are introduced at the ends of the model. Hence, due to the periodicity of the structure and the loading conditions, the study of the track is reduced to a single section having finite length L. The approach adopts a substructuring technique where rails and sleepers are treated separately. Different sleeper bay distances have been considered in order to take into account the dynamics of a constant radius curved track.

5.4.1 Formulation of the 1D Moving Element Method

To overcome problem (b), Koh *et al.* [167] presented a formulation called Moving Element Method (MEM) based on a relative coordinate system attached to the moving railway vehicle travelling at a constant velocity *V*, instead of a fixed coordinate system. This method was initially adopted for a finite Euler-Bernoulli beam (1D). A new class of finite elements associated with the moving coordinate system is defined. This relative motion requires considering the material derivative for the formulation of the rail dynamics. The concept was afterwards extended to 2D moving elements in order to study moving load on continuum [168].

The rail is modelled as an infinite Euler-Bernoulli beam with Young's modulus E, second moment of area I and mass per unit length $\overline{m}$. The beam is supported on a viscoelastic foundation whose stiffness and damping per unit length are $\bar{k}$ and $\bar{c}$, respectively. It is subjected to a dynamic force F at the wheel contact point, which is moving with a constant velocity *V*. The moving coordinate associated with the moving force/vehicle is defined as

$$r = x - x_I - Vt, \tag{5.27}$$

where x_I is the fixed coordinate of node I. The material derivative, $\mathrm{D}/\mathrm{D}t \equiv \partial/\partial t - V\,\partial/\partial r$, is used again to introduce the convective terms of the kinematic energy due to the moving reference system in the Lagrange equation. The governing equation for the rail beam in terms of the vertical displacements is obtained through a Galerkin's approach and, letting the displacement shape function be $\mathbf{N}$, it can be shown that the element mass, damping and stiffness matrices are, respectively,

$$\mathbf{M}^e = \overline{m}\int_0^L \mathbf{N}^\mathrm{T}\mathbf{N}\,\mathrm{d}r, \tag{5.28}$$

$$\mathbf{C}^e = -2\overline{m}V\int_0^L \mathbf{N}^\mathrm{T}\mathbf{N}_{,r}\,\mathrm{d}r + \bar{c}\int_0^L \mathbf{N}^\mathrm{T}\mathbf{N}\,\mathrm{d}r, \tag{5.29}$$

$$\mathbf{K}^e = EI\int_0^L \mathbf{N}^\mathrm{T}_{,rr}\mathbf{N}_{,rr}\,\mathrm{d}r + \overline{m}V^2\int_0^L \mathbf{N}^\mathrm{T}\mathbf{N}_{,rr}\,\mathrm{d}r - \bar{c}V\int_0^L \mathbf{N}^\mathrm{T}\mathbf{N}_{,r}\,\mathrm{d}r + \bar{k}\int_0^L \mathbf{N}^\mathrm{T}\mathbf{N}\,\mathrm{d}r, \tag{5.30}$$

where $(\ )_{,r}$ denotes partial derivative with respect to r. For beam elements, it is common to use the following Hermitian cubic polynomials as shape functions

$$N_1 = \frac{1}{L^3}\left(2r^3 - 3r^2L + L^3\right), \tag{5.31}$$

$$N_2 = \frac{1}{L^3}\left(r^3L - 2r^2L^2 + rL^3\right), \tag{5.32}$$

$$N_3 = \frac{1}{L^3}\left(-2r^3 + 3r^2L\right), \tag{5.33}$$

$$N_4 = \frac{1}{L^3}\left(r^3L - r^2L^2\right), \tag{5.34}$$

corresponding to the vertical and angular degrees of freedom $(y_1, \theta_1, y_2, \theta_2)$ of each element, where θ denotes rotation. Based on these shape functions, the element matrices can be derived. The element matrices are then assembled in the usual manner to form the corresponding structure matrices for the rail beam.

5.4.1.1 Study of the influence of the model parameters of a 1D finite cyclic rail using a ME approach

In this subsection, the 1D Moving Element cyclic rail model is evaluated to check the influence of the rail length, vehicle speed, refinement and type of the spatial discretisation. Since the MEM approach solves the temporal range limitation of the finite rail models locating the vehicle in a fixed position, this parameter study pretends to figure out how the model edges affects the receptance function of the rail model and from what approximated length (dependent on the configuration of other model parameters) permits to neglect their influence.

Fig. 5.3 shows the fundamental effect of the model edges on the receptance: reflected waves in the mid-frequency range (from around 0.1 to 2 kHz) considering 70 spans (70·0.6=42 m). The influence of the vehicle speed does not appear clear in this figure; therefore, Figs. 5.4 and 5.5 depict receptances for 0 and 100 km/h, respectively, increasing the length of the rail in order to see if these reflected waves are mitigated when the rail is longer, as expected.

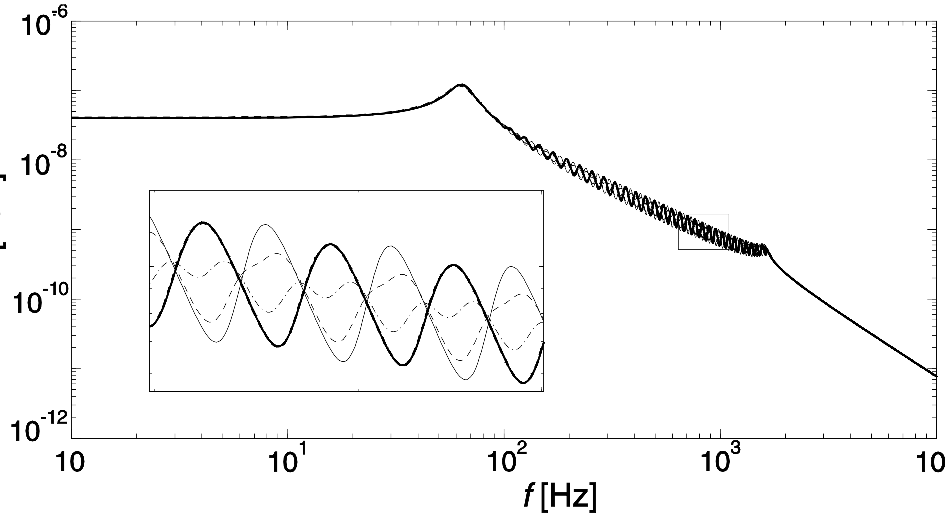

Fig. 5.3. Receptances of the 1D ME rail model for different vehicle speeds. Fixed 500 elements, 70 spans of length and uniform discretisation (lower figure: zoomed view around 1 kHz). ———: $V = 0$ km/h; – – – – –: $V = 50$ km/h; – · – · –: $V = 100$ km/h; ▬▬▬: $V = 150$ km/h; ■ ■ ■ ■: $V = 200$ km/h.

Fig. 5.4, especially its zoom capture, shows how these model reflections are important for 70 spans. As the spatial discretisation is more refined, the amplitude of these reflections markedly decreases; for 200 spans (200·0.6=120 m), these appear to be practically attenuated. These 120 m will be considered a reference length to avoid these reflected waves from the model edges. It can be observed a similar trend in Fig. 5.5; for a larger vehicle speed (100 km/h), the reflections are notably lower than in the previous case. The figure also shows how this effect is attenuated for higher speeds.

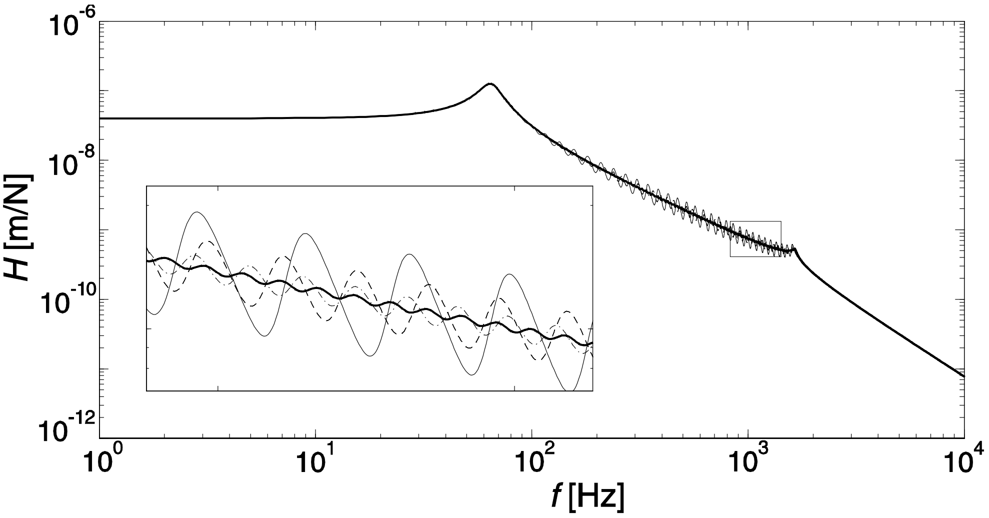

Fig. 5.4. Receptances of the 1D ME rail model for different refinements. Fixed 500 elements, vehicle speed $V = 0$ km/h and uniform discretisation (lower figure: zoomed view around 1 kHz). ———: 70 spans elements; – – – – –: 100 spans; – · – · –: 150 spans; ▬▬▬: 200 spans.

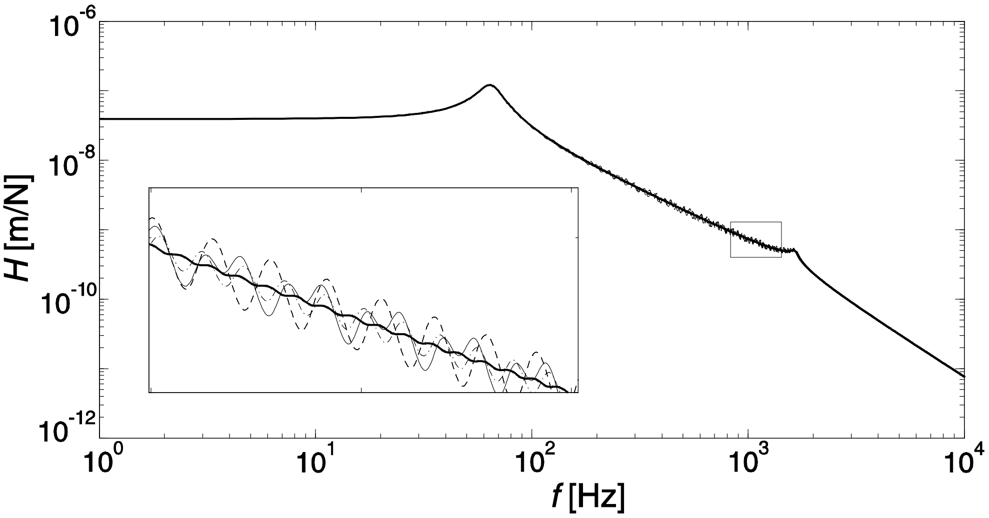

Fig. 5.5. Receptances of the 1D ME rail model for different refinements. Fixed 500 elements, vehicle speed $V = 100$ km/h and uniform discretisation (lower figure: zoomed view around 1 kHz). ———: 70 spans elements; – – – – –: 100 spans; – · – · –: 150 spans; ▬▬▬: 200 spans.

Now, the influence of the vehicle speed on the receptance is studied. In order to avoid the effect of the finite length, 200 spans have been set to neglect the previous reflections in the mid-frequency range. As seen in Fig. 5.6, the receptances practically coincide with each other and these reflections appear sufficiently mitigated. In the zoom view, small discrepancies when reproducing the second resonance peak around 1.7 kHz are observed; this peak goes down when the vehicle speed is increasing.

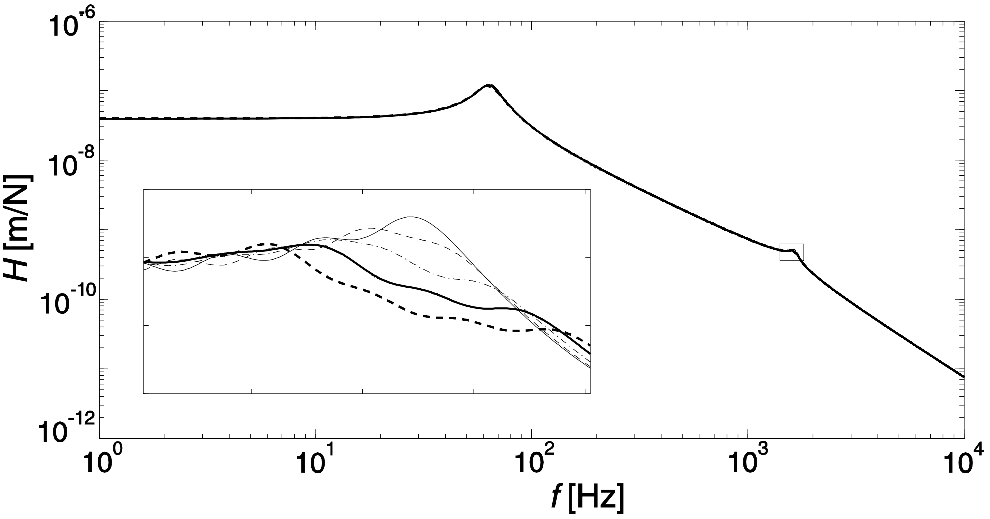

Fig. 5.6. Receptances of the 1D ME rail model for different vehicle speeds. Fixed 500 elements, 200 spans of length and uniform discretisation (lower figure: zoomed view around 1 kHz). ———: $V = 0$ km/h; – – – – –: $V = 50$ km/h; – · – · –: $V = 100$ km/h; ━━━━: $V = 150$ km/h; ▬ ▬ ▬ ▬: $V = 200$ km/h.

The refinement of the ME beam is also a factor to consider. Fig. 5.7 shows that the number of elements for a uniform spatial discretisation does not affect significantly the receptance from 200 elements for a finitely long rail of 200 spans and a vehicle speed of 100 km/h. For 100 elements, only the second resonance peak is markedly displaced and the inherent reflections appear slightly larger.

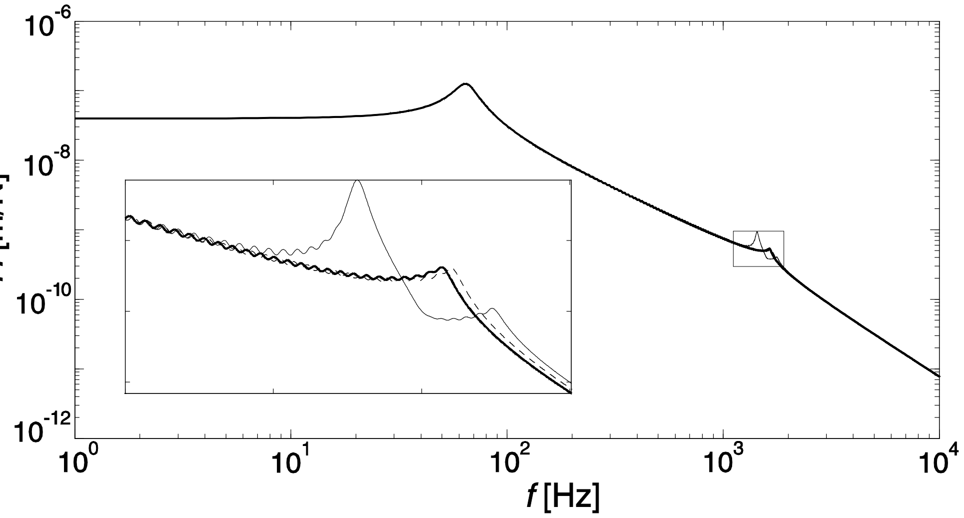

Fig. 5.7. Receptances of the 1D ME rail model for different number of elements in the spatial discretisation. Fixed vehicle speed $V = 100$ km/h, 200 spans of length and uniform discretisation (lower figure: zoomed view around 1 kHz). ——— : $N_{ex} = 200$; – – – – – : $N_{ex} = 300$; – · – · – : $N_{ex} = 500$; ━━━ : $N_{ex} = 1000$ elements.

Different types of refinement have been tested for the 1D ME beam model and for the 3D ME model in later sections in order to refine the mesh only around the contact zone and increase gradually the element size to the edges. This strategy can reduce significantly the number of elements (and hence, degrees of freedom) compared to a uniform and refined mesh. It aims to study how the spatial discretisation affects the mentioned reflections from the model edges. Besides the uniform one, three growing functions have been implemented increasing the length of the elements from the contact point. The length of the central element is 1 cm. These three functions are: linear, linear-uniform (linear along the 60% of the beam and uniform for the 20% and 20% of the lateral parts) and parabolic. The last one presents convergence problems for the solution, so it has not been depicted in Fig. 5.8. This figure shows how the uniform and linear-uniform discretisations maintain reflections enough attenuated (both practically overlap), while the linear one presents much larger amplitudes for these reflections probably due to the C^1 discontinuity of the element size. It concludes that the linear-uniform one can be a useful discretisation for the 3D MEM in order to reduce the number of elements.

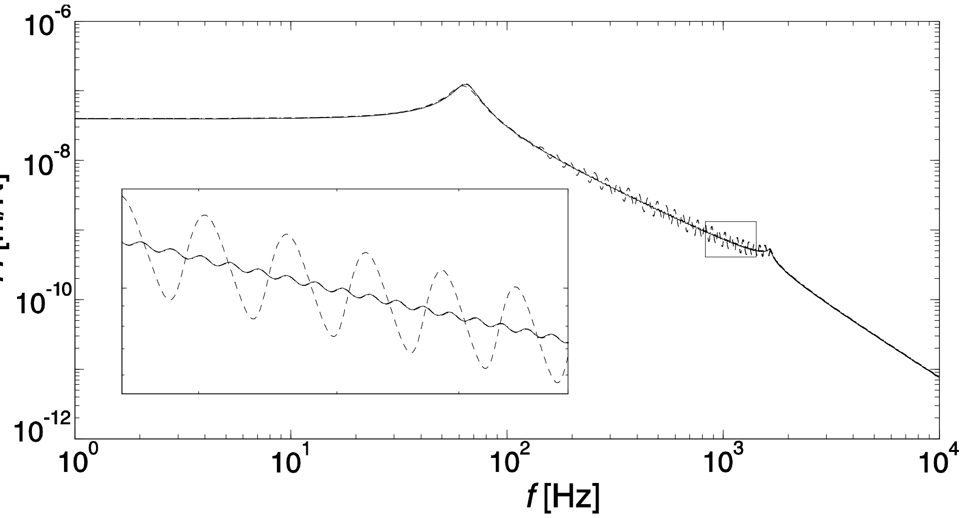

Fig. 5.8. Receptances of the 1D ME rail model for different refinement models. Fixed 500 elements, vehicle speed $V = 100$ km/h, 200 spans of length (lower figure: zoomed view around 1 kHz). ——— : uniform; – – – – – : linear; – · – · – : linear-uniform spatial discretisation.

5.4.2 3D Moving Element Method

Andersson [66] showed significant cross-sectional deformation of the rail already at frequencies around 200 Hz. This implies that the track model needs to capture the 3D dynamic behaviour of the rail at higher frequencies. A waveguide FE model (WANDS software) is commonly used for 3D rails [13,67], which takes advantage of the 2D geometry of the rail having a constant cross-section, but nonetheless consider the 3D nature of the vibration by assuming a wave-type solution along the rail.

An alternative is to model the rail by 3D solid elements. One of the most relevant contributions of the present thesis is the extension of the MEM concept to a tangent 3D track extruded from the UIC60 profile (see Fig. 5.9), adopting a FE technique and introducing cyclic boundary conditions. The new methodology is herein referred to as the 3D Moving Element Method (3D MEM). The 3D MEM avoids the moving vehicle exceeding the ‘downstream’ boundary end — problem (a) — since this class of moving rail elements is attached to the vehicle. The wheel/rail contact area is always positioned at the same railhead element (longitudinally in the middle of the rail) instead of crossing from one element into another. This has two immediate and important consequences: firstly, there is no need to update the force or displacement vectors in the contact patch ─ problem (b) ─ because it is fixed on the same element; secondly, it permits to refine the mesh just around the fixed contact patch, where forces and displacements are more pronounced. Both are hence important advantages in terms of computational cost compared to the FE models commonly employed. This formulation permits to widen the frequency range of validity of the Timoshenko beam model used in previous works of this research group [159,160].

The 3D MEM formulation developed in this section is utilised to compute numerically the resulting linear equation of motion, obtaining the element matrices and assembling them in global matrices by following the standard FE technique. These global matrices are not time dependent, and therefore they can be pre-calculated before the simulation starts and enable to adopt a modal approach.

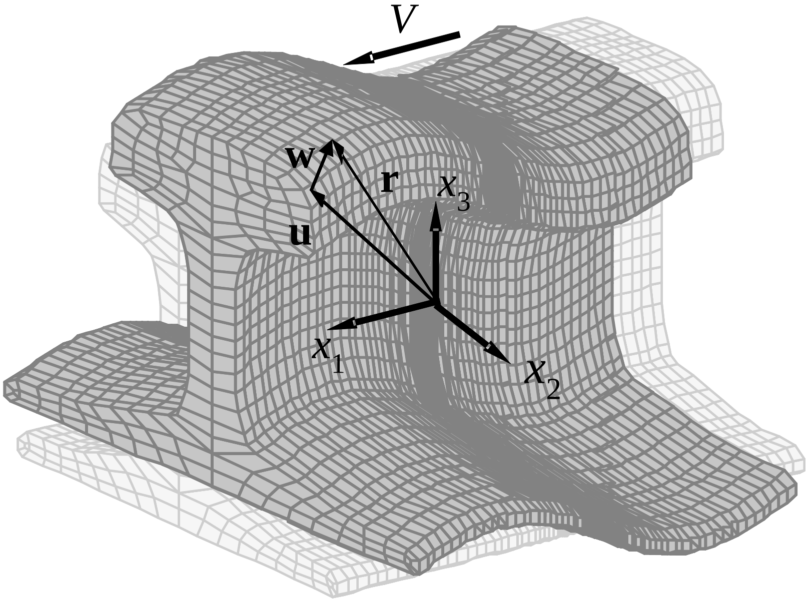

Fig. 5.9. Finite element mesh of the UIC60 rail. Deformed and undeformed configuration.

Both the MEM and the FEM need the following mathematical step:

$$\int_{\substack{solid\\volume}} f = \sum_{elements} \int_{\substack{element\\volume}} f. \tag{5.35}$$

As seen, the integral of the function f over the volume of the solid is the sum of the integrals over the finite element volume. This is correct if some conditions of continuity are satisfied. The MEM needs to compute the integral in Eq. (5.35)**¡Error! Marcador no definido.** with f being the second derivative of the shape functions. In the proposed model, quadratic shape functions are used with C^0 continuity between elements. Thus, Eq. (5.35) can only be applied if the maximum order of differentiation is 1 [169], which means that integration by parts is necessary in the current formulation to obtain lower order derivatives. This is a classic problem in FEM shell elements. The present model solves this mathematical gap on the convective acceleration term previously presented (see Eq. (5.16)), which has not been treated in previous works.

Let consider a fixed Cartesian coordinate system $\mathbf{x}_1\mathbf{x}_2\mathbf{x}_3$ while the mass of the rail 'flows' backwards with velocity V, see Fig. 5.9. An Eulerian position vector $\mathbf{u}$ defined through the coordinate system $\mathbf{x}_1\mathbf{x}_2\mathbf{x}_3$ is considered. Vector $\mathbf{u}$ defines the position of a spatial point and it does not depend on time. Vector $\mathbf{w} \equiv \mathbf{w}(\mathbf{u},t)$ is the displacement of a material point that occupies the position $\mathbf{u}$ at the instant t with respect the undeformed configuration. The position vector of the material point is

$$\mathbf{r} = \mathbf{u} + \mathbf{w}(\mathbf{u},t). \tag{5.36}$$

The cyclic boundary condition is satisfied if the displacements and the velocities at the left edge of the model are equal to the ones of the right edge, that is

$$\mathbf{w}\left((0,u_2,u_3)^{\mathrm{T}},t\right) = \mathbf{w}\left((L,u_2,u_3)^{\mathrm{T}},t\right),\ \dot{\mathbf{w}}\left((0,u_2,u_3)^{\mathrm{T}},t\right) = \dot{\mathbf{w}}\left((L,u_2,u_3)^{\mathrm{T}},t\right). \tag{5.37}$$

In the following sections, it is deduced the convective terms of the equation of motion associated with the Eulerian approach adopted by means of two methodologies: based on the virtual work associated with the inertial forces, and based on the Lagrange equation. Both obtain the same expression for the equation of motion.

5.4.2.1 Based on the virtual work associated with the inertial forces

In order to calculate the virtual work associated with the inertial forces, the acceleration has to be previously calculated. The velocity and, subsequently, acceleration of the material point are computed through the material derivative as follows

$$\mathbf{v} = \frac{\mathrm{D}\mathbf{r}}{\mathrm{D}t} = \frac{\partial \mathbf{r}}{\partial t} - V\frac{\partial \mathbf{r}}{\partial x_1} = \dot{\mathbf{w}} - V(1,0,0)^{\mathrm{T}} - V\frac{\partial \mathbf{w}}{\partial x_1}, \tag{5.38}$$

$$\mathbf{a} = \frac{\mathrm{D}\mathbf{r}}{\mathrm{D}t} = \frac{\partial \mathbf{r}}{\partial t} - V\frac{\partial \mathbf{r}}{\partial x_1} = \ddot{\mathbf{w}} - 2V\frac{\partial \dot{\mathbf{w}}}{\partial x_1} + V^2\frac{\partial^2 \mathbf{w}}{\partial x_1^2}. \tag{5.39}$$

The virtual work associated with the inertial forces is

$$\delta W = \int_V \rho\, \delta\mathbf{w}^{\mathrm{T}}\mathbf{a}\, \mathrm{d}\upsilon = \int_V \rho\, \delta\mathbf{w}^{\mathrm{T}}\ddot{\mathbf{w}}\, \mathrm{d}\upsilon - 2V\int_V \rho\, \delta\mathbf{w}^{\mathrm{T}}\frac{\partial \dot{\mathbf{w}}}{\partial x_1}\mathrm{d}\upsilon + V^2\int_V \rho\, \delta\mathbf{w}^{\mathrm{T}}\frac{\partial^2 \mathbf{w}}{\partial x_1^2}. \tag{5.40}$$

The convergence of the last integral, which contains a second-order derivative of the displacements, cannot be guaranteed due to the aforementioned continuity problem. The third term of Eq. (5.40) can be integrated by parts giving

$$\int_V \rho\, \delta\mathbf{w}^{\mathrm{T}}\frac{\partial^2 \mathbf{w}}{\partial x_1^2}\mathrm{d}x_1\mathrm{d}x_2\mathrm{d}x_3 = \int_S \rho\, \delta\mathbf{w}^{\mathrm{T}}\frac{\partial \mathbf{w}}{\partial x_1}\mathrm{d}x_2\mathrm{d}x_3 - \int_V \rho\frac{\partial\left(\delta\mathbf{w}^{\mathrm{T}}\right)}{\partial x_1}\frac{\partial \mathbf{w}}{\partial x_1}\mathrm{d}x_1\mathrm{d}x_2\mathrm{d}x_3. \tag{5.41}$$

The surface integral can be only computed into the lateral surfaces corresponding to the rail edges. It has been selected a rail length L long enough to have negligible displacements at the model edges; thereby the integrand is close to zero and the surface integral can be disregarded. Hence, the convergence of Eq. (5.40) is hence guaranteed for more refined spatial discretisations of the model, resulting as

$$\delta W = \int_V \rho\, \delta\mathbf{w}^{\mathrm{T}}\ddot{\mathbf{w}}\, \mathrm{d}\upsilon - 2V\int_V \rho\, \delta\mathbf{w}^{\mathrm{T}}\frac{\partial \dot{\mathbf{w}}}{\partial x_1}\mathrm{d}\upsilon - V^2\int_V \rho\frac{\partial\left(\delta\mathbf{w}^{\mathrm{T}}\right)}{\partial x_1}\frac{\partial \mathbf{w}}{\partial x_1}\mathrm{d}\upsilon. \tag{5.42}$$

Now, the FE interpolation is adopted. The mesh is moving with $x_1x_2x_3$ frame and consequently the material of the rail flows into this mesh. The displacements in the volume of the *e*-th element V^e are computed by means of the shape functions $\mathbf{N}^e(\mathbf{u})$ as follows

$$\mathbf{w}(\mathbf{x},t) = \mathbf{N}^e(\mathbf{u})\mathbf{w}^e(t), \qquad \text{if } \mathbf{u} \in V^e, \tag{5.43}$$

$\mathbf{w}^e$ being the nodal displacements. If Eq. (5.43) is implemented in Eq. (5.42), the following expression is obtained:

$$\delta W = \sum_e \delta \mathbf{w}^{e\mathrm{T}} \left(\int_{V^e} \rho\, \mathbf{N}^{e\mathrm{T}} \mathbf{N}^e \mathrm{d}\upsilon\, \ddot{\mathbf{w}}^e - 2V \int_{V^e} \rho\, \mathbf{N}^{e\mathrm{T}} \frac{\partial \mathbf{N}^e}{\partial x_1} \mathrm{d}\upsilon\, \dot{\mathbf{w}}^e \right. \\ \left. - V^2 \int_{V^e} \rho\, \frac{\partial \mathbf{N}^{e\mathrm{T}}}{\partial x_1} \frac{\partial \mathbf{N}^e}{\partial x_1} \mathrm{d}\upsilon\, \mathbf{w}^e \right). \tag{5.44}$$

The stiffness matrix $\mathbf{K}^e$ is the standard one in the FE method since the potential energy associated with the elastic deflection does not distinguish between the Eulerian and the Lagrangian coordinates. Consequently, the global equation of motion is

$$\mathbf{M}^e\, \ddot{\mathbf{w}} - 2V\, \mathbf{C}^e\, \dot{\mathbf{w}} + \left(\mathbf{K}^e - V^2 \mathbf{A}^e \right) \mathbf{w} = \mathbf{F}_c^e + \mathbf{F}_{sup}^e, \tag{5.45}$$

where:

$$\mathbf{M}^e = \int_{V^e} \rho\, \mathbf{N}^{e\mathrm{T}} \mathbf{N}^e\, \mathrm{d}\upsilon, \tag{5.46}$$

$$\mathbf{C}^e = \int_{V^e} \rho\, \mathbf{N}^{e\mathrm{T}} \frac{\partial \mathbf{N}^e}{\partial x_1} \mathrm{d}\upsilon, \tag{5.47}$$

$$\mathbf{A}^e = \int_{V^e} \rho\, \frac{\partial \mathbf{N}^{e\mathrm{T}}}{\partial x_1} \frac{\partial \mathbf{N}^e}{\partial x_1} \mathrm{d}\upsilon. \tag{5.48}$$

Matrix $\mathbf{C}^e$ is associated with the inertial force due to the convective velocity, $\mathbf{A}^e$ is related to the convective acceleration, $\mathbf{F}_c^e$ and $\mathbf{F}_{sup}^e$ are the force vectors that contain respectively the contact normal and tangential forces from the wheel/rail interaction applied in the head of the rail in its middle longitudinal position and the rail pad forces. Nodal coordinates are implemented in a global displacement vector $\mathbf{w}$, obtaining the global matrices $\mathbf{M}$, $\mathbf{C}$, $\mathbf{A}$, $\mathbf{K}$ and the global vectors $\mathbf{F}_c$ and $\mathbf{F}_{sup}$.

5.4.2.2 Based on the Lagrange equation

From the FE interpolation already adopted, see Eq. (5.43), the second option develops the Lagrange equation for each finite element considering a convective derivative since an Eulerian approach is adopted:

$$\frac{\mathrm{D}}{\mathrm{D}t}\left(\frac{\partial L^e}{\partial \dot{\mathbf{w}}^e}\right)-\frac{\partial L^e}{\partial \mathbf{w}^e}=\mathbf{F}_c^e+\mathbf{F}_{sup}^e, \tag{5.49}$$

where the Lagrangian for the e-th element is defined through its kinetic and potential energies, $L^e = E_K^e - E_V^e$. Replacing in the previous equation:

$$\frac{\mathrm{D}}{\mathrm{D}t}\left(\frac{\partial E_K^e}{\partial \dot{\mathbf{w}}^e}\right)-\frac{\partial E_K^e}{\partial \mathbf{w}^e}+\frac{\partial E_V^e}{\partial \mathbf{w}^e}=\mathbf{F}_c^e+\mathbf{F}_{sup}^e. \tag{5.50}$$

Now, both kinematic and potential energies for the e-th element are developed through the convective derivative from Eq. (5.38):

$$\begin{aligned}E_K^e &=\frac{1}{2}\int_V \rho\,\frac{\mathrm{D}\mathbf{r}^{\mathrm{T}}}{\mathrm{D}t}\frac{\mathrm{D}\mathbf{r}}{\mathrm{D}t}\,\mathrm{d}\upsilon=\frac{1}{2}\rho\left(\dot{\mathbf{w}}^{e^{\mathrm{T}}}\int_{V^e}\mathbf{N}^{e^{\mathrm{T}}}\mathbf{N}^e\mathrm{d}\upsilon\,\dot{\mathbf{w}}^e+V^2+V^{2e^{\mathrm{T}}}\int_{V^e}\frac{\partial \mathbf{N}^{e^{\mathrm{T}}}}{\partial x_1}\frac{\partial \mathbf{N}^e}{\partial x_1}\mathrm{d}\upsilon\,\mathbf{w}^e\right.\\ &\left.-2V(1,0,0)\int_{V^e}\mathbf{N}^e\mathrm{d}\upsilon\,\mathbf{w}^e-2V\,\dot{\mathbf{w}}^{e^{\mathrm{T}}}\int_{V^e}\mathbf{N}^{e^{\mathrm{T}}}\frac{\partial \mathbf{N}^e}{\partial x_1}\mathrm{d}\upsilon\,\mathbf{w}^e+2V^2(1,0,0)\int_{V^e}\frac{\partial \mathbf{N}^e}{\partial x_1}\mathrm{d}\upsilon\,\mathbf{w}^e\right),\end{aligned} \tag{5.51}$$

$$E_V^e=\frac{1}{2}\int_V k\,(\mathbf{r}(\mathbf{x},t)-\mathbf{x})^2\,\mathrm{d}\upsilon=\frac{1}{2}\int_V k\,\mathbf{w}(\mathbf{x},t)^{\mathrm{T}}\mathbf{w}(\mathbf{x},t)\mathrm{d}\upsilon=\frac{1}{2}\mathbf{w}^{e\mathrm{T}}\int_{V^e}k\,\mathbf{N}^{e^{\mathrm{T}}}\mathbf{N}^e\,\mathrm{d}\upsilon\,\mathbf{w}^e. \tag{5.52}$$

The $\frac{\partial E_K^e}{\partial \dot{\mathbf{w}}^e}$ term is now deduced:

$$\frac{\partial E_K^e}{\partial \dot{\mathbf{w}}^e}=\rho\left(\int_{V^e}\mathbf{N}^{e^{\mathrm{T}}}\mathbf{N}^e\,\mathrm{d}\upsilon\,\dot{\mathbf{w}}^e-V\int_{V^e}\mathbf{N}^{e\mathrm{T}}\frac{\partial \mathbf{N}^e}{\partial x_1}\mathrm{d}\upsilon\,\mathbf{w}^e\right), \tag{5.53}$$

and the convective derivative of the previous term is computed:

$$
\begin{aligned}
&\frac{\mathrm{D}}{\mathrm{D}t}\left(\frac{\partial E_K^e}{\partial \dot{\mathbf{w}}^e}\right)=\frac{\partial}{\partial t}\left(\frac{\partial E_K^e}{\partial \dot{\mathbf{w}}^e}\right)-V\frac{\partial}{\partial x_1}\left(\frac{\partial E_K^e}{\partial \dot{\mathbf{w}}^e}\right)=\\
&\rho\left[\int_{V^e}{\mathbf{N}^e}^{\mathrm{T}}\mathbf{N}^e\,\mathrm{d}\upsilon\,\ddot{\mathbf{w}}^e+V\int_{V^e}{\mathbf{N}^e}^{\mathrm{T}}\frac{\partial \mathbf{N}^e}{\partial x_1}\mathrm{d}\upsilon\,\dot{\mathbf{w}}^e-V\left(\int_{V^e}\frac{\partial {\mathbf{N}^e}^{\mathrm{T}}}{\partial x_1}\mathbf{N}^e\,\mathrm{d}\upsilon+\int_{V^e}{\mathbf{N}^e}^{\mathrm{T}}\frac{\partial \mathbf{N}^e}{\partial x_1}\mathrm{d}\upsilon\right)\dot{\mathbf{w}}^e\right.\\
&\left.+V^2(1,0,0)\int_{V^e}\frac{\partial \mathbf{N}^e}{\partial x_1}\mathrm{d}\upsilon+V^2\left(\int_{V^e}\frac{\partial {\mathbf{N}^e}^{\mathrm{T}}}{\partial x_1}\frac{\partial \mathbf{N}^e}{\partial x_1}\mathrm{d}\upsilon+\int_{V^e}{\mathbf{N}^e}^{\mathrm{T}}\frac{\partial^2 \mathbf{N}^e}{\partial x_1^2}\mathrm{d}\upsilon\right)\mathbf{w}^e\right].
\end{aligned}
\tag{5.54}
$$

As seen in Eq. (5.51), the kinematic energy is in this case coupled with the displacements, so the $\frac{\partial E_K^e}{\partial \mathbf{w}^e}$ term from the Lagrange equation Eq. (5.50) is not zero.

$$
\frac{\partial E_K^e}{\partial \mathbf{w}^e}=\rho\left(-V\int_{V^e}{\mathbf{N}^e}^{\mathrm{T}}\frac{\partial \mathbf{N}^e}{\partial x_1}\mathrm{d}\upsilon\,\dot{\mathbf{w}}^e+V^2(1,0,0)\int_{V^e}\frac{\partial \mathbf{N}^e}{\partial x_1}\mathrm{d}\upsilon+V^2\int_{V^e}\frac{\partial {\mathbf{N}^e}^{\mathrm{T}}}{\partial x_1}\frac{\partial \mathbf{N}^e}{\partial x_1}\mathrm{d}\upsilon\,\mathbf{w}^e\right). \tag{5.55}
$$

Finally, the $\frac{\partial E_V^e}{\partial \mathbf{w}^e}$ term gives the FE standard stiffness:

$$
\frac{\partial E_V^e}{\partial \mathbf{w}^e}=\mathbf{K}^e. \tag{5.56}
$$

Replacing Eqs. (5.54)–(5.56) in the left member of Eq. (5.50),

$$
\begin{aligned}
&\frac{\mathrm{D}}{\mathrm{D}t}\left(\frac{\partial E_K^e}{\partial \dot{\mathbf{w}}^e}\right)-\frac{\partial E_K^e}{\partial \mathbf{w}^e}+\frac{\partial E_V^e}{\partial \mathbf{w}^e}=\\
&\rho\int_{V^e}{\mathbf{N}^e}^{\mathrm{T}}\mathbf{N}^e\,\mathrm{d}\upsilon\,\ddot{\mathbf{w}}^e-2\rho V\int_{V^e}{\mathbf{N}^e}^{\mathrm{T}}\frac{\partial \mathbf{N}^e}{\partial x_1}\mathrm{d}\upsilon\,\dot{\mathbf{w}}^e+\rho V^2\int_{V^e}{\mathbf{N}^e}^{\mathrm{T}}\frac{\partial^2 \mathbf{N}^e}{\partial x_1^2}\mathrm{d}\upsilon\,\mathbf{w}^e+\mathbf{K}^e\\
&=\mathbf{M}^e\,\ddot{\mathbf{w}}^e-2V\,\mathbf{C}^e\,\dot{\mathbf{w}}^e+\left(\mathbf{K}^e-V^2\mathbf{A}^e\right)\mathbf{w}^e,
\end{aligned}
\tag{5.57}
$$

which results the same formulation obtained in Eq. (5.45), once replaced the second-order derivative integral term by first-order derivative one from Eq. (5.41) to guarantee the convergence of the solution. It confirms the robustness of the formulation developed for the extension of the ME method to a 3D model.

5.4.3 Rail support models

The rail support is the basis on which the rail rests. Three options has been contemplated and implemented in the dynamic interaction model presented in this thesis: discrete rail supports (sleepers), an elastic layer and a Winkler bedding. The interaction between the rail and the bedplate has been implemented through a substructuring technique in the time domain. This technique separates the track system in both elements, with their own reference systems, and they are analysed independently using their corresponding theoretical models that allow defining the equations of motion. Both substructures interrelate through external forces corresponding to the forces transmitted to the bedplate, calculated from the relative displacements and velocities between both subsystems, see Section 5.6.

The first option is to include sleepers as discrete rail supports introduced in the form of lumped parameter systems, see Fig. 5.10. The rail pads are modelled as lumped viscoelastic elements generating the interaction forces between the rails and the sleepers, represented as lumped masses. Ballast dynamics is neglected here, being not relevant for the dynamic behaviour of the wheelset, but the equivalent ballast stiffness and damping are accounted for by means of lumped spring and dashpot elements connected to the sleepers.

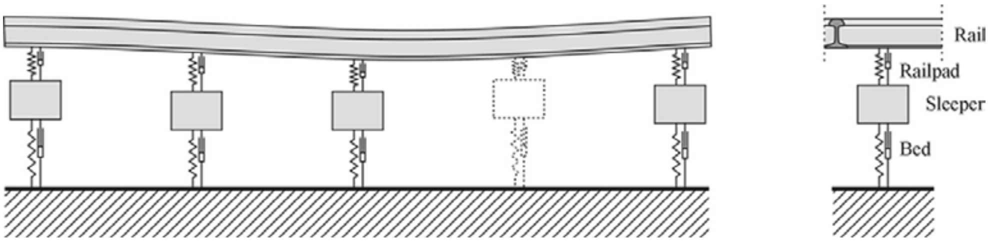

Fig. 5.10. Details of the track model. Left: sleeper bays. Right: sleeper and rail pad.

The second option is to consider continuously supported rails. This option has been implemented to represent the continuously supported rail of type BV50 used in Section 6.3, which is a common Swedish rail type. The model incorporates a viscoelastic pad layer under the rail, so that a uniformly meshed layer is located under the meshed BV50 profile and both are then extruded to generate a 3D meshed structure. This layer is directly connected node-to-node with the rail profile mesh, but their material properties are different.

The third option is the Winkler bedding, which consists of a uniform discrete viscoelastic layer implemented through independent discrete springs and dampers under each node of the underside rail surface, connecting it to the ground. It is a commonly used simplification to represent the dynamics of (a) discrete supports (sleepers) and (b) continuous support.

For discrete supports, an averaged vertical stiffness per squared metre is calculated from the stiffness of the ballast of the sleepers k_{3_b}. This stiffness is distributed uniformly node per node. Considering n_{sl} sleepers of width b under a finite rail of length L,

$$\bar{k}_{3_b} = \frac{n_{sl} k_{3_b}}{A} = \frac{n_{sl} k_{3_b}}{bL}. \tag{5.58}$$

Adding the contribution element by element, local corner nodes receive the half contribution since these are connected to other corner node of the adjacent element. The uniform vertical damping is estimated in the same way. Finally, the small longitudinal and lateral contributions are also included in order to stabilise the model on the tangential plane. They are estimated as $\bar{k}_{1,2_b} = \bar{k}_{3_b} / 100$.

For continuously supported rails, the equivalent contribution is estimated through the constitutive equations for plaques, assuming thickness is much lower than width of the plaque ($h_p << b$). The vertical stresses are calculated from

$$\sigma_{33}(x_1, x_2) = \frac{E_p}{1+\nu_p} \varepsilon_{33}(x_1, x_2), \tag{5.59}$$

where E_p and ν_p are the Young's modulus and the Poisson's ratio of the material of the continuous support, respectively. From the vertical displacement w_3, the relative displacement ε_{33} is defined as

$$\varepsilon_{33}(x_1, x_2) = \frac{w_3(x_1, x_2)}{h_p}. \tag{5.60}$$

Integrating the vertical stresses, the vertical force on the underside surface results

$$F_{3_p} = \int_S \sigma_{33}(x_1, x_2)\,\mathrm{d}x_1 \mathrm{d}x_2 = \frac{E_p / h_p}{1+\nu_p} \int_S w_3(x_1, x_2)\,\mathrm{d}x_1 \mathrm{d}x_2. \tag{5.61}$$

The corresponding vertical force for a Winkler bedding would be defined by a uniform equivalent stiffness throughout the surface:

$$F_{3_p} = \int_S k_{3_p}\left(x_1, x_2\right) w_3\left(x_1, x_2\right) \mathrm{d}x_1 \mathrm{d}x_2 = \bar{k}_{3_p} \int_S w_3\left(x_1, x_2\right) \mathrm{d}x_1 \mathrm{d}x_2. \tag{5.62}$$

From Eqs. (5.61) and (5.62), this equivalent stiffness results

$$\bar{k}_{3_p} = \frac{E_p / h_p}{1 + \nu_p}. \tag{5.63}$$

Now, it is deduced the convective terms of the equation of motion associated with the Winkler bedding adopted based on the associated virtual work. The corresponding Lagrange equation is now

$$\frac{\mathrm{D}}{\mathrm{D}t}\left(\frac{\partial L_{wink}^e}{\partial \dot{\mathbf{w}}^e}\right) - \frac{\partial L_{wink}^e}{\partial \mathbf{w}^e} = \mathbf{F}_c^e + \mathbf{F}_{sup}^e, \tag{5.64}$$

where both $L_{wink}^e = E_K^e - \left(E_V^e + E_{V,wink}^e\right)$, resulting

$$\frac{\mathrm{D}}{\mathrm{D}t}\left(\frac{\partial E_K^e}{\partial \dot{\mathbf{w}}^e}\right) - \frac{\partial E_K^e}{\partial \mathbf{w}^e} + \left(\frac{\partial E_V^e}{\partial \mathbf{w}^e} + \frac{\partial E_{V,wink}^e}{\partial \mathbf{w}^e}\right) = \mathbf{F}_c^e + \mathbf{F}_{sup}^e. \tag{5.65}$$

The potential energy associated with the Winkler bedding is

$$E_{V,wink}^e = \frac{1}{2} \mathbf{w}^{e^{\mathrm{T}}} \int_{S^e} \mathbf{N}^{e^{\mathrm{T}}} \overline{\mathbf{K}}_{wink}\, \mathbf{N}^e \,\mathrm{d}S\, \mathbf{w}^e, \tag{5.66}$$

where $\overline{\mathbf{K}}_{wink}$ is a 3×3 matrix which includes the longitudinal, lateral and vertical equivalent stiffness estimated above. The $\frac{\partial E_{V,w}^e}{\partial \mathbf{w}^e}$ term is computed:

$$\frac{\partial E_{V,w}^e}{\partial \mathbf{w}^e} = \int_{S^e} \mathbf{N}^{e^{\mathrm{T}}} \overline{\mathbf{K}}_{wink}\, \mathbf{N}^e \,\mathrm{d}S\, \mathbf{w}^e, \tag{5.67}$$

Developing again the total derivative,

$$\frac{\mathrm{D}\mathbf{w}}{\mathrm{D}t} \equiv \frac{\mathrm{D}\mathbf{w}(\mathbf{u}, t)}{\mathrm{D}t} = \dot{\mathbf{w}}(\mathbf{u}, t) - V \frac{\partial \mathbf{w}(\mathbf{u}, t)}{\partial x_1}, \tag{5.68}$$

the generalised force associated with the Winkler damping is:

$$\begin{aligned}\delta W^{e}_{c,wink} &= -\int_{S^e} \delta \mathbf{w}^{e\,\mathrm{T}} c \frac{\mathrm{D}\mathbf{w}^{e}}{\mathrm{D}t} \mathrm{d}S = \\ &-\int_{S^e} \delta \mathbf{w}^{e\,\mathrm{T}} \mathbf{N}^{e\,\mathrm{T}}\, \overline{\mathbf{C}}_{wink}\, \mathbf{N}^{e}\, \mathrm{d}S\, \dot{\mathbf{w}}^{e} + V \int_{S^e} \delta \mathbf{w}^{e\,\mathrm{T}} \mathbf{N}^{e\,\mathrm{T}}\, \overline{\mathbf{C}}_{wink} \frac{\partial \mathbf{N}^{e}}{\partial x_1} \mathrm{d}S\, \mathbf{w}^{e},\end{aligned} \tag{5.69}$$

where $\overline{\mathbf{C}}_{wink}$ is a 3×3 matrix with equivalent damping estimated. Since $\delta W^{e}_{c,wink} = \delta \mathbf{w}^{e\,\mathrm{T}} \mathbf{Q}^{e}_{c,wink}$, the damping term is deduced:

$$\mathbf{Q}^{e}_{c,wink} = -\int_{S^e} \mathbf{N}^{e\,\mathrm{T}}\, \overline{\mathbf{C}}_{wink}\, \mathbf{N}^{e}\, \mathrm{d}S\, \dot{\mathbf{w}}^{e} + V \int_{S^e} \mathbf{N}^{e\,\mathrm{T}}\, \overline{\mathbf{C}}_{wink} \frac{\partial \mathbf{N}^{e}}{\partial x_1} \mathrm{d}S\, \mathbf{w}^{e}. \tag{5.70}$$

Therefore, the total equation of motion for Winkler bedding includes three new terms respect to Eq. (5.45):

$$\mathbf{M}\,\ddot{\mathbf{w}} + \left(-2V\,\mathbf{C} + \mathbf{C}_{wink}\right)\dot{\mathbf{w}} + \left(\mathbf{K} - V^{2}\mathbf{A} + \mathbf{K}_{wink} + V\left(\mathbf{K}_{\mathbf{C}}\right)_{wink}\right)\mathbf{w} = \mathbf{F}_{c}\,, \tag{5.71}$$

where the element matrices are:

$$\mathbf{C}^{e}_{wink} = \int_{S^e} \mathbf{N}^{e\,\mathrm{T}}\, \overline{\mathbf{C}}_{wink}\, \mathbf{N}^{e}\, \mathrm{d}S, \quad \tilde{\mathbf{C}}_{wink} = \mathbf{\Phi}^{r\,\mathrm{T}} \left(\sum_{e=1}^{n_r} \mathbf{C}^{e}_{wink} \right) \mathbf{\Phi}^{r}, \tag{5.72}$$

$$\mathbf{K}^{e}_{wink} = \int_{S^e} \mathbf{N}^{e\,\mathrm{T}}\, \overline{\mathbf{K}}_{wink}\, \mathbf{N}^{e}\, \mathrm{d}S, \quad \tilde{\mathbf{K}}_{wink} = \mathbf{\Phi}^{r\,\mathrm{T}} \left(\sum_{e=1}^{n_r} \mathbf{K}^{e}_{wink} \right) \mathbf{\Phi}^{r}, \tag{5.73}$$

$$\left(\mathbf{K}_{\mathbf{C}}\right)^{e}_{wink} = \int_{S^e} \mathbf{N}^{e\,\mathrm{T}}\, \overline{\mathbf{C}}_{wink} \frac{\partial \mathbf{N}^{e}}{\partial x_1} \mathrm{d}S, \quad \left(\tilde{\mathbf{K}}_{\mathbf{C}}\right)_{wink} = \mathbf{\Phi}^{r\,\mathrm{T}} \left(\sum_{e=1}^{n_r} \left(\mathbf{K}_{\mathbf{C}}\right)^{e}_{wink} \right) \mathbf{\Phi}^{r}. \tag{5.74}$$

5.4.4 Pseudo-static deformation of the track based on MEM

The effect of the vehicle speed on the 3D MEM has been evaluated for the pseudo-static deformation of the rail supported on a viscoelastic Winkler bedding with a stiffness per unit length of 10^7 N/m^2 and a damping per unit length of 4900 Ns/m^2 [167]. The ‘pseudo’ prefix is added because it cannot be considered a static case since there is a load moving along the rail. For the Eulerian approach taken, the load is fixed in a spatial point while its corresponding speed is introduced in the formulation. For this purpose, the centreline of the rail has been selected to represent the deformation. Fig. 5.11(a) shows a negligible influence for the Winkler foundation used, in agreement with Thompson [7]. The pseudo-static deformation for 150 km/h has been compared to the results given by the 1D MEM detailed in Section 5.4.1, which has been implemented for this purpose. Fig. 5.11(b) shows a good agreement between both models, with a discrepancy of 3% at the contact point.

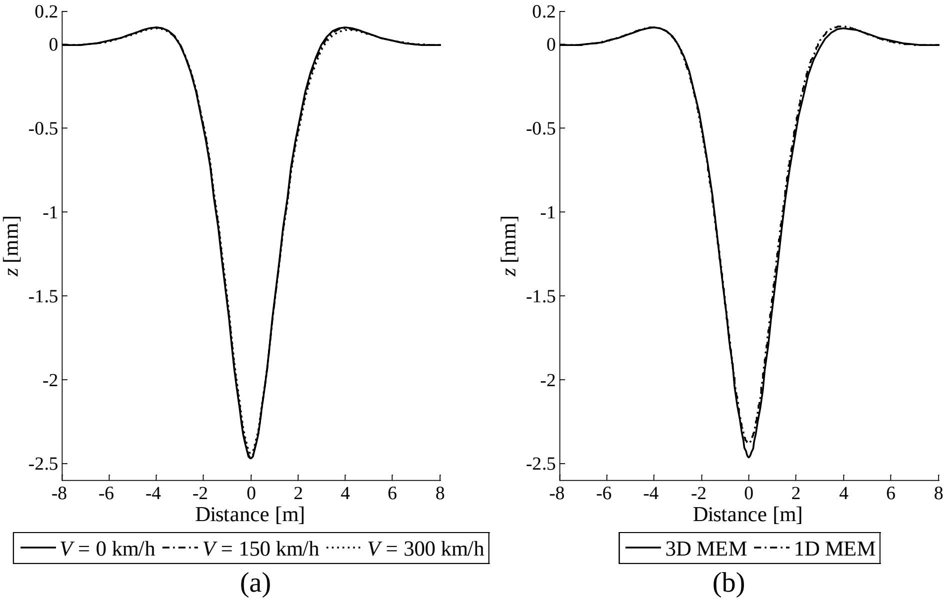

(a) (b)

Fig. 5.11. Pseudo-static deformation of the finitely long rail supported on a viscoelastic foundation: (a) different moving load speeds; (b) different ME models for $V = 150$ km/h.

5.5 METHOD FOR THE TIME SOLUTION OF THE TRAIN/TRACK INTERACTION

As explained in Section 1.2, one of the main objectives of the present thesis is to develop different numerical techniques to enhance the computational efficiency of the railway interaction model. The substructuring strategy employed in this work permits to introduce the coupling between the different elastic substructures of the global system through external forces calculated from the corresponding displacements and velocities. This requires small time steps to ensure the convergence of the solution. MATLAB offers *ode* functions as efficient routines for solving ordinary differential equations, but the dimension of the FE problem (it can be close to a million of degrees of freedom) makes their use unfeasible. Hence, modal techniques are usually adopted to reduce significantly the dimension of the problem while losing as little information as possible.

The present work adopts a modal transformation and develops a static modal correction to compensate the gain displacement due to this transformation. Additionally, an innovative decoupling technique is proposed to simplify the solving procedure and reduce the time consumption.

5.5.1 Modal approach for reducing the dimension of the problem

It is assumed a rail discretely supported by sleepers, so the modal approach is implemented on Eq. (5.45). The global displacement vector of the rail can be expressed through superposition of mode shapes:

$$\mathbf{w}^r(\mathbf{u},t) = \mathbf{\Phi}^r(\mathbf{u})\,\mathbf{q}^r(t), \tag{5.75}$$

where $\mathbf{\Phi}^r \equiv \mathbf{\Phi}^r(\mathbf{u})$ is the mode shape function matrix of the cyclic boundary rail and $\mathbf{q}^r(t)$ is the modal coordinate vector. Matrix $\mathbf{\Phi}^r$ is built solving the eigenproblem from the global standard matrices $\mathbf{M}$ and $\mathbf{K}$, truncating in m number of modes and normalising with respect to the mass matrix in order to make the system more efficient. Since the matrices of the equation of motion are symmetric, $\mathbf{\Phi}^r$ is orthonormal ($\mathbf{\Phi}^{r^{-1}} = \mathbf{\Phi}^{r^{\mathrm{T}}}$).

The small rigid body displacements of the solid are considered through the rigid body modes of the rail. It must be pointed out that the mode shape functions do not depend on time since the ‘flow’ of the mesh through the material coordinates does not change the mode shape functions in spatial coordinates, because the cross-sectional area remains invariable after the extrusion of the profile.

Once the modal transform of Eq. (5.75) is applied in Eq. (5.45), the resulting equation is pre-multiplied by $\mathbf{\Phi}^{r\mathrm{T}}$. The modal equation of motion results as

$$\ddot{\mathbf{q}}^r - 2V\tilde{\mathbf{C}}\dot{\mathbf{q}}^r + \left(\tilde{\mathbf{K}} - V^2\tilde{\mathbf{A}}\right)\mathbf{q}^r = \mathbf{\Phi}^{r\mathrm{T}}\mathbf{F}, \tag{5.76}$$

where the modal matrices are calculated from the global matrices as follows:

$$\tilde{\mathbf{K}} = \mathbf{\Phi}^{r\mathrm{T}}\mathbf{K}\mathbf{\Phi}^r = \begin{pmatrix} \omega_r^2 & 0 \\ 0 & \ddots \end{pmatrix}, \tag{5.77}$$

$$\tilde{\mathbf{C}} = \mathbf{\Phi}^{r\mathrm{T}}\mathbf{C}\mathbf{\Phi}^r, \tag{5.78}$$

$$\tilde{\mathbf{A}} = \mathbf{\Phi}^{r\mathrm{T}}\mathbf{A}\mathbf{\Phi}^r, \tag{5.79}$$

ω_r being the undamped natural frequencies. Since matrix $\mathbf{\Phi}^r$ is orthonormal, it diagonalises $\tilde{\mathbf{K}}$, while $\tilde{\mathbf{C}}$ and $\tilde{\mathbf{A}}$ are not diagonalised, thus the equation of motion is not decoupled. As recommended in the literature [7], a standard damping loss factor of $\zeta = 0.01$ is introduced in the rail. Therefore, a new modal damping matrix is included in the modal equation of motion as a diagonal matrix:

$$\tilde{\mathbf{C}}_\zeta = \begin{pmatrix} c_{rr} & 0 \\ 0 & \ddots \end{pmatrix} = 2\zeta\begin{pmatrix} \omega_r & 0 \\ 0 & \ddots \end{pmatrix}. \tag{5.80}$$

Hence, the modal equation of motion is

$$\ddot{\mathbf{q}}^r + \left(\tilde{\mathbf{C}}_\zeta - 2V\tilde{\mathbf{C}}\right)\dot{\mathbf{q}}^r + \left(\tilde{\mathbf{K}} - V^2\tilde{\mathbf{A}}\right)\mathbf{q}^r = \mathbf{\Phi}^{r\mathrm{T}}\mathbf{F}. \tag{5.81}$$

The methodology adopted for the calculation of the interaction forces $\mathbf{F}$ will be explained in Section 5.6. Eq. (5.81) is a linear second-order differential equation system and then the matrices are calculated only once at the beginning of the simulation. Now, the previous equation of motion is cast into first-order (state-space) form by adopting a new variable $\mathbf{Q}^r$ as vector of length $2N^r$ (N^r is the number of degrees of freedom of the rail mesh):

$$\mathbf{Q}^r = \begin{Bmatrix} \mathbf{q}^r \\ \dot{\mathbf{q}}^r \end{Bmatrix}, \tag{5.82}$$

and Eq. (5.81) results in a linear first-order differential equation system

$$\tilde{\mathbf{A}}\dot{\mathbf{Q}}^r + \tilde{\mathbf{B}}\mathbf{Q}^r = \tilde{\mathbf{F}}, \tag{5.83}$$

where:

$$\tilde{\mathbf{A}} = \begin{pmatrix} \tilde{\mathbf{C}}_\zeta - 2V\,\tilde{\mathbf{C}} & \mathbf{I} \\ \mathbf{I} & \mathbf{0} \end{pmatrix}, \tag{5.84}$$

$$\tilde{\mathbf{B}} = \begin{pmatrix} \tilde{\mathbf{K}} - V^2\tilde{\mathbf{A}} & \mathbf{0} \\ \mathbf{0} & -\mathbf{I} \end{pmatrix}, \tag{5.85}$$

$$\tilde{\mathbf{F}} \equiv \tilde{\mathbf{F}}(t) = \begin{Bmatrix} \mathbf{\Phi}^{r\,\mathrm{T}}\mathbf{F}(t) \\ \mathbf{0} \end{Bmatrix}. \tag{5.86}$$

Eq. (5.83) is pre-multiplied by the diagonal matrix $\tilde{\mathbf{A}}^{-1}$ to make the system more efficient:

$$\dot{\mathbf{Q}}^r + \left(\tilde{\mathbf{A}}^{-1}\tilde{\mathbf{B}}\right)\mathbf{Q}^r = \tilde{\mathbf{A}}^{-1}\tilde{\mathbf{F}}. \tag{5.87}$$

Note that $\tilde{\mathbf{A}}^{-1}\tilde{\mathbf{B}}$ is

$$\tilde{\mathbf{A}}^{-1}\tilde{\mathbf{B}} = \begin{pmatrix} \mathbf{0} & -\mathbf{I} \\ \tilde{\mathbf{K}} - V^2\tilde{\mathbf{A}} & \tilde{\mathbf{C}}_\zeta - 2V\,\tilde{\mathbf{C}} \end{pmatrix}. \tag{5.88}$$

5.5.2 Static modal correction

This section presents the formulation of a technique that corrects the static gain displacement of the solution from the modal approach. This estimates the deviations in the static solution between the non-reduced procedure and the modal transformation. From Eq. (5.85), the modal matrix $\tilde{\mathbf{B}}$ can be written as:

$$\tilde{\mathbf{B}} = \begin{pmatrix} \tilde{\mathbf{K}} - V^2\tilde{\mathbf{A}} & \mathbf{0} \\ \mathbf{0} & -\mathbf{I} \end{pmatrix} = \begin{pmatrix} \begin{pmatrix} \omega_r^2 & 0 \\ 0 & \ddots \end{pmatrix} - V^2\mathbf{\Phi}^{r\,\mathrm{T}}\mathbf{A}\mathbf{\Phi}^r & \mathbf{0} \\ \mathbf{0} & -\mathbf{I} \end{pmatrix}. \tag{5.89}$$

Now, $\tilde{\mathbf{B}}$ is expressed in physical coordinates through an inverse modal transformation as follows

$$\mathbf{B}^{\mathrm{m}} = \mathbf{\Phi}^{r}\left(\mathbf{M}\tilde{\mathbf{B}}\right)\mathbf{\Phi}^{r\mathrm{T}} = \begin{pmatrix} \mathbf{K}_{eq}^{\mathrm{m}} & \mathbf{0} \\ \mathbf{0} & -\mathbf{M}^{\mathrm{m}} \end{pmatrix}; \tag{5.90}$$

hence, the equivalent physical stiffness matrix computed from the modal transformation corresponds to the first N^{r} rows and columns of the $\mathbf{B}^{\mathrm{m}}$ matrix:

$$\mathbf{K}_{eq}^{\mathrm{m}} = \left(\mathbf{B}^{\mathrm{m}}\right)_{1:N^{r},1:N^{r}}. \tag{5.91}$$

Therefore, the solving methodology based on the modal approach gives an approximated stiffness matrix $\mathbf{K}_{eq}^{\mathrm{m}}$, introducing a small but non-negligible deviation respect to the original stiffness matrix $\mathbf{K}_{eq} = \mathbf{K} - V^{2}\mathbf{A}$ from the formulation deduced in Eq. (5.45). This deviation is the responsible for the static error introduced by the modal approach in the solution. The static response is computed as

$$\mathbf{w}_{st}^{\mathrm{modal}} = \left(\mathbf{K}_{\mathrm{T}}^{\mathrm{m}}\right)^{-1}\mathbf{F}, \tag{5.92}$$

while the static response from the original stiffness matrix is

$$\mathbf{w}_{st}^{\mathrm{physic}} = \left(\mathbf{K} - V^{2}\mathbf{A}\right)^{-1}\mathbf{F}. \tag{5.93}$$

The static modal correction, ϑ, is simply estimated as the difference between both approaches:

$$\vartheta = \mathbf{w}_{st}^{\mathrm{physic}} - \mathbf{w}_{st}^{\mathrm{modal}} = \left[\left(\mathbf{K} - V^{2}\mathbf{A}\right)^{-1} - \left(\mathbf{K}_{\mathrm{T}}^{\mathrm{m}}\right)^{-1}\right]\mathbf{F}. \tag{5.94}$$

Hence, this deviation can be easily corrected by adding this static deviation in the computed solution from the modal technique:

$$\mathbf{w}^{\mathrm{corr}} = \mathbf{w}^{\mathrm{modal}} + \vartheta. \tag{5.95}$$

Fig. 5.12 shows how this static modal correction works satisfactorily for a 1D ME model for UIC60 rail of 100 m of length supported by a Winkler bedding and subjected to a vertical constant moving force of 60 kN applied in the contact point of the rail (no wheel/rail interaction is considered in this example). The 1D mesh is longitudinally uniform and it consists of 5000 nodes. The black line has been simulated by solving the corresponding equation of motion for physic coordinates. The light-grey line shows the solution solving the modal equation of motion using 50 vibration modes. The deviation in the steady-state response reached for both simulations is compensated by the ϑ term, which adjusts the modal solution to the physic one (dark-grey line).

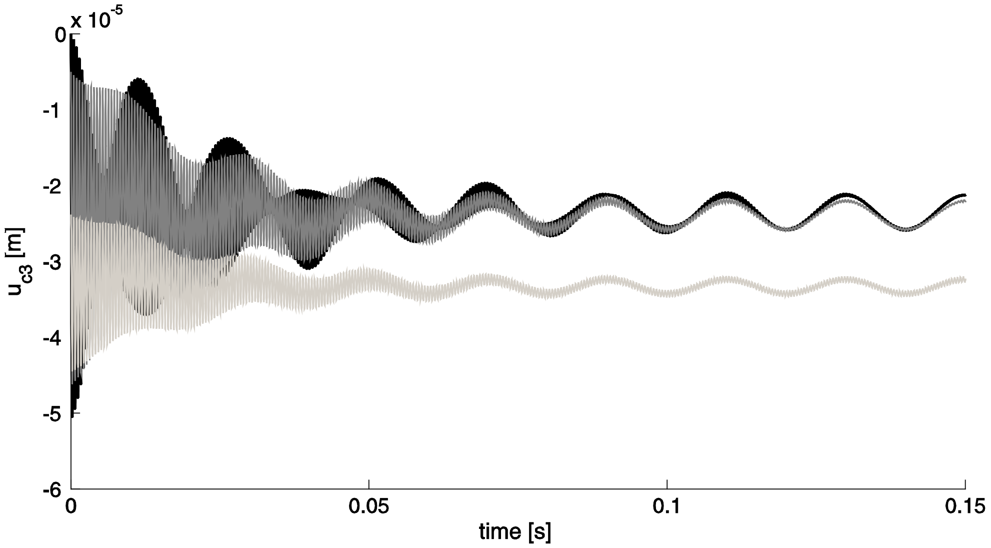

Fig. 5.12. Vertical displacement of the central node on the upper side of the rail. ▬▬ : result from physic coordinates (10^4 dof); ▬▬ : from modal coordinates (50 modes); ▬▬ : from modal coordinates and corrected by ϑ.

5.5.3 Method for decoupling the system after a modal approach

Solving the eigenproblem from the matrix $\tilde{\mathbf{A}}^{-1}\tilde{\mathbf{B}}$ without truncation, it is obtained m conjugated pairs of eigenvectors $\{\xi\}_r$ and eigenvalues λ_r. The eigenmatrix results $\boldsymbol{\Xi} = \left(\{\xi\}_r \quad \{\xi\}_r^* \quad ...\right)$ and the eigenvalues diagonal matrix, $\boldsymbol{\lambda} = \mathrm{diag}\left(\lambda_r \quad \lambda_r^* \quad ...\right)$. From the definition of the eigenvectors calculated:

$$\boldsymbol{\Xi}^{-1}\left(\tilde{\mathbf{A}}^{-1}\tilde{\mathbf{B}}\right)\boldsymbol{\Xi} = \boldsymbol{\lambda}. \tag{5.96}$$

A new transformation is adopted at this point, so that the modal vector $\mathbf{Q}$ can be expressed through:

$$\mathbf{Q} = \boldsymbol{\Xi}\mathbf{s}. \tag{5.97}$$

Replacing Eq. (5.97) in Eq. (5.87), pre-multiplying by $\boldsymbol{\Xi}^{-1}$ and considering the relationship expressed in Eq. (5.96), the linear first-order coupled equation system becomes in a decoupled equation system due to $\boldsymbol{\lambda}$ is a diagonal system:

$$\dot{\mathbf{s}} + \boldsymbol{\lambda}\,\mathbf{s} = \tilde{\mathbf{G}}, \tag{5.98}$$

where

$$\tilde{\mathbf{G}} = \boldsymbol{\Xi}^{-1}\tilde{\mathbf{A}}^{-1}\tilde{\mathbf{F}}. \tag{5.99}$$

The unknowns of Eq. (5.98) can be separated in $2m$ independent equations, simplifying hugely the solving procedure:

$$\left.\begin{aligned} \dot{s}_r + \lambda_r s_r &= \tilde{G}_r \\ \dot{s}_r + \lambda_r^* s_r &= \tilde{G}_r^* \end{aligned}\right\}, \quad r = 1,...m. \tag{5.100}$$

At this point, the computational cost can be halved by removing the conjugated pairs of $\boldsymbol{\Xi} = \left(\{\xi\}_r \quad \{\xi\}_r^* \quad ...\right)$ and $\boldsymbol{\lambda} = \mathrm{diag}\left(\lambda_r \quad \lambda_r^* \quad ...\right)$:

$$\boldsymbol{\Theta} = \left(\{\xi\}_1 \quad ... \quad \{\xi\}_m\right), \tag{5.101}$$

$$\boldsymbol{\Gamma} = \mathrm{diag}\left(\lambda_1 \quad ... \quad \lambda_m\right). \tag{5.102}$$

Hence, instead of the transformation expressed in Eq. (5.97), an equivalent transformation after discarding the conjugated pairs is adopted:

$$\mathbf{Q} = \boldsymbol{\Theta}\mathbf{p}, \tag{5.103}$$

and finally, Eq. (5.100) of $2m$ independent equations is reduced to m independent equations system:

$$\dot{p}_r + \lambda_r p_r = \tilde{H}_r, \quad r = 1,...m, \tag{5.104}$$

where

$$\tilde{\mathbf{H}} = \mathrm{pinv}(\boldsymbol{\Theta})\,\tilde{\mathbf{A}}^{-1}\tilde{\mathbf{F}}, \tag{5.105}$$

where pinv is the Moore-Penrose pseudoinverse for the non-square matrix $\boldsymbol{\Theta}$. The main advantage of getting a diagonalised formulation and, hence, decoupled linear first-order equations is that they can be solved analytically time step by time step through

$$p_r(t_{i+1}) = p_r(t_i)e^{\lambda_r \Delta t} + \frac{\tilde{H}_r(t_i)}{\lambda_r}\left(e^{\lambda_r \Delta t} - 1\right), \qquad r = 1,...m. \tag{5.106}$$

This technique is also applied in the wheelset formulation detailed in Section 5.2. A comparative with MATLAB *ode45* routine has been carried out for a harmonic contact force applied in the contact point. The decoupling strategy reduces the time consumption and, additionally, the user has control over the time step (*ode* routines use a variable time step to get an efficient convergence process step by step).

Time step adopted in case of continuous supports is $\Delta t = 3.6 \cdot 10^{-5}$ s; if it is increased, the integration solution becomes divergent. Setting this time step in the software, the time consumption per iteration is reduced around 30% compared to *ode45* routine. Even advanced numerical package NAG has been tested for the railway interaction model, giving time consumptions around 15% higher than the decoupling technique developed in this section.

A predictor-corrector technique has been implemented in order to increase the maximum time step to make the solution converge. Using Eq. (5.106), an intermediate (predictor) solution $\hat{p}_r(t_{i+1})$ allows calculating a new force term $\hat{\tilde{H}}_r(t_{i+1})$ through Eq. (5.105) for a new $\hat{\tilde{\mathbf{F}}}(t_{i+1})$. In order to soften the convergence of the method, the term $\hat{\tilde{H}}_r$ can be also estimated from:

$$\hat{\tilde{H}}_r = h\tilde{H}_r(t_i) + (1-h)\hat{\tilde{H}}_r(t_{i+1}), \qquad r = 1,...m. \tag{5.107}$$

where h is a homogenising constant, with a value between 0 and 1. Using again Eq. (5.106), the solution for the next time step is estimated:

$$p_r(t_{i+1}) = p_r(t_i)e^{\lambda_r \Delta t} + \frac{\hat{\tilde{H}}_r}{\lambda_r}\left(e^{\lambda_r \Delta t} - 1\right), \qquad r = 1,...m. \tag{5.108}$$

This predictor-corrector scheme permits to increase the time step around a 40% without losing precision in the integration solution, but doubles the time consumption since the estimation of the force must be calculated twice for each time step, see Table 5.1. Hence, Eq. (5.106) is directly implemented.

5.5.4 Simpson and Magnus integrators for solving the modal system

An alternative proposed in this work for solving the modal Eq. (5.83) is based on converting this equation into a homogeneous linear differential equation. For the first step, $\mathbf{Z}$ vector is defined:

$$\mathbf{Z} = \begin{Bmatrix} \mathbf{Q} \\ 1 \end{Bmatrix}. \tag{5.109}$$

Using this coordinate transformation, Eq. (5.83) can be defined as

$$\dot{\mathbf{Z}} = \begin{pmatrix} -\tilde{\mathbf{A}}^{-1}\tilde{\mathbf{B}} & \tilde{\mathbf{A}}^{-1}\begin{Bmatrix} \tilde{\mathbf{F}}(t) \\ \mathbf{0} \end{Bmatrix} \\ \mathbf{0} & 0 \end{pmatrix} \begin{Bmatrix} \mathbf{Q} \\ 1 \end{Bmatrix} = \mathbf{\Pi}(t)\mathbf{Z}. \tag{5.110}$$

The analytic solution for the previous matrix equation is

$$\mathbf{Z}(t_{i+1}) = e^{\mathbf{\Omega}(t_{i+1},t_i)}\mathbf{Z}(t_i), \tag{5.111}$$

where $\mathbf{\Omega}(t_{i+1},t_i) = \int_{t_i}^{t_{i+1}} \mathbf{\Pi}(\tau)\,\mathrm{d}\tau$. For an ordinary homogeneous differential matrix equation, the numerical integration for time-dependent matrices can be done applying Simpson's method using three-point Newton-Cotes quadrature rule:

$$\mathbf{\Omega}(t_{i+1},t_i) = \frac{\Delta t}{6}\left(\mathbf{\Pi}(t_i) + 4\mathbf{\Pi}\left(\frac{t_i + t_{i+1}}{2}\right) + \mathbf{\Pi}(t_{i+1})\right). \tag{5.112}$$

This method has been tested and shows a similar precision than the above procedure corresponding to Eq. (5.106) for time steps 25% larger, see Table 5.1. Nevertheless, it also requires an additional intermediate calculation point $(t_i + t_{i+1})/2$, as in the predictor-corrector scheme, doubling then the computational time needed for each iteration.

Magnus integrators [170] are more sophisticated methods for numerical integration. As a rule, $\mathbf{\Pi}(t)$ is evaluated at the Gauss-Legendre points but, in order to correct Simpson's method, Magnus also evaluates $\mathbf{\Pi}(t)$ at equispaced points. The last term of the following equation corrects Simpson's method:

$$\begin{aligned}\mathbf{\Omega}^{[4]}(t_{i+1},t_i) = {} & \frac{\Delta t}{6}\left(\mathbf{\Pi}(t_i)+4\mathbf{\Pi}\left(\frac{t_i+t_{i+1}}{2}\right)+\mathbf{\Pi}(t_{i+1})\right) \\ & -\frac{\Delta t^2}{72}\left[\mathbf{\Pi}(t_i)+4\mathbf{\Pi}\left(\frac{t_i+t_{i+1}}{2}\right)+\mathbf{\Pi}(t_{i+1}),\mathbf{\Pi}(t_{i+1})-\mathbf{\Pi}(t_i)\right],\end{aligned} \tag{5.113}$$

where the conmutator is defined as

$$[\mathbf{\Pi}(t_i),\mathbf{\Pi}(t_{i+1})] = \mathbf{\Pi}(t_{i+1}) - \mathbf{\Pi}(t_{i+1})\mathbf{\Pi}(t_i). \tag{5.114}$$

This is a fourth-order estimation respect to the time step Δt :

$$\mathbf{\Omega}^{[4]}(t_{i+1},t_i) = \mathbf{\Omega}(t_{i+1},t_i) + o(\Delta t^5). \tag{5.115}$$

This method also requires an additional intermediate calculation point $(t_i + t_{i+1})/2$, hence it needs more computational time for each iteration than Eq. (5.106) although it obtains convergent results with similar precision for time steps 52% longer, see Table 5.1. The maximum time step is limited by the convergence criteria established by Magnus [170]:

$$\int_{t_i}^{t_{i+1}} \left\|\mathbf{\Pi}(\tau)\right\|_2 \mathrm{d}\tau < \pi. \tag{5.116}$$

Magnus also proposes an equally valid expression for the same order and convergence criteria which allows not using an intermediate point [170]:

$$\mathbf{\Omega}^{[4]}(t_{i+1},t_i) = \frac{\Delta t}{2}\left(\mathbf{\Pi}(t_i) + \mathbf{\Pi}(t_{i+1})\right) - \frac{\sqrt{3}\Delta t^2}{12}\left[\mathbf{\Pi}(t_i),\mathbf{\Pi}(t_{i+1})\right]. \tag{5.117}$$

Using this new fourth-order estimation, time steps until 28% larger than $3.6\cdot10^{-5}$ s used for Eq. (5.106) have been evaluated without decreasing significantly the convergence and precision of the integration solution. Therefore, Eq. (5.117) increments the computational velocity for the numerical integration. Nevertheless, for the complete wheelset/track interaction model, time steps evaluated have had to be reduced after finding convergence problems for simulation times larger than 0.5 s while the diagonalisation procedure has shown a stronger numerical robustness for the interaction problem. So finally, Eq. (5.106) has been the integration method adopted for the present thesis. Table 5.1 summarises the above-mentioned results:

	Maximum time step ($\times 10^{-5}$ s)	Averaged time consumption per iteration (s)
MATLAB *ode45*	variable	2.7
NAG	variable	2.4
Decoupling method, Eq. (5.106)	3.6	1.2
Decoupling predictor-corrector method, Eq. (5.108)	5.0	1.9
Simpson integrator, Eq. (5.112)	4.5	2.1
Fourth-order Magnus integrator 1, Eq. (5.113)	5.5	2.1
Fourth-order Magnus integrator 2, Eq. (5.117)	4.6	1.0

Table 5.1. Maximum time steps for obtaining convergent integration solution and time consumptions per iteration for a conventional PC in each modal method.

5.5.5 Magnus expansion for periodic interaction forces

This subsection develops a complete formulation of an analytic approximation for first-order linear differential matrix equations in which the time-dependent terms are periodic based on Magnus expansion detailed in Ref. [170]. This method has successful applications in Quantum Mechanics. This approach pretends to take advantage of the periodic behaviour of interaction forces from the sleepers. This is implemented through a Winkler bedding with periodic stiffness and damping. The mathematical approach is considered relevant since its application in railway dynamics would permit to calculate the vibrating field of the train/track interaction system analytically, without the need for a numerical simulation in the time domain.

The approach is formulated in detail below. Nevertheless, its implementation has not resulted successful for various reasons. No convergence is found from the second-order terms of the solution for railway applications. Additionally, it requires the contact force is constant or with the same period than the sleepers action; thereby, its applicability is a priori limited to an isolated track without interaction with the vehicle. Nevertheless, the method is considered by the author as a promising tool for the next generation of railway simulators if an intense further work is dedicated to the adaptation of the associated equation of motion to the convergence criteria of Magnus expansion [170].

As explained in Section 5.4, the Eulerian approach adopted for the rail leads that sleepers are moving backwards with velocity V respect to the reference system associated with the vehicle. Hence, a particular spatial point of the mesh of the rail underside 'sees' a sleeper with a period $T_{sl} = L_{sl}/V$, where L_{sl} is the span or longitudinal distance between sleepers; hence, the corresponding frequency in radians is $\omega = 2\pi/T_{sl}$. A new time magnitude is defined for computational convenience, subtracting the covered periods:

$$t^* = t - \text{floor}\left(\frac{t}{T_{sl}}\right) \in \left[0, T_{sl}\right[. \tag{5.118}$$

The action of the sleepers is introduced as a harmonic Winkler bedding which introduces the corresponding additional time-dependent stiffness and damping matrices. These matrices are located in the right member of Eq. (5.71). The new equation of motion results:

$$\mathbf{M}\ddot{\mathbf{w}} - 2V\,\mathbf{C}\dot{\mathbf{w}} + \left(\mathbf{K} - V^2\mathbf{A}\right)\mathbf{w}^e = \mathbf{F}^e - \left(\mathbf{C}_w\left(t^*\right)\dot{\mathbf{w}} + \left(\mathbf{K}_w\left(t^*\right) + V\,\mathbf{K}\mathbf{C}_w\left(t^*\right)\right)\mathbf{w}\right). \tag{5.119}$$

Considering again the coordinate transformations $\mathbf{Y} = \begin{Bmatrix} \mathbf{w} \\ \dot{\mathbf{w}} \end{Bmatrix}$ and $\mathbf{Z} = \begin{Bmatrix} \mathbf{Y} \\ 1 \end{Bmatrix}$, Eq. (5.116) results as

$$\dot{\mathbf{Z}} = \begin{pmatrix} -\mathbf{A}^{-1}\mathbf{B} & \mathbf{A}^{-1}\begin{Bmatrix} \mathbf{G}\left(t^*\right) \\ \mathbf{0} \end{Bmatrix} \\ \mathbf{0} & 0 \end{pmatrix} \begin{Bmatrix} \mathbf{Y} \\ 1 \end{Bmatrix} = \mathbf{\Pi}\left(t^*\right)\mathbf{Z}, \tag{5.124}$$

where

$$\mathbf{G}\left(t^*\right) = \mathbf{M}^{-1}\left(\mathbf{F} - \left(\mathbf{C}_w\left(t^*\right)\dot{\mathbf{w}} + \left(\mathbf{K}_w\left(t^*\right) + V\,\mathbf{K}\mathbf{C}_w\left(t^*\right)\right)\mathbf{w}\right)\right), \tag{5.121}$$

and the external force $\mathbf{F}$ from the contact must be considered periodic with the same period T_{sl} or constant. From Eq. (5.111), the analytic solution for the previous matrix equation is

$$\mathbf{Z}\left(t^*\right) = e^{\mathbf{\Omega}}\mathbf{Z}_0. \tag{5.122}$$

where $\mathbf{\Omega} = \int_0^{t^*} \mathbf{\Pi}(\tau)\,\mathrm{d}\tau.$ Magnus expansion formulates an estimation for the matrix $\mathbf{\Omega}$:

$$\mathbf{\Omega} = \mathbf{\Omega}^{[1]} + \mathbf{\Omega}^{[2]} + \mathbf{\Omega}^{[3]} + o(4), \tag{5.123}$$

where the expressions for the matrices of first, second and third-order, respectively, are

$$\mathbf{\Omega}^{[1]} = \int_0^{t^*} \mathbf{\Pi}\left(t_a{}^*\right) \mathrm{d}t_a{}^*, \tag{5.124}$$

$$\mathbf{\Omega}^{[2]} = \frac{1}{2} \int_0^{t^*} \mathrm{d}t_a{}^* \int_0^{t_a{}^*} \mathrm{d}t_b{}^* \left[\mathbf{\Pi}\left(t_a{}^*\right), \mathbf{\Pi}\left(t_b{}^*\right)\right], \tag{5.125}$$

$$\mathbf{\Omega}^{[3]} = \frac{1}{6} \int_0^{t^*} \mathrm{d}t_a{}^* \int_0^{t_a{}^*} \mathrm{d}t_b{}^* \int_0^{t_b{}^*} \mathrm{d}t_c{}^* \left(\left[\mathbf{\Pi}\left(t_a{}^*\right), \left[\mathbf{\Pi}\left(t_b{}^*\right), \mathbf{\Pi}\left(t_c{}^*\right)\right]\right] + \left[\left[\mathbf{\Pi}\left(t_a{}^*\right), \mathbf{\Pi}\left(t_b{}^*\right)\right], \mathbf{\Pi}\left(t_c{}^*\right)\right]\right). \tag{5.126}$$

Since the force term $\mathbf{G}\left(t^*\right)$ is periodic, the matrix $\mathbf{\Pi}\left(t^*\right)$ can be written as Fourier series:

$$\mathbf{\Pi}\left(t^*\right) = \mathbf{\Pi}_0 + \mathbf{\Pi}_1 e^{i\omega t} + \mathbf{\Pi}_{-1} e^{-i\omega t^*} + \mathbf{\Pi}_2 e^{i2\omega t^*} + \mathbf{\Pi}_{-2} e^{-i2\omega t^*} + \cdots = \sum_{p=-\infty}^{\infty} \mathbf{\Pi}_p e^{ip\omega t^*}. \tag{5.127}$$

From the above equation, the conmutators from Eqs. (5.125) and (5.126) can be developed as

$$\begin{aligned}
\left[\mathbf{\Pi}\left(t_a{}^*\right), \mathbf{\Pi}\left(t_b{}^*\right)\right] &= \mathbf{\Pi}\left(t_a{}^*\right)\mathbf{\Pi}\left(t_b{}^*\right) - \mathbf{\Pi}\left(t_b{}^*\right)\mathbf{\Pi}\left(t_a{}^*\right) \\
&= \sum_p \mathbf{\Pi}_p e^{ip\omega t_a} \sum_q \mathbf{\Pi}_q e^{iq\omega t_b{}^*} - \sum_r \mathbf{\Pi}_r e^{ir\omega t_b{}^*} \sum_s \mathbf{\Pi}_s e^{is\omega t_a{}^*} \\
&= \sum_p \sum_q \mathbf{\Pi}_p \mathbf{\Pi}_q e^{ip\omega t_a{}^*} e^{iq\omega t_b{}^*} - \sum_r \sum_s \mathbf{\Pi}_r \mathbf{\Pi}_s e^{is\omega t_a{}^*} e^{ir\omega t_b{}^*} \\
&= \sum_p \sum_q \left(\mathbf{\Pi}_p \mathbf{\Pi}_q - \mathbf{\Pi}_q \mathbf{\Pi}_p\right) e^{ip\omega t_a{}^*} e^{iq\omega t_b{}^*} \\
&= \sum_p \sum_q \left(\mathbf{B}_{pq} - \mathbf{B}_{qp}\right) e^{ip\omega t_a{}^*} e^{iq\omega t_b{}^*},
\end{aligned} \tag{5.128}$$

$$
\begin{aligned}
&\left[\boldsymbol{\Pi}\left(t_a{}^*\right),\left[\boldsymbol{\Pi}\left(t_b{}^*\right),\boldsymbol{\Pi}\left(t_c{}^*\right)\right]\right]= \\
&=\sum_r \boldsymbol{\Pi}_r e^{ir\omega t_a{}^*}\left(\sum_p\sum_q\left(\boldsymbol{\Pi}_p\boldsymbol{\Pi}_q-\boldsymbol{\Pi}_q\boldsymbol{\Pi}_p\right)e^{ip\omega t_b{}^*}e^{iq\omega t_c{}^*}\right) \\
&-\left(\sum_p\sum_q\left(\boldsymbol{\Pi}_p\boldsymbol{\Pi}_q-\boldsymbol{\Pi}_q\boldsymbol{\Pi}_p\right)e^{ip\omega t_b{}^*}e^{iq\omega t_c{}^*}\right)\sum_r \boldsymbol{\Pi}_r e^{ir\omega t_a{}^*} \\
&=\sum_r\sum_p\sum_q\left(\boldsymbol{\Pi}_r\boldsymbol{\Pi}_p\boldsymbol{\Pi}_q-\boldsymbol{\Pi}_r\boldsymbol{\Pi}_q\boldsymbol{\Pi}_p\right)e^{ir\omega t_a{}^*}e^{ip\omega t_b{}^*}e^{iq\omega t_c{}^*} \\
&-\sum_p\sum_q\sum_r\left(\boldsymbol{\Pi}_p\boldsymbol{\Pi}_q\boldsymbol{\Pi}_r-\boldsymbol{\Pi}_q\boldsymbol{\Pi}_p\boldsymbol{\Pi}_r\right)e^{ir\omega t_a{}^*}e^{ip\omega t_b{}^*}e^{iq\omega t_c{}^*} \\
&=\sum_r\sum_p\sum_q\left(\boldsymbol{\Pi}_r\boldsymbol{\Pi}_p\boldsymbol{\Pi}_q-\boldsymbol{\Pi}_r\boldsymbol{\Pi}_q\boldsymbol{\Pi}_p-\boldsymbol{\Pi}_p\boldsymbol{\Pi}_q\boldsymbol{\Pi}_r+\boldsymbol{\Pi}_q\boldsymbol{\Pi}_p\boldsymbol{\Pi}_r\right)e^{ir\omega t_a{}^*}e^{ip\omega t_b{}^*}e^{iq\omega t_c{}^*} \\
&=\sum_r\sum_p\sum_q\left(\mathbf{C}_{rpq}-\mathbf{C}_{rqp}-\mathbf{C}_{pqr}+\mathbf{C}_{qpr}\right)e^{ir\omega t_a{}^*}e^{ip\omega t_b{}^*}e^{iq\omega t_c{}^*},
\end{aligned}
\tag{5.129}
$$

where $\mathbf{B}_{pq}=\boldsymbol{\Pi}_p\,\boldsymbol{\Pi}_q$ and $\mathbf{C}_{rpq}=\boldsymbol{\Pi}_r\,\mathbf{B}_{pq}=\mathbf{B}_{rp}\,\boldsymbol{\Pi}_q$ (in terms of computational efficiency, this last relationship is important). The sum of the conmutators gives

$$
\begin{aligned}
&\left[\boldsymbol{\Pi}\left(t_a{}^*\right),\left[\boldsymbol{\Pi}\left(t_b{}^*\right),\boldsymbol{\Pi}\left(t_c{}^*\right)\right]\right]+\left[\boldsymbol{\Pi}\left(t_c{}^*\right),\left[\boldsymbol{\Pi}\left(t_b{}^*\right),\boldsymbol{\Pi}\left(t_a{}^*\right)\right]\right]= \\
&=\sum_r\sum_p\sum_q\left(\boldsymbol{\Pi}_r\boldsymbol{\Pi}_p\boldsymbol{\Pi}_q-\boldsymbol{\Pi}_r\boldsymbol{\Pi}_q\boldsymbol{\Pi}_p-\boldsymbol{\Pi}_p\boldsymbol{\Pi}_q\boldsymbol{\Pi}_r+\boldsymbol{\Pi}_q\boldsymbol{\Pi}_p\boldsymbol{\Pi}_r\right)e^{ir\omega t_a{}^*}e^{ip\omega t_b{}^*}e^{iq\omega t_c{}^*} \\
&+\sum_q\sum_p\sum_r\left(\boldsymbol{\Pi}_r\boldsymbol{\Pi}_p\boldsymbol{\Pi}_q-\boldsymbol{\Pi}_r\boldsymbol{\Pi}_q\boldsymbol{\Pi}_p-\boldsymbol{\Pi}_p\boldsymbol{\Pi}_q\boldsymbol{\Pi}_r+\boldsymbol{\Pi}_q\boldsymbol{\Pi}_p\boldsymbol{\Pi}_r\right)e^{ir\omega t_a{}^*}e^{ip\omega t_b{}^*}e^{iq\omega t_c{}^*} \\
&=\sum_r\sum_p\sum_q\left(\boldsymbol{\Pi}_r\boldsymbol{\Pi}_p\boldsymbol{\Pi}_q-\boldsymbol{\Pi}_r\boldsymbol{\Pi}_q\boldsymbol{\Pi}_p-\boldsymbol{\Pi}_p\boldsymbol{\Pi}_q\boldsymbol{\Pi}_r+\boldsymbol{\Pi}_q\boldsymbol{\Pi}_p\boldsymbol{\Pi}_r\right. \\
&\left.+\boldsymbol{\Pi}_q\boldsymbol{\Pi}_p\boldsymbol{\Pi}_r-\boldsymbol{\Pi}_q\boldsymbol{\Pi}_r\boldsymbol{\Pi}_p-\boldsymbol{\Pi}_p\boldsymbol{\Pi}_r\boldsymbol{\Pi}_q+\boldsymbol{\Pi}_r\boldsymbol{\Pi}_p\boldsymbol{\Pi}_q\right)e^{ir\omega t_a{}^*}e^{ip\omega t_b{}^*}e^{iq\omega t_c{}^*} \\
&=\sum_r\sum_p\sum_q\left(2\mathbf{C}_{rpq}+2\mathbf{C}_{qpr}-\mathbf{C}_{rqp}-\mathbf{C}_{pqr}-\mathbf{C}_{qrp}-\mathbf{C}_{prq}\right)e^{ir\omega t_a{}^*}e^{ip\omega t_b{}^*}e^{iq\omega t_c{}^*}.
\end{aligned}
\tag{5.130}
$$

Once detailed the explicit expressions of the above conmutators, Eqs. (5.124), (5.125) and (5.126) can be analytically integrated.

First-order term:

$$
\boldsymbol{\Omega}^{[1]}=\int_0^{t^*}\sum_p \boldsymbol{\Pi}_p e^{ip\omega t_a{}^*}\mathrm{d}t_a{}^*=\sum_p \boldsymbol{\Pi}_p\int_0^{t^*}e^{ip\omega t_a{}^*}\mathrm{d}t_a, \tag{5.131}
$$

where

$$\begin{aligned}\int_0^{t^*} e^{ip\omega t_a{}^*}\,\mathrm{d}t_a &= \{p=0\}\quad t^* \\ &= \{\text{else}\}\quad \frac{i - i\,e^{ip\omega t^*}}{p\omega}.\end{aligned} \tag{5.132}$$

Second-order term:

$$\begin{aligned}\mathbf{\Omega}^{[2]} &= \frac{1}{2}\int_0^{t^*}\mathrm{d}t_a{}^*\int_0^{t_a{}^*}\mathrm{d}t_b{}^*\ \sum_p\sum_q\left(\mathbf{B}_{pq}-\mathbf{B}_{qp}\right)e^{ip\omega t_a{}^*}e^{iq\omega t_b{}^*} \\ &= \frac{1}{2}\sum_p\sum_q\left(\mathbf{B}_{pq}-\mathbf{B}_{qp}\right)\int_0^{t^*}\int_0^{t_a{}^*} e^{ip\omega t_a{}^*}e^{iq\omega t_b{}^*}\,\mathrm{d}t_b{}^*\mathrm{d}t_a{}^*,\end{aligned} \tag{5.133}$$

where

$$\begin{aligned}\int_0^{t^*}\int_0^{t_a{}^*} e^{ip\omega t_a{}^*}e^{iq\omega t_b{}^*}\,\mathrm{d}t_b{}^*\mathrm{d}t_a{}^* &= \{p=q=0\}\quad \frac{t^{*2}}{4} \\ &= \{p=0\}\quad \frac{1+i\omega q t^* - e^{iq\omega t^*}}{2\,\omega^2 q^2} \\ &= \{q=0\}\quad -\frac{1+i\omega p t e^{ip\omega t^*} - e^{ip\omega t^*}}{2\,\omega^2 p^2} \\ &= \{q=\text{-}p\}\quad -\frac{e^{-iq\omega t^*} + i\omega q t^* - 1}{2\,\omega^2 q^2} \\ &= \{\text{else}\}\quad \frac{(p+q)e^{ip\omega t^*} - q - p\,e^{i(p+q)\omega t^*}}{2\,\omega^2 p\,q\,(p+q)}.\end{aligned} \tag{5.134}$$

Third-order term:

$$\begin{aligned}
\mathbf{\Omega}^{[3]} &= \frac{1}{6}\int_0^{t^*}\mathrm{d}t_a{}^*\int_0^{t_a{}^*}\mathrm{d}t_b{}^*\int_0^{t_b{}^*}\mathrm{d}t_c{}^*\Big(\Big[\mathbf{\Pi}(t_a{}^*),\big[\mathbf{\Pi}(t_b{}^*),\mathbf{\Pi}(t_c{}^*)\big]\Big]-\Big[\mathbf{\Pi}(t_c{}^*),\big[\mathbf{\Pi}(t_a{}^*),\mathbf{\Pi}(t_b{}^*)\big]\Big]\Big)\\
&= \frac{1}{6}\int_0^{t^*}\mathrm{d}t_a{}^*\int_0^{t_a{}^*}\mathrm{d}t_b{}^*\int_0^{t_b{}^*}\mathrm{d}t_c{}^{*}\Big(\Big[\mathbf{\Pi}(t_a{}^*),\big[\mathbf{\Pi}(t_b{}^*),\mathbf{\Pi}(t_c{}^*)\big]\Big]+\Big[\mathbf{\Pi}(t_c{}^*),\big[\mathbf{\Pi}(t_b{}^*),\mathbf{\Pi}(t_a{}^*)\big]\Big]\Big)\\
&= \frac{1}{6}\int_0^{t^*}\mathrm{d}t_a{}^*\int_0^{t_a{}^*}\mathrm{d}t_b{}^*\int_0^{t_b{}^*}\mathrm{d}t_c{}^*\left\{\sum_r\sum_p\sum_q\big(2\mathbf{C}_{rpq}+2\mathbf{C}_{qpr}-\mathbf{C}_{rqp}-\mathbf{C}_{pqr}-\mathbf{C}_{qrp}-\mathbf{C}_{prq}\big)\,e^{ir\omega t_a{}^*}e^{ip\omega t_b{}^*}e^{iq\omega t_c{}^*}\right\}\\
&= \frac{1}{6}\sum_r\sum_p\sum_q\big(2\mathbf{C}_{rpq}+2\mathbf{C}_{qpr}-\mathbf{C}_{rqp}-\mathbf{C}_{pqr}-\mathbf{C}_{qrp}-\mathbf{C}_{prq}\big)\int_0^{t^*}\int_0^{t_a{}^*}\int_0^{t_b{}^*}\left\{e^{ir\omega t_a{}^*}e^{ip\omega t_b{}^*}e^{iq\omega t_c{}^*}\right\}\mathrm{d}t_c{}^*\mathrm{d}t_b{}^*\mathrm{d}t_a{}^*,
\end{aligned}\tag{5.135}$$

where

$$\begin{aligned}
&\frac{1}{6}\int_0^{t^*}\int_0^{t_a{}^*}\int_0^{t_b{}^*}\left\{e^{ir\omega t_a{}^*}e^{ip\omega t_b{}^*}e^{iq\omega t_c{}^*}\right\}\mathrm{d}t_c{}^*\mathrm{d}t_b{}^*\mathrm{d}t_a{}^*\\
&=\{p=q=r=0\}\quad \frac{t^{*3}}{36}\\
&=\{q=r=0\}\quad -\frac{-2i+p\omega t^*+\left(2i+p\omega t^*\right)e^{ip\omega t^*}}{6p^3\omega^3}\\
&=\{p=r=0\}\quad \frac{i\left(-2+2e^{iq\omega t^*}-2iq\omega t^*+q^2\omega^2t^{*2}\right)}{12q^3\omega^3}\\
&=\{p=q=0\}\quad \frac{-2i+\left((1+i)-ir\omega t^*\right)\left((1+i)+r\omega t^*\right)e^{ir\omega t^*}}{12r^3\omega^3}\\
&=\{q=-p,r=0\}\quad \frac{i\left(-2+2e^{ip\omega t^*}-2ip\omega t^*+p^2\omega^2t^{*2}\right)}{12p^3\omega^3}\\
&=\{r=0\}\quad \frac{i\left(p^2e^{i(p+q)\omega t^*}-(p+q)^2e^{ip\omega t^*}+q\left(2pq+ip(p+q)\omega t^*\right)\right)}{6p^2q(p+q)^2\omega^3}\\
&=\{r=-p,q=0\}\quad \frac{2i-2ie^{-ip\omega t^*}+2p\omega t^*-ip^2\omega^2t^{*2}}{12p^3\omega^3}\\
&=\{q=0\}\quad -\frac{i\left(p^2-(p+r)^2e^{ir\omega t^*}\right)+r\left(i(2p+r)+p(p+r)\omega t^*\right)e^{i(p+r)\omega t^*}}{6p^2r(p+r)^2\omega^3}
\end{aligned}$$

$$
\begin{aligned}
&= \{r = -q,\, p = 0\} \quad -\frac{2i + q\omega t^{*} + \left(-2i + q\omega t^{*}\right)e^{-iq\omega t^{*}}}{6q^{3}\omega^{3}} \\
&= \{p = 0\} \quad \frac{-iq^{2} + \left(ir^{2}\left(-1 + e^{iq\omega t^{*}}\right) + q\left(iq + r\left(q + r\right)\right)\omega t^{*}\right)e^{ir\omega t^{*}}}{6q^{2}r^{2}\left(q + r\right)\omega^{3}} \\
&= \{r = -\left(p + q\right)\} \quad \frac{e^{-i\left(p+2q\right)\omega t^{*}}\left(-i\left(q^{2} - \left(p + q\right)^{2}e^{ip\omega t^{*}}\right) - p\left(i\left(p + 2q\right) + q\left(p + q\right)\omega t^{*}\right)\right)}{6pq^{2}\left(p + q\right)^{2}\omega^{3}} \\
&= \{q = -p,\, r = -p\} \quad -\frac{\left(2i + p\omega t^{*} + \left(-2i + p\omega t^{*}\right)e^{-ip\omega t^{*}}\right)}{6p^{3}\omega^{3}} \\
&= \{r = -p\} \quad \frac{e^{-ip\omega t^{*}}\left(ip^{2}e^{i\left(p+q\right)\omega t^{*}} - iq^{2} + \left(p + q\right)\left(iq + p\left(-i + q\omega t^{*}\right)\right)e^{ip\omega t^{*}}\right)}{6p^{2}q^{2}\left(p + q\right)\omega^{3}} \\
&= \{q = -p\} \quad \frac{-ip^{2} + \left(ir^{2}\left(-1 + e^{ip\omega t^{*}}\right) + p\left(ip + r\left(p + r\right)\right)\omega t^{*}\right)e^{ir\omega t^{*}}}{6p^{2}r^{2}\left(p + r\right)\omega^{3}} \\
&= \{\text{else}\} \quad \frac{i}{6q\omega^{3}}\left(\frac{1 - e^{ir\omega t^{*}}}{r\,(p + q)} + \frac{e^{ir\omega t^{*}} - 1}{rp} + \frac{1 - e^{i\left(p+r\right)\omega t^{*}}}{p\,(p + r)} + \frac{e^{i\left(p+q+r\right)\omega t^{*}} - 1}{(p + q)(p + q + r)}\right).
\end{aligned}
\tag{5.136}
$$

The first order term contains the mean value of the steady-state solutions, while the rest have its harmonic contributions. No figures are shown because no-convergence is found for $\Delta t > 10^{-10}$ s due to the convergence criteria from Eq. (5.116) is not satisfied for larger time steps. This occurs due to the large magnitude of the stiffness matrix (around 10^{10} N/m^{2}). A re-sizing of the matrix involved in Eq. (5.45) could be a strategy to increase the suitable time step. Further work is proposed to take advantage of this powerful mathematical tool for dynamic interaction problems.

5.6 CALCULATION OF INTERACTION FORCES

5.6.1 Calculation of wheel/rail contact forces

Both wheelset and rail interrelate through contact forces considered as external forces calculated from the relative displacements and velocities between both subsystems.

Eqs. (5.26) and (5.106) are coupled by the wheel/rail contact forces, which can be defined as a function of the wheelset and rail modal coordinates $\left(\mathbf{q}^w, \mathbf{p}^r\right)$, where $\mathbf{p}^r \equiv \mathbf{p}$ coordinate used for the rail formulation in order to clarify the nomenclature, and their time derivatives $\left(\dot{\mathbf{q}}^w, \dot{\mathbf{p}}^r\right)$. The calculation of the contact forces is performed within the time step integration of the equations of motion for the wheelset and the rail. First, the motion (position and velocity) of the contact points on wheel and rail surfaces is determined. Then, the normal and tangential wheel/rail contact forces are computed as a function of the relative wheel/rail motion at the contact point. Finally, the generalised forces on the vehicle and rail coordinates are defined based on the principle of virtual work.

Using the modal superposition principle, the vectors $\mathbf{w}_{c,i}^{wr}$ of the wheel/rail displacements at the contact point (with $i = 1,2$ representing the inner and outer wheel) are computed from Eqs. (5.6), (5.75) and (5.103):

$$\Delta\mathbf{w}_{c,i}^{wr} = \mathbf{w}_{c,i}^{r} - \mathbf{w}_{c,i}^{w} = \mathbf{\Phi}^r\left(\mathbf{u}_{c,i}^{r}\right)\mathbf{\Theta}_{\mathbf{u}}\,\mathbf{p}^r - \mathbf{\Phi}^w\left(\mathbf{u}_{c,i}^{w}\right)\mathbf{q}^w, \tag{5.137}$$

with $\mathbf{u}_{c,i}^{w}$ and $\mathbf{u}_{c,i}^{r}$ the position of the contact point on the wheel and the rail, respectively, and $\mathbf{\Theta}_{\mathbf{u}} = \mathbf{\Theta}_{1:N^r,:}$ takes the displacements rows for the rail second-transformation matrix. In the same way, the velocity vectors of the wheel and rail, $\dot{\mathbf{w}}_{c,i}^{w}$ and $\dot{\mathbf{w}}_{c,i}^{r}$ respectively, define the wheel/rail velocity $\Delta\dot{\mathbf{w}}_{c,i}^{wr}$ as

$$\Delta\dot{\mathbf{w}}_{c,i}^{wr} = \dot{\mathbf{w}}_{c,i}^{r} - \dot{\mathbf{w}}_{c,i}^{w} = \mathbf{\Phi}^r\left(\mathbf{u}_{c,i}^{r}\right)\mathbf{\Theta}_{\dot{\mathbf{u}}}\,\dot{\mathbf{p}}^r - \mathbf{\Phi}^w\left(\mathbf{u}_{c,l}^{w}\right)\dot{\mathbf{q}}^w, \tag{5.138}$$

where $\mathbf{\Theta}_{\dot{\mathbf{u}}} = \mathbf{\Theta}_{N^r+1:2N^r,:}$ takes the velocities rows for the rail second-transformation matrix. If the model considers the effect of geometric imperfections in the rail due to irregularity and rail roughness, the term $\mathbf{x}_{c,i}^{r(irr)}$ is added to the second bracket of Eq. (5.138).

The model of wheel/rail contact used to reproduce the dynamic coupling between the vehicle and the track adopts an incremental technique to define the elastic penetration for the normal problem and the creepages for the tangential one. This penetration is calculated by projecting the relative wheel/rail displacements in the contact point along the direction normal to the contact plane.

The incremental procedure starts from a pre-processing step in which the complete railway system is run in the multibody dynamic simulation software [171]. This software obtains the steady-state solution for the displacements of the whole vehicle in the curve, from which the complete dynamic model developed in this thesis starts the simulation (from now, dashed magnitudes will refer to steady values). The software also provides information of the contact: lateral displacements for both wheels and rails (inner and outer), normal angle, curvatures and size of the contact patch, creepages and creep (contact) forces. The Eulerian approach in both wheelset and rail models (see Section 5.3 and 5.4, respectively) permits to fix the contact zone despite of the translational movement of the vehicle and the rotation of the wheelset. Hence, the geometrical data allow detecting the contact point in the wheelset and rails meshes where the both contact forces are applied. The normal angle in both rails determines the normal direction from the vertical axis. The creepages and creep (contact) forces on the both contact patches will be used as stationary values for the incremental technique adopted.

An ERRI-wagon is selected; more details of this model are given in Section 6.4. Note that a constant friction coefficient is considered since robust software for the unsteady contact process with falling friction coefficient has not been successfully achieved so far in this thesis. The inclination γ of both rails is 1/40 and the contact point is not in the nominal position (lateral displacement $\Delta y^{wr} \neq 0$). The normal force $\overline{N}$ is calculated as the vertical creep force $\overline{F}_3$ projected on the normal direction, whose angle from the vertical axis is $\overline{\theta}$. In the same way, the rolling radius r_{11} for contact estimations must be corrected according to the normal direction.

Two options were contemplated and implemented to locate the point where the contact forces are applied in both wheel and rail: (a) to find the closest nodes of each mesh; (b) to use the shape functions of the contact elements to calculate the displacements and velocities of the exact contact points from the displacements and velocities of the nodes of the contact elements. The first option is computationally more efficient since it requires less calculation, but the differences can be non-negligible especially in case of flange contact for small radius curves. Option (b) was finally used. A subroutine to calculate the four curvatures $\overline{r}_{11}$, $\overline{r}_{12}$, $\overline{r}_{21}$ and $\overline{r}_{22}$ from the corresponding wheel and rail profiles and the contact point has also been implemented.

The change in the location of the contact point due to the instantaneous deformation of the wheelset is neglected in the calculation of the contact forces. This simplification is justified because the magnitude of the elastic wheel deformation (in the order of 1–$10 \cdot 10^{-5}$ m) is much smaller than the rigid lateral movement of the wheelset relative to the rail, which is between $5 \cdot 10^{-3}$ and 10^{-2} m, depending on the track gauge, rail profiles and wheel profile. An alternative approach would be to compute the position of the contact point and the contact parameters at each time step of the numerical integration, considering also the deformation of the wheelset as in Ref. [159]. However, this approach would entail a much more CPU intensive calculation, whereas the focus in this work is to keep the computational effort as low as possible, while retaining in the model the main effects of wheelset and rail flexibility for the problem studied.

The orientation of the local wheelset reference frame is needed for the calculation of creepage from the incremental procedure. The present formulation assumes a negligible roll rotation ($\phi_1 \approx 0$, $\dot{\phi}_1 \approx 0$). The rotation velocity of the wheelset and its yaw rotation are defined, respectively, as

$$\Omega = \dot{\phi}_2 = \frac{V}{\bar{r}_{11_N}}, \tag{5.139}$$

$$\dot{\phi}_3 = \frac{V}{R^r}, \tag{5.140}$$

where V is the vehicle speed and R^r the curve radius. Integrating to obtain the corresponding angular displacements:

$$\phi_2 = \dot{\phi}_2 t, \tag{5.141}$$

$$\phi_3 = \dot{\phi}_3 t + \bar{\psi}, \tag{5.142}$$

where $\bar{\psi}$ is the angle of attack. With the angular displacements considered as Euler angles, the rotational matrices can be calculated:

$$\mathbf{R}_2(\phi_2) = \begin{pmatrix} \cos\phi_2 & 0 & \sin\phi_2 \\ 0 & 1 & 0 \\ -\sin\phi_2 & 0 & \cos\phi_2 \end{pmatrix}, \tag{5.143}$$

$$\mathbf{R}_3(\phi_3) = \begin{pmatrix} \cos\phi_3 & -\sin\phi_3 & 0 \\ \sin\phi_3 & \cos\phi_3 & 0 \\ 0 & 0 & 1 \end{pmatrix}. \tag{5.144}$$

From the local angular velocity defined as $\boldsymbol{\omega}^{w} = \left(0, \dot{\phi}_2, \dot{\phi}_3\right)$, its intermediate orientation after the rotation in the x_3-axis results

$$\boldsymbol{\omega}^{I} = \mathbf{R}_3(\phi_3)\boldsymbol{\omega}^{w} = \mathbf{R}_3(\phi_3)\begin{pmatrix} 0 \\ \dot{\phi}_2 \\ 0 \end{pmatrix} + \begin{pmatrix} 0 \\ 0 \\ \dot{\phi}_3 \end{pmatrix}, \tag{5.145}$$

and the angular velocity in global coordinates finally results

$$\boldsymbol{\omega}^{0} = \mathbf{R}_2(\phi_2)\boldsymbol{\omega}^{I} = \mathbf{R}_2(\phi_2)\mathbf{R}_3(\phi_3)\begin{pmatrix} 0 \\ \dot{\phi}_2 \\ 0 \end{pmatrix} + \mathbf{R}_2(\phi_2)\begin{pmatrix} 0 \\ 0 \\ \dot{\phi}_3 \end{pmatrix}. \tag{5.146}$$

This is needed for the definition of the local reference frame in the contact point. The unit vector $\mathbf{x}_1$ corresponding to the longitudinal local direction in each instant is defined as

$$\mathbf{x}_1 = \frac{\mathbf{x}_3 \times \boldsymbol{\omega}^{0}}{\left\| \mathbf{x}_3 \times \boldsymbol{\omega}^{0} \right\|}, \tag{5.147}$$

where $\mathbf{x}_3$ is the normal unitary vector $\mathbf{x}_3$. From both vectors, the lateral unitary vector that completes the orthonormal base is

$$\mathbf{x}_2 = -\mathbf{x}_1 \times \mathbf{x}_3. \tag{5.148}$$

At this point, the wheel/rail displacement from Eq. (5.137) is corrected taking into account the initial position of the wheelset, $\overline{\mathbf{w}}_c^{w}$, and rail, $\overline{\mathbf{w}}_c^{r}$. This corresponds to the pseudo-static state that is previously calculated by means of a static equilibrium from the creep forces given by the multibody software.

$$\Delta\mathbf{w}_c^{wr} = \left(\mathbf{w}_c^{r} - \overline{\mathbf{w}}_c^{r}\right) - \left(\mathbf{w}_c^{w} - \overline{\mathbf{w}}_c^{w}\right). \tag{5.149}$$

The incremental approach is computed by projecting the relative wheel/rail displacements in the contact point along the direction normal to the contact plane:

$$\Delta\delta = \left(\Delta\mathbf{w}_c^{wr}\right)^{\mathrm{T}} \cdot \mathbf{x}_3. \tag{5.150}$$

Now, the creepages for each instant are calculated adopting an incremental estimation once calculated the wheel/rail material velocity from Eq. (5.138), the local reference frame and the pseudo-static creepages given by the multibody software:

$$\xi_1 = \frac{\left(\Delta\dot{\mathbf{w}}_c^{wr}\right)^{\mathrm{T}}}{V} \cdot \mathbf{x}_1 + \bar{\xi}_1, \tag{5.151}$$

$$\xi_2 = \frac{\left(\Delta\dot{\mathbf{w}}_c^{wr}\right)^{\mathrm{T}}}{V} \cdot \mathbf{x}_2 + \bar{\xi}_2, \tag{5.152}$$

$$\xi_{sp} = \bar{\xi}_{sp}. \tag{5.153}$$

From Hertzian theory, the elastic penetration $\bar{\delta}$ can be estimated from Eq. (B.6) (see Appendix B) once the material properties (both wheelset and rail are made of steel, see Table 4.1), curvatures in the contact point and normal force are known:

$$\bar{\delta} = \sqrt[3]{\left(\frac{\bar{F}_3}{K_H}\right)^2}. \tag{5.154}$$

Once obtained $\bar{\delta}$ from Eq. (5.154) and $\Delta\delta$ from Eq. (5.150), the total normal force in the contact patch F_3 can finally be estimated again from Eq. (B.6) and adding the incremental penetration to the pseudo-static one:

$$F_3 = \bar{F}_3 + \Delta F_3 = \begin{cases} K_H\left(\bar{\delta} + \Delta\delta\right)^{3/2} & \text{if } \left(\bar{\delta} + \Delta\delta\right) > 0, \\ 0 & \text{if } \left(\bar{\delta} + \Delta\delta\right) \leq 0. \end{cases} \tag{5.155}$$

From the normal normal force F_3, the normal problem can be solved adopting an Hertzian or non-Hertzian (Kalker's algorithm) model. Since both wheelset and rail are made of the same material and, hence, the normal problem is decoupled from the tangential one [81], the tangential contact problem is addressed using the formulation based on Kalker's variational theory developed in Section 4.3, also applying regularisation of Coulomb's law. This permits to calculate the longitudinal and lateral forces, F_1 and F_2, respectively. F_1, F_2 and F_3 are applied in the wheel and in the rail (with opposite sign) in the corresponding contact points as external actions.

5.6.2 Calculation of forces in the rail supports

In case of considering a Winkler bedding or an elastic pad layer as continuous rail support, both are integrated in the FE model of the rail (in the global matrices that define the complete rail model). Therefore, a substructuring technique is only needed in case of discrete supports (see Fig. 5.10), in which external forces must be included between the corresponding points of the rail underside and the sleepers, and between the sleepers and the ground. The particularity of the ME rail model is that the reference frame is moving with the vehicle since an Eulerian approach is adopted; thereby, the fixed position of the contact point implies that the sleepers position is moving backwards (opposite to the vehicle speed sense) with velocity V. This location is calculated for each instant ($x_1^{sl} = x_{1,0}^{sl} - Vt$, where $x_{1,0}^{sl}$ is the initial location of the sleepers) and an implemented routine finds the corresponding element and position on the rail underside just above each sleeper. Again, two options has been implemented to locate the point where the interaction forces are applied in both rail and sleeper: (a) to find the closest nodes of the each mesh; (b) to use the shape functions of the contact elements to calculate the displacements and velocities of these points from the displacements and velocities of the nodes of the contact elements. Option (b) is finally selected.

The same procedure used in Eqs. (5.137) and (5.138) is taken to estimate the rail/sleeper incremental displacements, $\Delta\mathbf{w}_p^{r\,sl}$, and velocities, $\Delta\dot{\mathbf{w}}_p^{r\,sl}$. The rail/sleeper interaction force is produced through the railpad stiffness $\mathbf{k}_p$ and damping $\mathbf{c}_p$:

$$F_j^{r\,sl} = k_{p,j}\,\Delta w_{p,j}^{r\,sl} + c_{p,j}\,\Delta\dot{w}_{p,j}^{r\,sl}, \quad j = 1,2,3. \tag{5.156}$$

The sleeper and the rail underside surface receive the forces $\mathbf{F}^{r\,sl}$ and $-\mathbf{F}^{r\,sl}$ in the corresponding point, respectively. In the same way, the ballast acts on the sleeper from its displacement, $\Delta\mathbf{w}^{sl}$, and velocity $\Delta\dot{\mathbf{w}}^{sl}$:

$$F_j^{sl} = -\left(k_{b,j}\,\Delta w_j^{sl} + c_{b,j}\,\Delta\dot{w}_j^{sl}\right), \quad j = 1,2,3. \tag{5.157}$$

5.7 CONCLUSIONS

As regards to the development of a wheelset/track interaction model in the time domain, the following conclusions are derived:

- A complete methodology to model the dynamics of damped flexible wheelset has been presented, based on previous works of this research group [55,56,159,160]:

- This method models damped elastic solids of revolution rotating about their axis of revolution. It is based on a modal approach where the modal properties of the non-rotating solid form the modal basis of the system. The final formulation consists of a set of linear ordinary differential equations where the coefficients are time-independent. Therefore, the matrices are calculated only once at the beginning of the simulation, leading to a considerable reduction of computational cost.

- By introducing a trajectory coordinates set describing the large motion of the wheelset along the curved track and assuming small relative movements of the wheelset with respect to the trajectory frame, the terms appearing in the wheelset equations of motion can be efficiently computed, keeping the time required to carry the numerical simulation within acceptable limits.

- As one of the main contributions of the thesis, a new 3D model for a finitely long railway track has been formulated through the Moving Element Method (MEM) in order to improve the modelling in the high-frequency domain.

- The model considers an Eulerian coordinate system attached to the moving vehicle instead of a fixed coordinate system and it adopts cyclic boundary conditions. This approach permits to decrease the computational cost compared to the FE models commonly used.

- The matrices corresponding to a Winkler bedding has been included in the formulation in case this type of rail is utilised. If discrete supports are modelled, a lumped system consisting of rail pad, sleeper and ballast is adopted. A continuously supported rail is the third option implemented, in which a viscoelastic layer is aggregated under the rail.

- Wheel/rail contact forces are estimated through an incremental technique. From small displacements of the corresponding wheel and rail contact points and the estimation of the elastic penetration, the normal contact force and creepages are determined, which permit to calculate the tangential forces.

- A modal approach is adopted for both wheelset and rail models. A static modal correction is also developed in order to compensate the deviation in the static response introduced by the modal transformation.

- A decoupling technique is applied to diagonalise the matrices involved in the linear equation of motion systems, reducing the time consumption of the numerical integration.

- Simpson and Magnus integrators have been implemented and tested in the modal system equation. The previous decoupling method has shown a faster computational velocity and a more robust behaviour.

A formulation for periodic interaction forces on the rail has been developed based on Magnus expansion. Further work is needed to extend this theoretical contribution for dynamic interaction problems.

6 APPLICATIONS OF THE WHEELSET/TRACK INTERACTION MODEL

6.1 INTRODUCTION

In the present chapter, the dynamic train/track interaction model implemented in this thesis is run for different simulation cases divided in three sections. The first one (Section 6.2) pretends to test the 3D track model based on the Moving Element Method developed in Section 5.4, which permits to extend the range of validity of the Timoshenko beam considered in earlier studies of this research group. Simulation results are presented and discussed for different excitation sources including random rail roughness and singularities such as wheel flats. All the simulation cases are carried out for a Timoshenko beam and a 3D MEM track model when the vehicle runs on a tangent track in order to point out the differences in the contact forces above the range of validity of the Timoshenko beam.

The other two subsections run simulations in curving conditions. Assuming that railway curve squeal arises from self-excited vibrations during curving, Section 6.3 proposes a time-domain approach based on the Green's functions [33,34] for the evaluation of the stick/slip oscillations induced by the frictional instability in a work developed in collaboration with Chalmers University of Technology. Additionally, the linear stability is investigated through complex eigenvalue analysis in the frequency domain. The influence of the wheel/rail friction coefficient and the direction of the resulting creep force on the occurrence of squeal are investigated for vanishing train speed.

Section 6.4 runs a set of simulations with a wheelset negotiating a tight curve in order to investigate the stick/slip oscillations due to frictional instability. This research line pretends to confirm whether the coupling between normal and tangential dynamics can originate squeal as Section 6.3 seems to demonstrate theoretically and many researchers defend. Simulations are carried out with a constant friction law.

6.2 CONTRIBUTIONS OF THE 3D MEM TRACK MODEL IN THE HIGH-FREQUENCY DOMAIN FOR A SINGLE WHEELSET

6.2.1 Introduction

This section presents different results that test the track model based on the ME approach and compare it with the Timoshenko beam model used so far in the research group to which the author belongs. Simulations for a train/track model are carried out when the complete system is excited by random rail roughness and wheel flats. These results are gathered in Ref. [174].

All the simulations consider the vehicle running at 300 km/h through a tangent track and the system is excited up to 8.5 kHz; each case is run separately for a Timoshenko beam and a 3D MEM modelling the track. Both models are compared by the vertical and lateral contact forces obtained from the simulations above the range of validity of the Timoshenko beam (from 1.5 to 8.5 kHz) in order to study the contributions of the 3D MEM in the high-frequency range.

For the vehicle/track interaction model, a substructuring technique is followed, permitting to divide the whole system into three substructures: the vehicle, the rails and the discrete rail supports. The equations of motion of each substructure are coupled by the wheel/rail contact forces and by the forces generated at the rail pads (see Sections 5.6.1 and 5.6.2, respectively).

Considering the same materials for both bodies, the tangential contact is coupled with the normal contact, but not vice versa [81]. Hertzian model is adopted here for the normal contact and the model developed in Section 4.3 is the software used for the tangential contact that depends on the normal contact force and creepages. Wheel/rail displacements and velocities are updated at each time step to evaluate the online contact forces.

6.2.2 Vehicle model

The vehicle is confined to one flexible and rotating wheelset [160]. The effect of low frequency curving dynamics of the complete vehicle needs however to be included in the model, in order to obtain suitable mean values for the creepages and contact forces, which affect the coupled wheelset/track vibration also at higher frequency. This is accomplished by prescribing the forces applied by the primary suspension to the wheelset in the vertical plane and the yaw rotation of the bogie at the primary suspension. The approach followed in this section is to consider one single wheelset and to reproduce the steady-state curving effects by prescribing appropriate forces at the primary suspension: these forces are derived from the results of a low-frequency multibody simulation in which the whole vehicle is considered, but all bodies are assumed to behave as rigid. Compared to considering the complete bogie with two flexible wheelsets, this approach allows to reduce substantially the time required for the simulation, because the additional degrees of freedom of the second wheelset and of the bogie frame are not included in the analysis, and also because the time consuming procedure required to evaluate the contact forces at each time step is carried out for two wheels instead of four, whereas the low-frequency simulation of the whole vehicle requires a very short simulation time, on account of the assumption of neglecting the flexibility of all bodies.

The wheelset model adopted is the flexible and rotatory one detailed in Section 5.3. 400 vibration modes of the wheelset have been considered, covering a frequency range up to 8.5 kHz. It should be noted that the wheelset is a very stiff and low damped solid and consequently few modes above the maximum frequency of study are required to minimise errors due to modal truncation. In order to ensure that the contact forces and creepages are correctly initialised, the steady-state forces applied in the wheelset at the axle-boxes via the primary suspension along the $\mathbf{Z}_T$ and $\mathbf{Y}_T$ axes of the trajectory coordinate frame (see Fig. 5.2 in Section 5.3) are prescribed in Eq. (5.26) to match the values obtained in the low-frequency simulation. In this way, the steady-state $\mathbf{Z}_T$ component of the contact forces on the two wheels and the sum of the steady-state contact forces along the $\mathbf{Y}_T$ axis are correctly reproduced by the flexible wheelset/track model. Furthermore, the longitudinal stiffness of the primary suspension is introduced in Eq. (5.26) and the longitudinal displacements (i.e. directed along axis $\mathbf{X}_T$) of the bogie at the primary suspension are prescribed to match the values obtained from the low-frequency simulation. By doing so, the steady-state longitudinal and lateral creep forces on both wheels are correctly initialised in the high-frequency model. As shown in the results, cf. comments to Table 6.2, this procedure allows obtaining a very good agreement of the steady-state forces for the rigid body model of the complete vehicle and for the model of the single flexible wheelset.

The low frequency multibody simulation is performed using software ADTreS developed at Politecnico di Milano [175] and considers a vehicle formed by one carbody, two bogies and four wheelsets. It refers to the trailed car of a concentrated power train for high speed passenger service. The vehicle is equipped with a solid axle wheelset with monobloc, light design wheels. The track considered features UIC60 rails and track parameters are based on the EUROBALT project [175], considering a 'stiff' track. Table 6.1 summarises the input data used to set up the simulation model. All the above described boundary conditions are applied in the flexible wheelset model Eq. (5.26) by appropriately setting the terms in vector $\mathbf{Q}_s$. These consist of the generalised forces associated with the modal coordinates $\mathbf{q}$ of the concentrated forces applied at the axle-box seats, defined as explained above in this section.

Wheelset model data		**Track model data**	
Mass of wheelset [kg]	1375	Sleeper bay [m]	0.6
Axle load [kN]	120	Sleeper number	70
Primary susp. long. stiffness [MN/m]	7.5	Sleeper mass [kg]	324
Primary susp. lateral stiffness [MN/m]	7.1	Track bed stiffness [MN/m]	200
Primary susp. vertical stiffness [MN/m]	0.81	Track bed damping [kN s/m]	150
Primary susp. long. damping [kN s/m]	100	Rail pad stiffness [GN/m]	1
Primary susp. lateral damping [kN s/m]	100	Rail pad damping [kN s/m]	50
Primary susp. vertical damping [kN s/m]	30	Rail section	UIC60

Table 6.1. Simulation parameters and properties.

	Outer wheel		**Inner wheel**	
	Rigid multibody	Flexible wheelset	Rigid multibody	Flexible wheelset
Vertical force [kN]	69.57	70.01	49.82	49.71
Lateral force [kN]	5.68	5.91	-3.75	-3.99
Longitudinal force [kN]	14.39	15.16	-14.39	-15.16

Table 6.2. Steady-state wheel/rail contact forces for the rigid multibody model of the entire vehicle and for the single flexible wheelset model.

6.2.3 Track model

Timoshenko beam is used in this section to compare with the 3D MEM. This model allows including vertical/lateral bending and torsional deformations. Rail vibration is formulated as modal superposition for the unconstrained rail with cyclic boundary conditions, hence resulting into a set of decoupled 1-dof (degrees of freedom) equations. According to Ref. [7], for one single Timoshenko beam the frequency range of validity is up to 1.5 kHz for lateral rail vibration and up to 2 kHz for vertical vibration. In order to minimise errors caused by modal truncation, all the rails modes of vibration falling in the range below 8.5 kHz has been considered. A procedure for obtaining an optimised number of modes was proposed in Ref. [162]. The lateral and vertical displacements of the rail axis and the torsion and the rotations of the cross-section are, respectively:

$$w_\tau(x_1,t)=\sum_r W_{\tau,r}(x_1)\,q_{\tau,r}(t),\quad \tau=2{,}3, \tag{6.1}$$

$$\psi_j(x_1,t)=\sum_r \Psi_{j,r}(x_1)\,q_{j,r}(t),\quad j=1{,}2{,}3, \tag{6.2}$$

where $W_{\tau,r}(x_1)$ and $\Psi_{j,r}(x_1)$ are the r-th modal functions of the Timoshenko periodic beam, and $q_{\kappa,r}(t)$ are the modal coordinates associated with torsional, lateral and vertical rail vibrations, respectively. The resulting r-th equation of motion for the cyclic track model in modal coordinates take the form:

$$\ddot{q}_r+2\,\xi_r\,\omega_r\,\dot{q}_r+\omega_r^2\,q_r=f_r, \tag{6.3}$$

being ω_r the r-th undamped frequency and ξ_r the modal damping. The modal forces f_r are computed from the wheel/rail contact and rail pad forces acting on the track. In this way, the displacements of the rail in the present contact point can be evaluated from the displacements and rotations of the rail axis as follows:

$$\mathbf{x}_{r,i}=\mathbf{E}_i\begin{pmatrix}w_{2,i} & w_{3,i} & \psi_{1,i} & \psi_{2,i} & \psi_{3,i}\end{pmatrix}^{\mathrm{T}}, \tag{6.4}$$

where $\mathbf{x}_{r,i}$ is the vector of contact point displacements in i-th rail ($i=1{,}2$), and the matrix $\mathbf{E}_i$ relates the displacements in rail axis and contact points.

A 3D flexible finitely long rail through the ME technique (see Section 5.4) is also used in this section. For the simulations carried out, 400 vibration modes of each rail have been considered, covering a frequency range up to 8.5 kHz.

6.2.4 Wheel/rail contact model

The model of wheel/rail contact used for these simulations is different than the developed in Section 5.6, as a result of the collaboration with Politecnico di Milano. To reproduce the dynamic coupling between the vehicle and the track, a pre-tabulated, multi-Hertzian contact model [176] is adopted. Prior to the simulation, wheel/rail contact geometry is processed starting from measured or theoretical wheel and rail profiles and the contact parameters required to compute wheel/rail contact forces are stored in a contact table. According to this procedure, the change in the location of the contact point due to the instantaneous deformation of the wheelset is neglected in the calculation of the contact forces. This simplification is justified because the magnitude of the elastic wheel deformation is much smaller than the rigid lateral movement of the wheelset relative to the track.

The parameters stored in the contact table are the contact angle, the variation of the wheel rolling radius with respect to the nominal one, the curvatures of the wheel and rail profiles in the contact point region and an undeformed distance which is equal to zero for the geometric contact point and greater than zero for the other potential contact points. More details of the process used to derive the contact table can be found in [177]. With respect to the theory presented there, note that the effect of the angle of attack is neglected in this work and thus leading to a simplified planar contact problem.

In order to compute the contact forces at time t, the relative wheel/rail lateral displacement is computed and the contact tables are interpolated, finding the contact parameters for one or more wheel/rail potential contact points. Then, for each i-th potential contact point of the j-th wheel/rail couple the normal problem is solved. To this aim, the elastic penetration is computed by projecting the relative wheel/rail displacements in the contact point along the direction normal to the contact plane, which is defined by the contact angle parameter in the contact table. Eq. (5.150) is followed to obtain the incremental penetration. The normal force is computed as function of the elastic penetration according to Hertz’s formulae in Eq. (5.155) using the profile curvatures retrieved from the contact table. The creep forces are then computed as function of the creepages, computed according to Eqs. (5.151)−(5.153).

Finally, the normal and creep forces obtained at each *i*-th contact point are projected along the trajectory frame $\mathbf{X}_T\mathbf{Y}_T\mathbf{Z}_T$ and summed over all active contacts occurring in the same wheel/rail couple, and the components of the resulting contact forces along the modal coordinates $\mathbf{q}$ are derived by standard application of the principle of virtual work, providing vector $\mathbf{Q}_c$ in Eq. (5.26).

6.2.5 Results

Figs. 6.1 and 6.2 show the time history of the vertical and lateral contact forces respectively for excitation caused by randomly corrugated rails, assuming a corrugation spectrum corresponding to the ISO 3095 limit [178], which establishes a third-octave band spectrum of the rail roughness. As expected, the dynamic fluctuations of the vertical and lateral contact forces show a complex waveform, arising from the dynamic response of the wheelset/track system to broadband random excitation. The results for both track models present a similar trend and mean values, although higher frequency content is observed for the 3D MEM in the vertical contact force.

An alternative plot for the wheel/rail contact force is made in the frequency domain. Fig. 6.3 represents the third-octave band spectrum of the vertical contact forces. There appear peaks in the antiresonances of the track frequency between the P2 and pinned-pinned frequencies in the 100–300 Hz band, and also in the band between 900 and 1400 Hz, whereas the smaller responses are at the P2 frequency (below 100 Hz), pinned-pinned frequency (below 1 kHz) and at a resonance frequency below 3 kHz. It can be observed that the Timoshenko beam shows greater vertical contact forces in the low and medium frequency range (up to 1 kHz, range of validity for the Timoshenko beam), while the 3D MEM shows higher frequency content for higher frequencies (1–8.5 kHz band). These higher harmonics seem to be crucial to describe the high-frequency noise, as rolling and squeal noise.

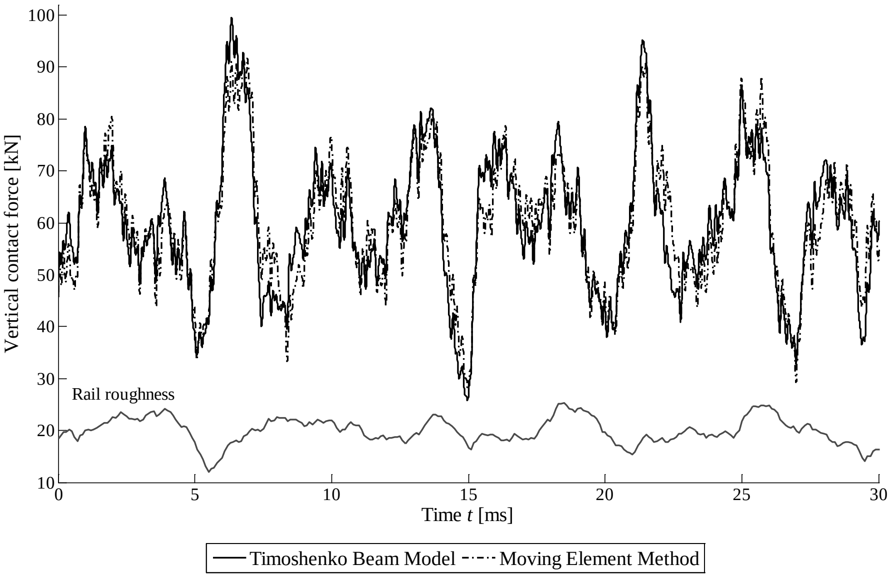

Fig. 6.1. Vertical wheel/rail contact forces for 300 km/h of speed on a randomly corrugated tangent track. Amplitudes corresponding to the ISO 3095 limit.

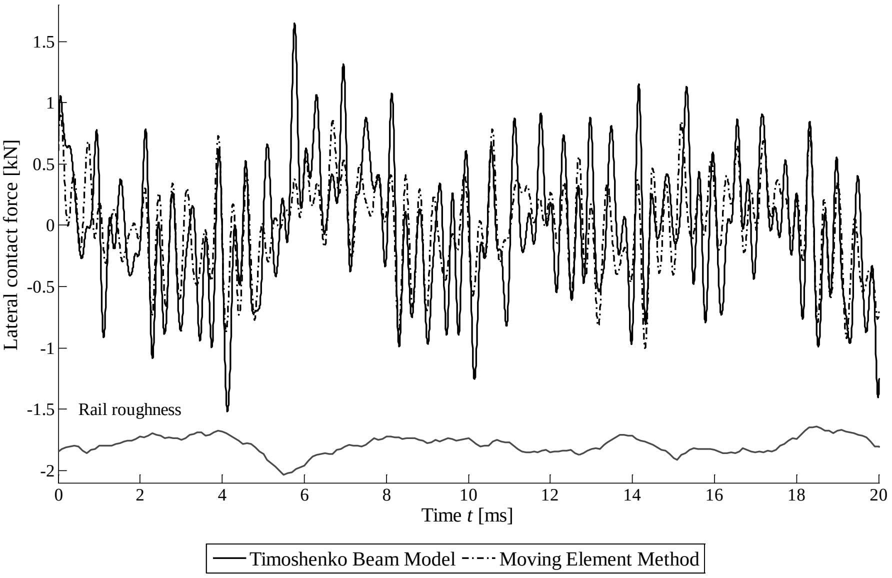

Fig. 6.2. Lateral wheel/rail contact forces for 300 km/h of speed on a randomly corrugated tangent track. Amplitudes corresponding to the ISO 3095 limit.

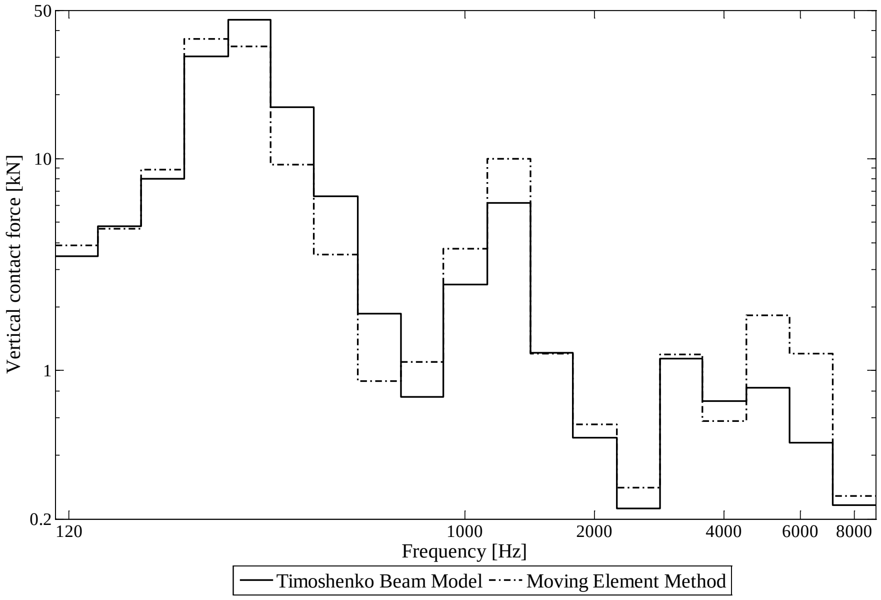

Fig. 6.3. Frequency domain plot of the vertical wheel/rail contact forces when the vehicle circulates at 300 km/h speed on a randomly corrugated tangent track. Amplitudes corresponding to the ISO 3095 limit.

Figs. 6.4 and 6.5 show the time history of the vertical and lateral contact forces with both rail models caused by a wheel flat when the wheelset runs over a perfectly even tangent track. In the simulations, a rounded geometry of the wheel flat with size 0.05 m is adopted. Intense dynamic effects are observed in both contact forces, initially leading to the occurrence of full loss of contact in the wheels, then followed by a severe impact causing peaks, and finally by a transient vibration that generates further dynamic fluctuations in all the force components. Results for both track models present again similar trends and mean values, the differences between both models being small in terms of duration of the contact loss. The maximum value of the vertical contact force, however, is larger when the 3D MEM is used. These results may indicate vertical contact forces will cause accelerated damage and degradation of the contacting surfaces as well as increased noise and vibration. The first overloading for this model is about 2.7 times the steady-state load, being 2.5 times for the Timoshenko beam. For the second overloading, the 3D MEM reaches 2.1 times the steady-state load, while Timoshenko approach yields 1.7. Finally, a higher frequency content in vertical contact force with the 3D ME model is observed.

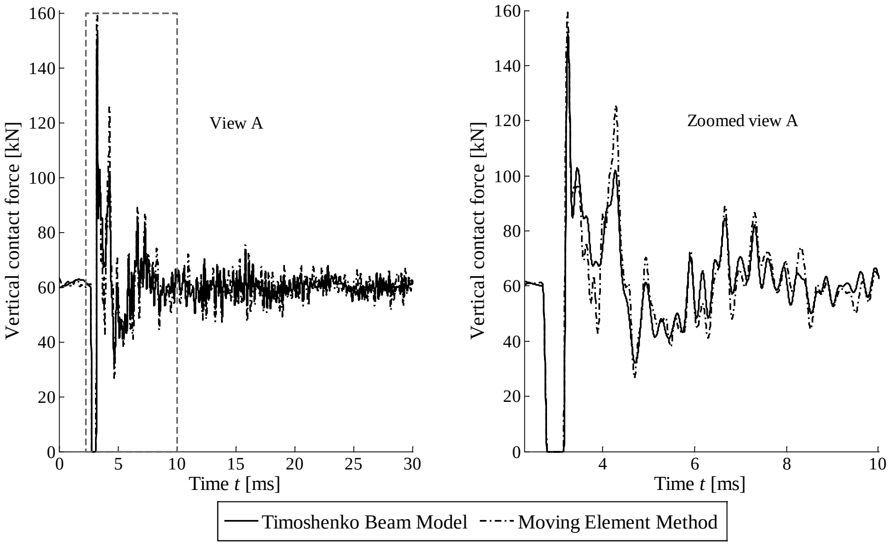

Fig. 6.4. Vertical wheel/rail contact forces when the vehicle circulates at 300 km/h speed on a perfectly even tangent track in presence of a 0.05 m wheel flat.

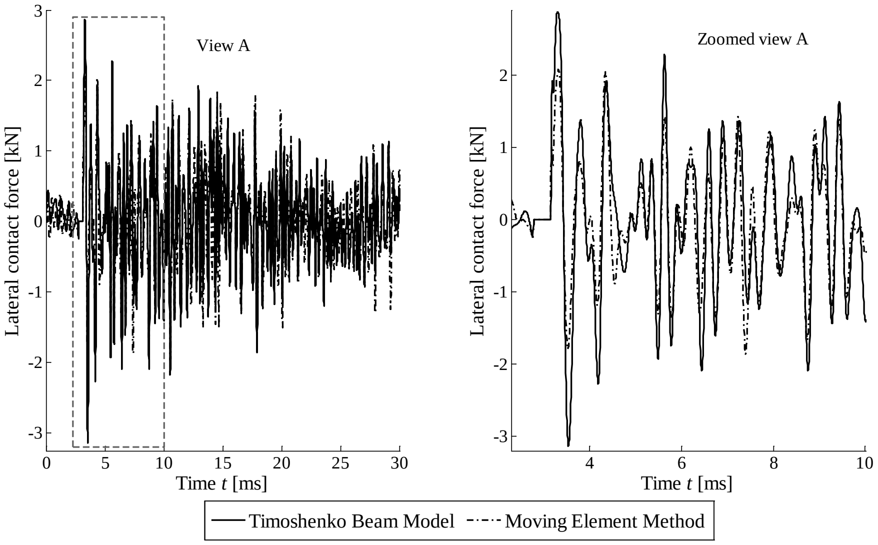

Fig. 6.5. Lateral wheel/rail contact forces when the vehicle circulates at 300 km/h speed on a perfectly even tangent track in presence of a 0.05 m wheel flat.

Fig. 6.6 represents the third-octave band spectrum of the vertical contact forces caused by a wheel flat. The Timoshenko beam shows a slightly higher vertical contact force in low-medium frequency range up to 450 Hz, but the 3D MEM reveals a markedly content for higher frequencies (450 Hz – 8.5 kHz band). These results are consistent with the previous figure in time domain, concluding that the 3D MEM describes the high-frequency dynamics more accurately than the Timoshenko model.

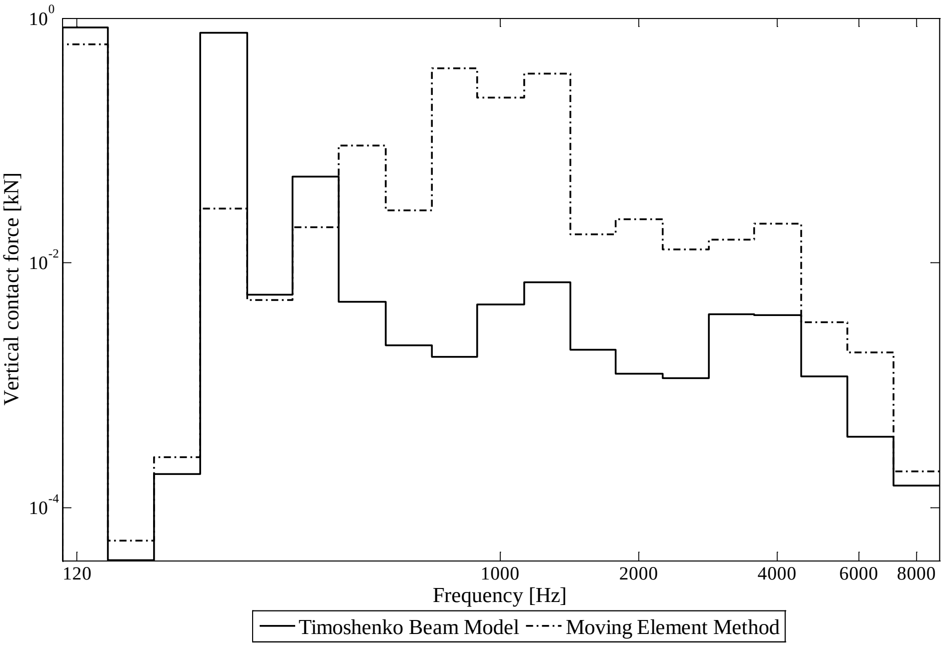

Fig. 6.6. Frequency domain plot of the vertical wheel/rail contact forces when the vehicle circulates at 300 km/h speed on a perfectly even tangent track in presence of a 0.05 m wheel flat.

6.2.6 Discussion

Results for the vertical and lateral contact forces are presented for two types of excitation: randomly corrugated tangent track and excitation arising from a wheel flat when the wheelset runs over a perfectly even track at 300 km/h. The 3D MEM and Timoshenko beam have been compared in all the simulations. Both models show a similar behaviour in the low and mid frequency domain for two excitation cases, where similar trends and mean values are observed.

In the randomly corrugated track case considered, the Timoshenko beam model shows a larger vertical contact force in low and mid frequency range up to 1 kHz (range of validity for the Timoshenko beam), but the 3D MEM shows a higher frequency content for the 1–8.5 kHz band. These higher harmonics seem to be crucial to describe the high-frequency phenomena, such as rolling and squeal noise.

For wheel flat excitation, the first and second overloading of the vertical contact force using 3D MEM are larger than those obtained with the Timoshenko beam model. Therefore, it may be expected to cause accelerated damage and degradation of the contacting surfaces as well as increased noise and vibration. In frequency domain, the Timoshenko beam shows slightly greater vertical contact forces in low and mid frequency range up to 450 Hz, but the 3D MEM model shows a remarkably higher frequency content in the 450 Hz – 8.5 kHz band.

Finally, these results validate the 3D MEM as an efficient flexible track model whereas it reproduces consistently the contrasted behaviour of the Timoshenko beam for its range of validity according to the literature. It is concluded that the proposed 3D MEM track model seems to be suitable to describe the high-frequency dynamics associated with different railway phenomena such as short pitch rail corrugation, wheel flat excitation, axle fatigue, rolling, squeal and braking noise.

6.3 LINEAR STABILITY ANALYSIS AND NON-LINEAR TIME-DOMAIN SIMULATION FOR A SINGLE WHEELSET NEGOTIATING A CURVE

6.3.1 Introduction

The first approach to the curve squeal phenomenon along the period of the thesis was possible thanks to the collaboration with the Department of Applied Mechanics in Chalmers University of Technology. As explained in Section 2.2, wheel/rail creep forces allow for steering of railway vehicles; but in unfavourable conditions, such as in small radius curves, this ability sometimes coincides with the generation of a high-frequency tonal noise referred to as curve squeal. Curve squeal originates due to friction-induced vibrations at frequencies corresponding to axial modes of the railway wheel [7]. At squeal frequencies, the wheel mobility exceeds that of the rail making the wheel to become the dominating noise source [7]. Hence, in the development of models for squeal prediction, it is of fundamental importance to accurately capture the high-frequency dynamic wheel behaviour.

Two instability mechanisms for squeal noise identified and explained in the literature review are: the constant friction mechanism [25] and the negative friction-velocity slope associated with ‘negative damping’ [5]. Most available models for curve squeal in the literature are formulated in the frequency-domain and adopt the negative friction-velocity slope as instability mechanism. In the related research area of automotive disc brake squeal, the constant friction mechanism in combination with linear complex eigenvalue analysis is recognised as one of the most accepted investigation procedures [179].

In this section, curve squeal of the Stockholm metro (details are found in Ref. [180]) is investigated using a combination of models for linear complex stability analysis in the frequency domain and non-linear wheel/rail interaction in the time domain. On one hand, the model for complex stability analysis of railway tread brake squeal presented in Ref. [181] is further developed to simulate curve squeal. On the other hand, the model for non-linear wheel/rail interaction adopted in this section is the one developed in Ref. [13]. The same submodels are used in both squeal models as far as possible to ensure comparability. The application of two different types of models allows the comparison and evaluation of a frequency and time-domain approach for curve squeal. Especially, the capability of the linear stability analysis to predict the onset of squeal and the squeal frequencies is evaluated. Conditions similar to those of a 120 m radius curve on the Stockholm metro exposed to severe curve squeal are studied [182].

6.3.2 Wheel and track models

Viewed from the wheel/rail contact, the rotation causes some of the wheel resonance peaks to split corresponding to waves travelling in opposite directions. By using a non-rotating wheel loaded by a wheel/rail contact force travelling at constant speed around the wheel perimeter, Thompson was able to account for the splitting of resonance peaks even though neglecting inertia effects due to rotation [7]. The introduction of a rotating flexible wheelset in Ref. [55,160] (see Section 5.3), which fully accounts for inertia forces such as gyroscopic forces and centrifugal stiffening, allows an important step in finding these wheel resonance peaks.

Table 6.3 lists the parameters of a C20 wheel parameters meshed with solid quadratic elements. The vehicle model does not include the wheel axle nor the bogie frame.

Young's modulus, E^w [GPa]	207
Poisson's ratio, ν^w [-]	0.29
Density, ρ^w [kg/m^3]	7820
Wheel mass, m^r [kg/m]	657
Wheel radius, r^w [mm]	0.39
Dof number	122880

Table 6.3. C20 wheel parameters.

As a consequence the dynamic interaction below 250 Hz is neglected. Clamped boundary conditions are modelled at the inner surface of the wheel hub. Wheel modal damping ζ is introduced according to the approximate values by Thompson [7]:

$$\zeta = \begin{cases} 10^{-3} & \text{for } n = 0, \\ 10^{-2} & \text{for } n = 1, \\ 10^{-4} & \text{for } n \geq 2, \end{cases} \tag{6.5}$$

where n is the number of nodal diameters of the eigenmode. The number of degrees of freedom is reduced through modal expansion retaining a truncated set of 200 modes corresponding to a highest eigenfrequency of about 13 kHz. Point receptances of the wheel calculated in the wheel/rail contact node are shown in Fig. 6.7.

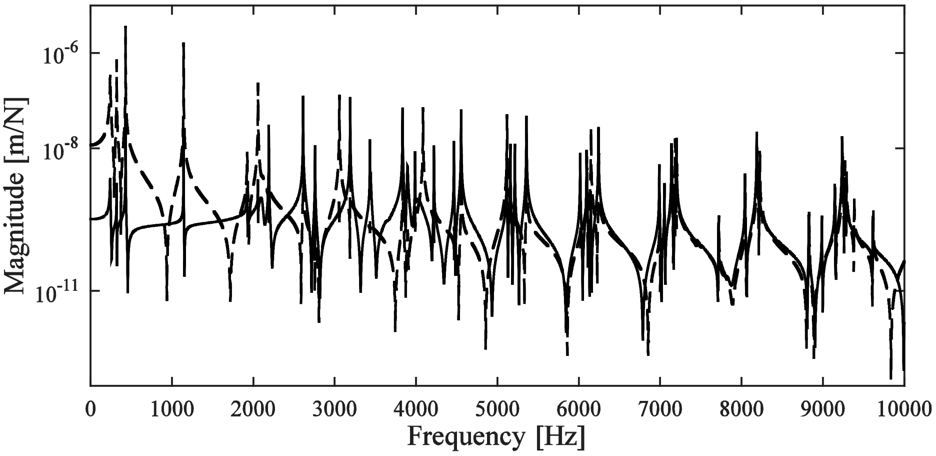

Fig. 6.7. Magnitudes of wheel receptance calculated for excitation at the wheel/rail contact node. ——: vertical point receptance, - — -: lateral point receptance.

The track is represented by a rail supported by a uniform viscoelastic Winkler bedding. Its structural flexibility is included by the 3D MEM approach from Eq. (5.71). A rail with BV50 profile is modelled with solid quadratic elements (20-nodes). The mesh corresponds to a longitudinal element length throughout the model of 5 cm for a uniform longitudinal mesh. Cyclic boundary conditions are modelled at the rail ends. Table 6.4.details the rail parameters. The Winkler bedding is modelled with a uniform distribution of vertical stiffness and damping equivalent to a discrete rail. The stiffness and damping in the longitudinal and lateral directions are modelled as 10% and 80% from previous values, respectively. Modal synthesis retaining a truncated set of the 2000 lowest frequency modes is performed. Point receptances calculated in the wheel/rail contact node are shown in Fig. 6.8. These receptances are close to the calculated ones by Pieringer [13] for the same parameters but using WANDS software [13,67] based on waveguide finite elements, which takes advantage of the 2D geometry of the rail having a constant cross-section and it considers the 3D nature of the vibration by assuming a wave-type solution along the rail.

Young's modulus, E^r [GPa]	207
Poisson's ratio, ν^r [-]	0.29
Density, ρ^r [kg/m^3]	7860
Rail length, L [mm]	42
Dof number	406065
Winkler vertical stiffness, $k_{w,3}$ [MN/m]	43.7
Winkler vertical damping, $c_{w,3}$ [kNs/m]	12.6

Table 6.4. BV50 rail parameters.

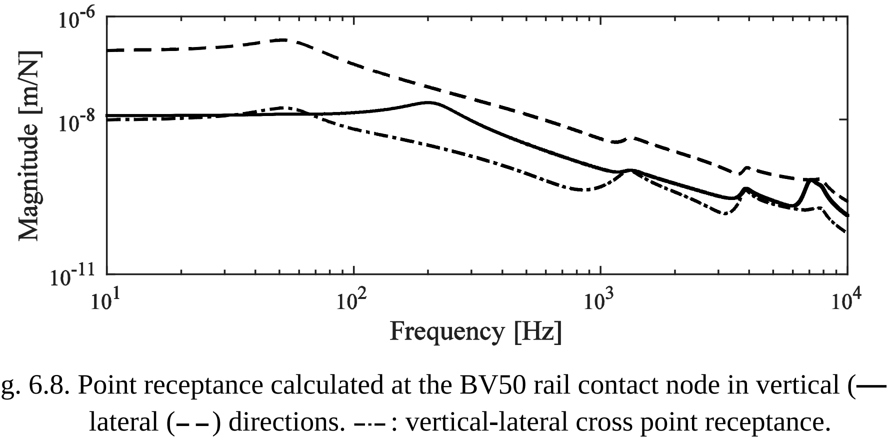

Fig. 6.8. Point receptance calculated at the BV50 rail contact node in vertical (—) and lateral (– –) directions. –·– : vertical-lateral cross point receptance.

6.3.3 Wheel/rail contact model

The wheel/rail contact is solved using an implementation of Kalker's variational method [81], which includes the algorithms NORM and TANG for normal and tangential contact, respectively. The local friction model applied in each contact element is Coulomb's law.

In Ref. [180], simulations for conditions corresponding to those in the studied curve on the Stockholm metro resulted in a lateral displacement and an angle of attack of the leading wheelset in a bogie of approximately y = 14 mm and ψ = 1.2°, respectively (see the sketch in Fig. 2.4 of Section 2.2.1). This case is modelled here for the low rail contact. The vertical preload is 55 kN. A nominal S1002 wheel profile and BV50 rail profile with inclination 1:40 are used. The contact angle is 5.1 mrad.

In the non-linear time-domain simulation, NORM and TANG are solved in each time step giving the contact pressure distribution, the tangential tractions and the division of the contact zone into stick and slip zones. The stability analysis requires the coupled equations of motion to be linearised around the quasi-static curving condition. In these simulations, the normal contact problem is modelled by a linear normal contact stiffness $K_H = 1.057$ GN/m corresponding to the slope of the force-displacement curve obtained with NORM at the vertical preload.

For large angle of attack as considered here, the complete contact zone is in slip at the onset of unstable vibrations [180]. In the limit cycle obtained in the time-domain simulation, the contact zone changes periodically between full slip and partial slip. As the stability analysis only considers the onset of unstable vibrations, it is sufficient to model full slip in the wheel/rail contact in this numerical approach. In order to allow for a direct comparison of the time- and frequency-domain approaches, time-domain simulations are performed for the linearised wheel/rail system as well.

The stability analysis described above requires the coupled equations of motion to be linearised around the quasi-static curving condition. The normal contact force is calculated as

$$F_3 = K_{H,lin}\,\delta, \tag{6.6}$$

expression linearised from Eq. (5.155):

$$K_{H,lin} = \left.\frac{dF_3}{d\delta}\right|_{\delta_0} = \frac{3}{2}K_H \delta_0^{1/2} = \frac{3}{2}\frac{F_{30}}{\delta_0}. \tag{6.7}$$

The elastic penetration is estimated as

$$\delta = \left(\mathbf{u}_c^r - \mathbf{u}_c^w\right) \cdot \mathbf{n}_c, \tag{6.8}$$

where $\mathbf{n}_c$ is the unit normal vector of the contact plane and $\mathbf{u}_c^r$ and $\mathbf{u}_c^w$ are the contact node displacement vector of rail and wheel. In order for Eq. (6.6) to be introduced into Lagrange equations it is transformed into a generalised force vector. Utilising Newton's third law, the following is obtained for the coupled wheel/rail system:

$$\mathbf{Q}_{c,n} = K_H \begin{pmatrix} \mathbf{\Phi}_{c,n}^r & \mathbf{0} \\ \mathbf{0} & \mathbf{\Phi}_{c,n}^w \end{pmatrix}^{\mathrm{T}} \begin{pmatrix} \mathbf{\Phi}_{c,n}^r & -\mathbf{\Phi}_{c,n}^w \\ -\mathbf{\Phi}_{c,n}^r & \mathbf{\Phi}_{c,n}^w \end{pmatrix} \begin{pmatrix} \mathbf{q}^r \\ \mathbf{q}^w \end{pmatrix}, \tag{6.9}$$

where

$$\mathbf{\Phi}_{c,n}^r = \mathbf{n}_c^{\mathrm{T}} \mathbf{\Phi}_c^r, \; \mathbf{\Phi}_{c,n}^w = \mathbf{n}_c^{\mathrm{T}} \mathbf{\Phi}_c^w. \tag{6.10}$$

The external tangential generalised force vector is then calculated as:

$$\mathbf{Q}_{c,t} = \mu \mathbf{Q}_{c,n} = \mu K_{H,lin} \begin{pmatrix} \mathbf{\Phi}_{c,t}^r & \mathbf{0} \\ \mathbf{0} & \mathbf{\Phi}_{c,t}^w \end{pmatrix}^{\mathrm{T}} \begin{pmatrix} \mathbf{\Phi}_{c,n}^r & -\mathbf{\Phi}_{c,n}^w \\ -\mathbf{\Phi}_{c,n}^r & \mathbf{\Phi}_{c,n}^w \end{pmatrix} \begin{pmatrix} \mathbf{q}^r \\ \mathbf{q}^w \end{pmatrix}, \tag{6.11}$$

where

$$\mathbf{\Phi}_{c,t}^r = \mathbf{t}(\varphi)_c^{\mathrm{T}} \mathbf{\Phi}_c^r, \; \mathbf{\Phi}_{c,t}^w = \mathbf{t}(\varphi)_c^{\mathrm{T}} \mathbf{\Phi}_c^w, \tag{6.12}$$

and where $\mathbf{t}(\varphi)_c$ is a unit vector acting in the plane of the wheel/rail contact in the direction given by φ, where $\varphi = 0^\circ$ corresponds to the longitudinal (vehicle travelling) direction on the rail.

6.3.4 Solution procedure

Both squeal models incorporate the wheel, track and contact models previously described. The solution procedure for the linear stability analysis and the non-linear time-domain model are briefly described in the following.

6.3.4.1 Linear stability analysis

Homogenous equations of motion for the coupled wheel/rail system are assembled by considering Eq. (5.26) for the rotating wheelset, Eq. (5.81) for both rails (inner *inn* and outer *out*) supported by a uniform viscoelastic Winkler bedding, and the previous Eqs. (6.9) and (6.11) for the simplified wheel/rail contact formulation proposed for the linear stability analysis:

$$
\begin{aligned}
&\begin{pmatrix} \ddot{\mathbf{q}}^{w} \\ \ddot{\mathbf{q}}^{r}_{inn} \\ \ddot{\mathbf{q}}^{r}_{out} \end{pmatrix}
+\begin{pmatrix} 2\left(\Omega\,\tilde{\mathbf{V}}^{w}+\tilde{\mathbf{P}}^{w}\right) & \mathbf{0} & \mathbf{0} \\ \mathbf{0} & -2V\tilde{\mathbf{C}}^{r}+\tilde{\mathbf{C}}^{r}_{wink}+\tilde{\mathbf{C}}^{r}_{\zeta} & \mathbf{0} \\ \mathbf{0} & \mathbf{0} & -2V\tilde{\mathbf{C}}^{r}+\tilde{\mathbf{C}}^{r}_{wink}+\tilde{\mathbf{C}}^{r}_{\zeta} \end{pmatrix}
\begin{pmatrix} \dot{\mathbf{q}}^{w} \\ \dot{\mathbf{q}}^{r}_{inn} \\ \dot{\mathbf{q}}^{r}_{out} \end{pmatrix} \\
&+\begin{pmatrix} \Omega^{2}\left(\tilde{\mathbf{A}}^{w}-\tilde{\mathbf{C}}^{w}\right)+2\,\Omega\,\tilde{\mathbf{S}}^{w}+\tilde{\mathbf{R}}^{w}-\tilde{\mathbf{B}}^{w}+\tilde{\mathbf{D}}^{w}+\tilde{\mathbf{k}}^{w,w}_{c,inn}+\tilde{\mathbf{k}}^{w,w}_{c,out} & -\tilde{\mathbf{k}}^{w,r}_{c,inn} & -\tilde{\mathbf{k}}^{w,r}_{c,out} \\ -\tilde{\mathbf{k}}^{r,w}_{c,inn} & \tilde{\mathbf{K}}^{r}-V^{2}\tilde{\mathbf{A}}^{r}+\tilde{\mathbf{K}}^{r}_{wink}+V\,\mathbf{K}\tilde{\mathbf{C}}^{r}_{wink}+\tilde{\mathbf{k}}^{r,r}_{c,inn} & \mathbf{0} \\ -\tilde{\mathbf{k}}^{r,w}_{c,out} & \mathbf{0} & \tilde{\mathbf{K}}^{r}-V^{2}\tilde{\mathbf{A}}^{r}+\tilde{\mathbf{K}}^{r}_{wink}+V\,\mathbf{K}\tilde{\mathbf{C}}^{r}_{wink}+\tilde{\mathbf{k}}^{r,r}_{c,out} \end{pmatrix}
\begin{pmatrix} \mathbf{q}^{w} \\ \mathbf{q}^{r}_{inn} \\ \mathbf{q}^{r}_{out} \end{pmatrix} \\
&=\ddot{\mathbf{q}}^{wr}+\tilde{\mathbf{C}}^{wr}\dot{\mathbf{q}}^{wr}+\tilde{\mathbf{K}}^{wr}\mathbf{q}^{wr}=\mathbf{0},
\end{aligned}
\tag{6.13}
$$

where $\mathbf{q}^{wr}=\left[\mathbf{q}^{w}\quad \mathbf{q}^{r}_{inn}\quad \mathbf{q}^{r}_{out}\right]^{\mathrm{T}}$ and

$$
\tilde{\mathbf{k}}^{i,j}_{c,k}=-K_{H,lin,k}\left(\mathbf{\Phi}^{i}_{(c,n),k}+\mu\mathbf{\Phi}^{i}_{(c,t),k}\right)^{\mathrm{T}}\mathbf{\Phi}^{j}_{(c,n),k},\quad i=w,r;\quad j=w,r;\quad k=inn,out. \tag{6.14}
$$

Linear stability is investigated through complex eigenvalue analysis. Eq. (6.15) is cast into first-order (state-space) form as:

$$
\tilde{\mathbf{A}}^{wr}\dot{\mathbf{z}}+\tilde{\mathbf{B}}^{wr}\mathbf{z}=\mathbf{0}, \tag{6.15}
$$

where

$$
\tilde{\mathbf{A}}^{wr}=\begin{pmatrix} \tilde{\mathbf{C}}^{wr} & \mathbf{I} \\ \mathbf{I} & \mathbf{0} \end{pmatrix},\ \tilde{\mathbf{B}}^{wr}=\begin{pmatrix} \tilde{\mathbf{K}}^{wr} & \mathbf{0} \\ \mathbf{0} & -\mathbf{I} \end{pmatrix},\ \mathbf{z}=\begin{pmatrix} \mathbf{q}^{wr} \\ \dot{\mathbf{q}}^{wr} \end{pmatrix}. \tag{6.16}
$$

Eq. (6.15) represents a linear non-symmetric (caused by inertia effects due to convective terms and the friction coupling) eigenvalue problem that is solved in the considered frequency range below 8.5 kHz. Unstable eigenmodes of the coupled train/track system are indicated by positive real-parts of the associated eigenvalues.

The magnitude of the positive real-part gives the rate of growth of the vibration amplitude of the associated eigenmode.

6.3.4.2 Non-linear time-domain simulations

In the time-domain model, wheel and rail are represented by impulse response functions or Green’s functions [172,173] that are calculated from the wheel and rail receptances at the contact point by inverse Fourier transform. As the wheel and the rail model incorporate effects of the train speed, the movement of the contact point around the wheel and along the rail is included in the Green’s functions. Instead of performing time integration, the wheel and rail displacements are obtained by convoluting the time series of contact forces with the pre-calculated Green’s functions. This procedure is relatively computationally efficient. The contact forces are calculated by solving the proposed normal and tangential contact models online in each time step. The detailed solution procedure is described in Ref. [65].

If squeal does not occur, the time series of the contact forces is (approximately) constant during quasi-static curving. If squeal occurs, an unstable vibration builds up which stops growing when it reaches the limit cycle.

6.3.5 Results

Negotiation of a C20 trainset through a curve of radius 120 m is considered. Conditions corresponding to the low rail contact of the leading wheelset in the second bogie are modelled. Both the influence of wheel/rail friction and of the direction of the resulting creep force on the occurrence of squeal is studied. The results presented in this section have been calculated for vanishing vehicle speed.

6.3.5.1 Linear stability analysis

Onset of instability is investigated for varying friction level and direction of the resulting creep force. The coloured markers in Fig. 6.9 correspond to eigenvalues that develop positive real-parts. In the following, the eigenmode associated with the largest magnitude positive real-part is referred to as the dominating unstable eigenmode. Instability is predicted from friction coefficient 0.2 and 0.5 upwards for the wheel in a purely under-radial ($\varphi=\pi/2$) and over-radial steering position ($\varphi=3\pi/2$), respectively. In addition, Fig. 6.9 shows the dominating unstable eigenmode to be influenced by the direction of the resulting creep force. For example instability is not predicted for a resulting creep force acting in the longitudinal direction (φ=0 or φ=π) independent of the friction level.

The spectrum of the real-parts of the eigenvalues calculated for μ=0.7 and φ=90° is shown in Fig. 6.10. The dominating unstable eigenmode at 430 Hz is found to correspond to a coupled wheel/rail vibration comprising the axial wheel mode with two nodal diameters (and zero nodal circles) and bending of the rail primarily in the lateral direction. The eigenmode corresponding to the peak at eigenfrequency 1140 Hz involves a vibration of the wheel mode with three nodal diameters.

Fig. 6.11 shows the spectrum of the real-parts of the eigenvalues calculated for μ=0.7 and φ=270°. Positive real-parts result at approximate frequencies 8220 Hz and 9264 Hz, which correspond to axial wheel modes with 10 and 11 nodal diameters, respectively.

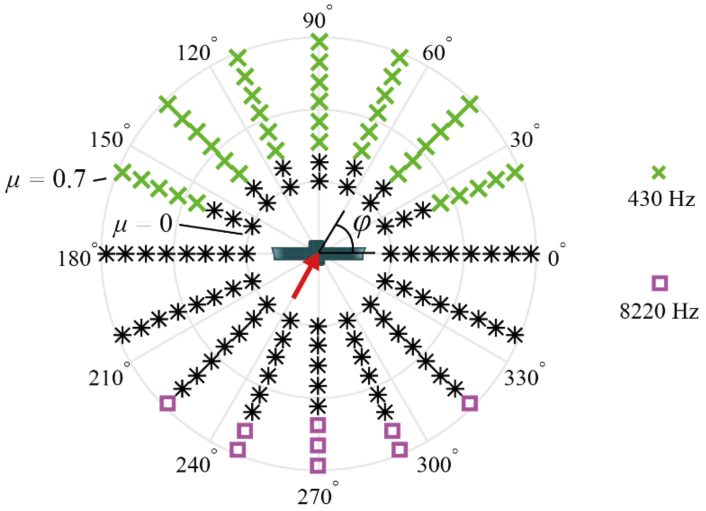

Fig. 6.9. Largest magnitude real-part of eigenvalues calculated for varying directions of the resulting creep force (acting in angle φ with respect to the vehicle running direction) and a wheel/rail friction coefficient in the range between 0 and 0.7. Unstable modes outlined with coloured markers. Black stars correspond to stable conditions.

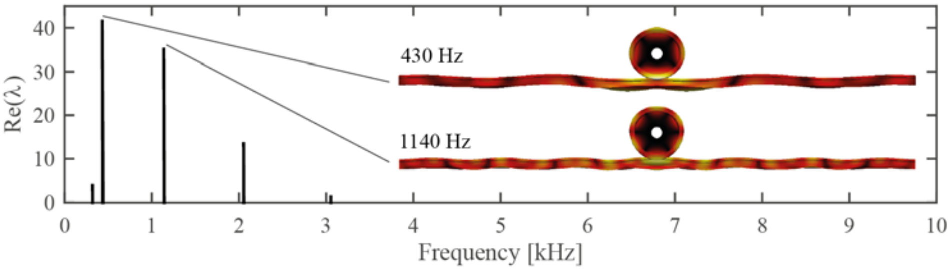

Fig. 6.10. Real-parts of eigenvalues calculated for φ=90° and μ=0.7. Eigenmodes associated with the largest magnitude real-parts are outlined.

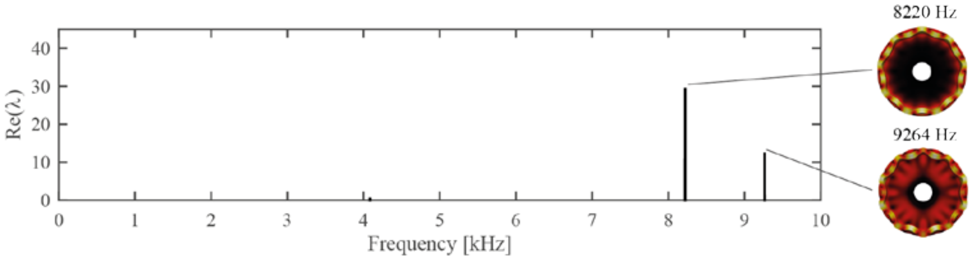

Fig. 6.11. Real-parts of eigenvalues calculated for φ=270° and μ=0.7. Eigenmodes associated with positive real-parts are outlined. The contribution from the track in the current eigenmodes was found insignificant (not shown here).

6.3.5.2 Non-linear time-domain simulations

The calculations for creep force directions φ=90° and φ=270° and the friction coefficient μ varying from 0.1 to 0.7 have been repeated with the time-domain model both including the linear and the non-linear contact model. A lateral creepage with absolute value of 2% has been assumed. The time step is 1.8×10^{-5} s and the spatial resolution in the contact area is 0.25 mm and 1 mm in longitudinal and lateral directions. The total simulated time is 3.5 s. If squeal occurs in the linear model, the amplitude of the vibration grows to infinity. In the non-linear model, a limit-cycle with finite amplitude is reached, where the contact zone changes periodically between full slip and partial slip.

The results are given in Fig. 6.12 in terms of the main frequency component of the lateral contact force. For comparison, the corresponding results from the stability analysis are also shown again. The power spectra of the lateral contact force for μ=0.7 and creep force directions 90° and 270° are given in Figs. 6.13 and 6.14, respectively.

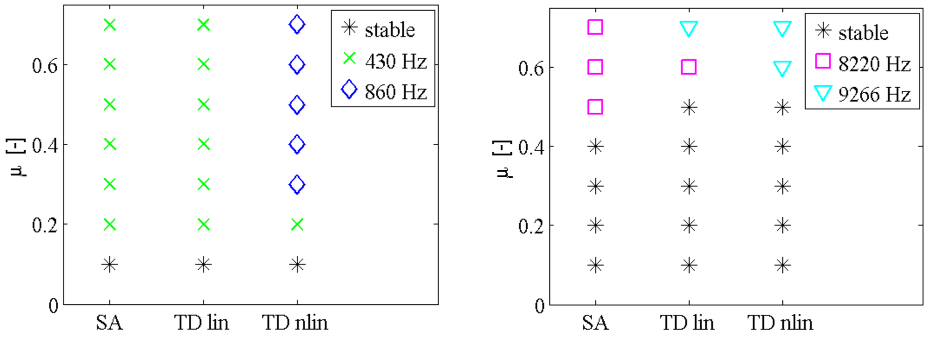

(a) (b)

Fig. 6.12. Frequency of the highest peak in the spectrum of the lateral contact force obtained in the linear time-domain (TD lin) and the non-linear time-domain simulations (TD nlin) in comparison to the frequency belonging to the largest positive real-part from the linear stability analysis (SA) for different friction coefficients: under-radial wheelset position, φ=90° (a) and over-radial wheelset position, φ=270° (b).

In the under-radial case, the results of the linear time-domain model agree with the results from the stability analysis in terms of the instability region and the main frequency component at 430 Hz, Fig. 6.12(a). The three peaks in the spectrum for μ=0.7, Fig. 6.13(a) agrees with the three main peaks in the spectrum of the real-parts of eigenvalues, see Fig. 6.11. The simulations with the non-linear time-domain model still give the same instability region and involve the same mode at 430 Hz, see Fig. 6.12(a), but the spectrum of the lateral contact force now shows also higher harmonics and the peak at the second harmonic is for most cases higher than the fundamental frequency, see Fig. 6.13(b).

In the over-radial case, results from the time-domain simulations are still similar to the stability analysis, see Fig. 6.12(b), but instability occurs at a slightly higher friction coefficient (0.6 instead of 0.5) and the main frequency component shifts from 8220 Hz to 9266 Hz for most squeal cases. A comparison of Fig. 6.11 and Fig. 6.14 shows that for μ=0.7, the same main unstable modes are detected with both models, but the order is reversed.

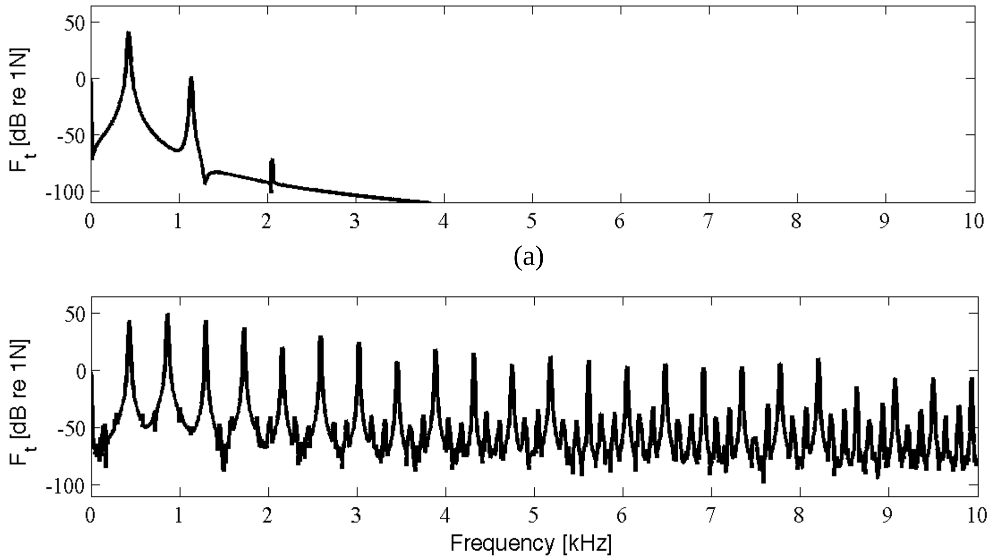

(a)

(b)

Fig. 6.13. Power spectrum of the lateral contact force for φ=90° and μ=0.7 obtained with the linear time-domain model (a) and the non-linear time-domain model (b).

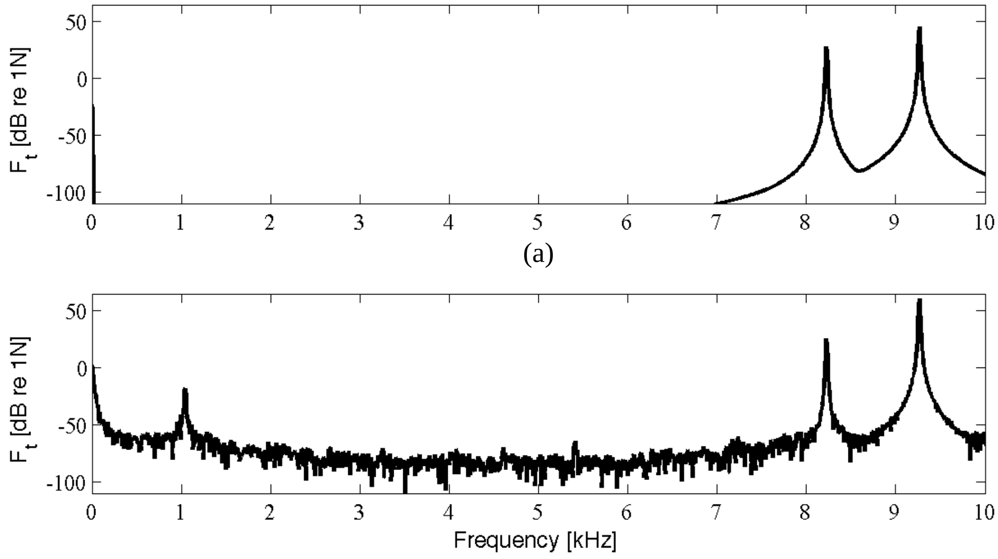

(a)

(b)

Fig. 6.14. Power spectrum of the lateral contact force for φ=270 and μ=0.7 obtained with the linear time-domain model (a) and the non-linear time-domain model (b).

6.3.6 Discussion

The linear stability analysis and the linear time-domain model give similar results, which supports that the models have been implemented correctly. The results are however not identical, which is reasonable since the same problem has been solved with two fundamentally different procedures. In addition, although the same submodels have been used in both the time- and frequency-domain approaches, there are still some small modelling differences. Currently, the time-domain model does for example not include the longitudinal dynamics of wheel and track, but only the lateral and vertical, while all three directions are included in the stability analysis. Another difference follows from the fact that the first value of the Green's functions in the time-domain model is set to zero. This value describes the instantaneous displacementof the contact point (partly due to the local deformation close to the contact point) at the wheel (or rail) in the moment a force is applied. Setting the first value of the Green's function to zero implies that in the time-domain approach the local instantaneous deformation at the contact point is only modelled in the contact model, while in the linear stability analysis there are in addition contributions from the FE-models of wheel and rail.

Comparing the linear and non-linear time-domain simulations reveals, on the one hand, the non-linear character of squeal since strong higher harmonics may be present and the main frequency component may differ between linear and non-linear simulations. On the other hand, the linear time-domain simulations and the linear stability analysis perform well in the prediction of the instability range and the unstable mode with the largest positive real part in the stability analysis corresponds in most of the investigated cases to the dominant unstable mode in the non-linear time-domain simulations.

In this discussion, it should be kept in mind that the magnitude of the real part of unstable modes in the stability analysis only provides the rate of growth of the instability and is not a selection criterion between different unstable modes. Massi *et al.* [183], who compared a linear and a non-linear approach for brake squeal, point out that the magnitude of the real part of unstable modes is not a selection criterion between different unstable modes. As the real part of the eigenvalue only provides the rate of growth of the instability, the system does not necessarily become unstable at the frequency corresponding to the largest positive real part. Instead they propose that “the modes involved in the squeal phenomenon are those characterised by larger amplitude of the deformed shape at the contact zone”. In addition, Massi *et al.* found that the complex eigenvalue analysis over-predicts the unstable regions in the parameter space in comparison to the non-linear time-domain simulations.

6.4 INVESTIGATION OF STICK/SLIP OSCILLATIONS IN CURVING CONDITIONS FOR CONSTANT FRICTION

6.4.1 Introduction

As a contribution to the controversial from the physical mechanism that originates curve squeal, the enhanced wheelset/track dynamic interaction model presented in this thesis is evaluated in curving conditions for constant friction in order to investigate whether these conditions can be sufficient to generate instabilities in the contact dynamics. In Section 2.1, this mechanism has been called constant friction mechanism, in contrast with the falling friction coefficient [5], based in the negative-damping effect caused.

In this section, curve squeal is investigated for two tight curve radii of 500 and 120 m and for different friction coefficients, which remain constant along the simulation. For these conditions, longitudinal creepage occurs since the outer wheel on a wheelset has a longer running distance through the curve than the inner wheel and the conicity of the wheels can only partly compensate for this difference in running distance. The leading wheelset in a bogie rolls with a high angle of attack against the rail in tight curves, which gives rise to a large lateral creepage. The simulations are run using the linear complex stability analysis in the frequency domain and the numerical time integration in the time domain.

6.4.2 Wheelset, track and contact models

Following the procedure detailed in Section 6.2.2, the vehicle is confined to one wheelset with primary suspension. The wheelset has been modelled as a flexible and rotating wheelset [55,160], in which Eulerian-modal coordinates are employed. 400 vibration modes of the wheelset have been considered, covering a frequency range up to 8.5 kHz in order to address the high-frequency range in which curve squeal occurs.

In order to reproduce the steady-state curving effects, appropriate forces are prescribed at the primary suspension; these forces are derived from the results of low-frequency multibody simulation in which the whole vehicle is considered, but all bodies are assumed to behave as rigid. The contact forces are applied in the contact patch that is reduced to a contact point. The stiffness of the primary suspensions is included in the wheelset model on the corresponding nodes where they are located. The weight of the axle boxes is introduced as discrete vertical forces. The weight of the wheelset is also included uniformly along the mesh using the FE method for its distribution. These implementations permit to calculate the pseudo-static deformed configuration of wheelset and rail.

The effect of low-frequency curving dynamics of the complete vehicle needs however to be included in the model in order to obtain suitable mean values for the creepages and contact forces. This is accomplished by prescribing the forces applied by the primary suspension to the wheelset in the vertical plane and the yaw rotation of the bogie at the primary suspension. While running through a curve, the wheelset develops steady-state values of the creepages and contact forces that are substantially different from the case of tangent track running. On account of the non-linearities of wheel/rail contact, these steady-state contact forces and creepages strongly affect the coupled wheelset/track dynamics in the entire frequency range addressed by the study, and therefore need to be properly taken into account in the numerical simulation procedure. It is also worth noticing that the elastic coupling of different wheelsets in the vehicle, typically via the primary suspensions and bogie frame, affects the steady-state contact forces and creepages in the curve. The low frequency multibody simulation is performed using multibody dynamic simulation software [171]. An ERRI-wagon is selected. It refers to the trailed car of a concentrated power train for high speed passenger service. The leading wheelset considered for the simulations is meshed with 12340 solid quadratic elements (20-nodes) and includes a total of 260145 degrees of freedom. It is equipped with a solid axle wheelset with monobloc, the brake discs and light S1002 design wheels.

The track is represented by a rail supported by a uniform viscoelastic Winkler bedding. Its structural flexibility is included by the 3D MEM approach from Eq. (5.71). A rail with UIC60 (60 kg/m) profile and 42 m length is modelled with 8452 solid quadratic elements (20-nodes) and includes a total of 170175 degrees of freedom. This corresponds to a uniform-linear longitudinal mesh in which the element length increases linearly from the central element to 60% of the half-length of the rail on each side, while the remaining 40% presents uniform element lengths. The central element length is 1 cm. Cyclic boundary conditions are modelled at the rail ends. The rail and the Winkler bedding present the same mechanical properties than the rail used in the previous set of simulations (see Section 6.3.2). Modal synthesis retaining a truncated set of the 2000 lowest frequency eigenmodes is performed, covering a frequency range up to 9.0 kHz.

In order to compute the contact forces at the instant *t*, the wheel/rail contact model adopted is based on the incremental method described in Section 5.6. The parameters that define the normal and tangential dynamics, approach and creepages, respectively, start from the pseudo-static deformations of wheelset and rail. These are pre-calculated from the quasi-static contact forces provided by the multibody. The relative wheel/rail displacement is computed, from which the incremental penetration and creepages are calculated for each instant. Again, the time step is 5.0×10^{-6} s and the spatial resolution in the contact area is 0.25 mm and 1 mm in longitudinal and lateral directions. The total simulated in each simulation in time is 1.0 s.

6.4.3 Results

It is intended to evaluate the interaction model in curving conditions with a constant coefficient of friction in order to see if the constant coefficient mechanism is sufficient itself to generate instabilities in the contact dynamics that can be potentially associated with curve squeal. Table 6.5 presents the relevant input data corresponding to eight simulations carried out for two curve radii and four friction coefficients. The vehicle speed V is set for both curve radii to make the non-compensated acceleration zero. Table 6.6 gathers the pseudo-static solution for the lateral displacements and creepages for both wheels of the leading wheelset corresponding to each simulation case computed by ADAMS multibody software.

Simulation	Curve radius, R^r [m]	Vehicle speed, V [km/h]	Friction coeff., μ [-]
I	120	39.13	0.20
II			0.32
III			0.40
IV			0.60
V	500	79.86	0.20
VI			0.32
VII			0.40
VIII			0.60

Table 6.5. Study cases simulated by the complete wheelset/track interaction model proposed.

Simulation	Lat. variation contact point outer wheel, Δy^{w}_{out} [mm]	Lat. variation contact point inner wheel, Δy^{w}_{inn} [mm]	Lat. creepage inner wheel, $\bar{\xi}_{2,inn}$ [-]	Lat. creepage outer wheel, $\bar{\xi}_{2,out}$ [-]
I	14.4	-32.8	0.0169	-0.0194
II	14.5	-35.1	0.0171	-0.0234
III	14.5	-36.2	0.0171	-0.0268
IV	14.5	-38.3	0.0172	-0.0437
V	14.0	-30.7	0.0052	-0.0056
VI	14.3	-32.5	0.0048	-0.0055
VII	14.3	-33.3	0.0046	-0.0055
VIII	14.4	-34.6	0.0046	-0.0056

Table 6.6. Pseudo-static lateral variations of the position of the contact point (with respect to the nominal contact point) and creepages for each simulation case.

Table 6.7 contains the quasi-static conditions of the leading wheelset for Simulation VII, with the lateral and vertical displacements of its centre of gravity, the angle of attack and the forces from the carbody. Table 6.8 lists the lateral variations of the position of the contact point (with respect to the nominal contact point) for both wheels, the contact contact angle, creepages and creep forces for Simulation VII (chosen for illustration purposes). ADAMS software uses the sign criteria defined by $\mathbf{X_T Y_T}$ in Fig. 5.2. All these values are used as mean values in the incremental contact algorithm adopted.

Lateral displacement, $\Delta\bar{y}^{COG}$ [mm]	6.2
Vertical displacement, $\Delta\bar{z}^{COG}$ [mm]	0.4
Angle of attack, $\bar{\psi}$ [º]	-0.264
Longitudinal force, $\bar{X}$ [N]	162
Lateral force, $\bar{Y}$ [N]	-1770
Vertical force, $\bar{Z}$ [N]	-109620

Table 6.7. Simulation VII: Quasi-static conditions for the leading wheelset.

Rail lat. var. contact point, $\Delta\bar{y}^r$ [mm]	-4.8/-29.8
Rolling radius, $\bar{r}_{11}$ [mm]	459.7/465.6
Normal angle, $\bar{\theta}$ [°]	-0.56/33.40
Longitudinal creepage, $\bar{\xi}_1$ [-]	0.0037/-0.0059
Spin creepage, $\bar{\xi}_{sp}$ [-]	0.021/-1.185
Longitudinal creep force, $\bar{F}_1$ [N]	-13672/13512
Lateral creep force, $\bar{F}_2$ [N]	-15243/17223
Vertical creep force, $\bar{F}_3$ [N]	52072/57783

Table 6.8. Simulation VII: Quasi-static conditions for the inner/outer wheels of the leading wheelset.

6.4.3.1 Linear stability analysis

The complex linear stability analysis is detailed in Section 6.3.4.1. The contact formulation is linearised using a normal contact stiffness $K_{H,lin}$ that depends on the contact conditions. The complete wheelset/track model in curve is computed and its corresponding eigenvalues are calculated for each simulation case. In order to analyse the influence of the rotating terms in the wheelset formulation, both interaction models with and without rotation ($\Omega = 0$) are evaluated.

Fig. 6.15 plots the real-part of the eigenvalues that develop positive values in Simulation III. Results obtained reveal that rotation completely modifies the distribution and magnitude of the unstable eigenmodes. The largest positive real-parts are associated with the dominating unstable eigenmodes corresponding to 1743 and 2221 Hz for the rotating case. It is observed that the most unstable modes are found for the rotating wheelset in a range between 1.5 and 2.2 kHz and even for higher frequencies, the real-parts are larger than the corresponding to the non-rotating wheelset. The exception is found for the peak at 168 Hz in the non-rotating case. Therefore, the stability analysis indicates for this simulation case that the rotating terms are instabilising the dynamics of the complete system

Fig. 6.16 depicts the deformed configuration (out of scale) of both rails and wheelset for the most unstable mode corresponding to 1743 Hz. Assuming that curve squeal is interpreted as self-induced unstable vibrations, this mode can be associated with the mode that is more prone to squeal in the curving and friction conditions set in Simulation III. The inner wheel presents a more pronounced deformation corresponding to the (2,0) mode with 2 nodal diameters and 0 nodal circles. The corresponding inner rail presents a more marked deformation in the lateral as in the vertical directions.

Rotating terms of the wheelset have similar effects in the rest of cases simulated. For Simulation VII (same friction and larger curve radius than the previous case), Fig. 6.17 shows that the largest real-part is again found at 1743 and 2221 Hz for the rotating case. Nevertheless, the unstable modes for the non-rotating case present more pronounced eigenvalue real-parts in this simulation, being higher than the rotating case from 2.5 kHz. Results suggest that the rotating terms for larger curve radii slightly instabilise the response of the wheelset/track system in the range of 1−2.2 kHz, but their contribution for higher frequencies displaces the unstable frequencies and reduces their eigenvalue positive real-parts. Table 6.9 gathers the main unstable frequencies and the real-part of the largest case for the eight simulations cases evaluated for rotating and non-rotating wheelset model.

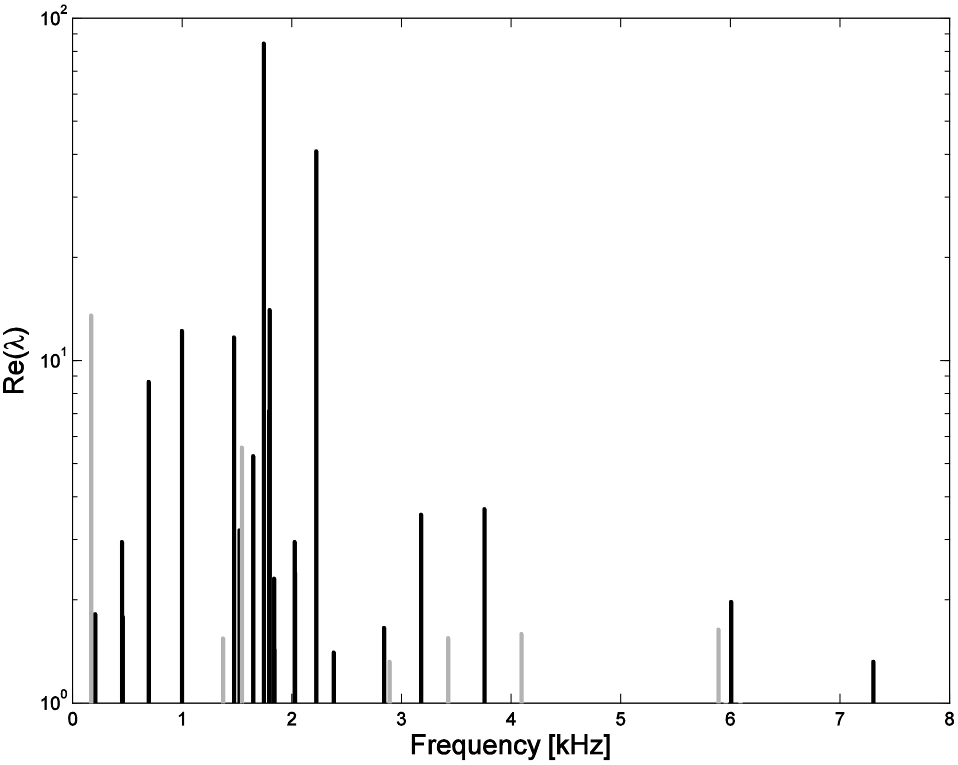

Fig. 6.15. Real-parts of eigenvalues for rotating (black) and non-rotating (grey) wheelset model (Simulation III).

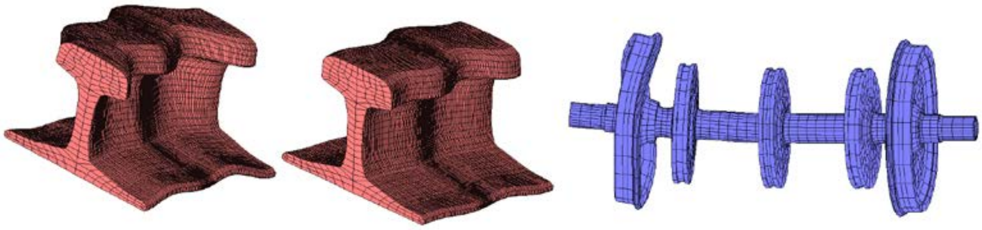

Fig. 6.16. Deformed configuration for the outer and inner rails and the wheelset corresponding to the largest eigenvalue real-part for the rotating wheelset model (Simulation III).

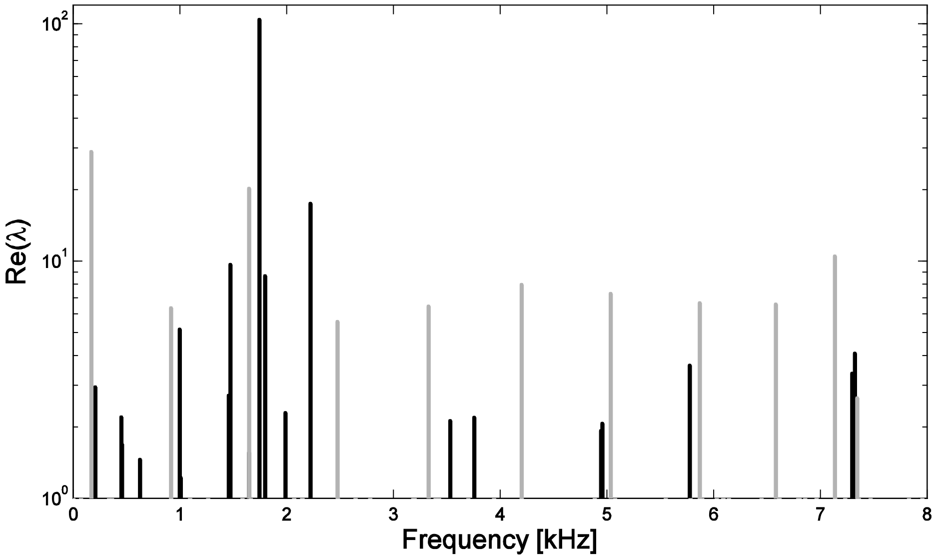

Fig. 6.17. Real-parts of eigenvalues for rotating (black) and non-rotating (grey) wheelset model for Simulation VII.

		$\mu = 0.20$	$\mu = 0.32$	$\mu = 0.40$	$\mu = 0.60$
R^r = 120 m	$\Omega > 0$	1742$_{(100.4)}$	1743$_{(87.8)}$, 2221	1743$_{(84.4)}$, 2221	1742$_{(75.8)}$, 2221
	$\Omega = 0$	4201, 7138$_{(3.1)}$	170$_{(6.7)}$, 1544, 5037	168$_{(13.6)}$, 1544	165$_{(45.4)}$
R^r = 500 m	$\Omega > 0$	1741$_{(107.8)}$	1742$_{(105.3)}$	1743$_{(104.2)}$	1745$_{(101.8)}$
	$\Omega = 0$	1648$_{(6.9)}$	170$_{(16.6)}$, 1648, 7137	170$_{(28.9)}$, 1647, 7136	170$_{(69.2)}$, 1646

Table 6.9. Main unstable frequencies in Hz (and real-part of the corresponding eigenvalue in brackets) through complex eigenvalue analysis of the complete system with and without rotating terms in the wheelset model.

The largest real-part in the rotating case corresponds to the same frequency around 1743 Hz for both curve radii, indicating an irrelevant influence on the complex stability analysis. This frequency slightly increases for higher friction coefficients, while the eigenvalue real-part decays significantly, obtaining higher values for the curve radius of 500 m. The non-rotating model presents a largest real-part around 170 Hz for both curves and other main unstable frequencies in the high-frequency range around 1544: 1648 Hz for the curve radius of 120 m, and 7136 Hz for 500 m. Eigenvalue real-parts are much lower than the rotating case. This indicates that rotation leads to instabilise the railway system.

6.4.3.2 Non-linear time-domain simulations

From the simulation cases run, tangential contact force is analysed. Fig. 6.18 presents the time response corresponding to Simulation VII. The amplitude of the tangential oscillations of the inner wheel is shown in Fig. 6.18(a) while the outer one is depicted in Fig. 6.18(b). The inner wheel shows an oscillating response that converges around a mean value of -12.8 kN and high amplitudes around 8.5 kN, ten times higher than the outer wheel. Much higher amplitudes for the tangential contact forces in the inner wheel have also been found in the rest of the simulations. These results are in agreement with the observations that indicate that highest squeal noise amplitudes are usually generated by the leading inner wheel of a bogie [4].

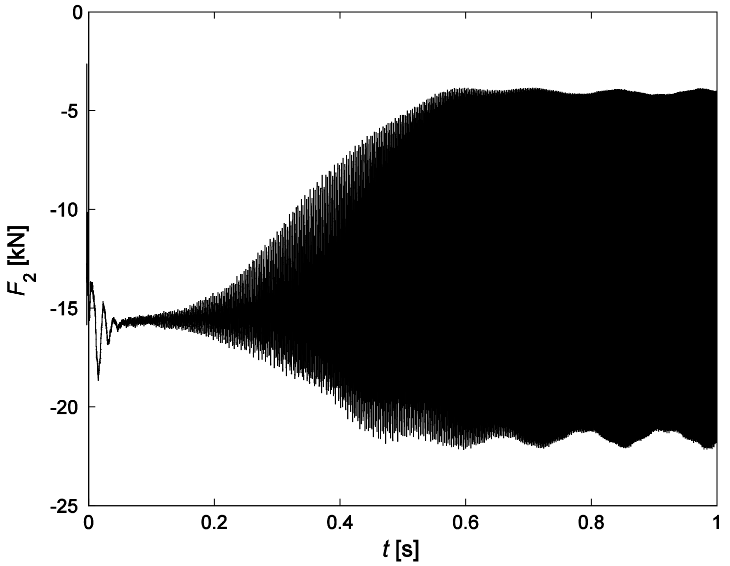

(a)

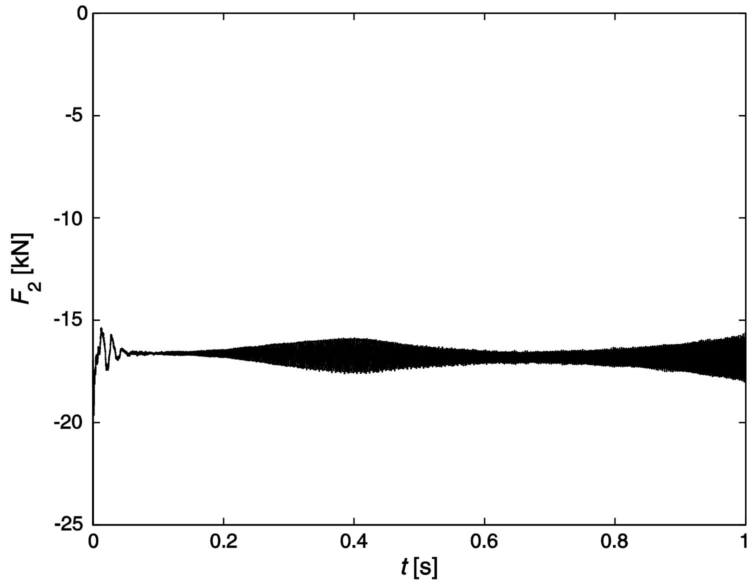

(b)

Fig. 6.18. Time response of the lateral contact force F_2 corresponding to Simulation VII for the inner (a) and outer (b) wheels.

Fig. 6.19 (zoomed views) compares the tangential contact force and the tangential traction limit defined by friction coefficient times normal contact force for Simulation VII. The inner wheel (Fig. 6.19(a)) presents cycles defined by a stick phase when the tangential total force (continuous line) is below the traction bound (dashed line), and the slip phase when both curves overlap. Step 1 marked in Fig. 6.19(a) corresponds to the stick phase (partial stick) in which the contact area is divided into a stick zone located in the leading edge and a slip zone that surrounds the previous one, as seen in Fig. 6.20(a)). Step 2 corresponds to the slip phase in which the contact area is in full slip: all the boundary elements in the contact area are slipping as seen in Fig. 6.20(b). For the outer wheel, Fig. 6.19(b) shows that the tangential force is continuously below the traction bound without reaching full slip at any time. Hence, these stick/slip cycles are only observed in the inner wheel and they can be interpreted as self-induced vibrations in curving conditions that come from the railway dynamics itself.

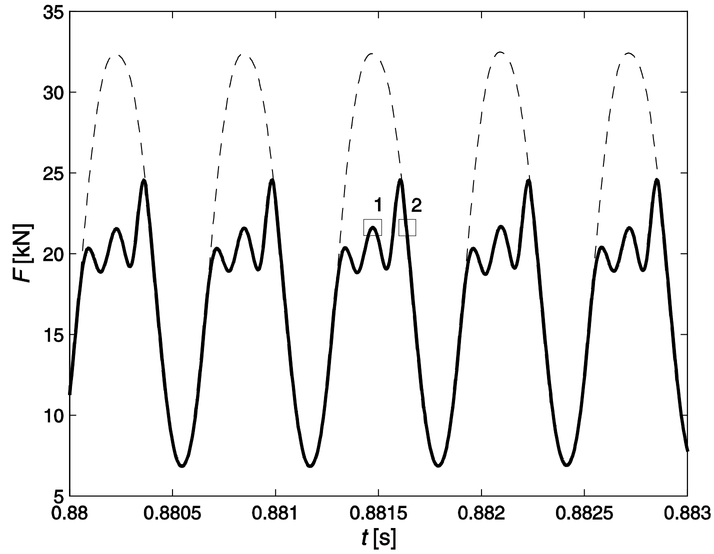

(a)

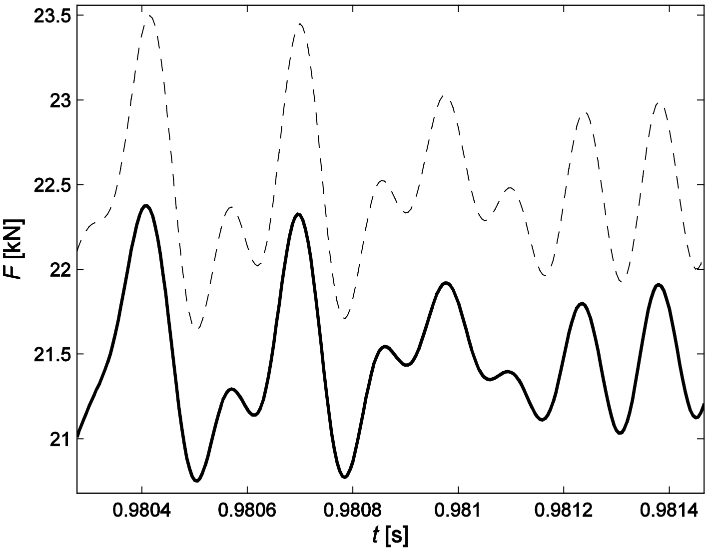

(b)

Fig. 6.19. Zoom on time response of the contact forces (corresponding to Simulation VII); ——: lateral force F_2; - - - : traction bound μF_3; some selected steps are marked with Arabic numerals. (a) Inner wheel; (b) outer wheel.

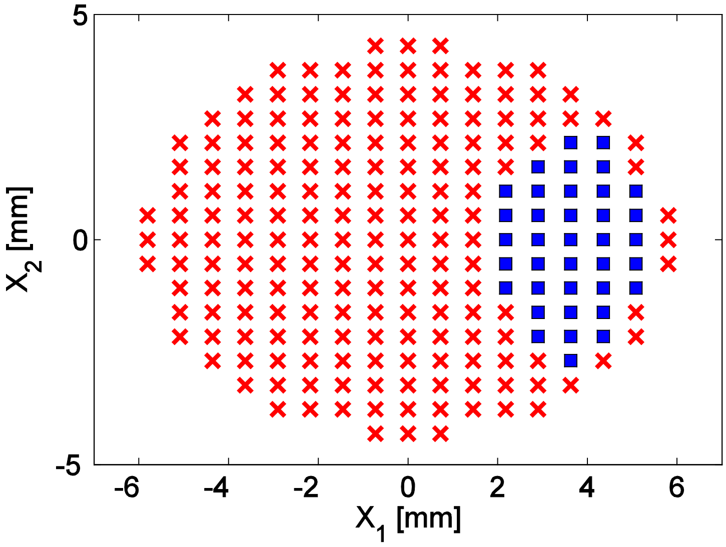

(a)

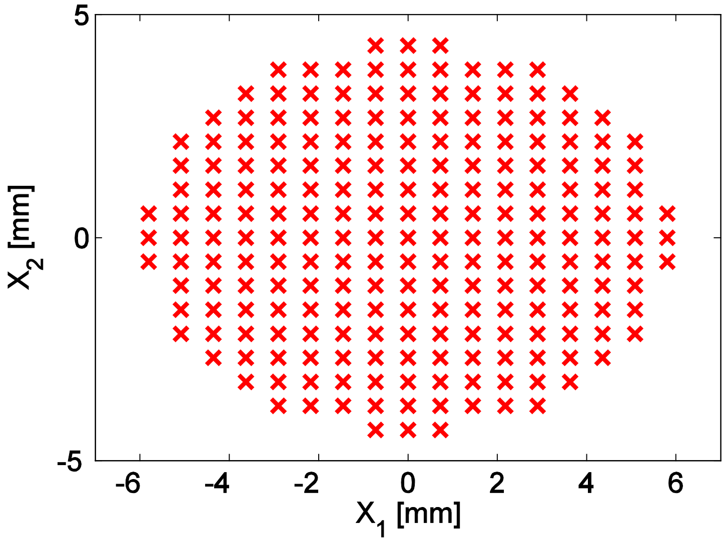

(b)

Fig. 6.20. Division of the contact zone in stick (■) and slip (✖) zones in the time steps 1 and 2 marked in Fig. 6.19(a). (a) Step 1, (b) step 2.

The frequency spectrum of the tangential contact force of the inner wheel is evaluated and shown in Fig. 6.21. It reveals strongly tonal peaks for particular frequencies in the high-frequency domain which correspond to the expected response of curve squeal phenomenon according to the literature [7]. For the simulations carried out, these peaks arise from the complex physical process that governs the contact dynamics throughout the computation. These results confirm that the wheelset/track model implemented in this work is able to reproduce this high-frequency tonal response even with a constant coefficient of friction and, hence, this mechanism is revealed as sufficient for the generation of squeal in curving conditions. The frequencies at which these peaks occur are associated with the oscillating frequencies of the stick/slip and the traction bound (corresponding to the normal contact force) cycles previously visualised, especially if most of the cycle is in full slip. The stick/slip frequencies are or close to be multiples of the traction bound frequency. As observed in Fig. 6.19(a), there is a stick/slip frequency around 4.8 kHz, which is three times higher than the one associated with the dashed limit (around 1.6 kHz). Other stick/slip contributions are around 3.2 and 6.4 kHz (two and four times, respectively).

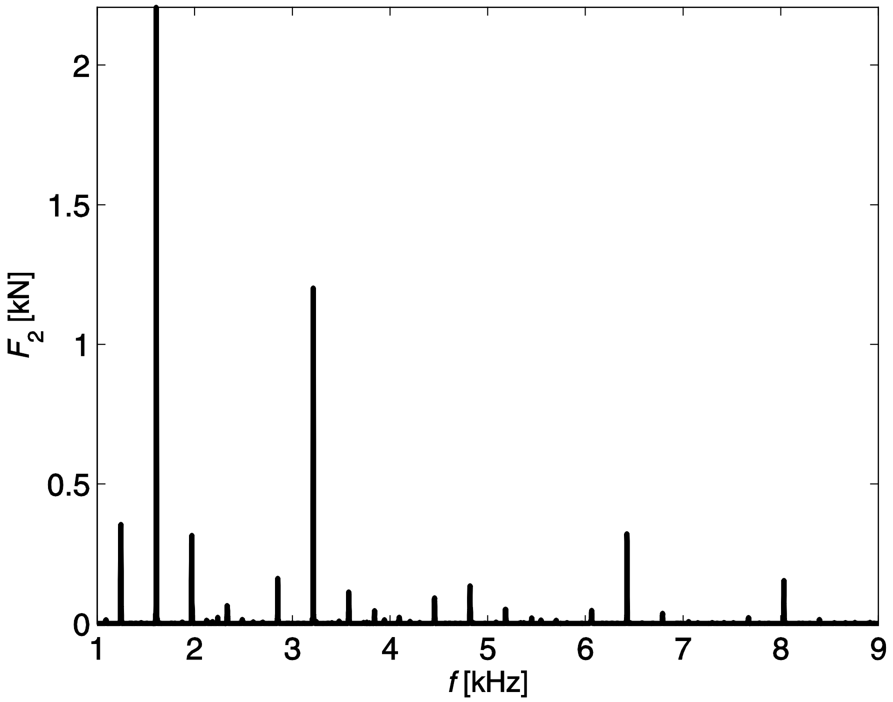

Fig. 6.21. Frequency spectrum of the tangential contact force corresponding to Simulation VII.

Table 6.10 summarises the frequency peaks corresponding to the tangential contact force for the inner wheel in all the simulations carried out. It is shown that all the cases present a tonal behaviour in the high-frequency domain but with no clear tendencies. For the curve radius of 120 m, the main peaks are found at high frequencies: 7.4 kHz for $\mu = 0.20$ and 0.60, and 4.5 kHz for $\mu = 0.32$ and 0.40. For the curve radius of 500 m, peaks are found however in lower frequencies around 1.6 kHz, and the maximum amplitudes are associated with higher coefficients of friction. These results suggest that high friction values favour a more pronounced tonal response in curving conditions, which is in agreement with the well-known fact that low friction conditions (wet weather, lubrication) reduce the likelihood of squeal [13]. Anyway, this parameter study should be extended to establish consistent relationships between squeal characteristics and curve radius and friction coefficient.

	$\mu = 0.20$	$\mu = 0.32$	$\mu = 0.40$	$\mu = 0.60$
$R^r = 120\,\mathrm{m}$	6.8, **7.4**$_{(1.2)}$, 8.0	1.4, **4.5**$_{(1.1)}$	**4.5**$_{(2.1)}$, 8.0	1.4, 1.6, 2.2, **7.4**$_{(0.5)}$
$R^r = 500\,\mathrm{m}$	**3.8**$_{(1.0)}$, 7.7	**1.6**$_{(1.4)}$, 3.8, 6.1, 7.7	**1.6**$_{(1.7)}$, 3.2, 4.8, 6.4	**1.6**$_{(2.2)}$, 3.2, 4.8, 6.4

Table 6.10. Main squeal frequencies in kHz (in bold for the main peak and in brackets for the amplitude in kN) from the lateral contact forces of the inner wheel.

As explained in the introduction, the squeal mechanism for constant friction has been associated in the literature with the wheel modal coupling since squeal frequencies found in measurements are close to some natural frequencies of the wheel [7]. Recent works that model the wheel as an individual substructure have found that the excited natural frequencies correspond to axial wheel modes with zero nodal circles (*m*=0) [9,13]. It is interesting at this point to evaluate the modes associated with the frequencies associated with the peaks in amplitude and gathered in Table 6.10 for a complete wheelset instead of separated wheel models for the inner and the outer ones. The classification of the wheelset modes has been made by visualising the deformed configuration associated with each mode considering the torsional, axial and radial contributions from the axle and the brake discs. Table 6.11 details the closest wheelset modes associated with the main squeal frequencies. Only frequencies in bold exactly correspond to a wheelset mode. Axial wheel mode (2,0,a) with two nodal diameters and zero nodal circles corresponds to the main frequency of 1.6 kHz for Simulation VII. Axial wheel modes with zero nodal circles are associated with squeal frequencies up to 4.5 kHz, which agrees with the literature [7,13]. Radial wheel modes and axial axle modes appear for higher frequencies.

Frequency [Hz]	Closest wheelset modes, (*n*,*m*)	Simulation
1361	Axial (0,0,a) wheel mode	II
1607	Axial (2,0,a) wheel mode	VI, VII
3213	Axial (4,0,a) wheel mode	VII, VIII
3841	Radial axle mode	V, VI
4518	Axial axle mode	II, III
4819	Radial (3,1,r) wheel mode	VII, VIII
6053	Radial (4,0,r) wheel mode	VI
6425	Axial axle mode	VII, VIII
7449	–	I, IV
7680	Axial axle mode	V, VI
7958	–	III

Table 6.11. Closest wheelset modes associated with the main squeal frequencies for the inner wheel. Frequencies in bold correspond exactly to wheelset modes.

The influence of the rotating matrix terms $\tilde{\mathbf{V}}$, $\tilde{\mathbf{A}}$, $\tilde{\mathbf{C}}$ and $\tilde{\mathbf{S}}$ associated with the angular velocity of the wheelset in Eq. (5.26) is evaluated on the previous simulations in curving conditions. Fig. 6.22 shows the comparison using a rotatory and non-rotatory wheelset in the interaction model, where relevant discrepancies arise in the frequency content of the lateral contact forces. For the curve radius of 500 m (Simulation VI), the non-rotating simulation (dashed line) presents more content in the high-frequency range, as seen in Fig. 6.22(a). The pronounced peaks around 1.6, 3.8 and 6.1 kHz are substantially more mitigated for the rotating case (solid line). Another interesting observation is that the unstable frequencies are slightly shifted to higher values for the rotating case since the values of the natural frequencies vary depending on the angular velocity following a monotone behaviour. In the simulation under study, it can be deduced that forward modes are especially influencing the curving dynamics in the occurrence of squeal. For the curve radius of 120 m (Simulations III and IV), the frequency content is appreciably higher than the previous one, especially in the range of 1−4 kHz as seen in Figs. 6.22(b) and (c). The attenuation of the rotating case with respect to the non-rotating one is not so clear in this range, but the frequency shift of the rotating peaks to the right can be appreciated. Fig. 6.22(c) shows that that the non-rotating case are strongly attenuated in the range of 7−9 kHz.

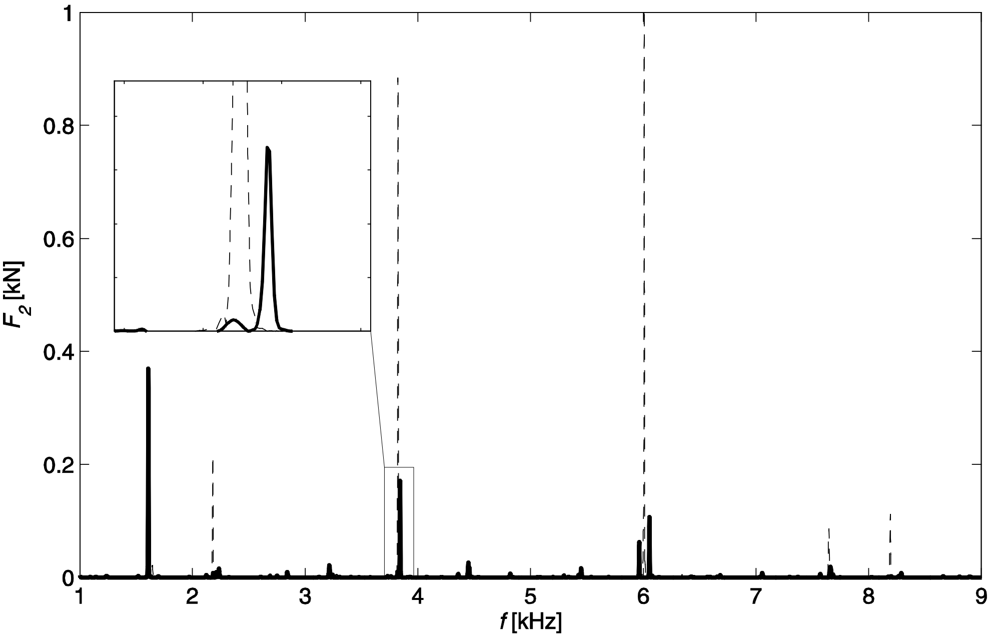
1
0.8
0.6
0.4
0.2
0
F_2 [kN]
1
2
3
4
5
6
7
8
9
f [kHz]

(a)

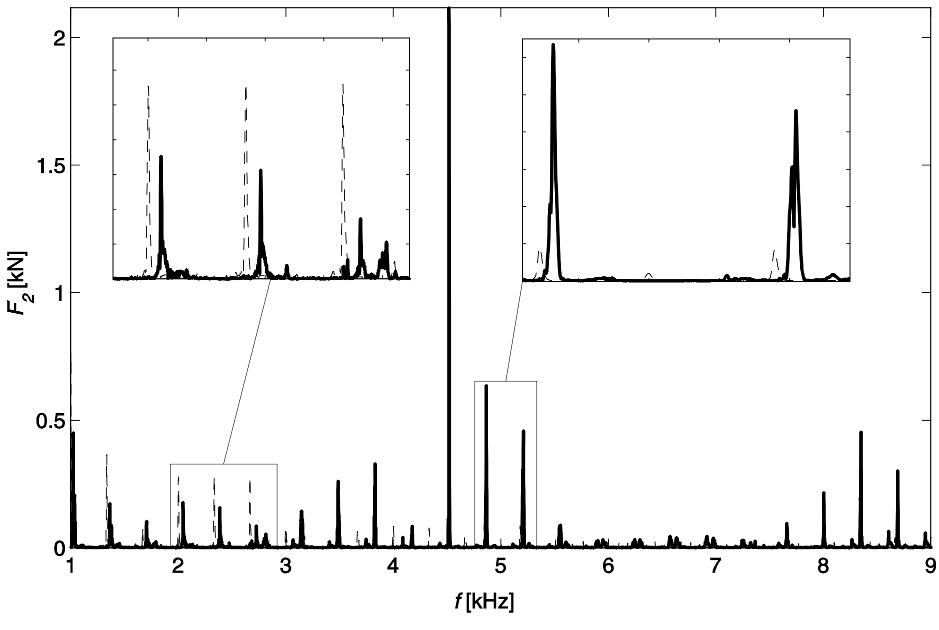
2
1.5
1
0.5
0
F_2 [kN]
1
2
3
4
5
6
7
8
9
f [kHz]

(b)

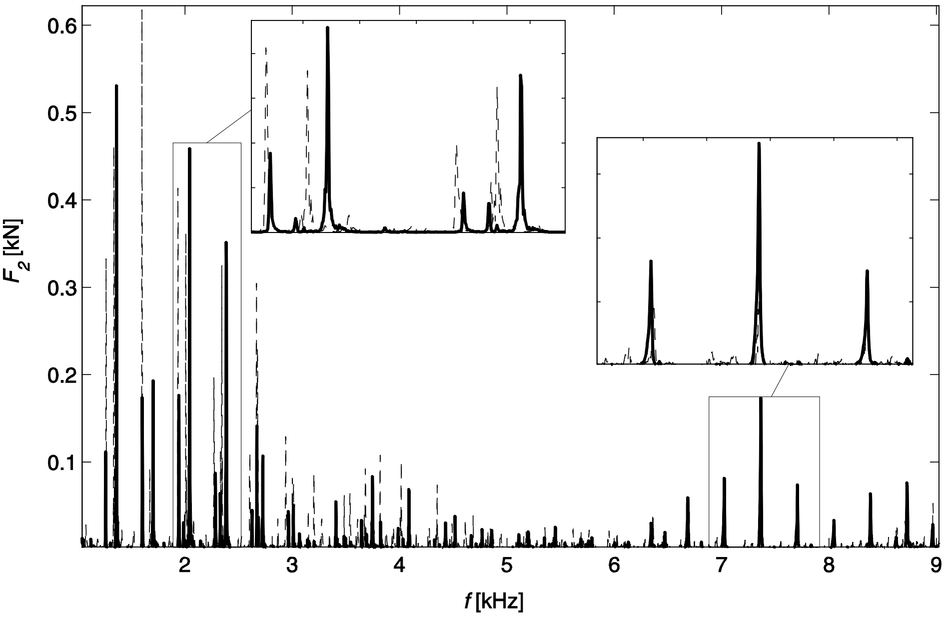

(c)

Fig. 6.22. Freq. spectrum of the lateral contact force of the inner wheel using a rotating wheelset model (——), and a non-rotating one (- - -) for Sim. VI (a), III (b), IV (c).

6.4.4 Discussion

The occurrence of squealing for constant friction values has been investigated for curving conditions. Time simulations are run for the wheelset negotiating tight curves in order to evaluate the tangential contact and to investigate curve squeal for constant friction parameters during the curve. Results give only limited insight into the precise underlying mechanism. They find strong unstable tangential contact forces with stick/slip oscillations for the inner wheel. The associated frequency spectrum reveals a strong tonal behaviour in the high-frequency domain. Therefore, the model proposed in this work permits to reproduce the unstable and tonal response that characterises squeal phenomenon in curving conditions even with constant friction. It is hence concluded that the constant friction mechanism is sufficient for squeal generation.

These results are also in good agreement with some observations reported in the literature about squeal. The unstable frequencies are associated with stick/slip cycles that arise from the non-linearities that govern the contact dynamics [9,13]. The unstable peaks decrease their amplitudes for low friction values, in line with the fact that low friction conditions reduce the likelihood of squeal [7]. Curve radius (associated with lateral creepage and lateral contact position) and frictional properties are key parameters with significant influence on the frequency content and intensity of curve squeal [5,7]. On other hand, results confirm that the rotation of the wheelset has a crucial influence on curve squeal. The inclusion of the terms associated with the rotation shifts squeal frequencies and it strongly affects the frequency content (amplitude of the tonal peaks) in the high-frequency range.

The complexity of the contact dynamics and the introduction of the complete wheelset instead of separated wheel models arise as direct responsible of curve squeal since its linearisation in the linear stability analysis gives completely different unstable frequencies than the time-domain model. Hence, it permits to conclude that the comprehension of the curve squeal phenomenon requires detailed unsteady and non-linear contact models, because simplifications do not permit to address this complex physical process.

6.5 CONCLUSIONS

In this chapter, the models described in the thesis have been integrated in a train/track dynamic interaction model that contains a non-Hertzian and instationary contact model and a flexible and rotatory wheelset model. A cyclic track model based on the ME technique is also introduced and compared to Timoshenko beam, which is commonly utilised in the literature. This complete interaction model is used for running simulations in curving conditions in order to address curve squeal.

Section 6.2 focuses on the deviations in the frequency content of the vertical and lateral contact forces between 3D MEM and Timoshenko beam for two types of excitation: randomly corrugated tangent track and excitation arising from a wheel flat when the wheelset runs over a perfectly even track at 300 km/h.

- These results validate the 3D MEM as an efficient flexible track model whereas it reproduces consistently the contrasted behaviour of the Timoshenko beam for its range of validity (low and mid-frequencies) according to the literature.

- For both types of excitation, the 3D MEM shows a remarkably higher frequency content for the 1–8.5 kHz band. These higher harmonics seem to be crucial to describe the high-frequency phenomena, such as rolling and squeal noise.

- The proposed 3D MEM track model seems to be suitable to describe the high-frequency dynamics associated with different railway phenomena such as short pitch rail corrugation, wheel flat excitation, axle fatigue, rolling, squeal and braking noise.

In Section 6.3, two different numerical approaches for railway curve squeal have been presented: a model for linear complex stability analysis and a model for non-linear time-domain simulations. Both squeal models have been applied for conditions similar to those of a 120 m radius curve on the Stockholm metro exposed to severe curve squeal.

- In both models, the frictional instability arises due to geometrical coupling.

- For an over-radial position of the wheelset no or only weak instability is detected, while pronounced squeal occurs for an under-radial position above a threshold of the wheel/rail friction coefficient. All identified squeal frequencies correspond to axial modes of the wheel with zero nodal circles.

- In the evaluated cases, both models show similar tendencies in terms of the instability range in the parameter space, but they differ in the predicted squeal frequencies. This can partly be attributed to the different nature of the squeal models and the fact that the magnitude of the real part of unstable modes in the stability analysis is not a selection criterion between different unstable modes.

- Another possible reason for the obtained differences in squeal predictions are small modelling differences between both models. This point needs further investigation and will be addressed in future work.

In Section 6.4, a new approach has been adopted for the estimation of the contact forces in curving conditions. The pseudo-static state of the wheel/rail system is given by multibody dynamic simulation software. From the pre-calculated pseudo-static wheel and rail displacements, the vertical and tangential dynamics are described by small displacements. The normal force is defined by a non-linear simplified normal relationship from the elastic penetration deviation calculated in each step of the simulation and the tangential forces are estimated from the creepages derived by using the same approach. A set of eight time-domain simulations for curve radii of 120 and 500 m and friction coefficients of 0.20, 0.32, 0.40 and 0.60 has been carried out.

- Time-domain simulations find strong unstable lateral contact forces with stick/slip oscillations. The inner wheel is the one that presents higher mean values and more pronounced peaks in the lateral contact force.

- Both parameters studied, curve radius and frictional properties, are key parameters with significant influence on the frequency content and amplitude of curve squeal.

- In the frequency spectrum, discrete tonal peaks are detected. These pronounced stick/slip peaks decrease their amplitudes for low friction values. Squeal frequencies do not exactly correspond to wheelset modes.

- The constant friction mechanism is hence revealed as a sufficient physical mechanism to generate squeal without the need to include a falling friction coefficient.

- The rotation of the wheelset has a crucial influence on curve squeal, shifting the squeal frequencies and affecting decisively the frequency content (amplitude of the tonal peaks) in the high-frequency range.

- The linearisation of the contact dynamics is revealed as insufficient to address curve squeal. This phenomenon is strongly dependent of the unsteady and non-linear physical processes that take place in the contact area.

7 CONCLUSIONS AND FUTURE WORK

7.1 CONCLUSIONS

The main objectives of the thesis, concerning the development of a simulation tool to address railway high-frequency phenomena and able to consider non-Hertzian and instationary effects in the wheel/rail contact model, have been achieved satisfactorily. The most relevant conclusions of the developed work are described below chapter by chapter, pointing out the contributions made.

The study of curve squeal has been the ultimate purpose that has justified the development of advanced models for the analysis of railway dynamic interaction in the high-frequency domain. Curve squeal is a high-frequency and strongly tonal noise which frequently appears when railway vehicles negotiate sharp curves. The particular conclusions related to the review of works about curve squeal carried out in Chapter 2 are detailed below.

- Insertion of a wheelset in a curve is a complex process that determines curve squeal, in which creep forces arise to steer the wheelset. Steering mechanism depends on wheel profile and diameter, curve radius, track width and stiffness of the primary suspension.

- Falling friction, which acts as negative damping, has been recognised the most accepted mechanism for the generation of squeal.

- Recent works indicate that the instabilities associated with squeal can arise even for contact models with constant friction coefficient from the coupling between the normal and tangential directions in the contact dynamics.

- Most cases reported involve 0-nodal-circle axial modes excited at the leading inner wheel but some unusual occurrences have been highlighted where different phenomena are involved.

Train/track dynamic interaction models in the mid and high-frequency range (from about 20 Hz to 5 kHz) are classified in Chapter 3 mainly according to the vehicle modelling, the track modelling, the wheel/rail contact and the solving strategies for the resulting equation of motion system.The conclusive remarks are listed below:

- The literature divides between finite and infinite track models. The first ones present a boundary effect that originates a reflection of the generated waves at the model edges that interact again with the vehicle, introducing errors in the simulation. In order to minimise this effect, important lengths must be adopted. The infinite track models are divided in two groups: the frequency-domain models and the ones based on the wave propagation along periodic structures (Green's functions). Both groups require adopting hypotheses of linearity about the mechanic properties of the track.

- The wheel/rail contact models are classified according to the elastic theory on which they are based (*Exact Theories* or *Simplified Theories*), if the inertial effects are or not considered (*Dynamic Theories* or *Quasi-Static Theories*), if instationary processes are or not considered (*Instationary Theories* or *Steady-State Theories*), and depending on the dimension of the contact problem (*2D Theories* or *3D Theories*). Regarding the hypotheses used when solving the normal and tangential problems, theories are also classified as follows: if Hertzian hypotheses are or not considered in the normal problem (Hertzian or non-Hertzian models), and if hypotheses of linearity are or not adopted in the calculation of the tangential forces (*Linear Theory* or non-linear models). With regard to the formulation of the elastic problem, contact models can also be divided in *Non-Conformal Contact* models and *Conformal Contact* models.

- It is usually considered that the elastic quasi-identity hypothesis is satisfied, which leads to decouple the normal and tangential contact problem. In the train/track dynamic interaction models, it is usual to solve the normal problem by means of a linear (frequency-domain) or non-linear (time-domain) Hertzian spring. Nevertheless, there exists a growing interest in the development of non-Hertzian normal contact models: advanced FE models or approximated models of low computational cost. The last ones can be divided in two groups: multi-Hertzian methods and virtual elastic penetration methods. In the tangential problem, it is common to implement steady-state models of low computational cost, such as Kalker's *Linear Theory* [105], Shen's *et al.* model [100] or FASTSIM [95]. It is unusual the implementation of non-Hertzian and instationary model, such as

CONTACT [70,81]. The transient contact conditions during squeal are also described.

- The methods for solving the equations of motion from the train/track interaction model are classified in: frequency domain, associated with a linear system and a lower computational cost; time domain, related to the non-linear behaviour of the elements of the train/track system and a higher computational cost. *Linear Theory* and FASTSIM algorithm are also described in the chapter as commonly used in the literature as simplifications of the tangential contact problem. Since they do not consider transient effects, instationary contact models are needed to explain high-frequency phenomena such as curve squeal.

As regards to the development of a 3D contact model (Chapter 4), the following conclusions are derived:

- The theoretical fundamentals of the wheel/rail contact problem and the corresponding formulation have been presented. Based on Kalker's variational theory, a 3D non-Hertzian and instationary contact model has been presented. In this model, the contact patch is discretised uniformly in rectangular elements in which the contact magnitudes are constant.

- The instationary tangential contact formulation has been modified to meet steady-state conditions.

- As one of the contributions of this thesis, a new approach has been adopted modifying the original method by means of the regularisation of Coulomb's law for the tangential contact problem.

    - This numerical strategy relates the tangential traction to the slip velocities, reducing by approximately half the number of unknowns of the contact equations system. Hence, the algorithm becomes more efficient.

    - The regularisation permits the introduction of a falling friction coefficient (with different kinematic and static values) in the steady-state tangential contact model, eliminating the discontinuity in the traction solution around the stick/slip transition. This discontinuity has been reported in the literature when using CONTACT algorithm [81].

- Another contribution of this thesis is the implementation of a method for introducing a falling friction coefficient in rolling contact mechanics. This method is suitable for creepages that slightly exceed the saturation conditions (lower than 3% if the solids in contact are made of steel), which correspond to the creepage range in most of the railway dynamic studies. The technique adopts steady-state conditions and the friction coefficient is a function of the local slip velocity through a simplified Stribeck curve.

    - The implementation of the velocity-dependent friction coefficient adds new variables that frequently have been chosen *ad hoc* in the literature. The present work develops the constrain equations that establish mathematical relationships between the different parameters associated with the falling friction rolling contact problem. These constrain equations facilitate to build models that produce realistic results from experimental data. This respect, the proposed model reasonably fits the experimental creepage vs. creep-force curves obtained from high-precision test-bench measurements.

    - The appearance of the creepage vs. creep-force curves obtained from the proposed methodology does not differ markedly from the one of a single friction coefficient. This conclusion is in accordance with previous test-bench measurements that present a slight decrease of the tangential force once the maximum is reached.

    - A global model that fits all the creepage range level is to the authors' best knowledge, undone. By considering the negligible role of the displacements due to the elastic deformation in high-creepage conditions, the present model can be adequate in traction locomotive problems if a suitable Stribeck curve is adopted. In such case, the above presented constrain equations associated with the parameter set have to be reconsidered.

In Chapter 5, the train/track dynamic interaction modelling is described in order to cover the high-frequency domain to address the squeal noise problem.

- In the frequency range of interest for the study of the railway noise, particularly squeal noise, the train model can be reduced to a wheelset model. Flexibility and inertial effects associated with the rotation have been included in the model developed in UPV [55,159,160] and employed in the present thesis. In this chapter, the formulation of the flexible and rotatory wheelset model based on the use of Eulerian-modal coordinates has been summarised.

- This chapter has also presented one of the most important research contributions of this thesis: a new 3D model for a cyclic finitely long railway track that has been formulated through the Moving Element Method (MEM) and developed as a FE approach in order to improve the modelling of the high-frequency dynamics. The model considers an Eulerian coordinate system attached to the moving vehicle instead of a fixed coordinate system and it adopts cyclic boundary conditions. This approach permits to decrease the computational cost compared to the FE models commonly used.

- The train/track interaction is solved in the time domain through a substructuring technique of the elements of the system: the wheelset and the track, which in turn consists of the rail, the bedplate and/or the sleepers.

- An important effort in the development of new techniques for the temporal solving of the train/track interaction has been made along the thesis. Apart from the Eulerian approach adopted in both wheelset and rail models to enhance the efficiency of the interaction modelling, a modal approach has been adopted in both elements separately in order to reduce the dimension of the complete system. This modal is accompanied by a static modal correction to minimise the errors associated with the truncation of the modal shapes taken in both models. Additionally, a diagonalisation technique has been developed to decouple the equations of motion of both wheelset and rail models, making the solving technique even more efficient. Simpson and Magnus integrators and Magnus expansion open a new research line to enhance the computational efficiency of the numerical integration.

In Chapter 6, the models described in the thesis have been integrated in a train/track dynamic interaction model that contains a flexible and rotatory wheelset model, a cyclic track model based on the ME technique and a non-Hertzian and instationary contact model. This complete interaction model has focused on curved track simulations in order to address curve squeal.

- Results from Section 6.2 validate the 3D MEM as an efficient flexible track model whereas it reproduces consistently the contrasted behaviour of the Timoshenko beam for its range of validity (low and mid-frequencies) according to the literature. For both randomly corrugated tracks and wheel flats as types of excitation, the 3D

MEM shows a remarkably higher frequency content for the 1–8.5 kHz band. These higher harmonics seem to be crucial to describe the high-frequency phenomena, such as rolling and squeal noise. Hence, it seems to be suitable to describe the high-frequency dynamics associated with different railway phenomena such as short pitch rail corrugation, wheel flat excitation, axle fatigue, rolling, squeal and braking noise.

- Two different numerical approaches for railway curve squeal have been presented in Section 6.3: a model for linear complex stability analysis and a model for non-linear time-domain simulations. Both squeal models have been applied for conditions similar to those of a 120 m radius curve on the Stockholm metro exposed to severe curve squeal. In both models, the frictional instability arises due to geometrical coupling.

  - In the evaluated cases, both models show similar trends in terms of the instability range in the parameter space, but they differ in the predicted squeal frequencies. This can partly be attributed to the different nature of the squeal models and the fact that the magnitude of the real part of unstable modes in the stability analysis is not a selection criterion between different unstable modes. Another possible reason for the obtained differences in squeal predictions are small modelling differences between both models. This point needs further investigation and will be addressed in future work.

- A new approach has been adopted in Section 6.4 for the estimation of the contact forces in curve conditions. Based on ADAMS/RAIL pseudo-static results, the vertical and tangential dynamics are described by an incremental procedure. A train/track interaction model in curving conditions for constant friction has been implemented through a flexible and rotatory wheelset and two finite MEM rails, coupled by a non-linear and instationary contact model. Time-domain simulation has been carried out taken the curve radius and the friction coefficient as study parameters.

  - Strong unstable lateral contact forces with stick/slip oscillations (partial stick/full slip cycles) are found for the inner wheel. In the frequency spectrum, pronounced tonal peaks arise around discrete unstable frequencies associated with curve squeal. These frequencies are close to certain wheelset resonances, leading to the wheel modal coupling as a sufficient physical mechanism to generate squeal without the need to include a falling friction coefficient. Both parameters studied have a significant influence on the frequency content and intensity of this phenomenon.

- The rotation of the wheelset has a crucial influence on curve squeal. The rotatory terms introduced in the equation of motion of the wheelset have a substantial impact on the time-domain simulations, shifting the squeal frequencies and affecting the frequency content (amplitude of the tonal peaks) in the high-frequency range.

- The linear stability analysis through complex eigenvalue calculation is not valid as an approximate tool to evaluate curve squeal in the cases evaluated in this section. The non-linear character of the contact dynamics is revealed decisive for the physical approach to this phenomenon. Hence, *Simplified Theories* seem not to be valid to address this problem.

7.2 FUTURE WORK

The work developed in the present thesis pretended to implement a complete train/track dynamic interaction model that permitted to run simulations when the vehicle negotiates tangent and curved tracks. In order to make it computationally efficient, only the leading wheelset with primary suspension is used to model the vehicle, and the contact model considers the contact point fixed during the time simulation and the friction coefficient has the same values along the curved track for real conditions. These simplfications could be overcome following the lines proposed above:

- A new complete vehicle model that includes the dynamic of the carbody and the axle boxes as sprung masses has been recently developed in this research group. This model permits to run the insertion in the curve, whose results are used as initial conditions for the curving negotiation without depending on external software.

- The development of a new contact algorithm that permits the efficient calculation of the position of the contact point at each instant is crucial for accurate simulations.

- The tribological study carried out in this thesis points out that falling friction coefficient has a negligible influence for steady-state contact conditions. Nevertheless, its influence in dynamic contact conditions could not be studied despite the multiple numerical strategies tested for the inclusion of the slip-velocity dependent friction coefficient in the instationary tangential contact model. This is a topic that should be investigated and the implementation of the regularisation of Coulomb's law seems to be a promising starting point.

- The resulting calculation times for the simulations run for curving conditions have been larger than 10 h in a standard PC for a time integration of 1 s. This computational cost is considered too large in engineering applications. Magnus integrators seem to be a good alternative for increasing the calculation velocity but further work in their numerical applications is needed. Additionally, Magnus expansion permits to find a pseudo-analytic integration solution for periodic interaction forces. This method opens a new way to address linear differential equation problems with time-dependent stiffness and damping matrices for discrete supports.

- Complementary work should be carried out to analyse the influence of different parameters on the squeal generation, extending the curve radius and friction cases and modifying other parameters such as creepages, vehicle speed, normal load or even roughness of the running surfaces as possible instability mechanisms.

- The work carried out in this thesis has the immediate objective of developing an algorithm for the calculation of the acoustic radiated power of the railway system. This model uses as input data the normal surface velocities of the wheels and rails given by the dynamic simulation. The obtained results will permit to find which wheel (or rail) modes are mainly responsible for squeal.

APPENDIX A

Influence coefficients for the elastic half-space

The normal contact model described in Section 4.3 and the tangential contact model described in Section 4.4 are based on influence coefficients for the elastic half-space. These coefficients are given in Kalker's book [24] and are listed here for convenience in the form needed in this work.

The coefficients are valid for the case where the potential contact patch between wheel and rail is divided into N_p rectangular elements with side lengths Δx_1 and Δx_2, see Fig. A.1, and the traction is taken as piecewise constant over the mesh of rectangles. Kalker gave the coefficients for the case where the two contacting bodies are made of different materials. Here it is additionally assumed that the two bodies, i.e. wheel and rail, are made of the same material, which has a modulus of rigidity G and a Poisson's ratio ν.

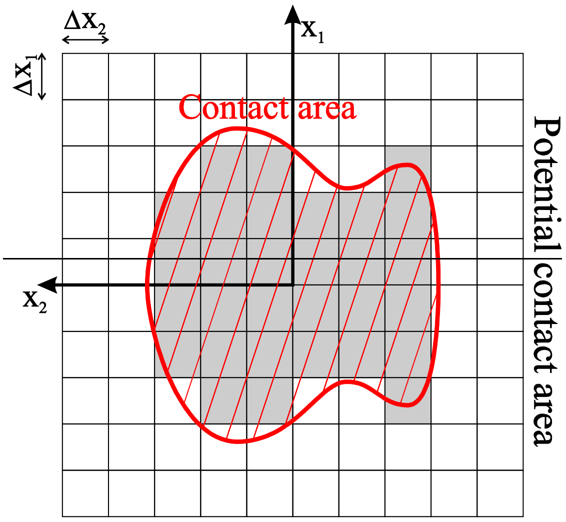

Fig. A.1. Potential contact patch divided into rectangular elements with side lengths Δx_1 and Δx_2.

The influence coefficient D_{ij}^{IJ} gives the displacement in i-direction at the centre of element I due to a unit traction in j-direction in element J. The coefficients are obtained as

$$D_{11}^{IJ} = \frac{1}{\pi G}\left(J_3 - \nu J_2\right), \tag{A.1}$$

$$D_{22}^{IJ} = \frac{1}{\pi G}\left(J_3 - \nu J_1\right), \tag{A.2}$$

$$D_{33}^{IJ} = \frac{1-\nu}{\pi G} J_3, \tag{A.3}$$

$$D_{12}^{IJ} = D_{21}^{IJ} = \frac{\nu}{\pi G} J_4 . \tag{A.4}$$

The remaining coefficients D_{13}^{IJ}, D_{31}^{IJ}, D_{23}^{IJ} and D_{32}^{IJ}, which would be responsible for the coupling between the normal and tangential directions, are zero for identical materials of the two bodies.

The functions J_1 to J_4 depend on the variables a, b, c and d giving the distances in x'- and y'-directions between the centre of element I and the corners of element J:

$$\begin{aligned} a &= \Delta x_{1,IJ} - \frac{\Delta x_1}{2},\ b = \Delta x_{1,IJ} + \frac{\Delta x_1}{2} \\ c &= \Delta x_{2,IJ} - \frac{\Delta x_2}{2},\ d = \Delta x_{2,IJ} + \frac{\Delta x_2}{2} \end{aligned} \tag{A.5}$$

where

$$\begin{aligned} \Delta x_{1,IJ} &= x'_{1,J} - x'_{1,I} \\ \Delta x_{2,IJ} &= x'_{2,J} - x'_{2,I} \end{aligned} \tag{A.6}$$

and $\left(x'_{1,I}, x'_{2,I}\right)$ and $\left(x'_{1,J}, x'_{2,J}\right)$ are the locations of the centres of elements I and J, respectively.

The function J_1 to J_4 are given by

$$J_1(a,b,c,d) = g(d,b) - g(d,a) - g(c,b) + g(c,a) \tag{A.7}$$

$$J_2(a,b,c,d) = g(b,d) - g(a,d) - g(b,c) + g(a,c) \tag{A.8}$$

$$J_3(a,b,c,d) = J_1(a,b,c,d) + J_2(a,b,c,d) \tag{A.9}$$

$$J_4(a,b,c,d) = -h(b,d) + h(a,d) + h(b,c) - h(a,c) \tag{A.10}$$

where the functions g and h are defined as

$$g(x,y) = x \ln\big(y + h(x,y)\big) \tag{A.11}$$

$$h(x,y) = \sqrt{x^2 + y^2} \tag{A.12}$$

and $\ln$ denotes the natural logarithm.

APPENDIX B

Hertzian model for normal contact

In the approach adopted in this section, non-conformal contact is assumed in which the contact patch is much lower than the dimensions of the bodies in contact. With this assumption, both bodies can be considered as half-spaces. This hypothesis is commonly accepted in the wheel/rail contact modelling and gives precise results when the railway axes circulate centred on the track. Assume that two non-conforming surfaces are brought into contact without loading. They only touch in one point that is taken as origin O of a Cartesian coordinate system $x_1x_2x_3$. The x_1x_2-plane is the tangent plane to the surfaces at the origin, and the x_3-axis is the common normal to the two surfaces pointing into wheel. The surfaces of the wheel and the rail can be described by quadratic functions in the vicinity of the contact point assuming the fourth Hertzian hypothesis, see Section 3.5.1:

$$x_3^w\left(x_1^w, x_2^w\right)=\frac{\left(x_1^w\right)^2}{2r_1^w}+\frac{\left(x_2^w\right)^2}{2r_2^w}, \tag{B.1}$$

$$x_3^r\left(x_1^r, x_2^r\right)=\frac{\left(x_1^r\right)^2}{2r_1^r}+\frac{\left(x_2^r\right)^2}{2r_2^r}, \tag{B.2}$$

where r_1^w and r_2^w are the principal radii of curvature of surface of the wheel at the origin, i.e. the minimum and maximum values of the radius of curvature of all possible cross-sections of the profile, which are found in perpendicular planes denoted the $x_1^w x_3$- and the $x_2^w x_3$-planes). The variables r_1^r and r_2^r are the principal radii of curvature of the rail surface at the origin, found in the $x_1^r x_3$- and the $x_2^r x_3$-planes. Each radius of curvature is positive if the curvature centre is located inside the body (convex surface) and negative if the curvature centre is located outside (concave surfaces). ψ is the angle between $x_1^w x_3$- and $x_1^r x_3$-planes.

In the railway case, the wheel rolling radius, r_1^r, and the rail transverse radius of curvature, r_2^w, are generally positive, while the wheel transverse radius of curvature,

r_2^r, can be positive or negative [184]. The rail radius in the rolling direction, r_1^w, is assumed to be infinite. Wheel and rail radii of curvature are determined at the geometric point of contact. The geometric contact point depends on the wheel and rail profiles and the translational and angular position of the wheel on the rail and it is calculated considering both bodies as rigid. From Eqs. (B.1) and (B.2), the distance between the undeformed surfaces is

$$h(x_1, x_2) = \frac{x_1^2}{2r_1} + \frac{x_2^2}{2r_2}, \tag{B.3}$$

with suitable orientation of the x_1- and x_2-axes. The variables r_1 and r_2 denote the principal relative radii of curvature of the surfaces, which can be calculated from the principal radii of curvature of both surfaces, r_1^w, r_2^w, r_1^r, r_2^r, and the angle ψ [32].

When both bodies are pressed together with a load F_3, they are locally deformed and the contact point develops into a contact ellipse with semi-axes a_1 and a_2 where, by definition, $a_1 > a_2$. Distant points in the two bodies approach by a distance δ. The ratio of the semi-axes of the contact ellipse, $A = a_1/a_2$, depends only on the relative principal radii of curvature, r_1 and r_2. The final equations for the semi-axes, a_1 and a_2, and the approach of distant points, δ, are:

$$a_1 = m\sqrt[3]{\frac{3\pi F_3\left(K^w + K^r\right)}{4K_\rho}}, \tag{B.4}$$

$$a_2 = n\sqrt[3]{\frac{3\pi F_3\left(K^w + K^r\right)}{4K_\rho}} = \frac{n}{m}a_1, \tag{B.5}$$

$$\delta = r\sqrt[3]{\left(\frac{3}{4}\pi F_3\left(K^w + K^r\right)\right)^2 K_\rho} = K_H F_3^{2/3}, \tag{B.6}$$

where:

$$K^w = \frac{1-\left(\nu^w\right)^2}{\pi E^w}, \tag{B.7}$$

$$K^r = \frac{1-\left(\nu^r\right)^2}{\pi E^r}, \tag{B.8}$$

$$K_\rho = \frac{1}{2}\left(\frac{1}{r_1^w} + \frac{1}{r_2^w} + \frac{1}{r_1^r} + \frac{1}{r_2^r}\right), \tag{B.9}$$

E^w, ν^w and E^r, ν^r are the Young's modulus and the Poisson's ratio of the wheel and the rail, respectively. m and n coefficients depend on the K_ρ^* / K_ρ, where K_ρ^* is defined as

$$K_\rho^* = \frac{1}{2}\sqrt{\left(\frac{1}{r_1^w} + \frac{1}{r_2^w}\right)^2 + \left(\frac{1}{r_1^r} + \frac{1}{r_2^r}\right)^2 + 2\left(\frac{1}{r_1^w} - \frac{1}{r_2^w}\right)\left(\frac{1}{r_1^r} - \frac{1}{r_2^r}\right)\cos 2\psi}. \tag{B.10}$$

m and n coefficients are determined by θ:

$$\theta = \cos^{-1}\left(K_\rho^* / K_\rho\right). \tag{B.11}$$

θ	m	n	θ	m	n	θ	m	n
0.5	61.4	0.1018	10	6.604	0.3112	60	1.486	0.717
1	36.89	0.1314	20	3.813	1.4123	65	1.378	0.759
1.5	27.48	0.1522	30	2.731	0.493	70	1.284	0.802
2	22.26	0.1691	35	2.397	0.53	75	1.202	0.846
3	16.5	0.1964	40	2.136	0.567	80	1.128	0.893
4	13.31	0.2188	45	1.926	0.604	85	1.061	0.944
6	9.79	0.2552	50	1.754	0.641	90	1.000	
8	7.86	0.285	55	1.611	0.678			

Table B.1. m and n coefficients function of θ (in º) [31].

From the Hertzian assumptions [31] detailed in Section 3.5.1, the equation of the contact patch is ellipsoidal:

$$\frac{x_1^2}{a_1^2} + \frac{x_2^2}{a_2^2} \leq 1. \tag{B.12}$$

The pressure distribution in the contact patch is also ellipsoidal:

$$p(x_1, x_2) = p_0\sqrt{1 - \left(\frac{x_1}{a_1}\right)^2 - \left(\frac{x_2}{a_2}\right)^2}, \tag{B.13}$$

where the maximum contact pressure occurs at the origin:

$$p_0 = \frac{3F_3}{2\pi a_1 a_2}. \tag{B.14}$$

Fig. B.1 shows an example of an ellipsoidal normal distribution defined by Eqs. (B.13) and (B.14) on the elliptical contact patch; material and geometric conditions are taken from Table 4.1 from Section 4.3. MATLAB function *surf* interpolates the discrete values to make the plotted surface continuous; this function has been used in the above figure. Nevertheless, the contact patch is meshed uniformly through rectangular boundary elements. In each BE element, the contact pressure is constant with the value of the centre of the element.

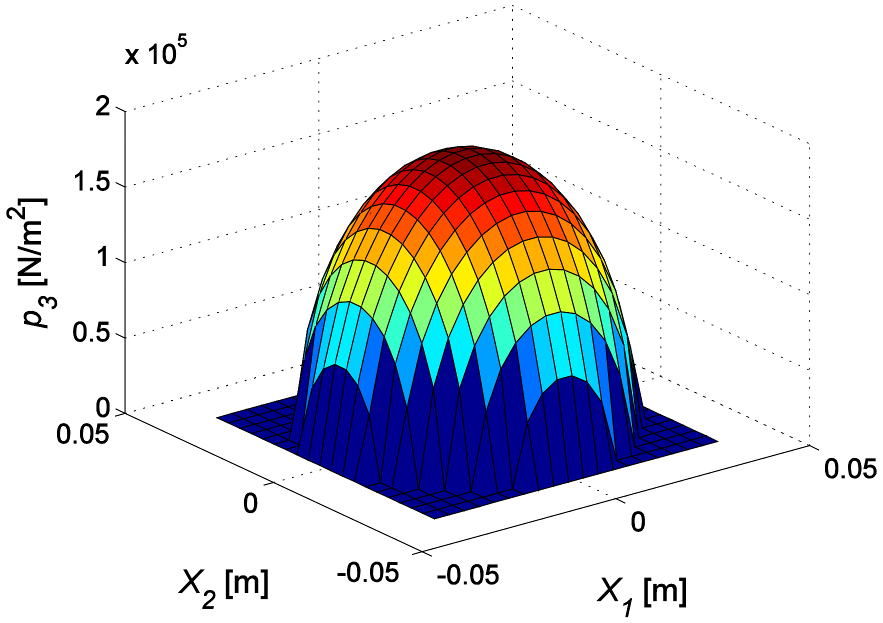

Fig. B.1. Implementation of the Hertzian contact model into a wheel/rail interaction model. The lower figure represents the overhead view, showing the elliptical contact patch.

In many interaction models operating in the time domain, a single non-linear spring is introduced as contact model between wheel and rail. The characteristic of this spring, $F_3(\delta)$, is obtained from Eq. (B.6):

$$F_3(\delta) = r\sqrt[3]{K_\rho}\,\sqrt[3]{\left(\frac{3}{4}\pi F_3\left(K^w + K^r\right)\right)^2} = K_H\delta^{3/2}. \tag{B.15}$$

The factor K_H is a function only of the principal relative radii of curvature and the material parameters. Frequently, Eq. (B.15) is further simplified. The characteristic is linearised for frequency-domain models around the elastic penetration, δ_0, corresponding to static preload, F_{30}. The stiffness of the linear Hertzian spring, $K_{H,lin}$, is obtained from the tangential gradient in the point $\left(\delta_0, F_{3_0}\right)$:

$$K_{H,lin} = \left.\frac{\mathrm{d}F_3}{\mathrm{d}\delta}\right|_{\delta_0} = \frac{3}{2} K_H \delta_0^{1/2} = \frac{3}{2}\frac{F_{3_0}}{\delta_0}. \tag{B.16}$$

APPENDIX C

Published papers linked to the Thesis

This Appendix lists the papers in journals and conferences related to the Thesis in which the author has participated.

Papers in journals:

Paper 1:

J. Martínez-Casas, J. Giner-Navarro, L. Baeza, F.D. Denia. Improved railway wheelset-track interaction model in the high-frequency domain. *Journal of Computational and Applied Mathematics*, 309, 642–653, 2016.

doi:10.1016/j.cam.2016.04.034

Paper 2:

J. Giner-Navarro, L. Baeza, P. Vila, A. Alonso. Study of falling friction effect on rolling contact parameters. *Tribology Letters*, 65:29, 2017.

doi:10.1007/s11249-016-0810-8

Papers in conferences:

Paper A1:

J. Giner-Navarro, P. Vila, A. Alonso, L. Baeza. Study of the falling friction effect on contact parameters through exact contact model. *Proceedings of the 2nd International Conference on Railway Technology: Research, Development and Maintenance*, Ajaccio, Corsica, France, pp. 495–501, 2014.

Paper A2:

J. Martínez-Casas, J. Giner-Navarro, F. D. Denia, P. Vila. Improved railway wheelset-track interaction model in the high-frequency domain. *Proceedings of the 17th Mathematical Modelling in Engineering & Human Behaviour Conference*, Valencia, Spain, pp. 212–217, 2015.

Paper A3:

A. Pieringer, P.T. Torstensson, J. Giner-Navarro. Curve squeal of rail vehicles: linear stability analysis and non-linear time-domain simulation. *Proceedings of the 3rd International Conference on Railway Technology: Research, Development and Maintenance*, Cagliari, Italy, pp. 1759–3433, 2016.

Paper A4:

A. Pieringer, P.T. Torstensson, J. Giner-Navarro, L. Baeza. Investigation of railway curve squeal using a combination of frequency- and time-domain models. *Proceedings of the 12th International Workshop on Railway Noise*, Terrigal, Australia, pp. 444–451, 2016.

Paper A5:

P. Vila, L. Baeza, J. Martínez-Casas, J. Giner-Navarro. Prediction of rail corrugation growth in curve using flexible and rotating wheelset model. *Proceedings of the 12th International Workshop on Railway Noise*, Terrigal, Australia, 2016 (added Paper).

Paper A6:

J. Giner-Navarro, J. Martínez-Casas, L. Baeza, F.D. Denia, J. Carballeira. Improved railway wheelset-track interaction model in curves in the high-frequency domain. *Proceedings of the 18th Mathematical Modelling in Engineering & Human Behaviour Conference*, Valencia, Spain, pp. 105–110, 2016.

Paper A7:

J. Martínez-Casas, E. Di Gialleonardo, S. Bruni, J. Giner-Navarro, J. Carballeira. Modelo de interacción dinámica del vehículo ferroviario completo con ejes y vía flexible en curva. *Actas del XXI Congreso Nacional de Ingeniería Mecánica*, Elche, Spain, pp. 810–817, 2016.

Paper A8:

J. Martínez-Casas, J. Giner-Navarro, L. Baeza, F.D. Denia, P. Vila. Mejora del modelo de interacción dinámica vehículo-vía en el dominio de alta frecuencia. *Actas del XXI Congreso Nacional de Ingeniería Mecánica*, Elche, Spain, pp. 818–825, 2016.

Paper A9:

J. Giner-Navarro, J. Martínez-Casas, F.D. Denia, J. Carballeira. Modelo mejorado de interacción vehículo ferroviario-vía negociando una curva en el dominio de la alta frecuencia. *Congreso de Métodos Numéricos en Ingeniería*, Valencia, Spain, 2017.

Paper A10:

P. Vila, J. Giner-Navarro, J. Martínez-Casas, L. Baeza. Estudio del crecimiento de la corrugación en carriles en vía curva utilizando un modelo de eje montado flexible rotatorio. *Congreso de Métodos Numéricos en Ingeniería*, Valencia, Spain, 2017.

Journal of Computational and Applied Mathematics 309 (2017) 642–653

Contents lists available at ScienceDirect

Journal of Computational and Applied Mathematics

journal homepage: www.elsevier.com/locate/cam

Improved railway wheelset–track interaction model in the high-frequency domain

José Martínez-Casas*, Juan Giner-Navarro, L. Baeza, F.D. Denia

Centro de Investigación en Ingeniería Mecánica, Universitat Politècnica de València, Camino de Vera s/n, 46022 Valencia, Spain

HIGHLIGHTS

- 3D Moving Element Method (MEM) to model the track is proposed.
- The model considers an Eulerian coordinate system attached to the moving vehicle.
- The resulting formulation permits to reduce the computational cost compared to the FE models commonly used.
- The proposed 3D MEM track model is suitable to describe the high frequency dynamics.

ARTICLE INFO

Article history:
Received 30 November 2015
Received in revised form 22 April 2016

Keywords:
Flexible wheelset
Flexible track
Moving Element Method
Train–track interaction
High frequency dynamics

ABSTRACT

As it is well known, there are various phenomena related to railway train–track interaction, some of them caused by the high frequency dynamics of the system, such as rolling noise when the vehicle runs over the track, as well as squeal noise and short-pitch rail corrugation for curved tracks. Due to these phenomena and some others unsolved so far, a large effort has been made over the last 40 years in order to define suitable models to study the train–track interaction. The introduction of flexibility in wheelset and rail models was required to have a more realistic representation of the wheel–rail interaction effects at high frequencies. In recently published train–track interaction models, the rails are modelled by means of Timoshenko beam elements, valid up to 1.5 kHz for lateral rail vibration and up to 2 kHz for vertical vibration. This confines the frequency range of validity for the complete train–track model to 1.5 kHz.

With the purpose of extending the range of validity above 1.5 kHz, a 3D track model based on the Moving Element Method (MEM) is developed in this paper to replace the Timoshenko beam considered in earlier studies, adopting cyclic boundary conditions and Eulerian coordinates. The MEM approach considers a mobile Finite Element (FE) mesh which moves with the vehicle, so the mass of the rail 'flows' with the vehicle speed but in the opposite direction through the mesh. Therefore, the MEM permits to fix the contact area in the middle of a finitely long track and to refine the mesh only around the contact area, where the forces and displacements will be more significant. Additionally, a modal approach is adopted in order to reduce the number of degrees of freedom of the rail model. Both strategies lower substantially the computational cost. Simulation results are presented and discussed for different excitation sources including random rail roughness and singularities such as wheel flats. All the simulation cases are carried out for a Timoshenko beam and a 3D MEM track model in order to point out the differences in the contact forces above the range of validity of the Timoshenko beam.

---

* Corresponding author. Tel.: +34 963877007x76267; fax: +34 963877629.
E-mail address: jomarc12@mcm.upv.es (J. Martínez-Casas).

http://dx.doi.org/10.1016/j.cam.2016.04.034

Tribol Lett (2017) 65:29
DOI 10.1007/s11249-016-0810-8

ORIGINAL PAPER

Study of the Falling Friction Effect on Rolling Contact Parameters

Juan Giner[1] · **Luis Baeza**[2] · **Paloma Vila**[1] · **Asier Alonso**[3]

Received: 21 March 2016 / Accepted: 31 December 2016 / Published online: 10 January 2017

Abstract The existence of a wheel–rail friction coefficient that depends on the slip velocity has been associated in the literature with important railway problems like the curving squeal and certain corrugation problems in rails. Rolling contact models that take into account this effect were carried out through the so-called Exact Theories adopting an exact elastic model of the solids in contact, and Simplified Theories which assume simplified elastic models such as Winkler. The former ones, based on Kalker's Variational Theory, give rise to numerical problems; the latter ones need to adopt hypotheses that significantly deviate from actual conditions, leading to unrealistic solutions of the contact problem. In this paper, a methodology based on Kalker's Variational Theory is presented, in which a local slip velocity-dependent friction law is considered. A formulation to get steady-state conditions of rolling contact by means of regularisation of the Coulomb's law is proposed. The model allows establishing relationships in order to estimate the global properties (creepage velocities vs. total longitudinal forces) through local properties (local slip velocity vs. coefficient of friction) or vice versa. The proposed model shows a good agreement with experimental tests while solving the numerical problems previously mentioned.

Keywords Rolling contact · Falling friction coefficient · Coulomb's law regularisation

1 Introduction

Rolling contact models are widely used in railway technology in order to compute wheel–rail contact forces or estimate wheel and rail wear. With few exceptions, these contact theories implement the original Coulomb's law with a constant friction coefficient. Nevertheless, the existence of a coefficient of friction falling with the slip velocity has been associated (together with another mechanisms) with corrugation of rails [1], or squeal noise in narrow curves [2]. Figure 1 shows the creep force versus creepage when both a constant finite and an infinite friction coefficients are considered. The same plot presents the expected creep force when a falling friction coefficient is adopted, which is differentiated by a local minimum that would explain stick–slip phenomena.

Some researchers have developed rolling contact theories that represent the dependence of the coefficient of friction on the slip velocity, generally by two coefficients of friction (static/kinematic). These models are either Simplified Theories (see definition in [3], and examples in [4, 5]), that somehow simplify the relationships between the contact traction distributions and the displacements in the contact area, or they are based on the Kalker's tangential Variational Theory [3], that introduces a half-space elastic model in the formulation (Exact Theory). The Simplified Theories are adjusted to converge to the results from the Exact Theories, giving a good agreement when comparing the velocity of the wheel–rail contact point (creepages) and forces [3]. However, this agreement does not occur for the local slip velocities [6] and consequently,

---

✉ Luis Baeza
L.Baeza@soton.ac.uk

[1] Centro de Investigación en Ingeniería Mecánica, Universitat Politècnica de València, Camino de Vera s/n, 46022 Valencia, Spain

[2] Institute of Sound and Vibration Research, University of Southampton - Highfield, B13/R3075, Southampton SO17 1BJ, UK

[3] CAF I+D, José Miguel Iturrioz, 26, 20200 Beasain, Spain

©Civil-Comp Press, 2014
Proceedings of the Second International Conference on
Railway Technology: Research, Development and
Maintenance, J. Pombo, (Editor),
Civil-Comp Press, Ajaccio, Corsica, France.

Paper 190

Study of the falling friction effect on contact parameters through exact contact models

Juan Giner[1], Paloma Vila[1], Asier Alonso[2] and Luis Baeza[1*].
[1]Centro de Investigación en Tecnología de Vehículos, Universidad Politécnica de Valencia, Spain.
[2]CEIT, San Sebastián, Spain
[*]e-mail for correspondence: baeza@mcm.upv.es

Abstract

The dependence of the coefficient of friction on the local slip velocity has been associated in the literature with many important railway problems such as the squeal noise that occurs in narrow curves, certain types of corrugation of rails, braking, etc. In order to consider this effect, some researchers have tried to develop models usually based on simplified theories from Kalker that would not be adequate for considering falling friction coefficient.

In this paper a methodology based on Kalker's variational theory is presented, in which a local slip velocity-dependent friction law is considered. It is proposed a formulation to get, firstly, steady-state conditions of contact through an exact elastic model and secondly, macro-properties (creepage velocities versus total longitudinal forces) through local-properties (local slip velocity versus coefficient of friction) and vice versa. Additionally, the unsteady variational theory by Kalker is modified by introducing a regularisation of the Coulomb law. Numerical and computational improvements and non-stationary convergence strategies will be discussed.

Keywords: rolling contact, non-steady state rolling contact, steady-state rolling contact, exact rolling contact theory, falling friction coefficient, Coulomb law regularisation.

1 Introduction

The existence of a coefficient of friction that falls with the slip velocity has been associated with certain corrugation problems (e.g. rutting, see Reference [1]) or squeal noise in narrow curves [2]. Some researchers have developed rolling contact theories that consider the dependence of the coefficient of friction on the slip velocity, by means of two coefficients of frictions (static/kinematic). These models are either simplified theories [3][4] that have not been tested with sufficient

Improved railway wheelset-track interaction model in the high–frequency domain

José Martínez-Casas[1], Juan Giner-Navarro[1], F. D. Denia[1], Paloma Vila[1] and L. Baeza[1]

[1]Centro de Investigación en Ingeniería Mecánica, Universitat Politècnica de València,

Camino de Vera s/n, 46022 Valencia, Spain.

e-mail address of corresponding author: jomarc12@mcm.upv.es

ABSTRACT

As it is well known, there are various phenomena related to railway train-track interaction, some of them caused by the high–frequency dynamics of the system, such as rolling noise, squeal noise and short-pitch rail corrugation. Due to these phenomena and some others unsolved so far, a large effort has been made over the last 40 years in order to define suitable models for studying train-track interaction. In most of the early works the vehicle was modelled as a rigid body system. Later, the introduction of the wheelset flexibility in the model was required to have a more realistic representation of the wheel–rail interaction effects at higher frequencies. Recently, more advanced train-track interaction models have been developed for vehicle running on straight track and negotiating a curved track, where the rails are modelled by means of Timoshenko beam elements with cyclic boundary conditions. Thus, the rail model is valid up to 1.5 kHz for lateral vibration and up to 2 kHz for vertical vibration. Therefore, this confines the frequency range of validity for the complete train-track model to 1.5 kHz.

The aim of this paper is to propose an improvement of the train-track interaction models so as to extend their range of validity above 1.5 kHz. With this purpose, a track model based on the 3D Moving Element Method (MEM) is developed to replace the Timoshenko beam considered in earlier studies, adopting cyclic boundary conditions and Eulerian coordinates. The MEM approach considers a mobile finite element (FE) mesh which moves with the vehicle speed, so the mass of the rail 'flows' with the velocity of the vehicle but in the opposite direction through the mesh. The MEM permits to fix the contact area in the middle of the finitely long track and, hence, to refine longitudinally the mesh only around the contact area. This Eulerian-modal approach reduces substantially the number of degrees of freedom of the problem whereby, together with a refinement just around the fixed contact area, the computational cost of the proposed model is much lower than FEM models widely used. Simulation results for the proposed modelling approach are presented and discussed for different excitation sources including random rail roughness and singularities such as wheel flats. All the simulation cases are made for a Timoshenko beam and a 3D MEM rail models, in order to point out the differences in the contact forces above the range of validity of the Timoshenko beam.

1. INTRODUCTION

The complexity of the train-track interaction comes from the vibration coupling between the railway vehicle and a flexible track, in which wheel–rail contact forces couple both sub-systems and their surface imperfections, such as rail roughness and wheel out-of-roundness, excite the global system. Unwanted phenomena such as damage of the rolling surfaces in the form of high levels of noise and vibration [1], corrugation [2], rolling contact fatigue [3] and dynamic stresses may appear in some cases due to large level of vibration and large dynamic fluctuations of the contact forces, which need to be carefully considered in order to avoid failures due to metal fatigue.

Paper 235

©Civil-Comp Press, 2016
Proceedings of the Third International Conference on
Railway Technology: Research, Development and
Maintenance, J. Pombo, (Editor),
Civil-Comp Press, Cagliari, Sardinia, Italy.

Curve Squeal of Rail Vehicles: Linear Stability Analysis and Non-linear Time-domain Simulation

A. Pieringer[1], P.T. Torstensson[2] and J. Giner[3],
[1]Department of Civil and Environmental Engineering/CHARMEC, Chalmers University of Technology, Gothenburg, Sweden
[2]Department of Applied Mechanics/CHARMEC, Chalmers University of Technology, Gothenburg, Sweden
[3]Department of Mechanical and Materials Engineering, Polytechnical University of Valencia, Spain

Abstract

Railway curve squeal arises from self-excited vibrations during curving. In this paper, a combination of frequency- and a time-domain approach for curve squeal is applied in order to compare and evaluate the two different approaches. In the frequency-domain, linear stability is investigated through complex eigenvalue analysis. The time-domain model is based on the Green's functions approach and uses a convolution procedure to obtain the system response. To ensure comparability, the same submodels are implemented in both squeal models. The wheel model includes a single flexible wheel and accounts for inertia effects due to rotation adopting Eulerian coordinates. The track is modelled using the moving element method technique corresponding to a finite element mesh that travels with the vehicle speed. Coulomb's law with a constant friction coefficient is applied to model the local friction characteristics in the contact zone. The frictional instability arises due to geometrical coupling. The rolling contact model applied is Kalker's variational method in the time domain and a linearized version of this method in the frequency domain. Conditions similar to those of a curve on the Stockholm metro exposed to severe curve squeal are studied with both squeal models. The influence of the wheel-rail friction coefficient and the direction of the resulting creep force on the occurrence of squeal is investigated for vanishing train speed. The results of both models show similar tendencies, but differ in the predicted squeal frequencies.

Keywords: curve squeal, instability, wheel-rail interaction, stability analysis, time domain, non-linearity, friction.

Prediction of rail corrugation growth in curves using a flexible and rotating wheelset model

P. Vila[1], L. Baeza[1], J. Martínez-Casas[1] and J. Giner[1]

[1] Centro de Investigación en Ingeniería Mecánica, Universitat Politècnica de València

Camino de Vera s/n, 46022 Valencia, Spain

Tel: +34 96 387 7000 (Ext: 76267), Fax: +34 96 387 7629, E-mail: mavitor2@upvnet.upv.es

Summary

In this study, a simulation tool for rail corrugation analysis which is based on a feedback process accounting for the dynamic vehicle-track interaction in the time domain, and for the damage due to wear at the wheel-rail contact patch is used. The vehicle-track interaction model comprises a rotating flexible wheelset model, a cyclic track model based on a substructuring technique and a three-dimensional, non-Hertzian and non-steady-state wheel-rail contact model based on the variational theory by Kalker. Archard’s wear model together with the non-Hertzian and non-steady-state contact model are used to compute the wear depths on the running surfaces of rails. The aim of this work is to analyse the combined effect of the dynamics of the rotating flexible wheelset, the vertical stiffness of railpads and the quasi-static curving behaviour of a wheelset on rail corrugation growth in large curves. Results confirm that the inertial effects caused by the wheelset rotation give rise to rail corrugation growth with wavelength 110 mm only on the low rail due to the simultaneous excitation of the backward wheel mode with two nodal diameters and the forward third bending mode (B-F modes) at 142 km/h. This may be an original wavelength-fixing mechanism, whose effects are significantly magnified when stiff railpads are considered.

1 Introduction

It is well known that the development of rail corrugation is closely related to certain resonances and antiresonances of the vehicle-track coupled system, which act as wavelength-fixing mechanisms. Moreover, wear is the damage mechanism responsible for most of the types of corrugation identified so far [1]. Roughness existing on the running surfaces of rails, even if they are brand new or recently ground together with the discontinuous support of the track by sleepers can excite the complex dynamics of the vehicle-track system and give rise to rail corrugation. Additionally, the onset of rail corrugation can be triggered by the presence of discrete defects on the running surfaces of rails, such as wheelburns, dipped joints and bad welds [2].

Nevertheless, after more than a century of field observations of rail corrugation and three decades of mathematical modelling, a definite solution to this problem is still lacking. The most effective treatments of rail corrugation (grinding and friction modifiers) are unable to avoid its reappearance and cause high maintenance costs to railway administrators. In this situation, simulation tools of rail corrugation can play an important role in identifying the mechanisms lying behind its formation and growth and possibly help to find solutions.

In this sense, further research is required to gain a better understanding of the influence of the dynamics of the wheelset on rail corrugation, since most of the wheelset models implemented into vehicle-track interaction models for corrugation analysis are rigid ones. On the other hand, the stiffness of railpads has proven to have a relevant influence on rail corrugation growth [3-5] but to the authors’ knowledge, its combined effect with the dynamics of the wheelset has not been studied yet. Moreover, the study of the influence of the wheel-rail contact conditions arising when a vehicle negotiates a curve on rail corrugation growth deserves special attention since curves are known to be prone to develop corrugation, even if they have large radii.

In this paper, the simulation tool to analyse rail corrugation growth presented in [6] is used. It is based on a feedback process accounting for the dynamic vehicle-track interaction in the time domain, and for the damage due to wear at the wheel-rail contact patch. The vehicle-track interaction model comprises a rotating flexible wheelset model [7], a cyclic track model based on a substructuring technique [8] and a three-dimensional, non-Hertzian and non-steady-state wheel-rail contact model based on the variational theory by Kalker [9]. Archard’s

Investigation of railway curve squeal using a combination of frequency- and time-domain models

A. Pieringer[1], P.T. Torstensson[2], J. Giner[3] and L. Baeza[3]

[1] Chalmers University of Technology, CHARMEC / Division of Applied Acoustics

41296 Göteborg, Sweden,

Tel: +46 31 772 2209, E-mail: astrid.pieringer@chalmers.se

[2] Chalmers University of Technology, CHARMEC / Department of Applied Mechanics, Sweden

[3] Universitat Politècnica de València, Centro de Investigación en Ingeniería Mecánica, Spain

Summary

Railway curve squeal arises from self-excited vibrations during curving. In this paper, a frequency- and a time-domain approach for curve squeal are compared. In particular, the capability of the frequency-domain model to predict the onset of squeal and the squeal frequencies is studied. In the frequency-domain model, linear stability is investigated through complex eigenvalue analysis. The time-domain model is based on a Green's functions approach and uses a convolution procedure to obtain the system response. To ensure comparability, the same submodels are implemented in both squeal models. The structural flexibility of a rotating wheel is modelled by adopting Eulerian coordinates. To account for the moving wheel–rail contact load, the so-called moving element method is used to model the track. The local friction characteristics in the contact zone is modelled in accordance with Coulomb's law with a constant friction coefficient. The frictional instability arises due to geometrical coupling. In the time-domain model, Kalker's non-linear, non-steady state rolling contact model including the algorithms NORM and TANG for normal and tangential contact, respectively, is solved in each time step. In the frequency-domain model, the normal wheel/rail contact is modelled by a linearization of the force-displacement relation obtained with NORM around the quasi-static state and full-slip conditions are considered in tangential direction. Conditions similar to those of a curve on the Stockholm metro exposed to severe curve squeal are studied with both squeal models. The influence of the wheel-rail friction coefficient and the direction of the resulting creep force on the occurrence of squeal is investigated for vanishing train speed. Results from both models are similar in terms of the instability range in the parameter space and the predicted squeal frequencies.

1 Introduction

Creep forces at the wheel/rail interface allow for steering of railway vehicles. In unfavorable conditions in small radius curves, this ability may coincide with the generation of a high-frequency tonal noise referred to as curve squeal. Curve squeal originates from self-excited vibrations of the railway wheel and occurs at frequencies corresponding to its axial normal modes [1].

At the squeal frequencies, the wheel mobility exceeds that of the rail making the wheel to become the dominating noise source [1]. Hence, in the development of models for squeal prediction, it is of fundamental importance to accurately capture the high-frequency dynamic wheel behaviour. Studies in the literature typically apply a non-rotating wheel modelled using the finite element method [2-4]. Fayos et al. [5] adopted Eulerian coordinates to develop a model of a rotating flexible wheelset that fully accounts for inertia forces such as gyroscopic forces and centrifugal stiffening. In [6], Pieringer et al. investigated the influence of wheel rotation on squeal predictions using the wheel model from [5,7]. While wheel rotation did not impact on the tendency to squeal and the resulting lateral contact forces in this study, it was recommended to investigate the influence of wheel rotation on the radiated sound.

The track represents a complex structure in terms of modelling. Cross-sectional deformation occurs already at frequencies around 200 Hz [8], which implies that the three-dimensional dynamic behaviour of the rail has to be accounted for at higher frequencies. One modelling alternative is to use waveguide finite elements that combine a discretization of the two-dimensional cross-section geometry of the rail with an analytical wave-type solution along the rail [4,9]. Koh et al. [10] presented a mathematical formulation of a railway track adopting Eulerian

Improved railway train-track interaction model in curves in the high-frequency domain

J. Giner-Navarro, J. Martínez-Casas, L. Baeza, F. D. Denia and J. Carballeira

Centro de Investigación en Ingeniería Mecánica, Universitat Politècnica de València, Camino de Vera s/n, 46022 Valencia, Spain. E-mail: juagina1@etsid.upv.es

EXTENDED ABSTRACT

1. Introduction

The interaction between a railway vehicle and the track is a very complex problem due to the vibrational coupling of both sub-systems through the forces appearing in the contact area. These contact forces depend on the surface imperfections, such as rail roughness and wheel out-of-roundness. Unwanted phenomena such as damage of the rolling surfaces in the form of high levels of noise and vibration [1], corrugation [2], wheelset axle fatigue [3] and stress damage are related to the large dynamic oscillation of the contact forces.

Although railways are generally considered an environmentally friendly mean of transportation, wheel-rail noise generation is one of their few environmental drawbacks. Curve squeal noise, the most annoying type of noise which generally appears when the train negotiates a sharp curve, is generated above 5 kHz according to the literature [1]. In order to get a better understanding of the phenomena, finite element (FE) wheel models have been introduced in railways research to take the flexibility of the wheelset into account, thus extending the frequency range; only very recently, further works have considered the inertial effects due to wheelset rotation running on a tangent [3] and curved track [4]. Additionally, a FE cyclic track model with a refined mesh in the contact area has been developed in [5] to extend the frequency range of validity of the track models commonly used (Timoshenko beam, [6]).

In this paper, some simulations for a curved track are carried out in the time domain using both the aforementioned wheelset and the track models and including the dynamics of the carbody and the bogie frames through two alternative strategies. Then, the results are compared with the simulations of a model using a Timoshenko beam, in order to verify if the proposed high-frequency interaction model can predict squeal noise by the occurrence of peaks in the tangential forces.

2. Overview of the mathematical approach

An Eulerian-modal approach is adopted for the FE wheelset model (see Fig. 1(a)), in which $\mathbf{\Phi}(\mathbf{u})$ is the mode shape function matrix of the free-boundary wheelset. This matrix does not depend on time since the rotation of the solid does not change the mode shape functions in fixed coordinates due to the axial symmetry of the wheelset. The modal properties are computed from a FE technique, resulting the following modal equation of motion

$$\ddot{\mathbf{q}} + \left(2\Omega\,\tilde{\mathbf{V}} + 2\,\tilde{\mathbf{P}}\right)\dot{\mathbf{q}} + \left(\Omega^2\left(\tilde{\mathbf{A}} - \tilde{\mathbf{C}}\right) + 2\Omega\,\tilde{\mathbf{S}} + \tilde{\mathbf{R}} - \tilde{\mathbf{B}} + \tilde{\mathbf{D}}\right)\mathbf{q} = \Omega^2\,\tilde{\mathbf{c}} - 2\Omega\,\tilde{\mathbf{U}} - \tilde{\mathbf{H}} + \tilde{\mathbf{N}} - \tilde{\mathbf{G}} + \mathbf{Q}_c + \mathbf{Q}_s\,, \qquad (1)$$

Modelo de interacción dinámica del vehículo ferroviario completo con ejes y vía flexible en curva

J. Martínez-Casas[1], E. Di Gialleonardo[2], S. Bruni[2], J. Giner-Navarro[1], J. Carballeira[1]

[1] *Centro de Investigación en Ingeniería Mecánica. Universitat Politècnica de València.* jomarc12@mcm.upv.es

[2] *Dipartimento di Meccanica. Politecnico di Milano*

Durante los últimos años, el modelado de la dinámica del vehículo ferroviario y la interacción vehículo-vía ha sido objeto de una intensa investigación, obteniéndose modelos matemáticos avanzados y potentes herramientas para la simulación numérica. Sin embargo, en la mayoría de los casos estos modelos consideran el vehículo circulando sobre una vía recta, despreciando los efectos relacionados con curva, cuando realmente existen una serie de fenómenos de interacción vehículo-vía específicos de la negociación de una curva. Por ejemplo: la generación de chirridos (squeal) y algunos tipos de corrugación del carril. El objetivo de este trabajo es definir un modelo para la interacción dinámica del vehículo completo con ejes flexibles y una vía flexible en curva. Es un modelo general, pero debido a que se asumen pequeños desplazamientos de los sólidos con respecto a un sistema de coordenadas de trayectoria, se obtiene una formulación eficiente que reduce los tiempos de simulación con respecto a otros planteamientos existentes en la literatura, haciendo por tanto que el modelo sea atractivo para su uso práctico, como puede ser en la etapa de diseño de un nuevo vehículo o vía. En este artículo, el modelo propuesto se aplica para analizar el efecto de un plano de rueda para diferentes condiciones de circulación, combinando velocidades del vehículo, radios de curva y peraltes.

1. Introducción

Durante los últimos años, el modelado de la dinámica del vehículo ferroviario y la interacción vehículo-vía ha sido objeto de una intensa investigación, obteniéndose modelos matemáticos avanzados y potentes herramientas para la simulación numérica.

Si se analiza el estado del arte, se deduce que hay dos enfoques diferentes para este problema: por un lado, se han desarollado modelos denominados de baja frecuencia, los cuales consideran la dinámica de todo el vehículo sobre vía rígida en un rango de frecuencias que rara vez excede de 20 Hz [1]. Estos modelos suelen definirse según un planteamiento de dinámica multicuerpo, lo cual permite analizar el comportamiento dinámico del vehículo, tanto en vía recta como curva, teniendo en cuenta los efectos no lineales relacionados con los grandes desplazamientos del sistema.

Y por otro lado, los modelos de interacción entre vehículo y vía que normalmente incluyen descripciones matemáticas más refinadas para la dinámica de la vía y están dirigidos a analizar un rango de frecuencias más amplio, haciendo posible el estudio del ruido de rodadura y de fenómenos de degradación como la corrugación de los carriles. Estos modelos por lo general sólo consideran las masas no suspendidas del vehículo, y a menudo adoptan un modelo simple de contacto rueda-carril, como una rigidez herciana en dirección normal y fuerzas de pseudo-deslizamiento lineales en dirección tangencial. Por lo general, los efectos en curva son despreciados.

Sin embargo, actualmente hay un interés práctico en ciertos fenómenos de interacción vehículo-vía que se producen específicamente en vías curvas. Los chirridos (squeal) se originan cuando el eje circula en curvas cerradas de radio pequeño. Según la literatura, el origen de este fenómeno se ha asociado a que el coeficiente de fricción se reduce con la velocidad de deslizamiento [2], mientras que otros autores afirman que se puede explicar a partir de una raíz inestable [3]. Además, ciertos tipos de corrugación se pueden encontrar en el carril interno de la curva, y algunos autores asocian la frecuencia de la corrugación con una frecuencia natural del sistema [4].

Para poder analizar los fenómenos mencionados anteriormente, se requiere que se considere a la misma vez la interacción dinámica de alta frecuencia del vehículo-vía mediante la flexibilidad de los ejes y la vía, y los efectos de baja frecuencia asociados al comportamiento en curva del vehículo (el cual depende fundamentalmente de las características del bogie y de la suspensión primaria), a la geometría real de la rueda y del carril y a la relación no lineal entre las fuerzas de contacto y las velocidades de pseudo-deslizamiento. Esto requiere por tanto un enfoque

Mejora del modelo de interacción dinámica vehículo-vía en el dominio de alta frecuencia

J. Martínez-Casas[1], J. Giner-Navarro[1], L. Baeza[1], F. D. Denia[1], P. Vila[1]

[1] *Centro de Investigación en Ingeniería Mecánica. Universitat Politècnica de València.* jomarc12@mcm.upv.es

En el ámbito ferroviario existen varios fenómenos muy conocidos relacionados con la interacción dinámica del vehículo y la vía y originados por la dinámica de alta frecuencia del sistema, tales como el ruido de rodadura del vehículo, los chirridos (squeal) y la corrugación de longitud de onda corta para circulaciones en vías curvas. Debido a estos fenómenos y algunos otros no resueltos a día de hoy, durante los últimos años se han llevado a cabo numerosos estudios sobre modelos de interacción dinámica vehículo-vía. Con el fin de tener una representación más precisa de los fenómenos de interacción a alta frecuencia, se necesita incorporar la flexibilidad del eje y del carril en los modelos correspondientes. En los trabajos de interacción vehículo-vía publicados recientemente, los carriles se modelan mediante vigas de Timoshenko, siendo válida esta aproximación hasta 1.5 kHz. Con el objetivo de extender el rango de validez, en este artículo se desarrolla un modelo de vía 3D basado en el Método de Elementos Móviles (MEM) para reemplazar la aproximación de vigas de Timoshenko utilizada en los estudios previos. Dicho planteamiento considera una malla móvil de elementos finitos del carril que se mueve junto al vehículo, por lo que la masa del carril "fluye" a través de su malla a la velocidad del vehículo en sentido opuesto al movimiento. Por lo tanto, la técnica MEM permite fijar el área de contacto en la mitad de la longitud del carril y refinar la malla solamente en su entorno. Adicionalmente se adopta un planteamiento modal del carril, reduciendo sustancialmente ambas estrategias el coste computacional y haciendo idóneo el modelo para simulaciones dinámicas de alta frecuencia en tiempos razonables. Se presentan y discuten diversos resultados de varias simulaciones dinámicas llevadas a cabo con diferentes fuentes de excitación, como rugosidad aleatoria del carril y singularidades como planos de rueda. Todas las simulaciones se han realizado tanto para el modelo 3D propuesto del carril como para el modelo de vigas de Timoshenko, con el fin de analizar y comparar las diferencias entre las fuerzas de contacto de ambos planteamientos en el dominio de alta frecuencia.

1. Introducción

La complejidad de la interacción dinámica vehículo-vía procede de la vibración acoplada entre el vehículo ferroviario y la vía flexible, donde las fuerzas de contacto rueda-carril acoplan ambos subsistemas. La excitación del sistema global viene originada por las imperfecciones presentes en las superficies del carril y de la rueda, tales como rugosidades y planos de rueda. En algunos casos, y debido a grandes niveles de vibraciones y elevados valores dinámicos de las fuerzas de contacto, aparecen fenómenos inesperados como daños severos en las superficies de rodadura, originando altos niveles de ruido y vibración [1], corrugación en los carriles [2], fatiga en el contacto de la rodadura [3] y considerables tensiones dinámicas. En consecuencia, la metodología utilizada debe considerar de forma rigurosa la dinámica de alta frecuencia, con el fin de ser capaz de contemplar dichos fenómenos y evitar el fallo por fatiga de los componentes mecánicos.

Durante los últimos 40 años, se han desarrollado diversos modelos dinámicos apropiados de interacción vehículo-vía, y algunos más recientes incorporan la flexibilidad del eje para ampliar el rango de análisis en frecuencia [1,4]. Además, para abordar el fenómeno de ruido de rodadura citado anteriormente y extender el rango de frecuencia válido por encima de 1 kHz, se han planteado modelos de Elementos Finitos (EF) en el ámbito ferroviario [5,6], pero sólo en trabajos recientes se ha considerado la flexibilidad y los efectos inerciales debidos a la rotación del eje sobre vía recta [3] y vía curva [7]. Con el fin de ampliar el rango de frecuencias válidas, en este trabajo se considera dicho modelo de eje en vía recta, el cual tiene en cuenta los efectos giroscópicos e inerciales asociados a la rotación del mismo haciendo uso de coordenadas modales Eulerianas, lo cual reduce en consecuencia el coste computacional.

En las publicaciones más recientes sobre modelos de interacción, los carriles vienen representados como vigas de Timoshenko con condiciones de contorno cíclicas [8], siendo válido dicho modelo hasta 1.5 kHz en la dinámica lateral y 2 kHz en la vertical [1], fijando en 1.5 kHz el rango válido de frecuencias para el modelo completo

Congreso de Métodos Numéricos en Ingeniería
3-5 julio 2017, Valencia, España

MODELO MEJORADO DE INTERACCIÓN VEHÍCULO FERROVIARIO-VÍA NEGOCIANDO UNA CURVA EN EL DOMINIO DE LA ALTA FRECUENCIA

J. Giner-Navarro[1], J. Martínez-Casas[1], F. D. Denia[1] y J. Carballeira[1]

1: Centro de Investigación en Ingeniería Mecánica (CIIM)
Universitat Politècnica de València
Camino de Vera s/n, 46022 Valencia, Spain
e-mail: juagina1@etsid.upv.es, web: http://www.ciim.upv.es

Palabras clave: interacción dinámica ferroviaria, chirridos en curva, eje rotatorio, vía cíclica, fricción constante

Resumen: *La interacción dinámica entre un vehículo ferroviario y la vía se presenta como un problema complejo dado el acoplamiento vibracional entre ambos subsistemas a través de las fuerzas que aparecen en el área de contacto. Aunque el transporte ferroviario se considera generalmente respetuoso con el medio ambiente, el ruido proveniente de la interacción rueda-carril es un inconveniente relevante que ha recibido especial atención en las últimas décadas.*

Los chirridos en curva, ruido de fuerte carácter tonal en el dominio de las altas frecuencias, aparecen generalmente cuando el tren negocia una curva cerrada. Con el objetivo de alcanzar una mejor comprensión del fenómeno, se han implementado modelos de Elementos Finitos (EF) de la rueda para incluir su flexibilidad y extender así el rango de frecuencias; recientes trabajos han introducido también los efectos inerciales debidos a la rotación del eje. Por otra parte, se ha desarrollado un modelo flexible de vía cíclica mediante un tipo de elementos finitos conocido como Moving Elements (ME), que permite refinar la malla únicamente alrededor del área de contacto.

En el presente artículo, se han llevado a cabo distintas simulaciones en el dominio del tiempo para circulación en vía curva considerando dos radios de curva y cuatro coeficientes de fricción distintos, evaluándose las fuerzas de contacto tangenciales en busca de inestabilidades que puedan estar asociadas a este fenómeno de chirridos en curva. A su vez, se ha estudiado la influencia de los efectos giroscópicos asociados a la rotación del eje.

Congreso de Métodos Numéricos en Ingeniería CMN2017
Valencia, 3-5 julio, 2017

Estudio del crecimiento de la corrugación en carriles en vía curva utilizando un modelo de eje montado flexible rotatorio

Paloma Vila[†]*, Juan Giner-Navarro[†], José Martínez-Casas[†] y Luis Baeza[††]

[†] Centro de Investigación en Ingeniería Mecánica (CIIM)
Universitat Politècnica de València
Camino de Vera s/n, 46022 Valencia, Spain
e-mail: mavitor2@upvnet.upv.es, web page: http://www.upv.es

[††] Institute of Sound and Vibration Research (ISVR)
University of Southampton
Southampton SO17 1BJ, United Kingdom
e-mail: L.Baeza@soton.ac.uk, web page: http://www.southampton.ac.uk

RESUMEN

En este artículo, con el fin de analizar el crecimiento de la corrugación en carriles ferroviarios, se utiliza una herramienta de simulación basada en un proceso retroalimentado que considera la interacción dinámica vehículo-vía en el dominio del tiempo y el daño debido al desgaste en el contacto rueda-carril [1]. El modelo de interacción vehículo-vía comprende un modelo de eje montado flexible rotatorio [2], un modelo de vía cíclica [3] y un modelo de contacto tridimensional, no herciano y no estacionario basado en la teoría variacional de Kalker [4]. El sistema vehículo-vía es excitado mediante rugosidad pseudoaleatoria en los carriles, de reducida amplitud [5]. Se emplea el modelo de Archard para el cálculo del desgaste y la tasa global de crecimiento de la corrugación [6] para predecir la evolución del defecto.

En trabajos previos de los autores [1, 7], se estudió el efecto de la excitación de dos resonancias coincidentes del eje flexible rotatorio en el crecimiento de la corrugación. En el presente trabajo se extiende el estudio realizado en [1] con el objetivo de analizar el efecto combinado de la dinámica del eje montado, la rigidez vertical de las placas de asiento de los carriles y las condiciones existentes en el contacto rueda-carril cuando el eje delantero de un bogie circula por una curva de radio elevado en el crecimiento de la corrugación. Los resultados obtenidos muestran que las placas de asiento de elevada rigidez vertical pueden incrementar significativamente el crecimiento de la corrugación a determinadas longitudes de onda.

REFERENCIAS

[1] P. Vila, L. Baeza, J. Martínez-Casas and J. Carballeira,” Rail corrugation growth accounting for the flexibility and rotation of the wheelset and the non-Hertzian and non-steady-state effects at contact patch”, *Veh. Syst. Dyn.,* **52**, 92-108 (2014).

[2] J. Fayos, L. Baeza, F.D. Denia and J.E. Tarancón, “An Eulerian coordinate-based method for analysing the structural vibrations of a solid of revolution rotating about its main axis”, *J. Sound Vib.,* **306**, 618-635 (2007).

[3] L. Baeza and H. Ouyang, “A railway track dynamics model based on modal substructuring and a cyclic boundary condition”, *J. Sound Vib.,* **330**, 75-86 (2011).

[4] J.J. Kalker, *Three-dimensional elastic bodies in rolling contact*, Kluwer Academic Publishers, Dordrecht, Boston London, (1990).

[5] EN ISO 3095:2005: Railway applications-acoustics measurements of noise emitted by railbound vehicles.

[6] K. Hempelmann and K. Knothe, “An extended linear model for the prediction of short pitch corrugation*”, Wear,* **191**, 161-169 (1996).

[7] P. Vila, J. Fayos and L. Baeza, “Simulation of the evolution of rail corrugation using a rotating flexible wheelset model”, *Veh. Syst. Dyn.,* **49**, 1749-1769 (2011).

References

[1] J.M. Fields, J.G. Walker. Comparing the relationships between noise level and annoyance in different surveys: A railway noise vs. aircraft and road traffic comparison. *Journal of Sound and Vibration*, 81(1):51–80, 1982.

[2] U. Moehler. Community response to railway noise: A review of social surveys. *Journal of Sound and Vibration*, 120(2):321–332, 1988.

[3] D.J. Thompson, C.J.C. Jones. A review of the modelling of wheel/rail noise generation. *Journal of Sound and Vibration*, 231(3):519–536, 2000.

[4] P.E. Gauthier, C. Talotte, P. Fodiman. La recherche à la SNCF pour la réduction du bruit des trains. *Revue générale des chemins de fer*, 6:9–19, 1999.

[5] M.J. Rudd. Wheel/rail noise – Part II: Wheel squeal. *Journal of Sound and Vibration*, 46(3):381–394, 1976.

[6] P.J. Remington. Wheel/rail squeal and impact noise: What do we know? What we don't know? Where do we go from here? *Journal of Sound Vibration*, 46(3):381–353, 1985.

[7] D.J. Thompson. *Railway Noise and Vibration: Mechanisms, Modelling and Means of Control*. Elsevier, Oxford, UK, 2009.

[8] D. Hanson, J. Jiang, B. Dowdell, R. Dwight. Curve squeal: causes, treatments and results. *INTER-NOISE and NOISE-CON Congress and Conference Proceedings*, 249:6316–6323, Melbourne, Australia, 2014.

[9] Ch. Glocker, E. Cataldi-Spinola, R.I. Leine. Curve squealing of trains: Measurement, modelling and simulation. *Journal of Sound and Vibration*, 324:365–386, 2009.

[10] N. Vicent, J.R. Koch, H. Chollet, J.Y. Guerder. Curve squeal of urban rolling stock – Part 1: State of the art and field measurements. *Journal of Sound and Vibration*, 293:691–700, 2006.

[11] J.R. Koch, N. Vincent, H. Chollet, O. Chiello. Curve squeal of urban rolling stock – Part 2: Parametric study on a 1/4 scale test rig. *Journal of Sound and Vibration*, 293:701-709, 2006.

[12] S.S. Hsu, Z. Huang, S.D. Iwnicki, D.J. Thompson, C.J.C. Jones, G. Xie, P.D. Allen. Experimental and theoretical investigation of railway wheel squeal. *Proceedings of the Institution of Mechanical Engineers, Part F: Journal of Rail and Rapid Transit*, 221:59–73, 2007.

[13] A. Pieringer. A numerical investigation of curve squeal in the case of constant wheel/rail friction. Journal of Sound and Vibration, 333(18):4295–4313, 2014.

[14] P.J. Remington. Wheel/rail noise – Part IV: Rolling noise. *Journal of Sound and Vibration*, 46(3):419–436, 1976.

[15] D.J. Thompson, C.J.C. Jones. Sound radiation from a vibrating railway wheel. *Journal of Sound and Vibration*, 253(2):401–419, 2002.

[16] B.E. Croft. *The Development of Rail-head Acoustic Roughness*. PhD thesis, Institute of Sound and Vibration Research, University of Southampton, Southampton, United Kingdom, October 2009.

[17] A. Pieringer, L. Baeza, W. Kropp. Modelling of railway curve squeal including effects of wheel rotation. In Noise and Vibration Mitigation for Rail Transportation Systems, J.C.O. Nielsen, D. Anderson, P.-E. Gautier, M. Iida, J. T. Nelson, D. Thompson, T. Tielkes, D. A. Towers, P. de Vos, (Editors), Notes on Numerical Fluid Mechanics and Multidisciplinary Design, Springer Berlin Heidelberg, 126:417–424, 2015.

[18] B. Ding, G. Squicciarini, D.J. Thompson. Effects of rail dynamics and friction characteristics on curve squeal. *XIII International Conference on Motion and Vibration Control and XII International Conference on Recent Advances in Structural Dynamics (MoViC/RASD)*, Southampton, 2016.

[19] Z.Y. Huang. *Theoretical Modelling of Railway Curve Squeal*. PhD thesis, University of Southampton, UK, 2007.

[20] O. Chiello, J.B. Ayasse, N. Vincent, J.R. Koch. Curve squeal of urban rolling stock - Part 3: Theoretical model. *Journal of Sound and Vibration*, 293:710–727, 2006.

[21] N. Hoffmann, M. Fischer, R. Allgaier, L. Gaul. A minimal model for studying properties of the mode-coupling type instability in friction induced oscillations. Mechanics Research Communications, 29:197–205, 2002.

[22] J. Le Rouzic, A. Le Bot, J. Perret-Liaudet, M. Guibert, A. Rusanov, L. Douminge, F. Bretagnol, D. Mazuyer. Friction-induced vibration by Stribeck’s law: application to wiper blade squeal noise. *Tribology Letters*, 49:563–572, 2013.

[23] L. Baeza, F.J. Fuenmayor, J. Carballeira, A. Roda. Influence of the wheel/rail contact instationary process on contact parameters. *Journal of Strain Analysis for Engineering Design*, 42:377–387, 2007.

[24] I. Zenzerovic. *Engineering model for curve squeal formulated in the time domain*, Thesis for the Degree of Licentiate of Engineering, Department of Civil and Environmental Engineering, Chalmers University of Technology, Gothenburg, Sweden, 2014.

[25] N. Hoffmann, M. Fischer, R. Allgaier, L. Gaul. A minimal model for studying properties of the mode-coupling type instability in friction induced oscillations. Mechanics Research Communications, 29(4):197–205, 2002.

[26] N. Hoffmann, L. Gaul. Effects of damping on mode-coupling instability in friction induced oscillations. *Journal of Applied Mathematics and Mechanics*, 83(8):524–534, 2003.

[27] J.J. Sinou, L. Jezequel. Mode coupling instability in friction-induced vibrations and its dependency on system parameters including damping. *European Journal of Mechanics-A/Solids*, 26(1):106–122, 2007.

[28] K.L. Johnson. *Contact Mechanics*. Cambridge University Press, 1987.

[29] U. Fingberg. A model of wheel/rail squealing noise. Journal of Sound and Vibration, 143(3):365–377, 1990.

[30] P.J. Remington. Wheel/rail noise, I: Theoretical analysis. *Journal of the Acoustical Society of America*, 81(6):1824–1832, 1987.

[31] P. Remington, J. Webb. Estimation of wheel/rail interaction forces in the contact area due to roughness. *Journal of Sound and Vibration*, 193(1):83–102, 1996.

[32] D.J. Thompson. The influence of the contact zone on the excitation of wheel/rail noise. *Journal of Sound and Vibration*, 267:523–535, 2003.

[33] J. Jergéus. *Railway Wheel Flats – Martensite Formation, Residual Stresses, and Crack Propagation*. PhD Thesis, Division of Solid Mechanics, Chalmers University of Technology, Gothenburg, Sweden, 1998.

[34] S.G. Newton, R.A. Clark. An investigation into the dynamic effects on the track of wheelflats on railway vehicles. *Journal of Mechanical Engineering Science*, 21(4):287–297, 1979.

[35] T.X. Wu, D.J. Thompson. On the impact noise generation due to a wheel passing over rail joints. *Journal of Sound and Vibration*, 267:485–496, 2003.

[36] T.X. Wu, D.J. Thompson. A hybrid model for the noise generation due to railway wheel flats. *Journal of Sound and Vibration*, 251(1):115–139, 2002.

[37] L. Baeza, A. Roda, J. Carballeira, E. Giner. Railway train/track dynamics for wheel flats with improved contact models. *Nonlinear Dynamics*, 45:385–397, 2006.

[38] EN 14363:2007. Railway applications. *Testing for the acceptance of running characteristics of railway vehicles. Testing of running behaviour and stationary tests*. Aennor, 2007.

[39] K. Knothe, S.L. Grassie. Modelling of railway track and vehicle/track interaction at high frequencies. *Vehicle System Dynamics*, 22:209–262, 1993.

[40] K. Popp, H. Kruse, I. Kaiser. Vehicle-track dynamics in the mid-frequency range. *Vehicle System Dynamics*, 31:423–464, 1999.

[41] P. Vila. *Modelado del crecimiento del desgaste ondulatorio en carriles ferroviarios*, Ph.D. Thesis, Centro de Investigación en Ingeniería Mecánica, Universitat Politècniva de València, València, Spain, 2015.

[42] T. Szolc. Medium frequency dynamic investigation of the railway wheelseet-track system using a discrete-continuous model. *Archive of Applied Mechanics*, 68:30–45, 1998.

[43] J.C.O. Nielsen. Numerical prediction of rail roughness growth on tangent railway tracks. *Journal of Sound and Vibration*, 267:537–548, 2003.

[44] P.T. Torstensson, A. Pieringer, J.C.O. Nielsen, Simulation of rail roughness growth on small radius curves using a non-Hertzian and non-steady wheel/rail contact model. *Proceedings of the 9th International Conference on Contact Mechanics and Wear of Rail/Wheel Systems (CM2012)*, Chengdu, China, 2012.

[45] H.D. Nelson, J.M. McVaugh. The dynamics of rotor-bearing systems using finite element. *Journal of Engineering for Industry*, 98:593–600, 1976.

[46] E.S. Zorzi, H.D. Nelson. Finite element simulation of rotor-bearing systems with internal damping. *Journal of Engineering for Power*, 99:71–76, 1977.

[47] L.W. Chen, D.M. Ku. Analysis of whirl speeds of rotor-bearing systems with internal damping by C° finite elements. *Finite Elements in Analysis and Design*, 9:169–176, 1991.

[48] D. Ku. Finite element analysis of whirl speeds for rotor-bearing systems with internal damping. *Mechanical Systems and Signal Processing*, 12:599–610, 1998.

[49] O.C. Zienkiewicz, R.L. Taylor, J.Z. Zhu. *The finite element method: Its basis and fundamentals*. Elsevier Butterworth-Heinemann, 2005.

[50] R. Sino, E. Chatelet, O. Montagnier, G. Jacquet-Richardet. Dynamic instability analysis of internally damped rotors. *Proceedings of ASME Turbo Expo 2007 Power for Land, Sea and Air*, Vol. 5, Montréal, pp.727–736, May 2007.

[51] M.A. Hili, T. Fakhfakh, M. Haddar. Vibration analysis of a rotating flexible shaft-disk system. *Journal of Engineering Mathematics*, 57:351–363, 2007.

[52] G. Jacquet-Richardet, G. Ferraris, P. Rieutord. Frequencies and modes of rotating flexible bladed disc-shaft assemblies: a global cyclic symmetry approach. *Journal of Sound and Vibration*, 191:901–915, 1996.

[53] J. Yu, A. Craggs. 3-D solid finite element modeling of rotating shafts. *Proceedings of the 15th International Modal Analysis Conference—Imac*, Vols. I and II, Vol. 3089, Orlando, pp. 1488–1494, 1997.

[54] E. Chatelet, D. Lornage, G. Jacquet-Richardet. A three dimensional modeling of the dynamic behavior of composite rotors. *International Journal of Rotating Machinery*, 8:185–192, 2002.

[55] J. Fayos, L. Baeza, F.D. Denia, J.E. Tarancón. An Eulerian coordinate-based method for analysing the structural vibrations of a solid of revolution rotating about its main axis. *Journal of Sound and Vibration*, 306:618–635, 2007.

[56] L. Baeza, J. Fayos, A. Roda, R. Insa. High frequency railway vehicle-track dynamics through flexible rotating wheelsets. *Vehicle System Dynamics*, 46 (7):647–662, 2008.

[57] P.T. Torstensson, J.C.O. Nielsen, L. Baeza. Dynamic train/track interaction at high vehicle speeds-Modelling of wheelset dynamics and wheel rotation. *Journal of Sound and Vibration*, 330:5309–5321, 2011.

[58] C. Esveld. *Modern Railway Track*. MRT-Productions Delft, The Netherlands, 2001.

[59] T.X. Wu, D.J. Thompson. Theoretical investigation of wheel/rail nonlinear interaction due to roughness excitation. *Vehicle System Dynamics*, 34:261–282, 2000.

[60] D.J. Thompson, N. Vincent. Track dynamic behaviour at high frequencies. Part 1: Theoretical models and laboratory measurements. *Vehicle System Dynamics*, Supplement 24:86–99, 1995.

[61] N. Vincent, D.J. Thompson. Track dynamic behaviour at high frequencies. Part 2: Experimental results and comparisons with theory. *Vehicle System Dynamics*, Supplement 24:100–114, 1995.

[62] J.C.O. Nielsen, A. Igeland. Vertical dynamic interaction between train and track - influence of wheel and track imperfections. *Journal of Sound and Vibration*, 187(5):825–839, 1995.

[63] D.J. Thompson. Wheel/rail noise generation, Part III: Rail vibration. *Journal of Sound and Vibration*, 161(3):421–446, 1993.

[64] W. Scholl. Schwingungsuntersuchungen and Eisenbahnschienen. *Acustica*, 52(1):10–15, 1982.

[65] L. Gry. Dynamic modelling of railway track based on wave propagation. *Journal of Sound and Vibration*, 195(3):477–505, 1996.

[66] C. Andersson. Modelling and simulation of train–track interaction including wear prediction. Ph. D. Dissertation, Department of Applied Mechanics, Chalmers University of Technology, Gothenburg, Sweden, 2003.

[67] C.-M. Nilsson, C.J.C. Jones, D.J. Thompson, J. Ryue. A waveguide finite element and boundary element approach to calculating the sound radiated by railway and tram rails. Journal of Sound and Vibration, 321:813–836, 2009.

[68] C. Andersson, J. Oscarsson. Dynamic train/track interaction including state-dependent track properties and flexible vehicle components. *Vehicle System Dynamics*, 33:47–58, 1999.

[69] A. Nordborg. Wheel/rail noise generation due to nonlinear effects and parametric excitation. *Journal of the Acoustical Society of America*, 111(4):1772–1781, April 2002.

[70] J.J. Kalker. Survey of wheel/rail rolling contact theory. *Vehicle System Dynamics*, 5:317–358, 1979.

[71] J. Boussinesq. *Application des Potentiels à l'Étude de l'Équilibre et du Mouvement des Solides Élastiques*. Gauthier-Villars, Paris, 1885.

[72] V. Cerruti. *Mem. fis. mat.* Accademia dei Lincei, Roma, 1882.

[73] T. Mazilu. Green's functions for analysis of dynamic response of wheel/rail to vertical excitation. *Journal of Sound and Vibration*, 306:31–58, 2007.

[74] F.J. Périard. *Wheel/rail Noise Generation: Curve Squealing by Trams*. PhD thesis, Technische Universiteit Delft, 1998.

[75] H. Hertz. Ueber die Berührung fester elastischer Körper. *Journal für reine und angewandte Mathematik*, 92:156–171, 1882.

[76] G. Lundberg, H. Sjövall. *Stress and Deformation in Elastic Contacts*. Publikation nr 4, The Institution of Theory of Elasticity and Strength of Materials, Chalmers University of Technology, Gothenburg, Sweden, 1958.

[77] W. Yan, D. Fischer. Applicability of the Hertz contact theory to rail-wheel contact problems. *Archive of Applied Mechanics*, 70:255–268, 2000.

[78] K. Knothe, S. Stichel. *Schienenfahrzeugdynamik*. Springer-Verlag, Berlin Heidelberg, 2003.

[79] H. Wu, J.M. Wang. Non-Hertzian conformal contact at wheel/rail interface. In *Proceedings of the 1995 IEEE/ASME Joint Railroad Conference*, April 4-6, 1995, Baltimore, Maryland, pages 137–144. Institute of Electrical and Electronics Engineering, 1995.

[80] K. Knothe, R. Wille, W. Zastrau. Advanced contact mechanics - road and rail. *Vehicle System Dynamics*, 35(4-5):361–407, 2001.

[81] J.J. Kalker. *Three-dimensional elastic bodies in rolling contact*. Kluwer Academic Publishers, Dordrecht, Boston, London, 1990.

[82] B. Paul, J. Hashemi. Contact pressure on closely conforming elastic bodies, *Journal of Applied Mechanics*, 48:543–548, 1981.

[83] H. Le-The. *Normal und Tangentialspannungberechnung beim rollenden Kontakt für Rotationskörper mit nichtelliptischen Kontaktflächen*, Doctoral Thesis. Technische Universität Berlin, Berlin, Germany, 1986.

[84] J. Piotrowski, H. Chollet. Wheel/rail contact models for vehicle system dynamics including multi-point contact. *Vehicle System Dynamics*, 43(6-7):455–483, 2005.

[85] J.P. Pascal, G. Sauvage. The available methods to calculate the wheel/rail forces in non Hertzian contact patches and rail damaging. *Vehicle System Dynamics*, 22:263–275, 1993.

[86] J.B. Ayasse, H. Chollet. Determination of the wheel rail contact patch in semi-Hertzian conditions. *Vehicle System Dynamics*, 43(3):161–172, 2005.

[87] J. Piotrowski, W. Kik. A simplified model of wheel/rail contact mechanics for non-Hertzian problems and its application in rail vehicle dynamic simulations. *Vehicle System Dynamics*, 46(1-2):27–48, 2008.

[88] A. Alonso, J.G. Giménez. A new method for the solution of the normal contact problem in the dynamic simulation of railway vehicles. *Vehicle System Dynamics*, 43: 149–160, 2005.

[89] C. Cattaneo. Sul contatto di due corpi elastici: distribuzione locale degli sforzi. *Rendiconti dell'Accademia nazionale dei Lincei*. Ser. 6, 27: 342–478, 1938.

[90] R.D. Mindlin. Compliance of elastic bodies in contact. Trans. ASME, Series E, *Journal of Applied Mechanics*, 16:259–268, 1949.

[91] F.W. Carter. On the action of a locomotive driving wheel. *Proceeding of the Royal Society of London*, Series A, 112(760):151–157, 1926.

[92] H. Fromm. Berechnung des Schlupfes beim Rollen deformierbaren Scheiben. *Zeitschift für angewandte Mathematik und Mechanik*, 7:27–58, 1927.

[93] K. Knothe. History of wheel/rail contact mechanics: from Redtenbacher to Kalker. *Vehicle System Dynamics*, 46 (1-2):9–26, 2008.

[94] A. Pieringer. *Time-domain modelling of high-frequency wheel/rail interaction*, Ph.D. Thesis, Department of Civil and Environmental Engineering, Chalmers University of Technology, Gothenburg, Sweden, 2011.

[95] J.J. Kalker. A fast algorithm for the simplified theory of rolling contact. *Vehicle System Dynamics*, 11:1–13,1982.

[96] J.J. Kalker. Wheel/rail rolling contact theory. *Wear*, 144:243–261, 1991.

[97] J.J. Kalker. Simplified theory of rolling contact. *Delft Progress Report Series C1*, 1:1–10, 1973.

[98] A. Alonso, J.G. Giménez. Non-steady state modelling of the wheel/rail contact problem for the dynamics simulation of railway vehicles. *Vehicle System Dynamics*, 46(3):179–196, 2008.

[99] P.J. Vermeulen, K.L. Johnson. Contact of nonspherical bodies transmitting tangential forces. *Journal of Applied Mechanics*, 31:338–340, 1964.

[100] Z.Y. Shen, J.K. Hendrick, J.A. Elkins. A comparison of alternative creep force models for rail vehicle dynamics analysis. *Vehicle System Dynamics*, 12(1-3):79–83, 1983.

[101] O. Polach. Creep forces in simulations of traction vehicles running on adhesion limit. *Wear*, 258:992–1000, 2005.

[102] K. Knothe, A. Groβ-Thebing. Derivation of frequency dependent creep coefficients based on an elastic half-space model. *Vehicle System Dynamics*, 15(3):133–153, 1986.

[103] E.A.H. Vollebregt, S.D. Iwnicki, G. Xie, P. Shackleton. Assessing the accuracy of different simplified friictional rolling contact mechanisms. *Vehicle System Dynamics,* 50:1–17, 2012.

[104] J.J. Kalker. Book of tables for the Hertzian creep-force law. *Proceedings of the 2nd Mini Conference on Contact Mechanics and Wear of Wheel/Rail Systems,* Budapest, 11–20, 1996.

[105] J.J. Kalker. *On the rolling contact of two elastic bodies in the presence of dry friction*, PhD Thesis, Technical University of Delft (Holland), 1967.

[106] Z.Y. Shen, Z. Li. A fast non-steady state creep force model based on the simplified theory. *Wear*, 191:242–244, 1996.

[107] O. Polach. A fast wheel/rail forces calculation computer code. *Vehicle System Dynamics*, 33:728–739, 1999.

[108] A. Alonso, J.G. Giménez. Tangential problem solution for non-elliptical contact patches with the FastSim algorithm. *Vehicle System Dynamics*, 45(4):341–357, 2007.

[109] A. Guiral, A. Alonso, L. Baeza, J.G. Giménez. Non-steady state modelling of wheel/rail contact problem. *Vehicle System Dynamics*, 51(1):91–108, 2013.

[110] E.A.H. Vollebregt, P. Wilders. FASTSIM2: a second-order accurate frictional rolling contact algorithm. *Computational Mechanics*, 47:105–116, 2011.

[111] K. Kraft. Der Einfluβ der Fahrgeschwindigkeit auf den Haftwert zwischen Rad und Scheine. *Archiv für Eisenbahntechnik*, 22:58–78, 1967.

[112] Z.Y. Huang, D.J. Thompson, C.J.C. Jones. Squeal prediction for a bogied vehicle in a curve. *Notes on Numerical Fluid Mechanics*, 99:313–319, 2008.

[113] G. Squicciarini, S. Usberti, A. Barbera, R. Corradi, D.J. Thompson. Curve squeal in the presence of two wheel/rail contact points. *In Proceedings of the 11th IWRN,* Uddevalla, volume 2, pages 671–678, 2013.

[114] G. Squicciarini, S. Usberti, D.J. Thompson, R. Corradi, A. Barbera. Curve squeal in the presence of two wheel/rail contact points. In: *Proceedings of the 11th International Workshop on Railway Noise,* Springer, 126:603–610, Heidelberg, 2015.

[115] G. Xie, P. D. Allen, S. D. Iwnicki, A. Alonso, D.J. Thompson, C.J.C. Jones, Z. Y. Huang. Introduction of falling friction coefficients into curving calculations for studying curve squeal noise. *Vehicle System Dynamics*, 44(sup 1):261–271, 2006.

[116] E.A.H. Vollebregt, H.M. Schuttelaars. Quasi-static analysis of two-dimensional rolling contact with slip-velocity dependent friction. *Journal of Sound and Vibration*, 331:2141–2155, 2012.

[117] J.G. Giménez, A. Alonso, E. Gómez. Introduction of a friction coefficient dependent on the slip into the FastSim algorithm. *Vehicle System Dynamics*, 43(4): 233–244, 2005.

[118] E.A.H. Vollebregt. Numerical modeling of measured railway creep versus creep-force curves with CONTACT. *Wear*, 314:87–95, 2014.

[119] K. Knothe and A. Groβ-Thebing. Short wavelength rail corrugation and non-steady state contact mechanics. *Vehicle System Dynamics*, 46(1-2):49–66, 2008.

[120] S.L. Grassie, R.W. Gregory, D. Harrison, K.L. Johnson. The dynamic response of railway track to high frequency vertical/lateral/longitudinal excitation. *Journal of Mechanical Engineering Society*, 24:77–102, 1982.

[121] B. Ripke, K. Knothe. Die unendlich lange Schiene auf diskreten Schwellen bei harmonicher Einzellasterregung. *VDI Fortschritt-Berichte*, Dusseldorf, 1991.

[122] K. Knothe. Gleisdynamik and Wechselwirkung zwischen Fahrzeug und Fahrweg. *Zeitschrift für Angewandte Mathematik und Mechanik*, 79:723–737, 1999.

[123] D.J. Thompson. Wheel/rail noise generation, Part IV: Contact zone and results. *Journal of Sound and Vibration*, 161(3):447–466, 1993.

[124] H. Ilias, K. Knothe. Ein diskret-kontinuierliches Gleismodell unter Einfluss schnell bewegter, harmonisch schwankender Wanderlasten. *Fortchritt-Berichte VDI*, Reihe 12, 177, 1992.

[125] H. Ilias, S. Müller. A discrete-continuous track model for the wheelsets rolling over short wavelength sinusoidal rail irregularities. *Vehicle System Dynamics*, 23:221–233, 1994.

[126] P.J. Remington. Wheel/rail noise – Part I: Characterization of the wheel/rail dynamic system. *Journal of Sound and Vibration*, 46(3):359–379, 1976.

[127] P.J. Remington. Wheel/rail noise, II: Validation of the theory. Journal *of the Acoustical Society of America*, 81(6):1833–1841, 1987.

[128] D.J. Thompson. Wheel/rail noise generation, Part I: Introduction and interaction model. *Journal of Sound and Vibration*, 161(3):387–400, 1993.

[129] D.J. Thompson. Wheel/rail noise generation, Part II: Wheel vibration. *Journal of Sound and Vibration*, 161(3):401–419, 1993.

[130] D.J. Thompson. Wheel/rail noise generation, Part V: Inclusion of wheel rotation. *Journal of Sound and Vibration*, 161(3):467–482, 1993.

[131] D.J. Thompson, B. Hemsworth, N. Vincent. Experimental validation of the TWINS prediction program for rolling noise, Part 1: Description of the model and method. *Journal of Sound and Vibration*, 193(1):123–135, 1996.

[132] H. Ilias. The influence of railpad stiffness on wheelset/track interaction and corrugation growth. *Journal of Sound and Vibration*, 227:935–948, 1999.

[133] C. Andersson, T. Abrahamsson. Simulation of Interaction between a train in a general motion and a track. *Vehicle System Dynamics*, 38:433–455, 2002.

[134] J.C.O. Nielsen, J. Oscarsson. Simulation of dynamic train/track interaction with state-dependent track properties. *Journal of Sound and Vibration*, 275:515–532, 2004.

[135] J. Oscarsson. *Dynamic Tran-track Interaction: Linear and Non-Linear Track Models with Property Scatter*, Ph.D. Thesis, Department of Solid Mechanics, Chalmers University of Technology, Gothenburg, Sweden, 2001.

[136] M. Heckl. Proposal for a railway simulation program. *In A Workshop on Rolling Noise Generation*, pp. 128–148. Institut für Technische Akustik, Technische Universität Berlin, October 1989.

[137] M.A. Heckl, I.D. Abrahams. Curve squeal of train wheels, Part 1: Mathematical model for its generation. *Journal of Sound and Vibration*, 229(3):669–693, 2000.

[138] N. Correa, E.G. Vadillo, J. Santamaría, J. Gómez. A rational fraction polynomials model to study vertical dynamic wheel-rail interaction. *Journal of Sound and Vibration*, 331:1844–1858, 2012.

[139] D.J. Thompson, N. Vincent. Track dynamic behaviour at high frequencies. Part 1: Theoretical models and laboratory measurements. *Vehicle System Dynamics*, Supplement 24:86–99, 1995.

[140] J. Jiang, R. Dwight, D. Anderson. Field verification of curving noise mechanism. *In Proceedings of the 10th IWRN*, pages 349–360, Nagahama, Japan, 2010.

[141] G.T. Mase, G.E. Mase. Continuum mechanics for engineers. *CRC Press*, Boca Raton, Florida, 1999.

[142] E. Vollebregt. *User Guide for CONTACT, Vollebregt & Kalker's Rolling and Sliding Contact Model (Technical Report TR09-03).* Version 12.2, VORtech, 2012.

[143] E.A.H. Vollebregt, J.J. Kalker, H.X. Lin. A fast solver for normal and tangential contact mechanics in the half-space. *Transactions on Engineering Sciences*, 1:235–242, 1993.

[144] C. T. Kelley. *Solving nonlinear equations with Newton's method (Fundamentals of algorithms)*. SIAM, Philadelphia, USA, 2003.

[145] J. Giner-Navarro, L. Baeza, P. Vila, A. Alonso. Study of falling friction effect on rolling contact parameters. *Tribology Letters*, 65:29, 2017.

[146] C. Tomberger, P. Dietmaier, W. Sextro, K. Six. Friction in wheel/rail contact: a model comprising interfacial fluids, surface roughness and temperature. *Wear*, 271:2–12, 2011.

[147] M. Avlonitis, K. Kalaitzidou, J. Streator. Investigation of friction statics and real contact patch by means a modified OFC model. *Tribology International,* 69:168–175, 2014.

[148] E.J. Berger, T.J. Mackin. On the walking stick–slip problem. *Tribology International*, 75:51–60, 2014.

[149] A. Alonso, A. Guiral, L. Baeza, S.D. Iwnicki. Wheel–rail contact: experimental study of the creep forces–creepage relationships. *Vehicle System Dynamics*, 52 Suppl. 1:469–487, 2014.

[150] O. Polach. Influence of locomotive tractive effort on the forces between wheel and rail. *Vehicle System Dynamics*, 25:7–22, 2001.

[151] J.G. Giménez, A. Alonso, E. Gómez. Introduction of a friction coefficient dependent on the slip in the FastSim algorithm. *Vehicle System Dynamics*, 43:233–244, 2005.

[152] L. Baeza, P. Vila, A. Roda, J. Fayos. Prediction of corrugation in rails using a non-stationary wheel/rail contact model. *Wear*, 265:1156–1162, 2008.

[153] M. Spiryagin, O. Polach, C. Cole. Creep force modelling for rail traction vehicles based on the Fastsim algorithm. *Vehicle System Dynamics,* 51:1765–1783, 2013.

[154] E. Rabinowicz. The nature of the static and kinematic coefficients of friction. *Journal of Applied Physics*, 22:1373–1379, 1951.

[155] J. Martínez-Casas, L. Mazzola, L. Baeza, S. Bruni. Numerical estimation of stresses in railway axles using a train/track interaction model. *International Journal of Fatigue*, 47:18–30, 2013.

[156] P. Vila, L. Baeza, J. Martínez-Casas, J. Carballeira. Rail corrugation growth accounting for the flexibility and rotation of the wheelset and the non-Hertzian and non-steady state effects at contact patch. *Vehicle System Dynamics*, 52:92–108 (Supplement 1), 2014.

[157] K. Popp, I. Kaiser. Interaction of elastic wheelsets and elastic rails: modelling and simulation. *Vehicle System Dynamics*, 44:S932–S939 (Suppl.), 2006.

[158] I. Kaiser. Refining the modelling of vehicle-track interaction, *Vehicle System Dynamics*, 50:S229–S243 (Suppl.), 2012.

[159] J. Martínez-Casas, J. Fayos, F.D. Denia, L. Baeza. Dynamics of damped rotating solids of revolution through an Eulerian modal approach. *Journal of Sound and Vibration*, 331:868–882, 2012.

[160] J. Martínez-Casas, E. Di Gialleonardo, S. Bruni, L. Baeza. A comprehensive model of the railway wheelset/track interaction in curves. *Journal of Sound and Vibration*, 333:4152–4169, 2014.

[161] L. Baeza, A. Roda, J.C.O. Nielsen. Railway vehicle/track interaction analysis using a modal substructuring approach. *Journal of Sound and Vibration*, 293:112–124, 2006.

[162] L. Baeza, H. Ouyang. A railway track dynamics model based on modal substructuring and cyclic boundary condition. *Journal of Sound and Vibration*, 330:75–86, 2011.

[163] P.M. Mathews. Vibrations of a beam on elastic foundation, *Zeitschrift f_ur Angewandte Mathematik und Mechanik*, 38:105–115, 1958.

[164] P.M. Mathews. Vibrations of a beam on elastic foundation II. *Zeitschrift f_ur Angewandte Mathematik und Mechanik*, 39:13–19, 1959.

[165] L. Jézéquel. Response of periodic systems to a moving load. *Journal of Applied Mechanics (ASME)*, 48:613–618, 1981.

[166] S. Timoshenko, D.H. Young, W. Weaver Jr. *Vibration Problems in Engineering* (4th edn). John Wiley: New York, 1974.

[167] C.G. Koh, J.S.Y. Ong, D.K.H. Chua, J. Feng. Moving Element Method for train/track dynamics. *International Journal for Numerical Methods in Engineering*, 56:1549–1567, 2003.

[168] C.G. Koh, G.H. Chiew, C.C. Lim. A numerical method for moving load on continuum. *Journal of Sound and Vibration*, 300:126–138, 2007.

[169] A.L. Kimball. Internal friction theory of shaft whirling. *General Electric Review*, 27:224–251, 1924.

[170] S. Blanes, F. Casas, J.A. Oteo, J. Ros. The Magnus expansion and some of its applications. *Physics Reports*, 470:151–238, 2009.

[171] L. Chen, Y. Zhang, W. Ren, G. Qin. *Dynamic Analysis of Mechanical Systems and Application Guide ADAMS*. Beijing: Tsinghua University Publishing Company, 2000.

[172] J.C.O. Nielsen, A. Igeland. Vertical dynamic interaction between train and track – influence of wheel and track imperfections. *Journal of Sound and Vibration*, 187(5):825–839, 1995.

[173] J.C.O. Nielsen. Dynamic interaction between wheel and track – a parametric search towards an optimal design of rail structures. *Vehicle System Dynamics*, 23(2):115–132, 1994.

[174] J. Martínez-Casas, J. Giner-Navarro, L. Baeza, F.D. Denia. Improved railway wheelset-track interaction model in the high-frequency domain. *Journal of Computational and Applied Mathematics*, 309, 642–653, 2016.

[175] L. Mazzola, Y. Bezin, S. Bruni. *Vehicle-Track interaction: MB simulation for track loading limits and damage identification ECCOMAS Thematic Conference Multibody Dynamics 2011*, July 4-7 2011, Brussels, Belgium.

[176] I. Kaiser. Refining the modelling of vehicle-track interaction. *Vehicle System Dynamics*, 50(Suppl.):S229–S243, 2012.

[177] F. Braghin, S. Bruni. G. Diana. Experimental and numerical investigation on the derailment of a railway wheelset with solid axle. *Vehicle System Dynamics*, 44(4): 305–325, 2006.

[178] ISO 3095:2005. *Railway applications. Acoustics. Measurement of noise emitted by railbound vehicles*. CEN, Brussels, August 2005.

[179] H. Ouyang, W. Nack, Y. Yuan, F. Chen. Numerical analysis of automotive disc brake squeal: a review. International Journal of Vehicle Noise and Vibration, 1(3-4):207–231, 2005.

[180] P.T. Torstensson. Rail corrugation growth on curves. Ph. D. Dissertation, Department of Applied Mechanics, Chalmers University of Technology, Gothenburg, Sweden, 2012.

[181] P.T. Torstensson, A. Pieringer, L. Baeza. Towards a model for prediction of railway tread brake noise. In The ISMA conference on Noise and Vibration Engineering (ISMA2014), Leuven, Belgium, 3543–3556, 2014.

[182] P.T. Torstensson, J.C.O. Nielsen. Monitoring of rail corrugation growth due to irregular wear on a railway metro curve. Wear, 267(1-4):556–561, 2009.

[183] F. Massi, L. Baillet, O. Giannini, A. Sestieri. Brake squeal: Linear and nonlinear numerical approaches. Mechanical Systems and Signal Processing, 21:2374–2393, 2007.

[184] J.B. Ayasse, H. Chollet. Wheel/rail contact. In S. Iwnicki, editor, *Hand-book of Railway Vehicle Dynamics*, chapter 4. CRC Press, Taylor and Francis Group, Boca Raton, FL, 2006.